UNIVERSITÉ DU LUXEMBOURG

PhD-FSTM-2020-29
The Faculty of Sciences, Technology and Medicine

DISSERTATION

Defence held on 19/06/2020 in Luxembourg

to obtain the degree of

DOCTEUR DE L'UNIVERSITÉ DU LUXEMBOURG

EN SCIENCES DE L'INGÉNIEUR

by

András Sándor KOZMA
Born on 17 September 1990 in Miskolc, (Hungary)

DEMOUNTABLE COMPOSITE BEAMS: ANALYTICAL CALCULATION APPROACHES FOR SHEAR CONNECTIONS WITH MULTILINEAR LOAD-SLIP BEHAVIOUR

Dissertation defence committee

Prof. Dr.-Ing. Christoph Odenbreit, Dissertation supervisor
Professor, University of Luxembourg, Faculty of Science, Technology and Medicine

Prof. Dr.-Ing. Markus Schäfer, Chairman
Professor, University of Luxembourg, Faculty of Science, Technology and Medicine

Dr.-Ing. Renata Obiala, Vice-chairman
Head of Construction and Infrastructure Applications Department, ArcelorMittal Global R&D

Prof. Dr.-Ing. Wolfgang Kurz
Professor, Fachgebiet Stahlbau, Technische Universität Kaiserslautern

Dr.-Ing. Wioleta Barcewicz
Assistant Professor, Faculty of Civil Engineering, Warsaw University of Technology

Preface

This thesis was realised during my time as a research assistant at the ArcelorMittal Chair of Steel Construction at the University of Luxembourg.

First of all, I would like to express my special thanks to my supervisor *Prof. Christoph Odenbreit* for offering me the opportunity to perform this research work and for his patient guidance. I would also like to thank him for supporting me both professionally as well as personally during the past four years.

I would like to express my special appreciation to the members of my thesis supervision committee: *Dr. Renata Obiala* and *Prof. Markus Schäfer* for their support and their constructive criticism along the way, which helped me in the realisation of this thesis.

My thanks are also due to all members of the REDUCE group, with whom it was a pleasure to work together on this interesting research topic. I would like to give special thanks to *Dr. Michael Sansom* for taking the burden of being the project coordinator. In addition, I would like to thank *Prof. Mark Lawson, Prof. Dennis Lam* and *Prof. Milan Veljković* for their valuable comments and for the constructive discussions that we had during our personal and online meetings. I am particularly grateful to *Dr. Ana M. Girão Coelho* for working together with me.

I would like to offer special thanks to †*Prof. István Bódi*, my former supervisor at the Budapest University of Technology and Economics, who is sadly no longer with us. I would like to thank him for his support and encouragement that led me to the path of science.

Furthermore, I would like to thank all members of the ArcelorMittal Chair of Steel Construction. Special thanks to *Jie Yang, Matthias Braun, Yves Staudt, Job Duarte da Costa, Maciej Chrzanowski, Valentino Vigneri and Ali Azim Azary* who accompanied me during my research work. In addition, I would like to thank the support team of the laboratory of the University of Luxembourg. Special gratitude to *Marc Seil, Logan Freitas, Claude Collé, Vincent Reis Adonis, Ed Weyer* and *Gilbert Klein.*

I am grateful for the students who contributed to this research work, *Sara Jung* and *Valter Pereira de Matos* in particular.

I would like to thank my colleagues *Anja Degens, Haiqin Huang, Steffen Bechtel* and *Sebastian Latz*, with whom I shared the office. They contributed greatly for the pleasant work environment that I experienced during the past four years.

Last but not least, I would like to express my sincere thanks to my wife and my family who have emotionally supported me to execute the presented research.

Trier, in May 2020 *András Kozma*

Abstract

The work carried out throughout the thesis focused on the behaviour of demountable composite beams in order to facilitate the integration of steel-concrete composite construction into the concept of circular economy. There are several hindrances in the way of reuse when considering traditional composite structures. One of them is the method that the current construction practice applies for connecting the concrete deck to the steel beam. The traditionally applied welded studs are advantageous in the terms of structural performance; however, they do not provide the ability of dismounting. In order to overcome this issue, different demountable shear connection types were investigated that use pretensioned bolted connections. The investigations included laboratory experiments in the means of push-out tests and full-scale beam-tests. The experiments were complemented by numerical simulations and parametric studies.

The experiments showed that the developed shear connections have highly a nonlinear load-slip behaviour. When these types of connections are applied in a composite beam, the nonlinearity of the shear connection causes a nonlinear load-deflection response already in the elastic phase. Analytical equations were derived for the description of the elastic properties of composite beams with nonlinear shear connection. For the calculation of the elastic deflections an iterative procedure was developed. This method is capable of capturing the nonlinear load-deflection response. With the developed iterative method, the elastic deflections can be determined with a similar accuracy by using spreadsheet calculations as by using nonlinear finite element simulations.

Due to the highly nonlinear behaviour of the tested shear connections the basic assumptions of Eurocode 4 for the determination of the plastic moment resistance of composite beams with partial shear connection are not valid anymore. The code does not enable the use of equidistant shear connector spacing and the design needs to be conducted using fully elastic analysis. This would make the use of demountable shear connections complicated and uneconomic. In the face of these issues, the probability of the practical application of demountable and reusable composite structures would be very low. On the other hand, experiments and numerical simulations show that composite beams can develop plasticity even if a non-ductile shear connection is applied. In order to overcome these issues, a new calculation method was developed for the prediction of the plastic moment resistance of demountable composite beams. A simplified method was proposed based on the developed procedure by defining an effective shear resistance for the demountable shear connections. The effective shear resistance allows the current calculation method to be extended for demountable shear connections. In this way, the benefits of composite construction can be maintained while providing the possibility of reuse.

Keywords: Demountable composite beams, Circular Economy, Push-out tests, Iterative procedure, Effective second moment of area, Plastic moment resistance, Partial shear connection.

Table of contents

List of Figures

List of Tables

Chapter 1. Introduction

1.1 Motivation

Sustainable development is about our relationship with the natural environment, with the global economic system and with each other [1]. The concept of the circular economy is an essential part of sustainable development. This concept is based on the efficient allocation of resources. Three terms are frequently used when talking about this concept: reduce, reuse and recycle. Reducing is cutting back on the amount of waste we produce; reusing is finding a new way to use our products so that they do not become waste; and recycling is using the materials of our products to produce new materials.

The traditional life-cycle of a building usually does not follow a circular model but a linear one from the extraction of the raw materials through material production, component manufacturing, building construction and building use. Finally, the building is usually demolished and most of the materials become debris and go into landfill [2]. Sustainable development requires the end-of-life impact of a building to be minimized [3]. In order to change from a linear model to a circular one some sort of recycling process have to be applied when the lifetime of a building is over. To be able to do this, the demolition process has to be replaced with a deconstruction process. This means that instead of destroying the undesired buildings, we dismount them in such a way that the building components are preserved in a valuable condition.

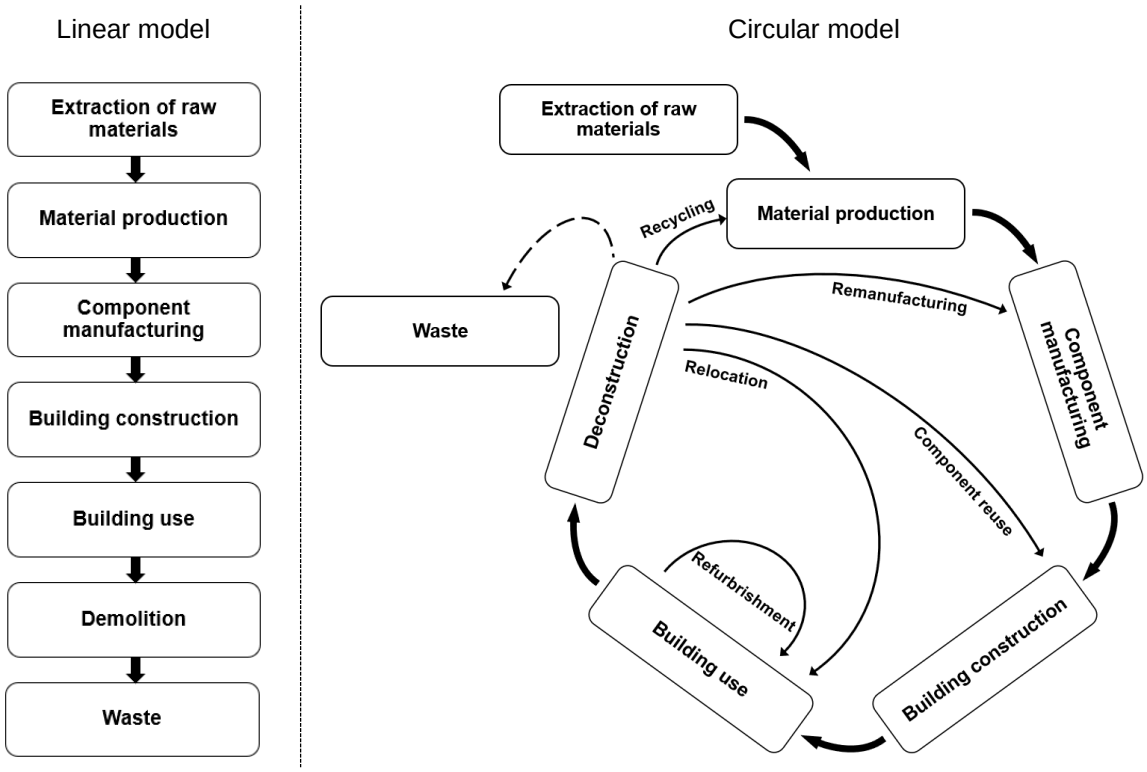

Figure 1.1 Linear vs. circular model of the life-cycle of a building

This way we can reduce waste production and the overall environmental impact. Figure 1.1 shows how the deconstruction process enables the change from a linear to a circular model.

Deconstruction of buildings has a long tradition throughout human history. Reusing building components was an obvious choice during times when the labour costs were low and the transportation was slow and expensive. A series of legal documents from the third and the fourth century indicate that even the Romans had a proper culture in reusing architectural components [4]. We can find several examples from the ensuing centuries when a city or a state organised auctions to sell the deconstructed building components such as stones, bricks, marble pieces, cast iron elements, woodworks, and complete windows as well. This tradition came to an end somewhere between the First and the Second World War due to the industrialisation of the construction sector. There were several factors that contributed to this change: parallel to the increase of labour costs, the transportation of building materials became easier, faster and cheaper. In cities, which were undergoing a rapid development like for example New York, the time pressure on the deconstruction companies increased significantly. It was no longer worth preserving the building materials from the economic aspect. The developers wanted to have the obsolete buildings disappear as quickly as possible. With the appearance of new inventions like the wrecking ball, the jackhammer and the multifunctional excavators, the deconstruction process quickly transformed to be a demolition process. Destroying buildings with no regard to the potential value in its components became a standard until very recently when sustainability is becoming increasingly important in the face of climate change and the depletion of finite natural resources. This is especially true in the construction industry, which is responsible for the 11% of global carbon dioxide emissions [5]. Nowadays, the potential environmental, social and economic benefits of the circular economy becoming more and more evident. Nonetheless, its application is still not a common practice [6].

There are five possible end-of-life scenarios for a building when the principles of the circular economy are applied, [2]:

(i) reuse in place (refurbishment),
(ii) relocation,
(iii) component reuse in a new building,
(iv) remanufacturing of the building components, and
(v) material recycling into new building materials.

These scenarios are in a hierarchic relationship with each other (see Figure 1.2): building relocation and component reuse are more desirable options with regard to environmental aspects than recycling and remanufacturing as they require less energy input and they produce less waste and CO_2.

Structural steel is highly compatible with the concept of circular economy. As a material, it is 100% recyclable for an infinite number of times. Steel is the most recycled material in the world today [7] because it can be reused in many ways due to its durability. Also, structural steel works are highly

prefabricated and the components are usually connected together by dismountable mechanical connections. These attributes make structural steel an ideal candidate for reuse.

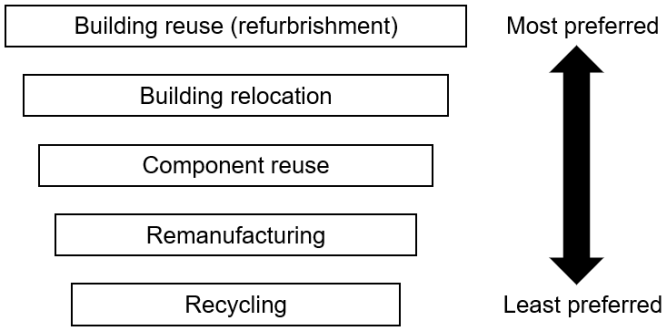

Figure 1.2 Hierarchic relation between the different end-of-life scenarios

Steel-concrete composite structures are very efficient in terms of structural performance; however, they are more difficult to dismount. The structural efficiency is reached by connecting the two materials so that they act as a single member. Each material is used where it is most efficient: the concrete is placed where predominantly compression forces arise and the steel is placed where the member is usually in tension. For the structural performance it is crucial to have an adequate connection between the members. The connection needs to be capable of transferring the shear forces at the steel-concrete interface. Traditionally, this is provided by headed stud shear connectors. During the construction of a composite beam, the studs are first welded to the flange of the beam and then concrete is cast. As a result, the members are firmly connected together. This is good for in terms of structural efficiency, but it is quite unfavourable from the demountability point of view. It is not possible to deconstruct this kind of structures, but they need to be demolished. This process is a labour and cost intensive work because the separation of the materials requires a vast amount of cutting. As a result, reusing the structural members is not an option, and already the recycling process is relatively difficult. In order to make steel-concrete composite structures demountable, the shear connection needs to be demountable first.

The behaviour of demountable shear connections is usually different from the behaviour of welded studs. Although there has been a certain amount of research conducted on this topic; this amount is still relatively low when compared to welded studs. As a result, the determination of the longitudinal shear resistance of the shear connection and the calculation of the occurring deflections can be challenging. This thesis aims to fill this knowledge gap by identifying the advantages and drawbacks of the different types of demountable shear connections; it investigates different types of connections that can overcome some of the identified hindrances; and it provides calculation methods for the description of the behaviour of composite beams with shear connections that have a multilinear load-slip curve. This includes an iterative procedure for the calculation of the elastic deflection and an algorithm for the calculation of the plastic bending resistance of composite beams with shear connections that have a multilinear load-slip behaviour..

1.2 Scope and limitations

The aim of the presented work is to provide calculation methods for composite beams in buildings with shear connections that have a nonlinear load-slip behaviour. The presented approaches are limited to simply supported downstand steel-concrete composite beams with cross section Class 1 and Class 2 according to Eurocode 3 [8]. Only symmetrical load cases are considered in the thesis: sinusoidal loading, uniformly distributed loading, and one- or two-point concentrated loads. The nonsymmetric load cases can be considered in an analogous manner. The questions of stability, the effects of fatigue, prestressing by tendons and fire actions are not considered.

1.3 Methodology

The following methodology was followed during the thesis:

(i) The available international literature on demountable shear connections (Chapter 2.1), the typical idealised load slip behaviours (Chapter 2.6) and the existing design code for composite beams (Chapter 2.3 and 2.4) were reviewed.

(ii) The different ductility definitions (Chapter 2.5) and the calculation methods for the approximation of the occurring end slip at the ultimate limit state (Chapter 2.7) were investigated.

(iii) The requirements for demountable shear connections were reviewed and new types of demountable shear connections were investigated (Chapter 3).

(iv) An experimental campaign was performed including push-out tests (Chapter 4) and full-scale beam tests (Chapter 5) using demountable shear connections.

(v) The experiments were reproduced numerically with the help of nonlinear finite element simulations (Chapter 6).

(vi) Parametric studies were conducted on the validated numerical models (Chapter 7).

(vii) First, the elastic behaviour of composite beams with conventional shear connections was investigated. Then, new equations were derived and an iterative procedure was developed for the description of the elastic behaviour of composite beams with shear connections that have a multilinear load-slip curve (Chapter 8).

(viii) The behaviour of composite beams in ultimate limit state was investigated. A new algorithm was developed for the determination of the plastic moment resistance of composite beams with partial shear connection using shear connections with multilinear load-slip curves and a simplification was proposed. The proposed methods are aligned with the current design code (Chapter 9).

The followed methodology is presented in Figure 1.3.

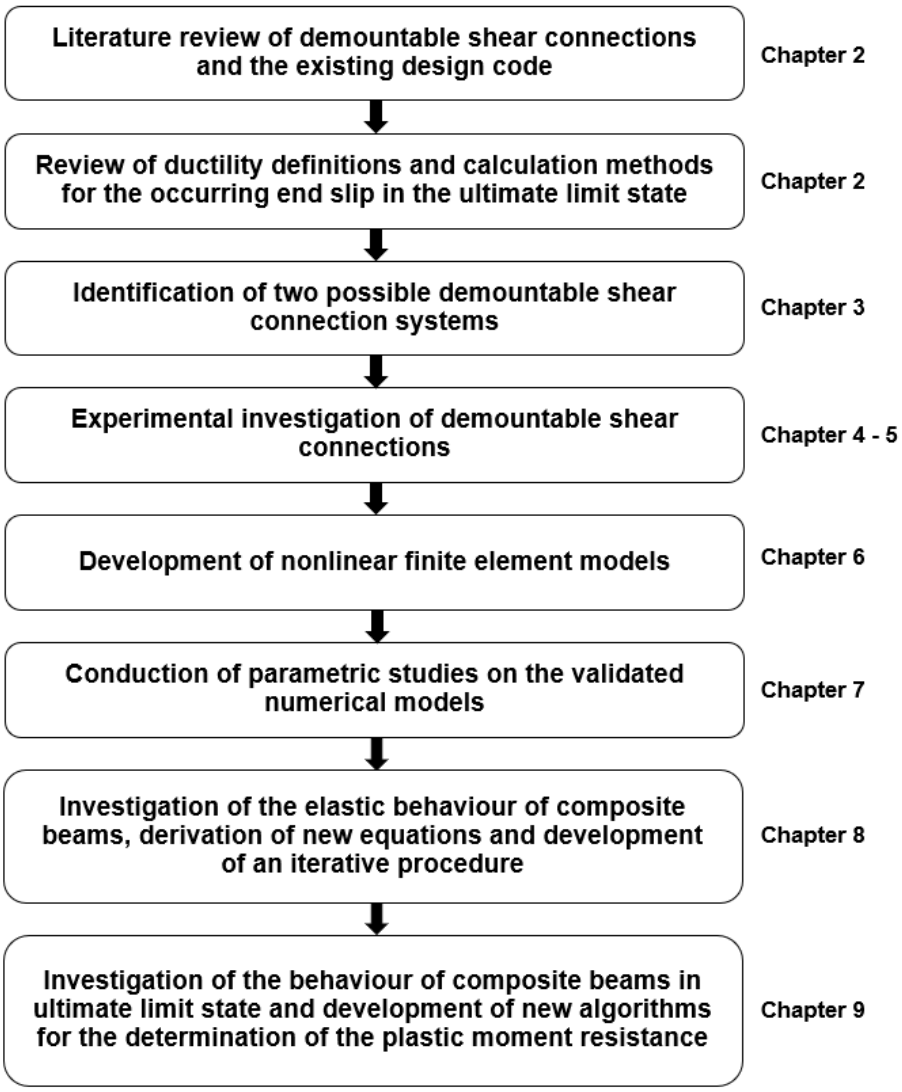

Figure 1.3 Methodology followed in the thesis

Chapter 2. State of the art

2.1 Demountable shear connectors

2.1.1 General

Dallam [9] and Marshall [10] investigated high-strength bolted shear connectors already five decades ago. However, the research on demountable shear connections is still very limited when compared to welded studs. The questions of demountability and reusability are becoming increasingly important as more emphasis is placed on sustainability. Different types of demountable bolted shear connections have been developed in the recent years. This chapter provides a brief overview on demountable shear connections.

2.1.2 Encased bolts and studs

The most commonly investigated demountable shear connectors are encased bolts. They are constructed by placing structural bolts into predrilled holes in the flange before casting concrete. The first report on this topic appeared in the international literature in 1968 by Dallam [9]. He conducted push-out tests on prestressed high strength friction grip (HSFG) bolt shear connectors (Figure 2.1) and found that the bolts exhibit zero slip in the working range of the load and their shear capacity is about twice that of studs.

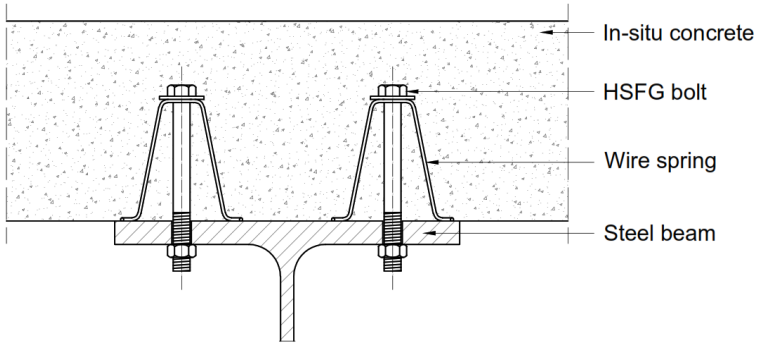

Figure 2.1 High-strength friction grip bolts tested by Dallam [9]

Dallam was followed by Dedic and Klaiber [11] who conducted two series of push-out tests on high strength bolted shear connectors for the strengthening of existing bridges. In the first series, they used bolts that were placed in openings in the concrete. The openings were filled with grout afterwards (Figure 2.2 left). In the second series, they investigated through bolts with pockets in the concrete. The pocket was filled with grout after tightening the bolt (Figure 2.2 right).

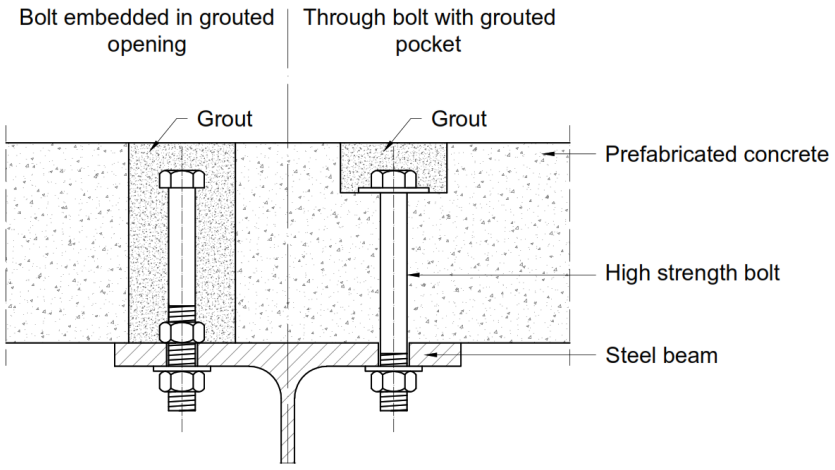

Figure 2.2 Bolted shear connectors tested by Dedic and Klaiber [11]

In the frame of a European project, Sedlacek et al. [12] investigated different shear connection types for small and medium span composite bridges. They conducted eighteen push-out tests. Ten of them investigated the static behaviour and eight of them examined the fatigue performance of the shear connections. The main objective of their research was the improvement of the shear connection using partially or fully prefabricated deck elements. The partially prefabricated deck elements used in-situ concrete around welded studs; and therefore, they were not demountable. The fully prefabricated slabs were connected to the steel beam by structural bolts of grade 10.9. The schematic view of the tested demountable solutions is presented in Figure 2.3 (Type Ia) and Figure 2.4 (Type Ib).

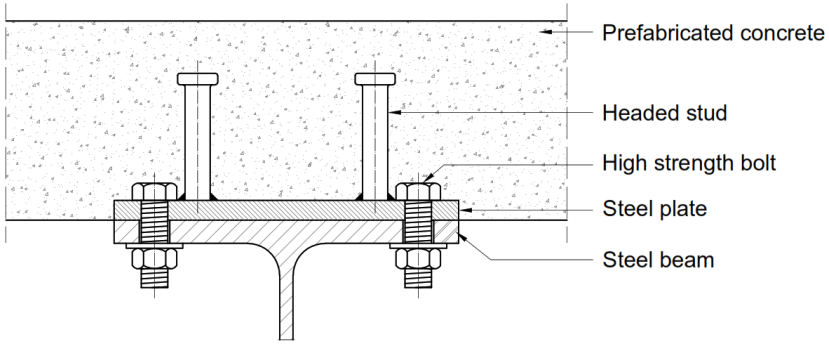

Figure 2.3 Headed studs in combination with bolts of grade 10.9 tested by Sedlacek et al. (Ia) [12]

They propose the following formulations for the total shear resistance of the connection type Ia for the critical section located above the steel plate:

$$F_u = n_s \cdot F_{stud} + n_b \cdot F_{c,bolt} \tag{2.1}$$

Where n_s is the number of studs, F_{stud} is the stud resistance n_b is the number of bolts and $F_{c,bolt}$ is the resistance at the head of the bolt. The stud shear resistance F_{stud} can be taken as the smaller resistance value obtained using the following equations:

$$P_{stud,1} = 0.35 \cdot d^2 \sqrt{E_{cm} \cdot f_{ck}} \tag{2.2}$$

$$P_{stud,2} = \pi \cdot d^2 f_u / 4 \tag{2.3}$$

Where d is the stud diameter, E_{cm} is the Youngs's modulus of the concrete, f_{ck} is the characteristic compressive strength of the concrete and f_u is the specified ultimate tensile strength of the material of the stud.

For the resistance at the bolt head $F_{c,bolt}$ they propose:

$$F_{c,bolt} = \sigma_{c,R} \cdot s_b \cdot h_{hb} \tag{2.4}$$

With:

$$\sigma_{c,R} = \beta \cdot f_{ck} \tag{2.5}$$

Where s_b and h_{hb} are the width and height of the head of the bolt, and β is a factor taking into account the effect of local stress concentration in front of the head of the bolt. It can be taken as twice the cylinder strength of concrete.

For the second critical section, which is located between the steel plate and the steel beam, they recommend to use the shear resistance of the bolt:

$$F_{v,R} = 0.6 \cdot f_{ub} \cdot A \tag{2.6}$$

Where f_{ub} is the tensile strength of the bolt material and A is the cross-sectional area of the bolt.

For connection type Ib, there are two critical failure modes. The first failure mode is crushing of concrete in front of the nuts and the bolt, and the second failure mode is bolt shear failure. For the first failure mode they give the resistance F_u as the sum of the resistance determined by the shank of the bolt $F_{c,s}$ and by the nut $F_{c,nut}$.

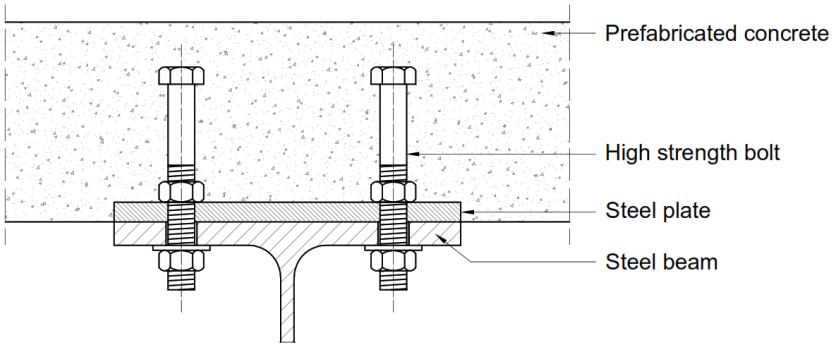

Figure 2.4 Shear connection with bolts of grade 10.9 tested by Sedlacek et al. (Ib) [12]

$$F_u = n_b(F_{c,s} + F_{c,nut}) \tag{2.7}$$

$$F_{c,s} = 0.35\, d_s^2 \sqrt{E_{cm} \cdot f_{ck}} \tag{2.8}$$

$$F_{c,nut} = \sigma_{c,R} \cdot s_n \cdot 2 \cdot h_n \tag{2.9}$$

Where d_s is the diameter of the bolt shank and s_n and h_n are the width and height of the nut.

For the bolt shear failure, Equation (2.6) can be used.

Schaap [13] conducted several push-out tests on post-installed shear connectors. He discussed the behaviour of embedded bolts, friction grip bolts and anchor bolts (see Figure 2.5) in his thesis. His research was continued by Kwon et al. [14], [15] who summarised the strengthening possibilities of existing non-composite steel bridges using post-installed shear connectors. They investigated the shear connection behaviour under static and fatigue loading. They proposed to use the following equation for the shear resistance of bolted shear connectors:

$$F_{v,R} = 0.5 \cdot f_{ub} \cdot A \tag{2.10}$$

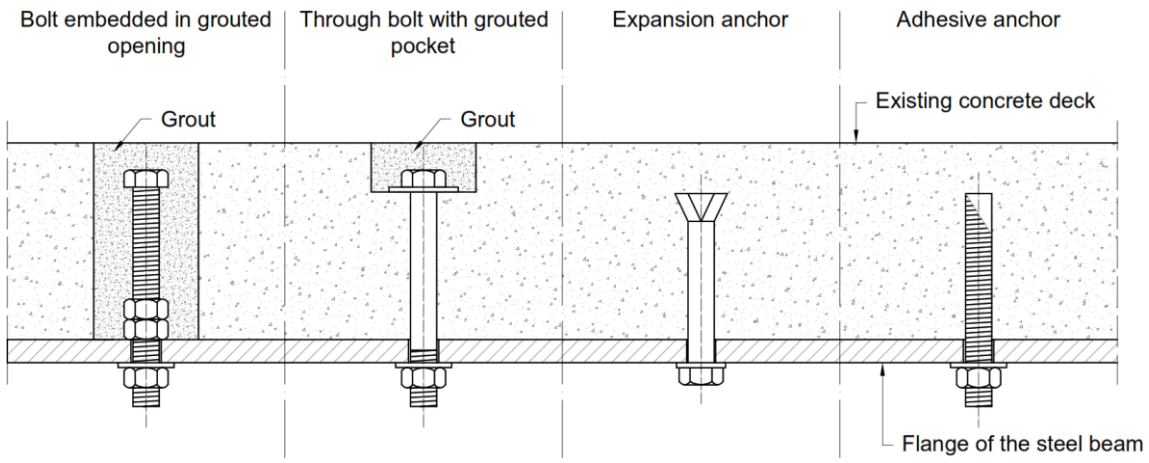

Figure 2.5 Post-installed demountable shear connectors tested by Schaap [13] and Kwon et al. [14]

More recently, Pavlovic [16] investigated encased bolts. He conducted two series of push-out tests with different bolt diameters (Figure 2.6). He used prefabricated concrete elements with openings at the shear connectors. The openings were filled with concrete after the positioning of the deck elements. He developed a numerical model based on the experimental results and derived the following formulae for the determination of the shear resistance of the investigated shear connections:

$$P_{b,u} = \alpha_b f_{ub} A_s, \text{ with } \alpha_b = 0.6(34/d)^{0.23} \tag{2.11}$$

$$P_{c,u} = 55 \cdot \alpha_c \cdot d^{1.9}(f_{cm} \cdot h_{sc}/d)^{0.4} + 22000, \text{ with } \alpha_c = 22.5/(d+3) \leq 1.0 \tag{2.12}$$

Where P_{bu} is the resistance of the bolt, f_{ub} is the tensile strength of the bolt material, *As* is the shear area of the bolt, *d* is the bolt diameter, P_{cu} is the resistance of the concrete, f_{cm} is the mean value of the concrete cylinder strength and h_{sc} is the height of the shear connector.

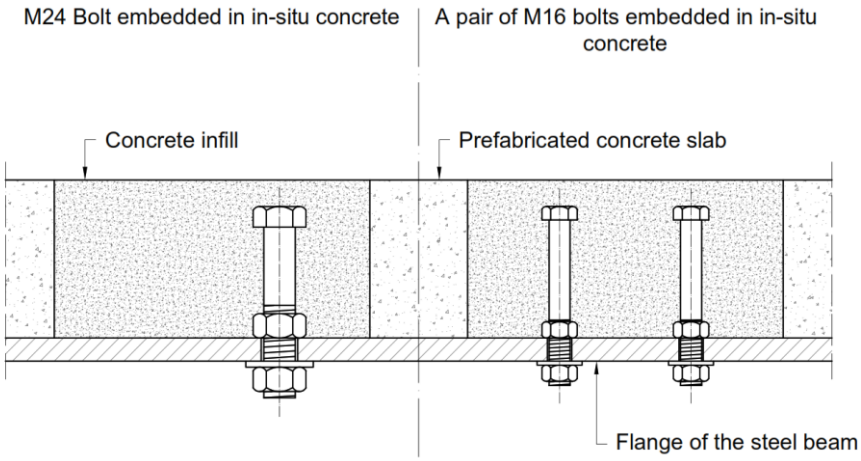

Figure 2.6 Demountable shear connectors tested by Pavlovic [16]

Moynihan and Alwood [17] conducted tests on three composite beams of different lengths using M20 bolts as demountable shear connectors (Figure 2.7). Two beams were loaded until service loads, unloaded, dismounted and reassembled in order to test the demountability and reusability of the system. Afterwards, all three beams were loaded until failure. They found that the longer specimens (5 m and 10 m) behaved similarly to comparable composite beams with welded shear connectors. The tested beams had higher resistance than calculated using Eurocode 4 [18].

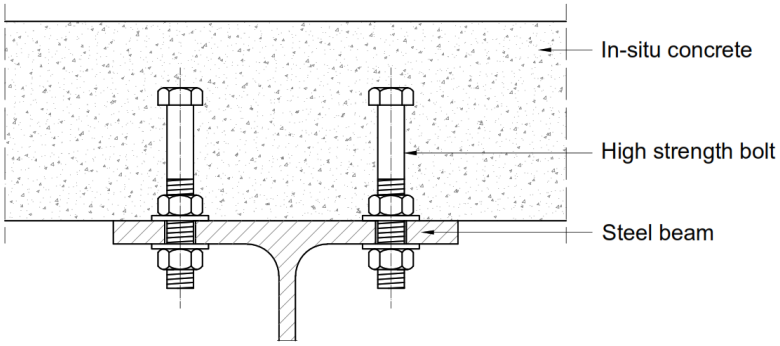

Figure 2.7 Demountable shear connectors tested by Moynihan and Alwood [17]

Lam and Dai [19], [20] developed a demountable shear connector that can be manufactured from headed studs by cutting threads into the end of the studs (Figure 2.8). As a result, no welding is necessary and the shear connectors can be installed through predrilled holes in the flange. They conducted push-out tests, and found that the performance and the behaviour is similar to the welded studs. Also, the tests showed a high level of ductility but a lower initial stiffness. Rehman et al. [21] continued their research

by investigating different types of demountable shear connectors in slabs with profiled decking. Twelve push-out tests were prepared including M20 bolts and threaded studs with different diameters. The high level of ductility and the relatively low initial stiffness was confirmed. Additionally, they found that concrete strength affects the behaviour of the connectors. An increase in the concrete strength results in higher shear connector resistance but a lower level of ductility.

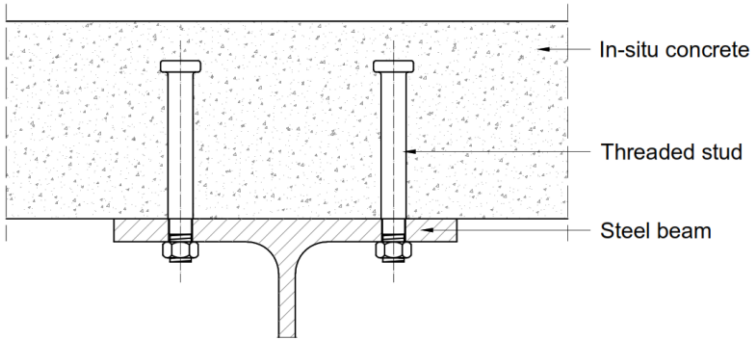

Figure 2.8 Threaded stud shear connectors tested by Lam et al [19]

Wang et al. [22] conducted push-out tests on demountable shear connectors similar to the ones tested by Lam et al. [19] - [21]. They used Ultra High Performance Concrete (UHPC) and threaded headed studs with different diameters and collar lengths. They found that the tested shear connectors did not have 6 mm deformation capacity; and therefore, they proposed to use an elastic design method when demountable shear connectors are used in steel-UHPC composite beams.

2.1.3 Through bolts

The earliest identified research on tests with through bolts was conducted by Marshall et al. [10] in 1971. He conducted eleven push-out tests and five beam tests on friction grip connectors. He observed that the friction coefficient was 0.45 between the precast slab and the steel beam, and it was possible to achieve full interaction under service loads.

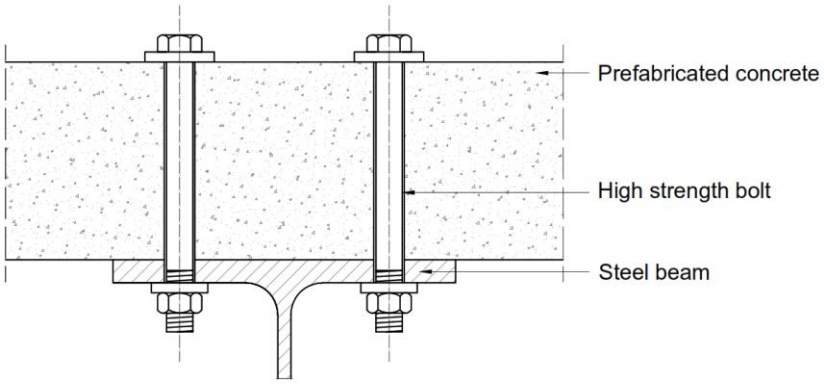

Figure 2.9 Bolted shear connection tested by Marshall [10]

Roik and Bürkner [23] investigated the friction coefficient between steel and prefabricated concrete decks in 1978. They conducted four types of tests: Group 1 used two 15 mm thick steel plates and two concrete elements. Group 2 had an identical test setup to Group 1 but with 10 mm thick steel plates.

The test setup of Group 3 was similar to the push-out test setup given by Eurocode 4 [18]. These tests consisted of an IPE 300 steel profile and four prefabricated deck elements (Figure 2.10). Each of the deck elements were connected to the steel profile by three pretensioned M16 bolts. These three test groups were subjected to a single load cycle in displacement controlled mode with a speed of 1 mm / min without unloading . Group 4 used identical specimens to Group 1 but it was subjected to a dynamic loading that included 3 million cycles with 10 Hz frequency. They tested different levels of pretension and found that the friction coefficient varied between 0.501 and 0.555.

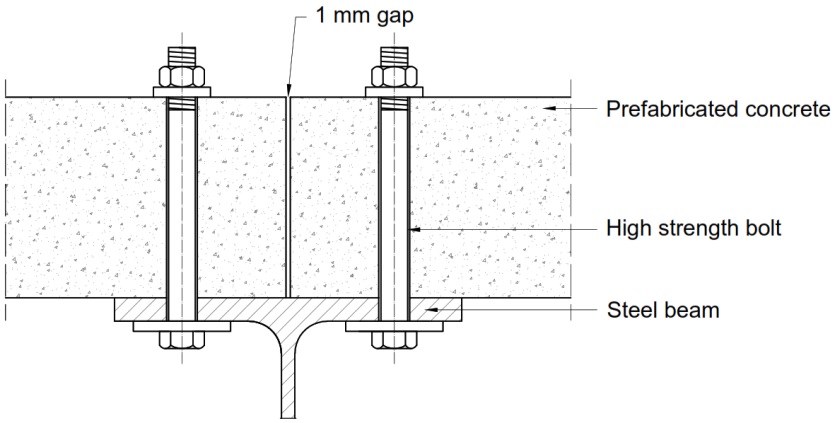

Figure 2.10 Friction connection tested by Roik and Bürkner [23]

Bürkner [24] in his thesis investigated composite beams with headed studs experimentally and numerically. While reviewing the different shear connection systems he gave the following connection type as a possible shear connection for carparks:

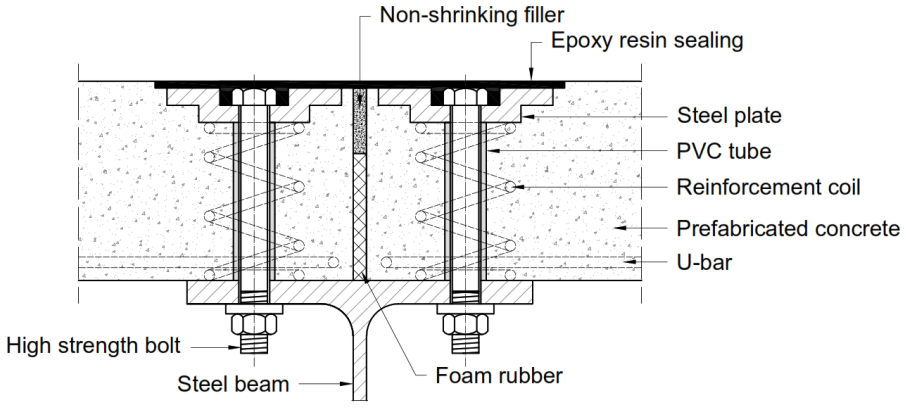

Figure 2.11 Demountable shear connection for carparks proposed by [24]

He also developed a finite element solution model as well as an approximation formula for the deflections of composite beams with partial shear connection. This is described in a more detailed way in Chapter 2.2.

A similar system was developed by the company Krupp-Druckenmüller GmbH in Germany. Their system was called as the Krupp-Montex system [25] and was applied majorly in carparks in the 1970s. The schematic drawing of their system is presented in the following figure:

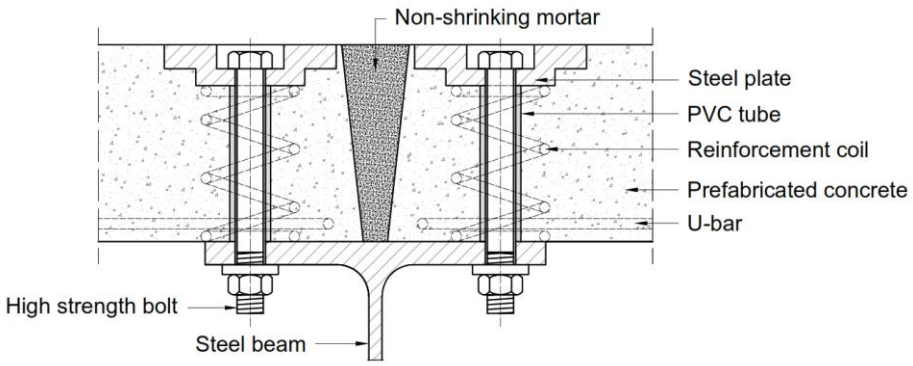

Figure 2.12 The Krupp-Montex system [25]

The research of Dedic and Klaiber [11], Schaap [13] and Kwon [14], [15] included tests on through bolts; however, in these tests the pockets above the bolt head was filled with grout or concrete. Therefore, these types of bolts are not accessible from the top of the deck after installation (see Figure 2.2 and Figure 2.5). Chen et al. [26] conducted push-out tests using through bolts placed in PVC tubes (Figure 2.13). The test parameters included the bolt diameter, the level of the bolt pretension and the steel-concrete contact surface properties. They observed that the ultimate shear capacity was similar to the one of welded studs, but the first slip occurred in a significantly lower load level. A mechanical model was proposed to predict the ultimate capacity. Afterwards, a finite element model was built to investigate the behaviour of demountable composite bridge girders using the proposed demountable connectors.

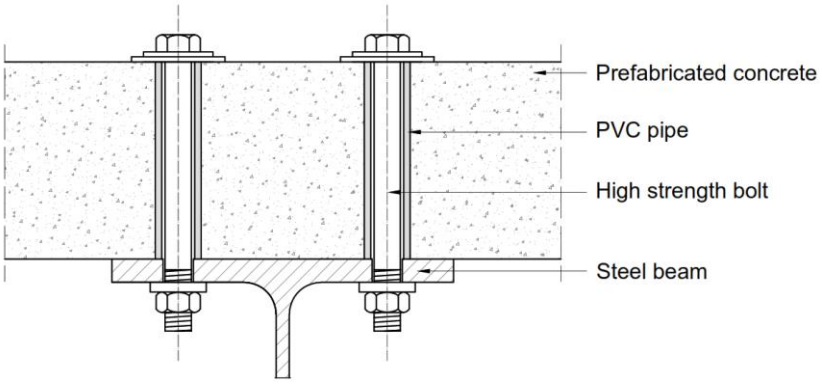

Figure 2.13 Through bolts tested by Chen et al. [26]

They gave the following equation for the bolt shear resistance:

$$V_R = (k_s \cdot \sin\alpha + \cos\alpha) \cdot T_{tot} + 0.6 \cdot A_b \cdot f_{ub} \cdot \sqrt{1 - \left(\frac{T_{tot}}{A_b \cdot f_{ub}}\right)^2} \tag{2.13}$$

Where k_s is the friction coefficient, the first part of the equation is the contribution of the friction, α is angle of the bolt measured from its original axis after deformation, T_{tot} is the sum of the bolt pretension and the tension due to connection slip, A_b is the area of the bolt and f_{ub} is the ultimate tensile strength of the bolt. In this formula the first part represents the contribution of the friction to the load bearing capacity. This contradicts the findings of Pavlović [16] who pointed out that the pretension force and the friction resistance do not influence the load-bearing capacity.

Through bolts used as demountable shear connectors were tested extensively at the University of New South Wales by Lee and Bradford [27], Ataei et al. [28], [29] and Liu et al. [30], [31]. The shear connection was similar to the ones tested by Marshall et al. [10] (Figure 2.9). They conducted several push-out tests [27], [28] on high strength friction grip bolted shear connectors and found that the load-slip behaviour can be divided into three distinct parts.

1) First, there is full interaction between the steel and the concrete until the friction resistance is overcome.
2) Second, bolt slip occurs until the bolt become in contact with the inner surface of the bolt hole.
3) Third, bearing and shear deformation takes place until the ultimate shear capacity is reached.

Based on these observations, they proposed a multilinear idealised elastic load-slip response (see Figure 2.14). They also conducted full scale beam tests using prefabricated concrete deck elements on 7 m long beam test specimens [31]. They developed a three-dimensional numerical model using the commercial finite element software Abaqus [32]. It was found that their numerical model could capture the fundamental behaviour of the demountable composite beam. The increase in the degree of partial shear connection resulted in higher resistance values. They recommended using a small number of shear connectors with large diameters instead of a large number of connectors with smaller diameters for the same degree of shear connection.

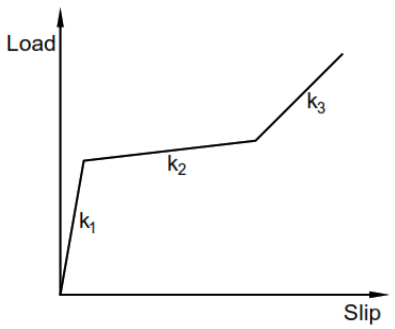

Figure 2.14 Idealised response in the elastic range by Lee and Bradford [27]

2.1.4 Other types of demountable connectors

A prefabricated and demountable composite bridge was already realised in 1975 using a shear connection that purely relies on friction [33]. Figure 2.15 shows the applied shear connection, which was comprised of a through bolt, a sleeper clip, a double lock washer and a neoprene plate.

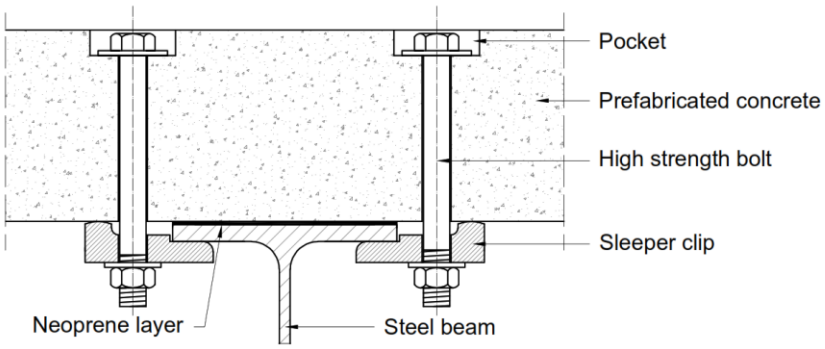

Figure 2.15 Friction connection used in the AB bridge [33]

Single shear connector tests on expansive and adhesive anchor bolts were performed by Schaap [13] and Kwon et al. [14], [15] (see Figure 2.5). Ban et al. [34] conducted push-out tests on blind bolt shear connectors and investigated the time dependent behaviour of composite beams using blind bolts as shear connectors under sustained loading. They installed the blind bolts prior to concrete casting. This is different from the procedure applied in the retrofitting of existing structures where the bolts are installed after the concrete has hardened. They were followed by Pathirana et al. [35] who conducted push-out tests and full-scale composite beam tests using blind bolts as shear connectors. The behaviour of the tested demountable composite beams was similar to the behaviour of beams with welded studs in terms of stiffness, strength and ductility. Uy et al. [36] investigated blind bolts using numerical simulations.

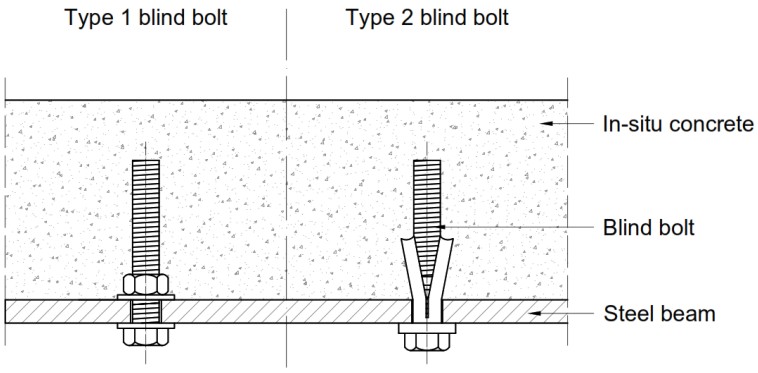

Figure 2.16 Blind bolts applied in beam tests by Ban et al. [34]

Suwaed and Karavasilis [37] developed a demountable shear connection with through-bolts, where the bolt clearance was grouted after installation (see Figure 2.17).

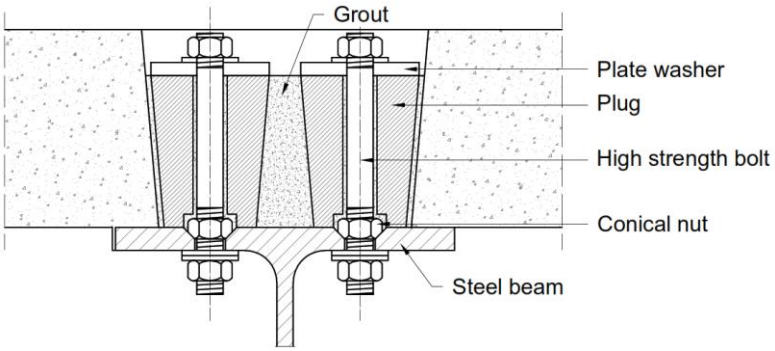

Figure 2.17 Demountable shear connection tested by Suwaed and Karavasilis [37]

Feidaki and Vasdravellis [38] conducted push-out tests on a shear connection that use a steel-yielding mechanism provided by a cold formed hollow steel section with slotted holes (Figure 2.18).

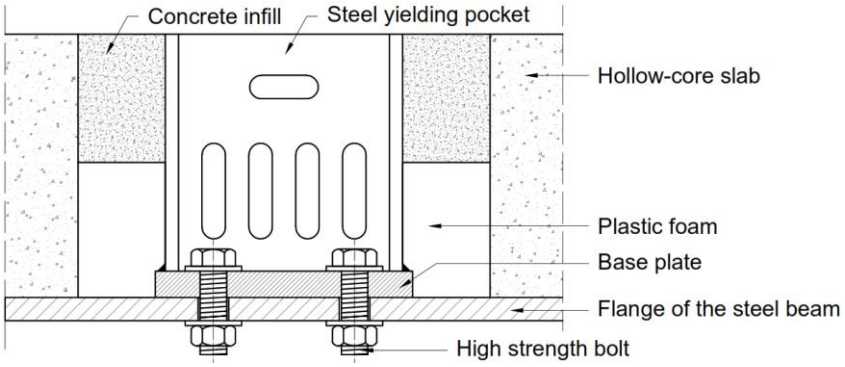

Figure 2.18 Steel yielding mechanism shear connection developed by Feidaki and Vasdravellis [38]

2.1.5 Summary

A number of researchers developed and investigated demountable shear connections in the past five decades. Although all of the previously reviewed solutions facilitate the demounting process, they provide different level of reusability. The primary focus was often put on the reusability of the steel beam alone, but not on the reusability of the concrete slab.

For example, when dismounted, the embedded bolts and studs (See ex.: Figure 2.7 and Figure 2.8) protrude from the surface of the slab. This makes them vulnerable during manoeuvring, transportation and storage. If the threads are damaged, the reuse potential of the slab is lost (or reduced) because these bolts being embedded in the concrete are not replaceable. According to EN 1090-2 [39], *"if a bolt assembly has been tightened to the minimum preload and is later un-tightened, it shall be removed and the whole assembly shall be discarded.*" This implies that if embedded bolts are preloaded, the slab is not reusable anymore.

Through bolts (Figure 2.13) are easily replaceable, and therefore more preferable in terms of reusability. However, their fabrication is a more complicated task. If the slabs are prefabricated, they require special

attention in terms of tolerances. It should be ensured that the predrilled holes in the flange and the holes in the slab align. Additionally, when friction grip bolts are used, creep and shrinkage can cause a loss in the pretension force in the bolt. BS 5400-5 [40] mentions that account should be taken of this effect, but it does not elaborate how.

Table 2.1 summarises the advantages and the disadvantages of the most commonly applied generic demountable shear connection types.

In terms of load-slip behaviour, preloaded through bolts (friction grip bolts) behave differently than traditional welded studs. Their behaviour can be divided into three distinct parts: a rigid part until the friction resistance is overcome, a more or less horizontal part representing the bolt slip inside the bolt hole, and a linear or nonlinear part caused by the shear and bearing deformation.

On the other hand, embedded bolts and studs reach their ultimate load at around 1-2 mm relative slip and they can maintain more or less this load level for at least 6 mm slip. This means that among the investigated demountable shear connections this is the only type that behaves similarly to welded studs.

Table 2.1 Demountable shear connections overview

Shear connection	Image	Advantages	Disadvantages
Encased bolts	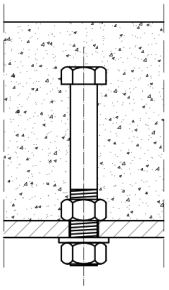	- Similar to the traditional solution. - High strength. - Possible use of pretensioning.	- Lower stiffness than welded studs. - The end of the bolt protrudes from the slab when removed. - The bolt is not replaceable. - Reuse of the slab is questionable. - Prefabrication is complicated.
Threaded studs	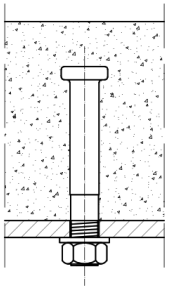	- Similar to the traditional solution. - Relatively low cost.	- Lower stiffness than welded studs. - When removed the end of the bolt protrudes. - The stud is not replaceable. - Reuse of the slab is questionable. - Prefabrication is complicated.
Through bolts	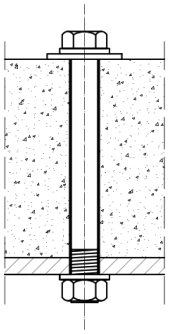	- The bolt is replaceable. - Relatively high strength. - No protruding parts from the slab when removed. - Provides access from the top.	- Lower stiffness than welded studs. - Loss of pretension due to creep and shrinkage. - Special attention is required for tolerances.
Anchor bolts and blind bolts	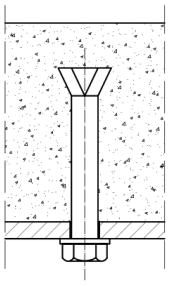	- No problems with tolerances. - Works with prefabrication and with in-situ concrete as well.	- Drilling in the concrete is necessary when prefabricated. - Lower stiffness than welded studs. - Relatively low strength.

2.2 Investigations of composite beams with flexible shear connection

The determination of the longitudinal shear force is important with regard to the elastic and plastic calculations of composite beams. The elastic longitudinal shear force is linearly proportional to the vertical shear force if rigid shear connection is used [41]:

$$v_{L,0}(x) = \frac{V_z(x) \cdot S_{i0}}{I_{y,eff}} \tag{2.14}$$

The concrete compression force can be calculated as:

$$F_0(x) = \frac{M_y(x) \cdot S_{i0}}{I_{y,eff}} \tag{2.15}$$

where $V_z(x)$ is the vertical shear force at a distance x from the support, $M_y(x)$ is the bending moment, S_{i0} is the static moment of the concrete section to the centroidal axis of the composite section and $I_{y,eff}$ (see Chapter 8) is effective the second moment of area of the composite section.

In the case of a flexible shear connection, the longitudinal shear force depends also on the flexibility of the connection as well as the loading situation. Hoischen [41] gave the closed solutions of the differential equation of composite beams for the longitudinal shear and the concrete compression forces for basic load cases.

For a uniformly distributed load:

$$F(x) = F_0 \left[1 - 2 \frac{\cosh \omega \frac{L}{2} - \cosh \omega \left(\frac{L}{2} - x \right)}{x(L-x)\omega^2 \cdot \cosh \omega \frac{L}{2}} \right] \tag{2.16}$$

$$v_L(x) = v_{L,0}(x) \left[1 - \frac{\sinh \omega \left(\frac{L}{2} - x \right)}{\left(\frac{L}{2} - x \right) \cdot \omega \cdot \cosh \omega x} \right] \tag{2.17}$$

For a point load acting at mid-span:

$$F(x) = F_0(x) \left[1 - \frac{\sinh \omega x}{\omega x \cosh \omega \frac{L}{2}} \right] \tag{2.18}$$

$$v_L(x) = v_{L,0}(x) \left[1 - \frac{\cosh \omega x}{\cosh \omega \frac{L}{2}} \right] \tag{2.19}$$

For a point load acting at a distance *z* from the support:

$$F(x) = F_0(x)\left[1 - \frac{L \cdot \sinh \omega\ z}{z\ \omega\ x \sinh \omega\, L} \sinh \omega\, x\right] \tag{2.20}$$

$$v_L(x) = v_{L,0}(x)\left[1 - \frac{L}{z}\frac{\sinh \omega\, x}{\sinh \omega\, L} \cosh \omega\, x\right] \tag{2.21}$$

Where ω is defined as:

$$\omega = \sqrt{\frac{k_{sc} \cdot a \cdot n \cdot I_{y,eff}}{a_b \cdot E_c \cdot A_c (I_{y,c} + I_{y,a})}} \tag{2.22}$$

where k_{sc} is the stiffness of the shear connection, a is the centroidal distance of the concrete and the steel, n is the modular ratio, $I_{y,eff}$ is the second moment of area of the composite section, a_b is the centroidal distance of the concrete and the composite section, E_c, A_c and $I_{y,c}$ are the Young's modulus, the cross-sectional area and the second moment of area of the concrete deck, respectively; and finally $I_{y,a}$ is the second moment of area of the steel.

Zhou et al. [42] also gave the closed solutions of the differential equation while complementing the derivations of Hoischen [41] by giving the solutions also for the deflection calculations. Because these equations are rather complex, they are not suitable for practical applications. To address this issue, they developed an approximation method, which is based on a spring model with an equivalent spring stiffness K_F. The effective normal stiffness and bending stiffness can be calculated as follows:

$$(EA)_{eff} = \frac{E_c A_c \cdot K_F \cdot E_a \cdot A_a}{E_c A_c + K_F L + E_a A_a} \tag{2.23}$$

$$\beta_{eff} = \frac{(EA)_{eff} a^2}{EI} \tag{2.24}$$

$$(EI)_{eff} = EI(1 + \beta_{eff}) \tag{2.25}$$

Where EI is the sum of $E_c I_{y,c}$ and $E_a I_{y,a}$.

The comparison of the results obtained by the exact and the approximate solutions showed a good agreement in the terms of bending stiffness, internal forces and deflections.

Hanswille and Schäfer [43] derived the second moment of area $I_{y,eff}$ of composite beams with flexible shear connection for a sinusoidal load. This corresponds to a sine shaped moment diagram but can also be used as an approximation for beams loaded uniformly, which have a second order moment diagram.

They define the longitudinal shear force as:

$$v_L(x) = \frac{k_{sc}}{s_{sc,eq}} \cdot s(x) \tag{2.26}$$

Where k_{sc} is the stiffness of one shear connector, $s_{sc,eq}$ is the equivalent shear connector spacing and $s(x)$ is the slip distribution function. A sinusoidal moment diagram corresponds to a cosine shaped slip distribution function:

$$s(x) = \bar{s} \cdot \cos\left(\frac{\pi x}{L}\right) \tag{2.27}$$

where $\bar{s}$ is the end slip, L is the span of the beam, and x is the distance along the length of the beam from a support.

As a result, the corresponding longitudinal shear force distribution also has a cosine shape:

$$v_L(x) = \frac{k_{sc}}{s_{sc,eq}} \cdot \bar{s} \cdot \cos\left(\frac{\pi x}{L}\right) \tag{2.28}$$

Lawson et al. [44] also started their derivations from the same assumptions as Hanswille and Schäfer [43] and obtained mathematically equivalent expressions for both the longitudinal shear force as well as the second moment of area:

$$I_{y,eff} = I_{y,a} + \frac{I_{y,c}}{n} + \frac{A_c/n}{1 + \frac{A_c}{nA_a} + \left(\frac{E_a}{k_{sc}/s_{sc,eq}}\right)\left(\frac{\pi}{L}\right)^2\left(\frac{A_c}{n}\right)} \cdot a^2 \tag{2.29}$$

The detailed presentation of these derivations is presented in Chapter 8.4 and in Annex C.

Bürkner [45] analysed composite beams with different types of shear connection using a self-developed finite element model. He used a Newton-Raphson iterative procedure that can follow the nonlinear behaviour of the steel and concrete materials beyond their elastic limit stresses. He applied an incremental equation that contains the elastic virtual work, an incremental correction part for the elastic work and the internal elastic-plastic work, which is equivalent to the external load increment. He performed the iterations as long as the stress that belongs to the correction part of the equation and the deformation increment is below a certain limit value. For the determination of the global plastic deformations of the composite beam he also used an iterative Newton-Raphson procedure. He compared his numerically obtained results with the results of the experiments that he conducted on 7.5 m long composite beams subjected to two-point concentrated loading, and he obtained a good correlation. He also gave an approximation formula for the elastic deflections (W_v^*) of composite beams with partial shear connection ($0.5 < \eta < 1$):

$$W_v^* = 1.1 \cdot W_v + \alpha(W_{st} - W_v)(1 - \eta) \tag{2.30}$$

Where W_v is the elastic deflection of an identical composite beam with full shear connection (η = 1) using perfectly rigid connectors, W_{st} is the deflection of the steel beam alone, η is the degree of shear connection and α = 0.1 – 0.2 is a parameter that depends on the height of the steel sheeting.

Kurz et al. [46] gives an iterative procedure for the determination of the stresses in the composite cross-section when the stresses in the section exceed their elastic limit. They propose an effective cross-section divided into lamellas in the *z*-direction:

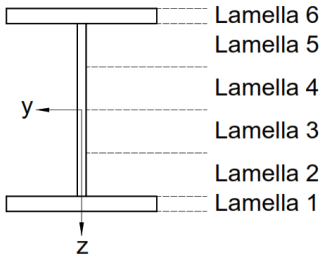

Figure 2.19 Lamellas of the section according to Kurz et al. [46]

The method is based on an iterative approximation method, which determines the resulting deformation and normal force transformation with reduced cross-sectional values of the elements, by the exceeding of the linear-elastic state due to a load ΔP. Then, the load under which the entire lamella 1 of steel or of concrete section reaches its critical yield point is determined iteratively. This load is decelerated during the iteration; and the normal force and the distribution of the stresses are determined due to an additional load ΔP using a reduced steel section in which lamella 1 is not considered anymore. In the next iteration step, the additional load ΔP is gradually increased until the entire lamella 2 reaches the yield stress. The cross-section values are reduced from the last load point, and the iterative process is performed on the remaining lamellae. Using this iterative method in combination with the differential equations solved by Zhou [42], they could reproduce the shear stresses on the shear interface of adhesive bonded composite beams with a high accuracy.

2.3 Resistances of cross-sections of beams according to Eurocode 4

2.3.1 General

Eurocode 4 [18] section 6.2.1.1 gives three approaches for the calculation of the bending resistance of a composite beam:

1) Rigid-plastic theory
2) Elastic analysis
3) Nonlinear theory

2.3.2 Rigid-plastic theory

The most frequently applied approach is the rigid-plastic theory in building construction. Eurocode 4 [18] clause 6.2.1.1 (1) allows to use this theory only if the effective composite section is Class 1 or Class 2 and where no pre-stressing tendons are used. This condition is usually satisfied in the case of simply supported beams where usually only a small part of the web is in compression (if any) and the concrete slab prevents the plate buckling of the compression flange [47].

This theory uses the following assumptions:

(i) The cross-section remains plane after deformations.
(ii) The steel is stressed to its design yield strength f_{yd} both in tension and in compression.
(iii) The effective concrete area above the plastic neutral axis is stressed to a stress of $0.85\, f_{ck} / \gamma_c$ where f_{ck} is the characteristic cylinder compressive strength.
(iv) The tensile resistance of the concrete is neglected.
(v) Reinforcement in compression is usually neglected.

Based on these assumptions, the location of the plastic neutral axis (PNA) and the plastic moment resistance can be determined using the equilibrium and the moment equations. As presented in Figure 2.20, the plastic neutral axis can be located in three different parts of the section. The following conditions help to decide whether it is in the concrete, in the flange or in the web of the steel beam:

PNA is in the concrete if $N_{pl,c} > N_{pl,a}$ (2.31)

PNA is in the flange if $N_{pl,\mathrm{a}} > N_{pl,c} > N_{pl,\mathrm{w}}$ (2.32)

PNA is in the web if $N_{pl,w} > N_{pl,c}$ (2.33)

where:

$N_{pl,c} = b_{eff} \cdot h_c \cdot 0.85 \cdot f_{cd}$ is the plastic compression resistance of the concrete,

$N_{pl,a} = A_a \cdot f_{yd}$ is the plastic tensile resistance of the steel, and

$N_{pl,w} = N_{pl,a} - 2 \cdot b \cdot t_f \cdot f_{yd}$ is the plastic tensile resistance of the web.

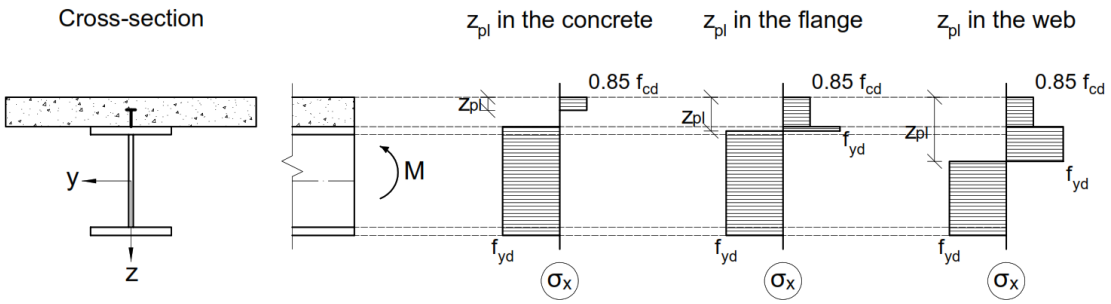

Figure 2.20 Possible plastic stress distributions for full shear connection

Due to the equilibrium condition, the maximum compression force that can develop in the concrete is limited by the resistance of the concrete or by the steel beam:

$$N_{cf} = \min\left(N_{pl,c}, N_{pl,a}\right) \tag{2.34}$$

According to Eurocode 4 [18] clause 6.1.1 (7)P, a beam has full shear connection when increase in the number of shear connectors would not increase the design bending resistance of the member. This means that for a full shear connection the shear connectors should be able to transfer the force that corresponds to the aforementioned plastic stress distribution. Otherwise, we are talking about partial shear connection.

When the shear connectors can be represented by a rigid-plastic behaviour each of them develops the same shear force irrelevant of the slip. As a result, the developing compression force in the concrete can be determined by multiplying the shear connector resistance with the number of shear connectors between the critical sections:

$$N_c = n_{sc} \cdot P_{Rd} \leq N_{cf} \tag{2.35}$$

The ratio of the force that can be transferred by the shear connectors (N_c) to the maximum possible compression force in the concrete (N_{cf}) is called the degree of shear connection (η). Alternatively, η can be expressed as the ratio of the number of the shear connectors placed within the shear length (n_{sc}) to the number required for full shear connection (n_f):

$$\eta = N_c / N_{cf}, \text{ or} \tag{2.36}$$

$$\eta = n_{sc} / n_f \tag{2.37}$$

Clause 6.2.1.3 (3) permits to use the concept of partial shear connection only if ductile shear connectors are used. Then, the plastic moment resistance can be calculated based on the plastic stress distribution. In this case, N_c should be used for the compression force in the concrete instead of the force N_{cf}. As a result, a part of the steel beam should also be in compression for equilibrium. Hence, there are two neutral axes. Figure 2.21 presents the possible plastic stress distributions for partial shear connection.

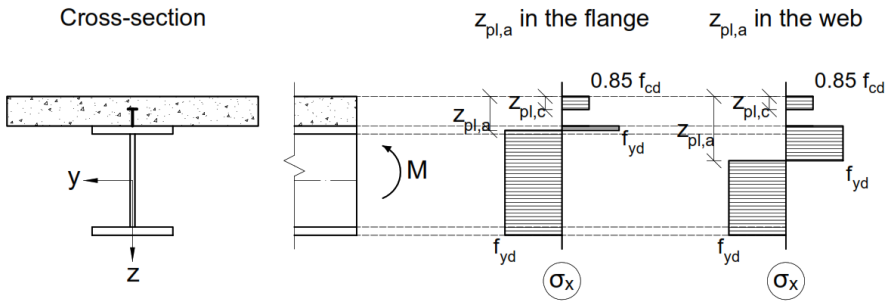

Figure 2.21 Possible plastic stress distributions for partial shear connection

The code permits to approximate the moment resistance using a linear interpolation between the bending resistances of the steel beam alone and of the composite section with full shear connection because the relation between M_{Rd} and N_c can be described by a convex curve (Figure 2.22),:

$$M_{Rd} = M_{pl,a,Rd} + \left(M_{pl,Rd} - M_{pl,a,Rd}\right)\frac{N_c}{N_{cf}} \tag{2.38}$$

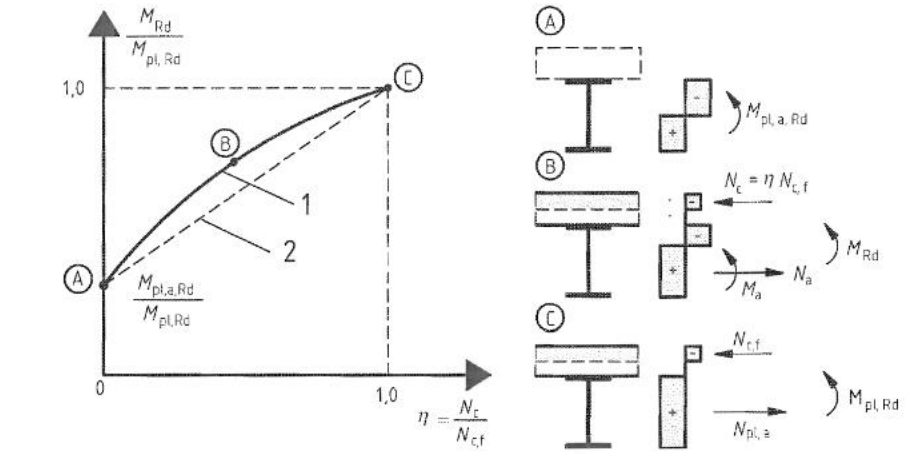

Key

1 plastic theory

2 simplified method

Figure 2.22 Relation between M_{Rd} and N_c (for ductile shear connectors) (taken from EN1994-1-1 [18])

Ductile shear connectors may be placed equidistantly when rigid-plastic analysis is used [18].

2.3.3 Elastic resistance to bending

Eurocode 4 [18] gives the following formula for the calculation of the elastic bending resistance:

$$M_{el,Rd} = M_{a,Ed} + kM_{c,Ed} \tag{2.39}$$

Where:

$M_{a,Ed}$ is the design bending moment applied to the structural steel section before composite behaviour,

$M_{c,Ed}$ is the design bending moment applied to the composite section, and

k is the lowest factor such that a stress limit is reached.

The following limiting stresses are defined:

1) f_{cd} – concrete in compression,
2) f_{yd} - structural steel in tension or in compression,
3) f_{sd} – reinforcement in tension or in compression.

The stresses in the composite section can be determined using the standard formulae of elastic theory. For that, an effective (homogenised) cross-section is usually used.

When elastic design is used, the shear connectors should be placed in accordance with the longitudinal shear flow calculated based on elastic theory:

$$v_{L,Ed} = \frac{V_{Ed} \cdot S_{y,c}}{I_{y,eff}} \tag{2.40}$$

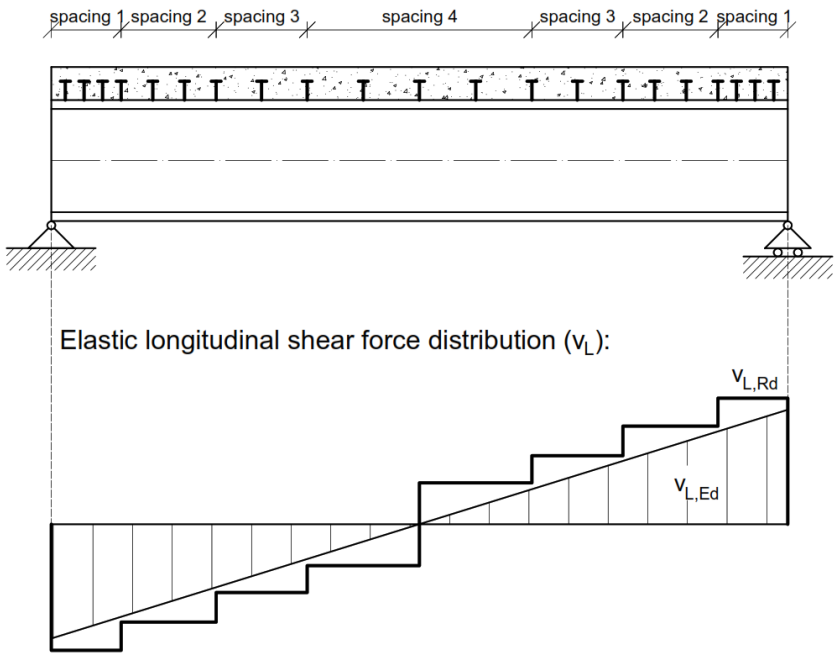

Figure 2.23 Shear connectors placed according to the elastic shear flow

2.3.4 Nonlinear resistance to bending

When the bending resistance of composite section is determined using nonlinear theory, the nonlinear behaviour of the steel and concrete materials should be taken into account. This is not a simple task, and therefore in practice it is usually done by a software [47]. Eurocode 4 [18] gives a simplified conservative approximation for Class 1 and Class 2 sections as a function of the compression force:

$$M_{Rd} = M_{a,Ed} + \left(M_{el,Rd} - M_{a,Ed}\right)\frac{N_c}{N_{c,el}} \qquad \text{for } N_c \le N_{c,el} \qquad (2.41)$$

$$M_{Rd} = M_{el,Rd} + \left(M_{pl,Rd} - M_{el,Rd}\right)\frac{N_c - N_{c,el}}{N_{c,f} - N_{c,el}} \qquad \text{for } N_{c,el} \le N_c \le N_{c,f} \qquad (2.42)$$

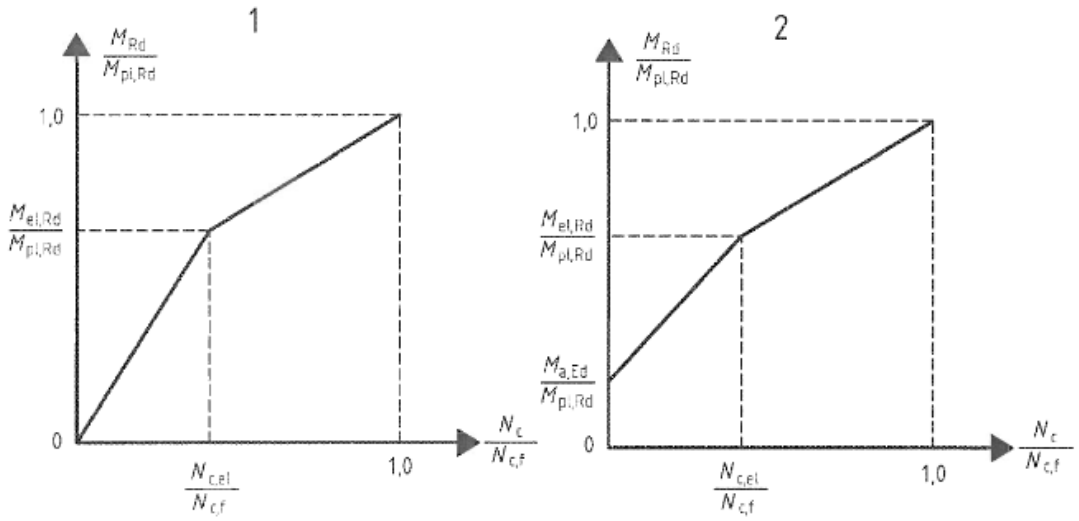

Key

1 propped construction

2 unpropped construction

Figure 2.24 Simplified relationship between M_{Rd} and N_c (taken from EN1994-1-1 [18])

2.4 Serviceability limit states

2.4.1 General

Eurocode 4 [18] refers to the criteria given by EN1990 [48] for the verification of the serviceability limit states. It gives the following design checks:

1) Stresses
2) Deformations
3) Cracking of concrete

2.4.2 Stresses

In the calculation of the stresses for beams at the serviceability limit state Eurocode 4 [18] section 7.2.1 prescribes the following effects to be taken into consideration:

1) shear lag,
2) creep and shrinkage,
3) cracking and tension stiffening of concrete,
4) sequence of construction,
5) increased flexibility due to incomplete interaction (slipping of the shear connection),
6) inelastic behaviour of steel and reinforcement,
7) torsional and distorsional warping.

Nevertheless, stress limitation is usually not required for beams in buildings except where fatigue verification is required in the ultimate limit state or pre-stressing by tendons or by controlled imposed deformations is provided (clause 7.2.1 (1)).

2.4.3 Deformations

According to clause 7.3.1 (2), the deflections should be calculated using elastic analysis. Clause 7.3.1 (4) allows to ignore the effects of incomplete interaction where

1) the design of the shear connection is in accordance with Eurocode 4 [18] Chapter 6.6;
2) the degree of shear connection is not less than 0.5, or the shear connector forces in SLS do not exceed P_{Rd}; and
3) the height of the ribs of a profiled sheeting does not exceed 80 mm.

However, where the above conditions are not satisfied, the code does not give guidance on how the effects of the incomplete interaction could be considered.

Concerning the vibrations, the code refers to the criteria given by EN1990 [48].

2.4.4 Cracking of concrete

For the calculation of the crack width and the corresponding limits, the code refers to EN992-1-1 [49]. The limitation crack width depends on the exposure class. Alternatively, the code defines a minimum amount of reinforcement in section 7.4.2 and a maximum bar spacing or diameter in section 7.4.3. These depend on the mean value of the tensile strength of the concrete, the area of the tensile zone, the arising stress and the yield strength of the reinforcement bars. If the minimum reinforcement is provided and the bar spacing or diameters do not exceed the defined limits, the crack width verification does not need to be performed.

2.5 Definition of ductility

2.5.1 Ductility according to Eurocode 4

According to Eurocode 4 [18] clause 6.6.1 (5) a shear connector can be considered ductile, when its characteristic slip capacity (δ_{uk}) is at least 6 mm. The characteristic slip capacity is defined as the minimum test value of δ_u reduced by 10% or determined by statistical evaluation. The slip capacity δ_u is defined on the descending branch of the load-slip curve (see Figure 2.25).

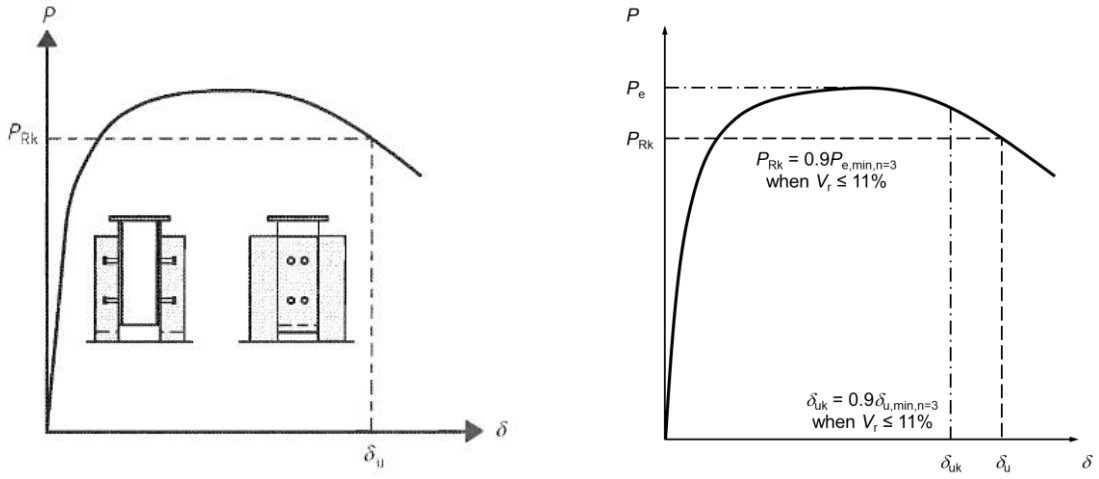

(a) (b)

Figure 2.25 Determination of slip capacity δ_u (a) Eurocode 4, Annex B [18], (b) Eurocode 4, Annex B background document [50]

This definition is adequate for traditional headed stud connectors, but it can be misleading for other type of connectors.

2.5.2 Ductility according to Sause and Fahnestock

Sause and Fahnestock [51] investigated the behaviour of flexural girders. They used two measures for the ductility: the rotation capacity R and the maximum inelastic rotation $\theta_{inel,u}$. In Equation (2.43), θ_p represents the hypothetical rotation of one end of the I-girder when the plastic moment capacity M_p is

reached, and θ_u is the rotation at which the moment capacity returns to M_p. They assumed that the beam remains completely elastic until M_p is reached (see Figure 2.26).

$$R = \frac{\theta_u}{\theta_p} - 1 \tag{2.43}$$

They anticipate that the rotation capacity R reaches or exceeds 3 for a compact and adequately braced I-girder.

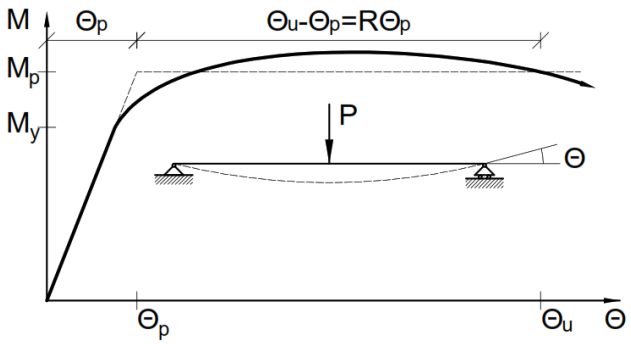

Figure 2.26 Moment vs. end rotation behaviour of a flexural member by Sause and Fahnestock [51]

2.6 Typical idealised load-slip behaviours

Bärtschi [52] lists four basic idealised load-slip curves based on the ductility and the flexibility of the shear connection. The idealised curves are either flexible or rigid, ductile of brittle. Using the previously introduced notations, the four basic cases are summarised in Table 2.2 and shown in Figure 2.27.

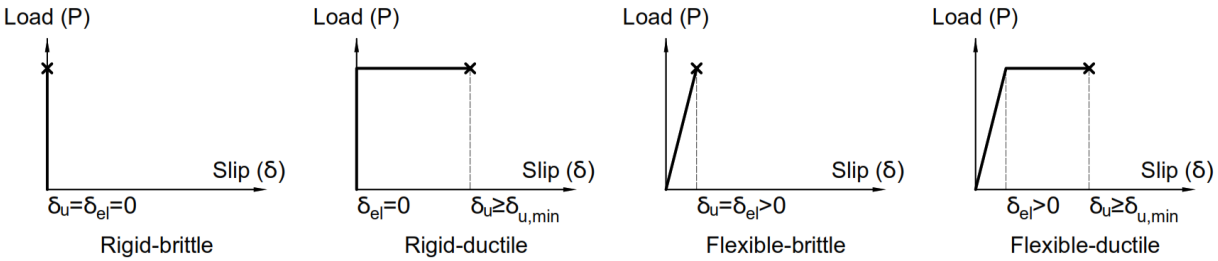

Figure 2.27 Typical idealised load slip behaviours

Table 2.2 Typical idealised load-slip behaviours

Load-slip behaviour	Elastic slip	Deformation capacity	Ductility parameter
Rigid-brittle	$\delta_{el} = 0$	$\delta_u = 0$	D = 0
Rigid-ductile	$\delta_{el} = 0$	$\delta_u > \delta_{u,min}$	D = ∞
Flexible-brittle	$\delta_{el} > 0$	$\delta_u = \delta_{el}$	D = 0
Flexible ductile	$\delta_{el} > 0$	$\delta_u > \delta_{u,min}$	$D > D_{min}$

Headed stud connectors usually have a load-slip behaviour similar to the one presented in Figure 2.25, and they are often idealised by a rigid-ductile curve.

Among the previously introduced demountable shear connections, embedded bolts and studs could be characterised by a flexible-ductile curve. Through bolts however, could not be characterised by any of the idealised curves presented in Figure 2.27. As mentioned earlier, the load-slip curve of preloaded friction grip bolts has three parts: a nearly vertical part, a nearly horizontal part and a linear or nonlinear part (see Figure 2.14).

2.7 Controlling end slip in the ultimate limit state

2.7.1 General

In a composite beam, a relative strain difference occurs at the steel-concrete interface during deformation. This strain difference is usually referred to as “slip strain”. If we integrate the slip strains from the point of the maximum bending moment to the support we obtain the end slip. The determination of the end slip is not a complicated task as long as all of the components (the steel beam, the concrete and the shear connection) are in elastic state (see Chapter 8.4). When it comes to ultimate limit state, the determination of the end slip becomes a complex task due to the nonlinear behaviour of the materials. However, it is important to control the end slip in order to avoid premature failure of the connectors. This chapter presents different methods that can be used for the approximation or the limitation of the end slip.

2.7.2 Minimum degree of shear connection by Eurocode 4

Eurocode 4 [18] rules are mainly based on studies on welded studs. The traditionally applied studs usually have at least 6 mm slip capacity [47]. The code does not contain a slip limitation nor a method for the calculation of the occurring end slip. Instead, it gives an indirect slip limitation by providing rules for the minimum degree of shear connection. These rules intend to ensure that the occurring end slip does not exceed the aforementioned 6 mm. In the current form of the code, the minimum degree of shear connection for steel sections with equal flanges is given by equations (2.44) and (2.45).

$$L_e \leq 25 \qquad \eta \geq 1 - \left(\frac{355}{f_y}\right)(0.75 \cdot 0.03 L_e) \qquad \eta \geq 0.4 \qquad (2.44)$$

$$L_e > 25 \qquad \eta \geq 1 \qquad (2.45)$$

However, it was shown by Romero [53] that composite beams with a degree of shear connection, which is close to the minimum defined by the code can still experience slips that exceed 6 mm. It is planned that in the next version of the code, the limitation would be modified [54]. For propped construction, equation (2.44) will become:

$$L_e \leq 25 \qquad \eta \geq \left[1 - \left(\frac{355}{f_y}\right)(0.75 \cdot 0.03 L_e)\right]\delta_1^2 \qquad \eta \geq 0.4 \qquad (2.46)$$

For unpropped construction:

$$L_e \leq 25 \qquad \eta \geq \left[1 - \left(\frac{355}{f_y}\right)(0.75 \cdot 0.03 L_e)\right]\delta_1^2 \cdot k_{unpr} \qquad \eta \geq 0.3 \qquad (2.47)$$

where:

δ_1 is the utilization factor, and

k_{unpr} is the reduction factor accounting for the influence of an unpropped beam.

2.7.3 Oehlers and Bradford

Because plasticity in the steel and concrete elements only occurs in a small volume of the composite beam, Oehlers and Bradford [55] assume that the steel and the concrete remain elastic, but all the shear connectors are in plastic state, i.e. the force in each shear connector equals to the shear resistance of the connection. This assumption is in accordance with the assumption of Aribert [56]. The maximum slip can be calculated as:

$$s_{max} = A_m K_1 - A_{shear} K_2 \qquad (2.48)$$

where:

A_m is the area of the moment diagram between the maximum moment and the support,

A_{shear} is the area of the axial force diagram over the same region,

$$K_1 = \frac{h_c + h_a}{E_c I_c + E_a I_a}, \quad \text{and} \qquad (2.49)$$

$$K_2 = \left(\frac{1}{E_c A_c} + \frac{1}{E_a A_a}\right) + \frac{(h_c + h_a)^2}{E_c I_c + E_a I_a} \qquad (2.50)$$

Alternatively, they give an equation, which was originally proposed by Johnson and Molenstra [57]. The equation is not based on a mechanical model but it was created with the help of multiple linear regressions using exponential and polynomial functions and the results of nonlinear finite element simulations of 45 beams. According to the authors, the best compromise between simplicity and accuracy was found to be the following equation:

$$s_{max} = \left(\frac{M_{pl,a} \cdot L \cdot h_a}{6 \cdot E_a \cdot I_a}\right)\left(\frac{L}{D}\right)^{\alpha}\left(\frac{M_{pl} - M_{pl,a}}{M_{pl,a}}\right)^{\beta} \tag{2.51}$$

where:

D is the depth of the composite section,

$\alpha = -0.13$ and $\beta = 1.03$ for $\eta = 0.5$, and

$\alpha = -0.24$ and $\beta = 1.70$ for $\eta = 0.75$.

In equation (2.51), the first term refers to the elastic end slip with no shear connection:

$$s_0 = \frac{M_{pl,a} \cdot L \cdot h_a}{6 \cdot E_a \cdot I_a} \tag{2.52}$$

This equation is based on the assumption that the concrete part does not exist:

$$h_c = I_c = E_c = 0 \tag{2.53}$$

2.7.4 Eggert

Eggert [58] investigated composite beams with low degrees of shear connections. He carried out full scale beam tests as well as numerical investigations and he gave equations for the calculation of the occurring slip at ultimate limit state:

$$s_{max} = s_0 \cdot \left(\alpha_1\left(\frac{L}{h_a}\right)^{0.325} + \alpha_2\left(\frac{w_p - w_{pa}}{w_{pa}}\right)^{1.373} + \alpha_3 \cdot \left(\frac{z_{pl,1}}{h_c}\right)^{0.163} + \alpha_4\left(\frac{F_c}{F_a}\right)^{0.666}\right) - \alpha_5 \tag{2.54}$$

where:

s_0 is the elastic end slip with no shear connection (same as in equation (2.52)),

$\alpha_1 = 0.049$,

$\alpha_2 = 0.118 \cdot (-51.353 \cdot \eta + 48.411)$,

$\alpha_3 = 0.015 \cdot (622.87 \cdot \eta^2 - 669.35 \cdot \eta + 209.76)$,

$\alpha_4 = 0.0005 \cdot (143.58 \cdot \eta^3 - 139.28 \cdot \eta^2 + 40.108 \cdot \eta - 4.170)$,

$\alpha_5 = 5.119$,

$w_p = \frac{8 \cdot M_{pl}}{L^2}$,

$w_{pa} = \frac{8 \cdot M_{pl,a}}{L^2}$,

$F_c = A_c \cdot f_c$, and

$F_a = A_a \cdot f_y$.

2.7.5 Bärtschi

Bärtschi [52] derived a formulation for the determination of the elastic slip if there is no shear connection. He determined the end slip at ultimate load from the results of numerical simulations. He found that in beams with no shear connection the slip at which the plastic bending resistance is reached is 1.5 times more than the slip at first yield:

$$s_{ult,0} = \alpha \cdot \frac{L}{2} \cdot \frac{1.5 \cdot f_y - \sigma}{E_a} \left(1 + \frac{h_c + h_p}{0.5 \cdot h_a}\right) \tag{2.55}$$

where α = 2/3 for uniformly distributed load, α = 1/2 for concentrated load that acts at mid-span, $\alpha = 1 - e/L$ or symmetrical two point loads that act in a distance e from the supports, and σ is the maximum normal stress in the steel beam due to unpropped construction.

For beams with full shear connection, he recommends to use the differential equation of nonlinear composite action or a finite element analysis. Both of these methods require a large computational effort.

For partial shear connection the analytical determination of the occurring end slip is even more difficult. Nevertheless, he remarks that the slip in a composite beam with partial shear connection is smaller than in a beam with no shear connection and larger than in a beam with full shear connection. As a greatly simplified model, he recommends to use a linear interpolation (see Figure 2.28) between the end slip with no shear connection and the end slip with full shear connection according to the degree of partial shear connection.

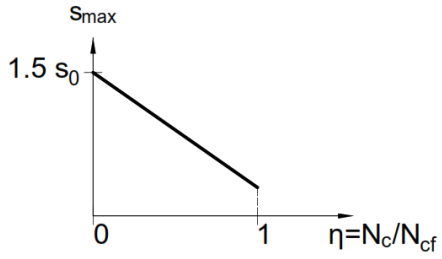

Figure 2.28 Linear interpolation of the end slip based on the degree of shear connection proposed by Bärtschi [52]

2.7.6 Summary

This chapter presented different methods for the calculation or the limitation of the occurring slip at the ultimate limit state. Among these methods, only the equation (2.48) by Oehlers and Bradford [55] is based on a mechanical model. Additionally, Bärtschi gives the differential equation for nonlinear composite action, but because of its complexity it can only be solved by means of numerical methods. The indirect limitation of Eurocode 4 [18], the formulation (2.51) of Johnson and Molenstra [57] and the equation (2.54) of Eggert [58] are all based on the statistical evaluation of experimental and numerical investigations of composite beams with welded studs. This means that the scope of their application is limited to the cases that are similar to the original data set, i.e. they are only applicable in the case of welded headed studs or equivalent shear connectors. Also, the method of Oehlers and Bradford [55] assumes that the shear connection can be described with a rigid-ductile curve. As presented in section 2.1, demountable shear connectors behave differently than welded studs in general. Their initial stiffness is lower than the one of welded studs, so they cannot be considered as a rigid connection, but rather as a flexible one. The determination of the occurring slip in the case of flexible shear connection is a relatively easy task as long as all the components are in elastic state (see chapter 8.4). It is a much more complex task in the ultimate limit state because of the nonlinear behaviour of the steel, of the concrete and possibly of the shear connection. Accordingly, no closed analytical solution could be identified in the international literature. The occurring slip is usually determined using finite element simulations.

Chapter 3. New types of demountable shear connections

3.1 General

In the frame of the conducted research, two types of shear connections have been investigated and tested in the laboratory. The solutions are somewhat similar to other shear connections that can be found in the international literature; however, there are certain differences, which will be pointed out in this chapter. During their design process, the focus was put on the matters of demountability, reusability and structural performance. This chapter presents the requirements that were considered and the investigated shear connections.

3.2 Requirements of demountable shear connections

Demountable shear connections should fulfil several criteria at the same time. These criteria include the matters of

1) structural performance,
2) safety,
3) tolerances,
4) corrosion resistance,
5) aesthetics,
6) economy,
7) adaptability,
8) standardisation,
9) environmental impact,
10) construction,
11) deconstruction, and
12) reuse.

This section summarises the different requirements that were taken into consideration.

3.2.1 Structural performance

The primary purpose of the shear connection is to connect the steel beam and the concrete deck in such a way that they withstand the external loads as a single member. For that, the shear connection should be capable of transmitting the occurring longitudinal shear force on the steel-concrete interface; and therefore, the shear connectors should have sufficient shear resistance. Transverse separation should be prevented; so the connection should have a certain tension resistance. The stiffness of the shear connection is also an important factor as it directly affects the stiffness of the composite beam. Additionally, a certain deformation capacity is required to ensure that the connection does not fail prematurely before the curvature required to develop the moment resistance is reached. Furthermore, ductility plays an important role when the design relies on the inelastic redistribution of the shear forces.

3.2.2 Construction, deconstruction and reuse

Crowther [2] identifies 27 different aspects of design for deconstruction (DFD). Among these aspects, those that are relevant for demountable composite flooring systems are listed here:

1) Use recycled and recyclable materials.
2) Use dismountable mechanical connections and dry joints.
3) Use an open building system where parts are freely interchangeable.
4) Use modular design and a standard structural grid.
5) Use construction technologies that are compatible with standard building practice and common tools.
6) Use prefabrication.
7) Provide access to all parts.
8) Make components of a size that suits the intended means of handling.
9) Provide tolerances for assembly and disassembly.
10) Use a minimum number of fasteners or connectors.
11) Use a minimum number of different types of fasteners or connectors.
12) Design to withstand repeated use.
13) Use lightweight materials and components.

Additionally, other aspects have been identified that are more specific to composite floors:

14) Preferably, provide access from the top of the slab for safety reasons.
15) Avoid any protruding parts from the slab to facilitate transportation and storage.
16) The potential damage should occur in the easily replaceable elements.

3.3 Investigated demountable shear connections

Two types of demountable shear connections were investigated by the means of laboratory testing. This section presents the investigated connections.

3.3.1 Friction bolts in cast in cylinders (System P3)

Shear connection type P3 is a through bolt type connection. This system is similar to the Krupp-Montex system [25] (see Figure 2.12), but it uses a steel tube instead of a PVC one to avoid any losses of pretension from the effects of creep and shrinkage. The connection uses a cast-in steel cylinder welded to an L-profile (not included in the Krupp-Montex system), a top plate welded to the cylinder and a pre-tensioned M20 bolt with a grade of 8.8. The steel cylinder protects the concrete from any damage that might occur due to bearing. The L-profile provides steel-to-steel contact between the slab and the beam and it helps to protect the edge of the deck element throughout its lifetime. The bolt is placed inside the cylinder from the direction of the top plate during the assembly process, and it connects the deck element to the steel beam through ϕ24 pre-drilled holes in the flange. The oversized hole facilitates the hole alignment during the assembly process. Pockets (voids) are created in the concrete in order to avoid any

protruding part on the top surface and to provide access to the connection from the top of the slab. This makes the disassembly process safer as there is no need for workers being underneath the slab during deconstruction. The layout of this shear connection system is presented in Figure 3.1.

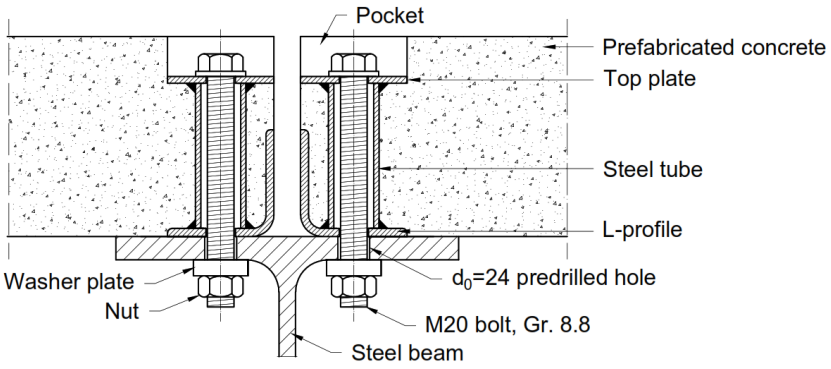

Figure 3.1 Layout of the shear connection system P3

3.3.2 Coupled bolts (System P15)

Generally, the end of an embedded bolt protrudes from the bottom surface of the slab. As a result, special care is required during the assembly, the disassembly and the transportation processes to avoid any damages in the threads. Furthermore, the application of pre-tension is possible only if the deck elements are not meant to be reused because once the bolts has been tightened to a minimum preload they are not reusable [39]. Embedded bolts being fully encased in the concrete are not replaceable.

In order to overcome these issues, shear connection type P15 uses an embedded bolt coupled with an external bolt. An embedded DIN 6334 [59] mechanical coupler device provides the connection between the two bolts. This way, there are no protruding parts and the external bolt is replaceable. The coupler has a grade of 10.9, while the bolts are made of 8.8 material. If thread damage occurs during pre-tensioning, it would occur in the replaceable bolt and not in the embedded coupler due to its higher material strength. L-profiles are used similarly to system P3, but no welding is necessary in this case. The external bolts are placed from below the flange through oversized pre-drilled holes.

Two variants of this connection type have been developed. The two variants are mostly identical, but P15.1 uses pre-tensioned bolts and P15.2 uses epoxy resin injected bolts i.e. the bolt hole is filled with resin around the bolt. This solution allows larger clearance in the flange as the resin prevents the slippage of the bolt. Figure 3.2 shows the layout of the two variants of the shear connector system.

A similar connection system was proposed by Yang et al. (2018) [60] parallel to the conduction of the research presented in this thesis. They investigated M18, M22 and M27 bolts in combination with a coupler device similar to the one presented here. The schematic drawing of their solution is presented in Figure 3.3. he main differences between their solution and shear connection system P15 are the following:

(i) Their investigation did not include preloaded bolts.

(ii) Their solution did not include L-profiles.

(iii) Their embedded bolts had 200 mm height and were encased in a relatively thick (500 mm) concrete slab. In the case of shear connection type P15 the investigated deck thickness was 150 mm as given by Eurocode 4, Annex B [18].

(iv) During the fabrication of the push-out tests, they first placed the bolts inside the pre-drilled holes of the steel beam together with the coupler device. This was followed by concrete casting. Therefore their system corresponds to an in-situ construction method, not like shear connection type P15, where the concrete deck is prefabricated.

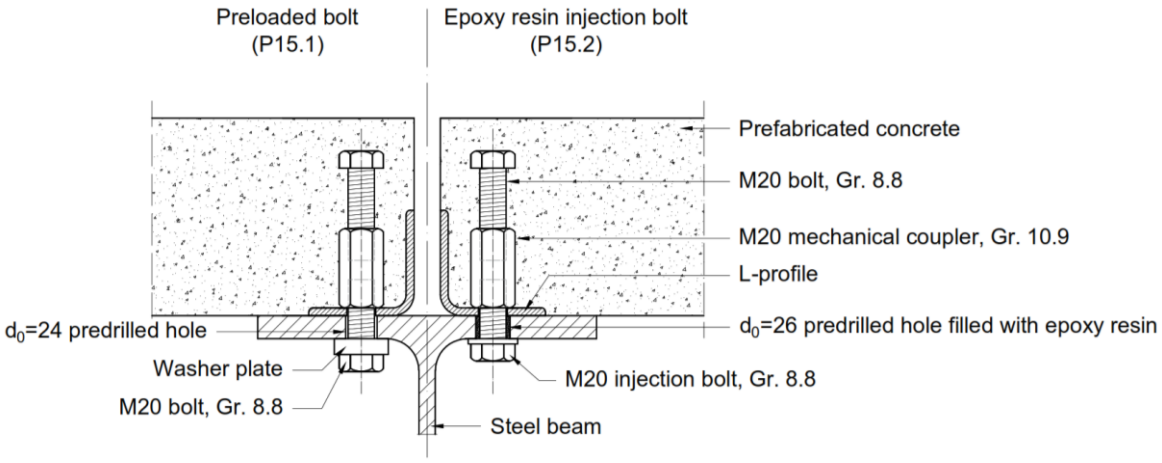

Figure 3.2 Layout of the shear connection system P15

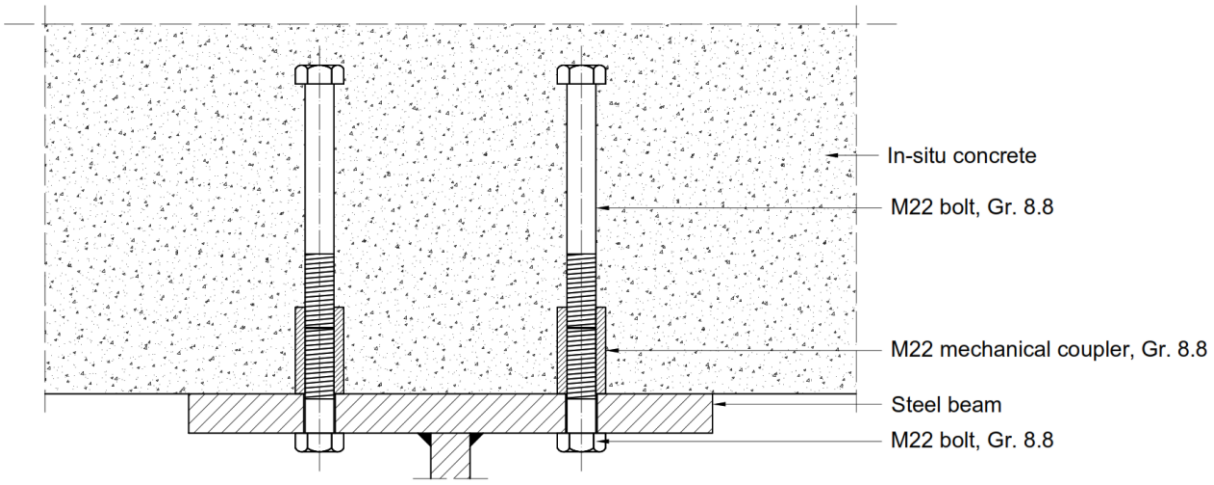

Figure 3.3 Layout of the shear connection system tested by Yang et al. [60]

3.3.3 Fulfilment of the relevant requirements

Table 3.1 summarises how the presented demountable shear connections (Type P3 and P15) fulfil the different requirements that were presented in section 3.2.

Table 3.1 Fulfilment of the requirements of demountable shear connections

#	Requirement	How do the connections fulfil the requirement?
1	Use recycled and recyclable materials.	The connections use steel and concrete, which are recyclable, and do not use non-recyclable materials (for example certain types of plastics)
2	Use dismountable mechanical connections and dry joints.	The connections use bolted connections.
3	Use an open building system where parts are freely interchangeable.	Equidistant placement of the shear connections is preferred to have interchangeable parts.
4	Use modular design and a standard structural grid.	The placement of the connectors should be in accordance with the basic module.
5	Use construction technologies that are compatible with standard building practice and common tools.	The connections use commercially available standard products.
6	Use prefabrication.	The connection types use prefabricated concrete deck elements.
7	Provide access to all parts.	The connections are accessible from below the flange. System P3 is also accessible from the top.
8	Make components of a size that suits the intended means of handling.	The deck elements should respect the size and weight limitations defined by the building constructor.
9	Provide tolerances for assembly and disassembly.	The connections use oversized holes.
10	Use a minimum number of fasteners or connectors.	The connections use high-stregth bolts to minimise the numer of connectors.
11	Use a minimum number of different types of fasteners or connectors.	The connections use standard M20 bolts, which are widely applied in the current construction practice.
12	Design to withstand repeated use.	The connections use steel L-profiles that provide edge protection to the slabs during handling and transportation. The connections also use relatively high strength concrete to fulfil this requirement.
13	Use lightweight materials and components.	Composite slabs can be used, which have lower weight than solid slabs.
14	Preferably, provide access from the top of the slab for safety reasons.	System P3 fulfils this requirement, P15 does not.
15	Avoid any protruding parts from the slab to facilitate transportation and storage.	Both connections fulfil this requirement.
16	The potential damage should occur in the easily replaceable elements.	The failure occurs always in the replaceble bolts.

Chapter 4. Push-out tests

4.1 General

Five series of push-out tests were conducted on different variants of the shear connections presented in section 3.3. Each series consisted of three nominally identical specimens with a geometrical layout similar to the one recommended by Eurocode 4 [18]. The tests on the two most heavily loaded specimens were repeated with new bolts to assess the reusability of the specimens. This chapter presents the details of the conducted push-out tests including the description of the test specimens, the test setup, the measurements, the testing procedure and the results in the terms of load-slip behaviour and observed damages. Parts of the results shown here were presented in [61] and [62].

4.2 Tests specimens

The tests specimens comprised of an HE 260B hot-rolled steel beam and four concrete deck elements. The deck elements were prefabricated in a horizontal position and were connected to the steel beam by eight demountable shear connectors after the concrete had hardened. Figure 4.1 (a) shows the schematic view of the test specimen.

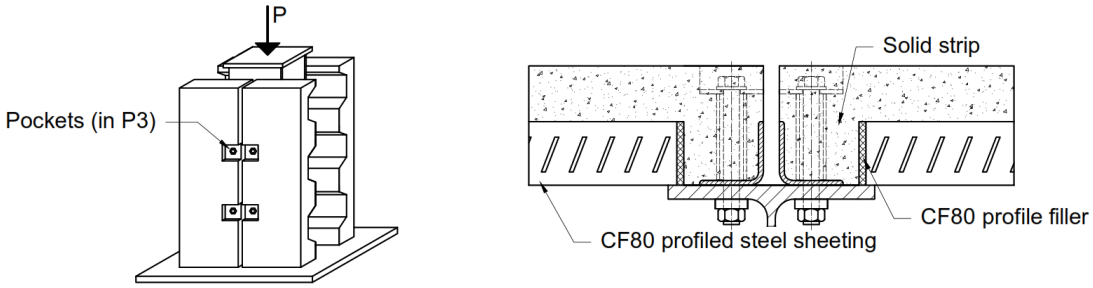

Figure 4.1 (a) The test specimen, (b) Solid strip in combination with profiled steel sheeting

Two test series (P3.2 and P3.3) used ComFlor® 80 [63] profiled steel sheeting but they had full depth in the vicinity of the shear connectors (see Figure 4.1, b). As a result, it was possible to achieve a reduced weight compared to solid slabs without compromising the shear connection behaviour.

In series P3.2, the steel beam, the L-profiles and the bolts were galvanized in order to assess the effect of galvanization on the friction resistance by comparing the obtained friction coefficients of the galvanised and the non-galvanised specimens. This corresponds to surface treatment class B according to EN1090-2 [39]. In all of the other series, the surface of the steel beam and the L-profiles were first cleaned from any chemical contaminants, then the loose rust was removed by wire brushing before the assembly of the specimens (surface treatment class C). Table 4.1 presents the overview of the test parameters.

The testing matrix consists of three series using system P3 and two series using system P15. The first test parameter was the type of the shear connection. The performance of the different shear connection types can be assessed by comparing the results of test series P3.1 with the results of P15.2. The only difference in these test series was the type of the connection.

The second test parameter was the type of the slab. Test series P3.1 and P3.3 were almost identical: the only difference was that in P3.3 profile sheeting was applied in combination with a solid strip, while P3.1 used fully solid slabs. This way, it is possible to assess whether a solid strip in the vicinity of the shear connector is sufficient to provide a solid like behaviour or not.

The third test parameter was the surface treatment. The geometry and the applied material grades of series P3.2 and P3.3 were identical, but in series P3.2 the elements were galvanised. The comparison of these test series can show how galvanisation affects the friction coefficient.

The fourth test parameter was the effects of epoxy resin injection. To assess this effect the results of P15.1 (preloaded bolts) should be compared to the results of P15.2 (injection bolts).

Table 4.1 Test parameters

Series	Shear connection	Slab type	Remark	Surface treatment class
P3.1	Friction bolts in cylinders	Solid		C
P3.2	Friction bolts in cylinders	Solid + CF80	Galvanized elements	B
P3.3	Friction bolts in cylinders	Solid + CF80		C
P15.1	Coupled bolts	Solid		C
P15.2	Coupled bolts	Solid	Injection bolts	C

In all cases, ϕ8/75, B500 B reinforcement was applied. The solid slabs had two layers of reinforcement in both directions. The slabs with profiled steel sheeting had only one layer in both directions. U-bars were placed around the shear connectors as defined by Eurocode 4 [18] for shear connectors that are placed near the edge of the concrete slab. The concrete was cast on two different occasions. The concrete strength was measured at the age of 28 days on standard cube specimens.

The pre-tensioning was applied using the combined method defined by EN 1090-2 [39]. This method includes two steps:

1) a tightening step to a snug tight condition;
2) a tightening step in which a specified part turn is applied to the turned part of the assembly.

As it was shown by complementary pretension tests (see Annex A.3), the pretension force can be accurately controlled by applying a certain amount of rotation. In shear connection type P3, the tightening was performed by turning the nut, while in the case of shear connection type P15, by turning the head of the external bolt. In test series P15.2, injection bolts were applied. First, the bolts were tightened with the help of a common wrench to a snug-tight condition. Afterwards, two-component

epoxy resin was injected to the clearance between the bolt and the inside surface of the hole through a small hole in the head of the bolt according to EN 1090-2 [39].

Figure 4.2 shows photos taken during the fabrication of the specimens. Table 4.2 presents the measured concrete strength values (see Annex A.2), the applied reinforcement and the applied pretension force for each specimen. The reason behind the relatively high concrete strength was to represent reusable elements that have an extended lifespan because they need to withstand multiple use. They have a high demand for robustness; and therefore, it is necessary that they have a high resistance against mechanical impacts.

Table 4.2 Concrete strength, reinforcement and pretension

Series	**Concrete cube strength $f_{c,28}$ [N/mm^2]**	**Reinforcement**	**Applied pretension [kN]**
P3.1	59.4	2 layers ϕ8/75	100
P3.2	59.4	1 layer ϕ8/75	120
P3.3	59.4	1 layer ϕ8/75	120
P15.1	44.3	2 layers ϕ8/75	176
P15.2	44.3	2 layers ϕ8/75	0

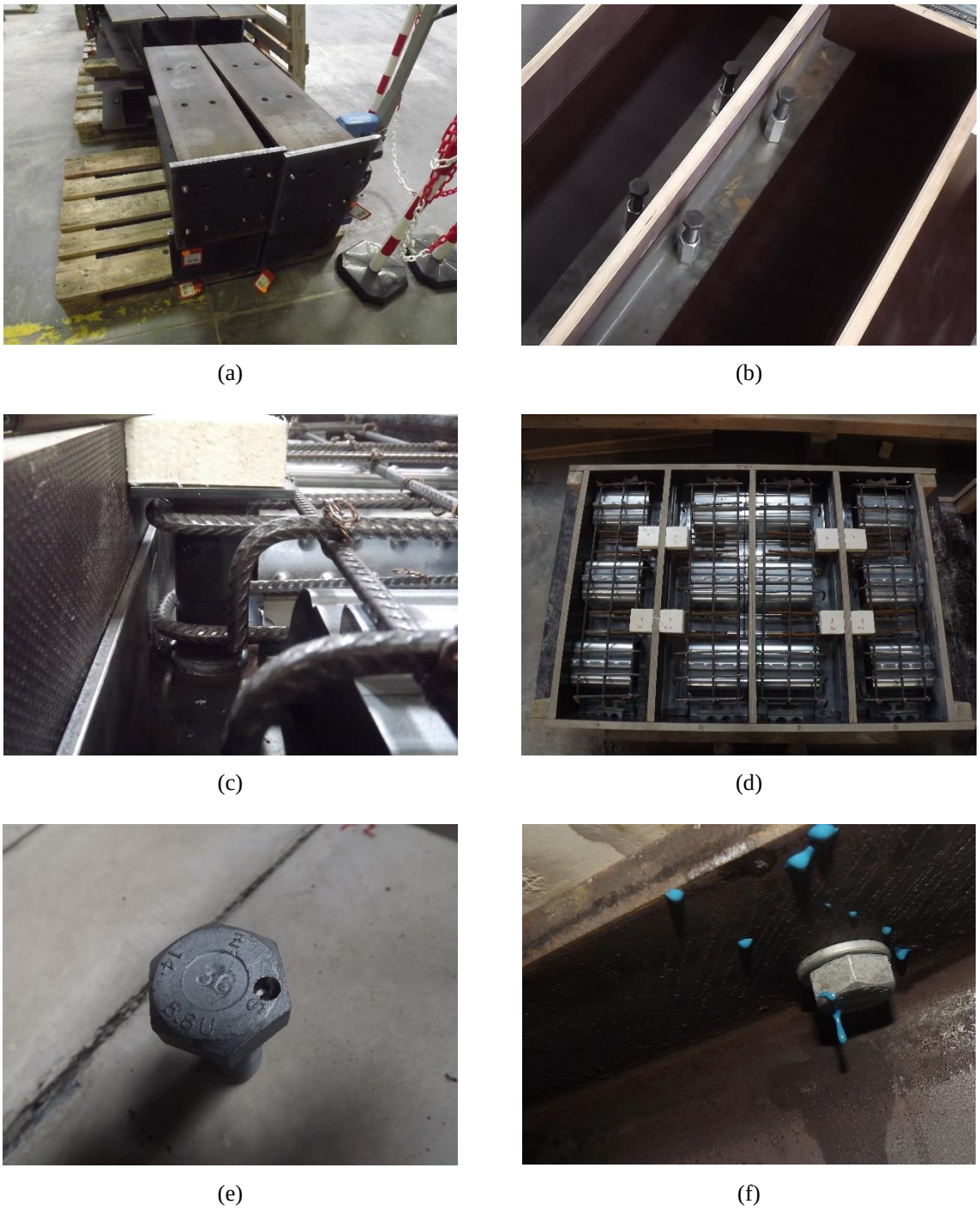

Figure 4.2 *(a) Beams with pre-drilled holes, (b) embedded bolt with coupler in the formwork, (c) cast-in cylinder with welded top plate and U-bars, (d) reinforcement mesh in the formwork, (e) injection bolt with a small hole in the head, (f) injection bolt after injection*

4.3 Test setup

The specimens were placed on a steel base plate with mortar bedding one day before testing. The tests were conducted using a hydraulic jack with a load capacity of 1000 kN. A vertical force / displacement was imposed on the endplate of the steel beam during the tests. Belts were put around the specimens to prevent the parts from falling apart once the continuity was lost (see Figure 4.3). The force in the hydraulic jack and the displacements were continuously monitored during test conduction.

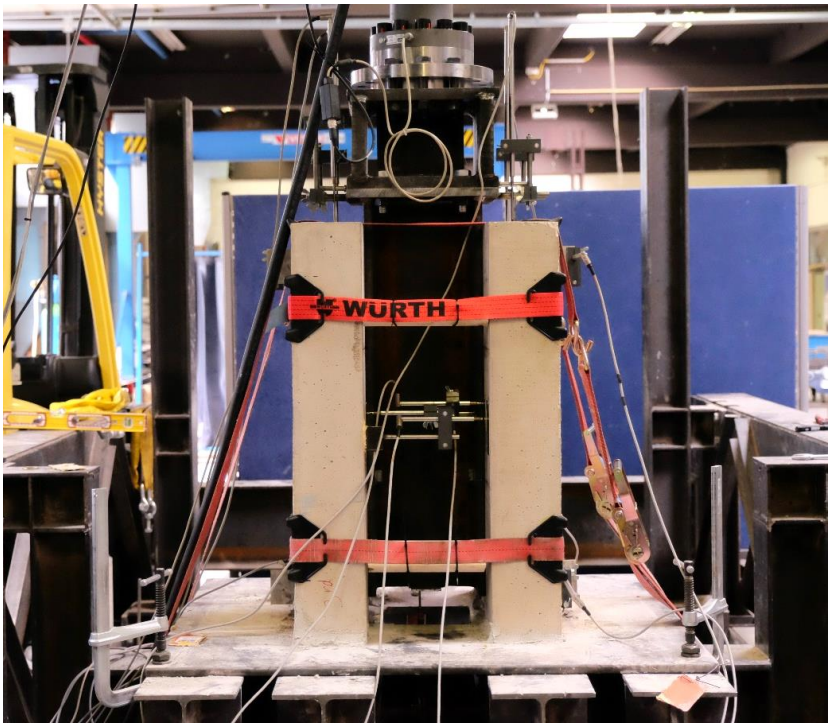

Figure 4.3 Test setup

4.4 Measurements

Fifteen displacement transducers (LVDTs) were applied for each specimen to measure the

(i) relative vertical displacement between the steel beam and the slab elements,
(ii) the vertical displacement of the beam measured from the ground floor,
(iii) the transversal separation between the steel beam and the slab elements,
(iv) the relative horizontal displacement between the adjacent slab elements, and
(v) the relative horizontal displacement between the slabs on the different flanges of the beam.

Figure 4.4 shows the layout of the applied displacement transducers.

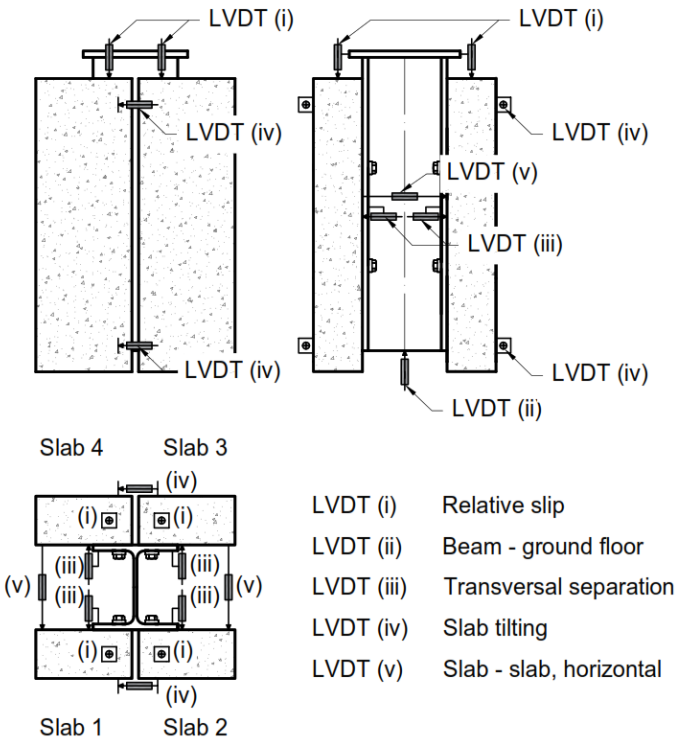

Figure 4.4 The layout of the LVDTs

Additionally, compression tests were conducted on concrete cube specimens and uniaxial tensile tests on steel coupon specimens fabricated from the L-profiles and from the applied bolts. The detailed results of these tests can be found in 0.

4.5 Test procedure

The following loading regime was applied:

LR1: The first test of each series was conducted with monotone increasing load without cycles in order to determine the failure load.

LR2: In the second test of each series, 25 cycles were performed between the 5% and the 40% of the failure load measured during LR1. The frequency of the cycles was 1 cycle / 2 minutes (0.0083 Hz).

LR3: The third test of each series included 25 cycles between the same limits and with the same frequency as in LR2. In addition, several unloading – reloading cycles were performed after every 0.5 mm – 1 mm increments in the relative slip.

The specimens were loaded in force-controlled mode with 20 kN / min load rate until the first slip had occurred. Afterwards, the loading procedure continued in displacement-controlled mode with a speed of 0.5 mm / min.

As the specimens were loaded differently, the obtained results cannot be used for the statistical evaluation of the shear connection resistance. However, they can be used for the evaluation of the

general behaviour of the connections as well as for the validation of numerical models where – if necessary- the different loading regimes can be simulated.

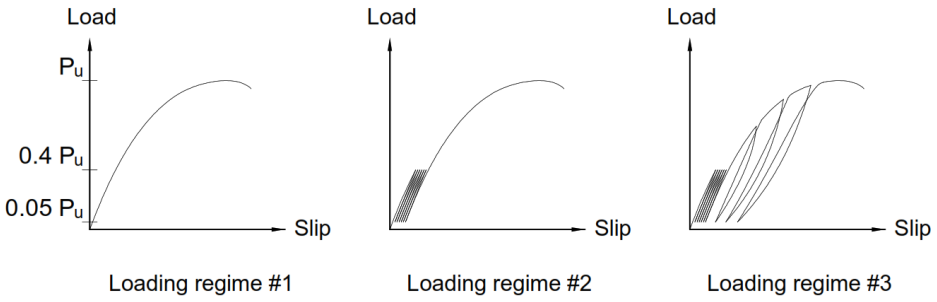

Figure 4.5 The loading regimes

The applied bolts had in all cases at least 20% overstrength compared to their characteristic strength value (see Annex A.1.2). As a result, the 1000 kN capacity of the hydraulic jack was not sufficient to cause failure when 8 bolts were applied in test P15.2-1. Therefore, in the subsequent test series, the tests started with 8 bolts until the total load level of 500 kN in load regime 1 (LR1). Then the specimens were unloaded, and the 4 bolts in the upper row were removed. This was also useful for the assessment of the demountability. Afterwards, the specimens were tested with only the four lower bolts. In LR2 and LR3, the four upper bolts were removed before testing. Because the rigidity and the bearing capacity of the steel beam and the concrete elements are very high compared to the shear stiffness of the connection, the relative slip and the load on the upper and lower bolt row was assumed to be equal. This assumption was supported by the experimental measurements as no difference could be observed between the load-slip curves of the specimens with 8 bolts and with 4 bolts.

The use of only one row of bolts along the loading direction could lead to tilting and separation of the slabs relative to the beam. In order to justify that the applied test setup is suitable for the push-out tests, the following experimental results were used: LVDTs (iv) (see Figure 4.4) measured the tilting of the slab elements, which was between 0.16 and 0.74 degrees (2.8 mrad and 13.8 mrad, respectively) in all cases. The maximum transverse separation at failure measured by LVDTs (iii) was 0.3 mm. The maximum relative horizontal displacement measured by LVDTs (v) was 1.1 mm. Based on these measurements it was concluded, that the setup with four bolts was suitable for push-out tests.

4.6 Test results

4.6.1 General

EN1990-1-1, Annex B [18] prescribes that the longitudinal slip between each concrete slab and the steel section should be measured at least until the load has dropped to 20% below the maximum load. During the tests, bolt shear failure occurred in all cases, which is a brittle failure. Due to the fracture of the bolts, the concrete slab elements were not connected to the steel beam anymore, and a sudden load drop was observed from the maximum load to zero. The failure was defined at this point where the integrity of

the specimens was lost. In the subsequent sections, the term “initial stiffness” is used for the description of the stiffness of the specimens before bolt slip inside the bolt holes occurred at load levels exceeding the friction resistance. The initial stiffness S_{ini} was determined as the secant stiffness at this point:

$$S_{ini} = \frac{F_s}{s_{Fs}} \tag{4.1}$$

where F_s is the measured friction resistance and s_{Fs} is the corresponding value of the slip.

4.6.2 Friction bolts in cast in cylinders (System P3)

The following figure shows the measurements obtained by the displacement sensors denoted as LVDT (i) (see Figure 4.4) for specimen P3.1-1. These measurements correspond to the relative slip between the steel beam and each individual slab element.

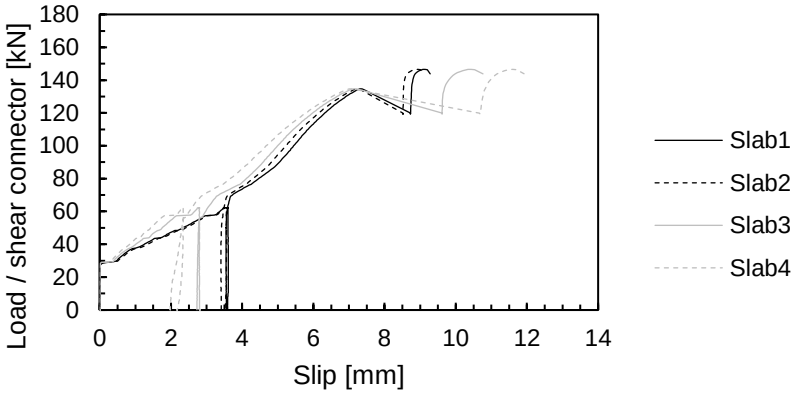

Figure 4.6 Load slip curves of Specimen P3.1-1 at each slab element (LVDT i)

As one can see, the four slab elements had a similar load-slip behaviour, which indicate that during the test conduction the load was distributed uniformly among the four shear connectors. However, in this particular test specimen, the four shear connectors did not fail at the same time. At 7.2 mm relative slip, the bolt that connected Slab 4 to the steel beam failed at a load level of 134.7 kN. This is represented by a sudden jump in the load-slip curve. Afterwards, the displacement was further increased, and the other three bolts failed at 143.7 kN. All bolts failed due to bolt shear.

The following figures show the measurements obtained by LVDT (iii) (transverse separation) and LVDT (v) (slab–to–slab relative horizontal displacement). In the figures positive values denote separation.

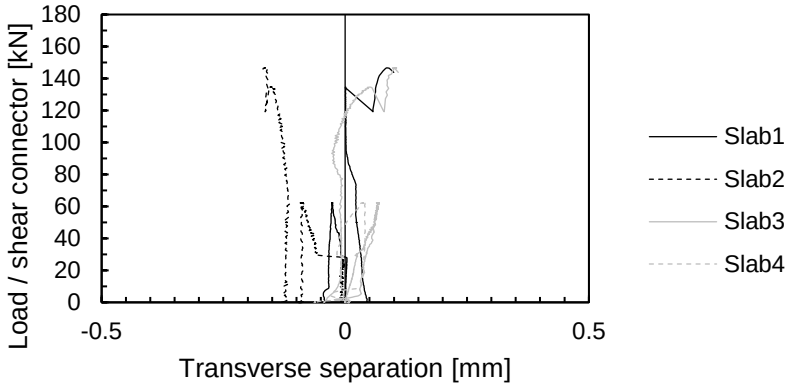

Figure 4.7 Transverse separation measurements of specimen P3.1-1 (LVDT iii)

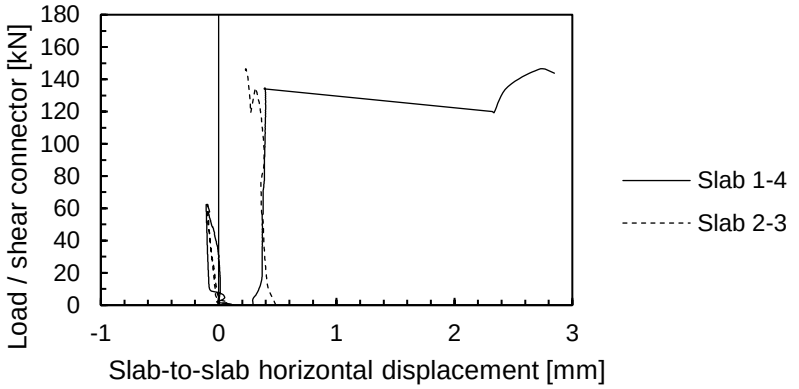

Figure 4.8 Slab-to-slab relative horizontal displacement of specimen P3.1-1 (LVDT v)

Figure 4.7 shows that only minor (less than 0.2 mm) relative horizontal displacements occurred during the test between the beam and the slab elements at the shear connectors. Similarly, Figure 4.8 indicates that the relative horizontal displacement between Slab 1 and Slab 4, and between Slab 2 and Slab 3 were negligible during the tests. When the bolt that connected Slab 4 to the steel beam failed, the connection between this slab element and the steel beam was completely lost. This resulted a sudden jump in the measurement representing the relative displacement between Slab 1 and Slab 4.

Figure 4.9 shows the measurements of the relative horizontal displacement between the adjacent slab elements (LVDT (iv)). As these measurements were performed at the top and the bottom of the slabs, these measurements show the tilting of the slab elements. In the figure the positive values indicate when the distance between the slab decreased and negative values when it increased. The results indicate, that there were only minor relative displacements at the bottom of the slabs close to the supporting plate. On

the other hand we can observe higher relative displacement values at the top of the slabs. Both measurements (Slab 1-2 top and Slab 3-4 top) show that the top of the adjacent slab elements came closer to each other as the load increased. This represents and inward tilting. As the two curves overlap it also shows that this occurred in a symmetric manner between the opposite sides of the beam. The maximum value of the measured relative displacement when bolt shear failure occurred was 5 mm at the top and -0.5 mm at the bottom. This corresponds to a 5.5 mm relative displacement over an 800 mm height, which is 0.4 degrees or 6.87 mrad relative rotation between the slab elements. On average the slabs had a relative rotation of 0.2 degrees (3.44 mrad) to the steel beam. As these values are relatively low, it was concluded that the test setup is suitable for the assessment of the shear resistance of the connectors.

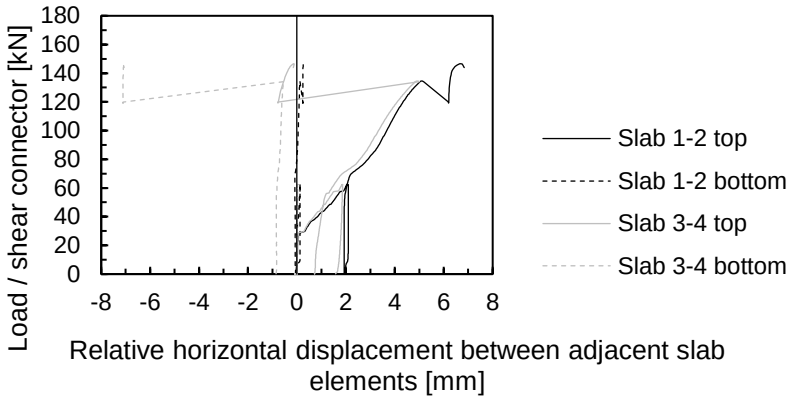

Figure 4.9 Relative horizontal displacement between the adjacent slab elements P3.1-1 (LVDT iv)

Similar behaviours (negligible transverse separation and minor inward tilting) were observed in all of the other tests.

The load-displacement curves of the friction bolts in cast in cylinders with solid slabs (P3.1) are shown in Figure 4.10. In the figure the relative slip corresponds to the average measured slip between the steel beam and the four slab elements. Due to the pre-tensioning, the initial stiffness of the system was relatively high (250 kN / mm) in the early load stages until the friction resistance was overcome at a load level of 26 kN / shear connector. Afterwards, the stiffness decreased significantly to 15 kN / mm. Only minor nonlinear behaviour was observed. In all cases, shear failure of the bolts occurred at an average load level of 141 kN / shear connector. The failure happened in a very brittle way at a relative slip level between 7 mm and 10 mm with no or minor descending branch. The load-displacement curves of specimens P3.1-1 and P3.1-3 are in a good agreement, while P3.1-2 shows larger slip capacity. This is due to the fact that the hole clearance was not deducted from the presented slip values, and the bolts have been positioned randomly inside the holes. In the case of P3.1-1, the sudden jump in the curve at 7 mm slip is caused by the failure of one bolt, which failed earlier than the others.

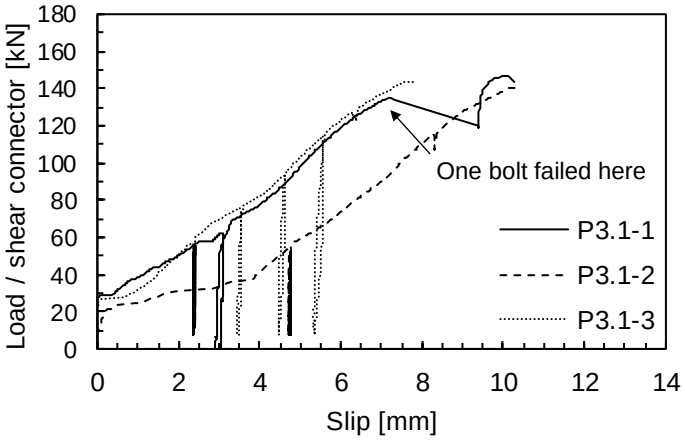

Figure 4.10 Load slip curves of System P3.1

As shown in Figure 4.11, minor damages were observed on the steel elements of the specimens: bearing deformation of the holes in the L-profiles, and thread penetration on the bearing surface of the holes in the steel beam.

(a) (b)

Figure 4.11 Observed damages, (a) bearing deformation, (b) thread penetration in the flange

The load-displacement curves of the specimens where solid slabs were applied in combination with profiled steel sheeting are illustrated in Figure 4.12 and Figure 4.13.

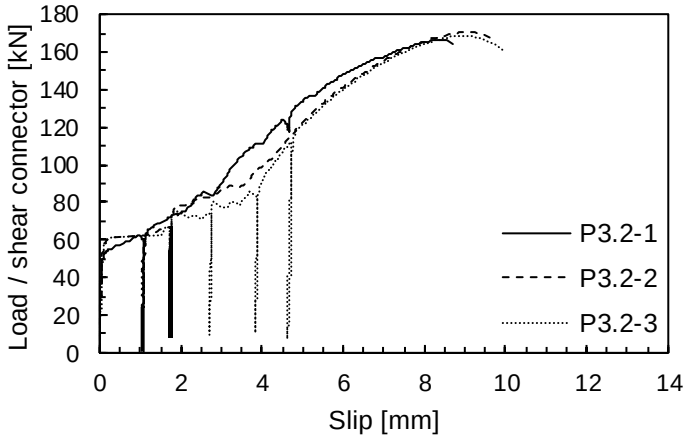

Figure 4.12 Load slip curves of System P3.2

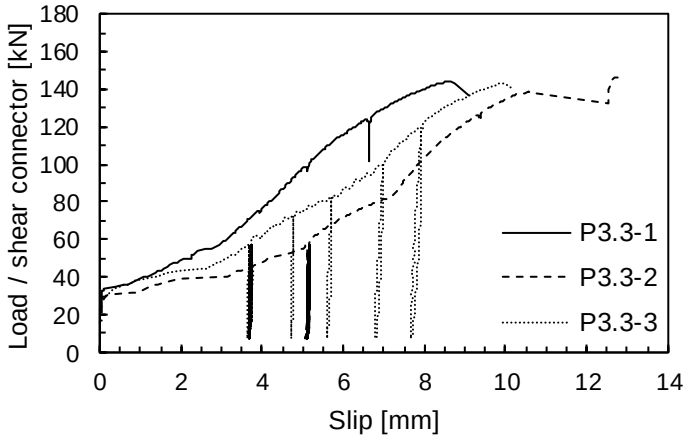

Figure 4.13 Load slip curves of System P3.3

The initial stiffness of P3.2 and P3.3 was 500 kN / mm and 300 kN / mm, respectively. In the case of the galvanized specimens (P3.2), the first slip occurred at a load level of 57 kN / shear connector, while in the case of specimens with no surface finish (P3.3), the friction resistance was 31 kN / shear connector. The stiffness decreased to 15 kN / mm after the first slip had occurred. Figure 4.14 shows the failure surface of the failed galvanized bolts.

It can be noticed that for the bolts of series P3.2 the resistance is higher (168 kN) when compared to the results of P3.3 (143 kN). This is due to the higher material strength, which was confirmed by uniaxial tensile tests that had been conducted on four bolts of each type (see Annex A.1.2). The resulting mean values of the ultimate strengths were 1045.6 MPa and 948.7 MPa, respectively. All bolts failed in shear and similar minor damages were observed as in series P3.1.

Figure 4.14 Failure surface of the bolts

4.6.3 Coupled bolts

The following figure presents the slip measurements (LVDT (i) on Figure 4.4) of specimen P15.1-1 at each slab element. As on can see, the load-slip curves of Slab 1 and Slab 4 overlap with each other, as well as the curves of Slab 2 and Slab 3. However, at a certain load level Slab 2 and 3 had around 1 mm greater slip than Slab 1 and Slab 4. This is due to the different positions of the bolts in the holes.. Apart from this effect, the curves are parallel and all the bolts failed at the same time. This indicates that the load was distributed uniformly among the bolts.

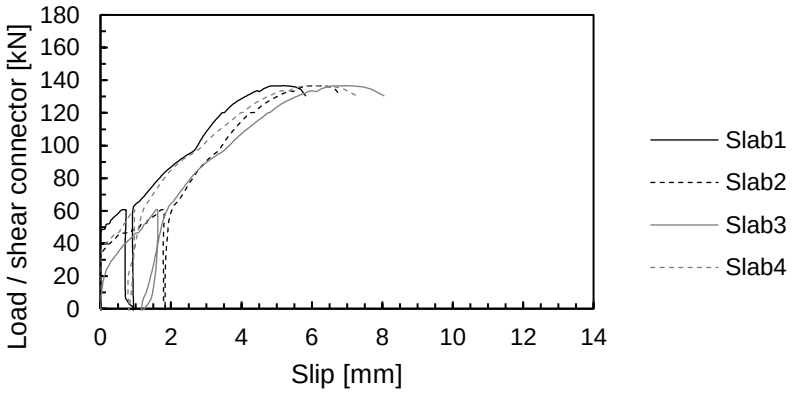

Figure 4.15 Load slip curves of Specimen P15.1-1 at each slab element (LVDT i)

Figure 4.16 shows the measurements of the transverse separation. In the figure positive values denote separation. Similarly to the results presented in Figure 4.7, only minor displacements (less than 0.2 mm) could be observed here. Figure 4.17 indicates that the relative horizontal displacement between the slabs at different sides of the beam were also negligibly small (less than 0.3 mm). Figure 4.18 presents the relative horizontal displacement measured between the adjacent slab elements at the top and at the

bottom. These measurements can also show the tilting of the slab elements from the difference in the displacements measured at the top and at the bottom of the specimen.

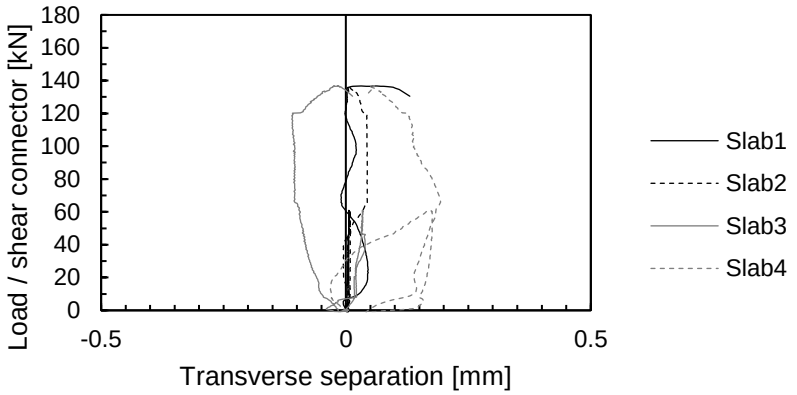

Figure 4.16 Transverse separation measurements of specimen P15.1-1 (LVDT iii)

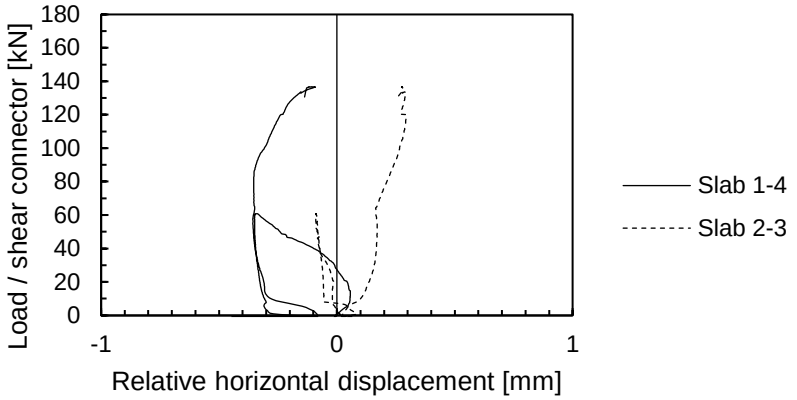

Figure 4.17 Slab-to-slab relative horizontal displacement of specimen P15.1-1 (LVDT v)

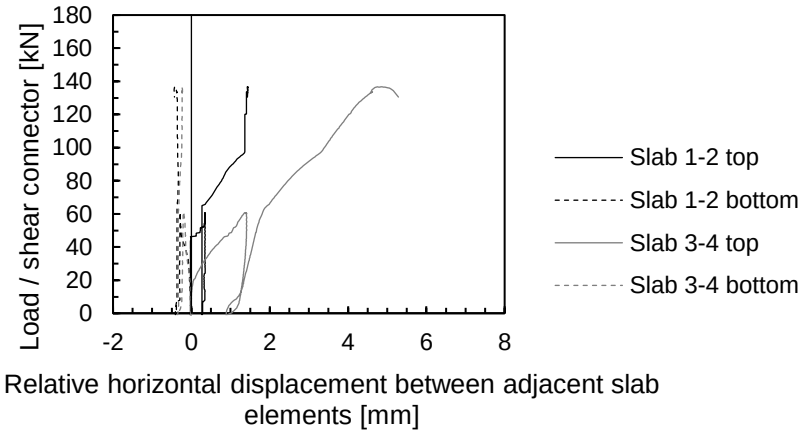

Figure 4.18 Relative horizontal displacement between the adjacent slab elements P15.1-1 (LVDT iv)

In the previous figure positive values denote closing and negative values denote separation. Similarly to the previously shown measurements (Figure 4.9), higher displacements could be measured at the top of the specimens. This also represents and inward tilting. The maximum value of the measured relative displacement when bolt shear failure occurred was 4.9 mm at the top and -0.2 mm at the bottom. This corresponds to a 5.1 mm relative displacement over an 800 mm height, which is 0.4 degrees or 6.37 mrad relative rotation between the slab elements. On average, this means that the slabs had a relative rotation of 0.2 degrees (3.28 mrad) to the steel beam.

Similar behaviour could be observed in the case of each test specimens. Based on the presented measurements, it was concluded that the test setup is suitable for the assessment of the shear resistance and the general load-slip behaviour of the connectors.

The load-slip curves of the tests with coupled bolts with pretension are presented in Figure 4.19. The initial stiffness was 70 kN / mm. The first slip occurred at a load level of 50 kN / shear connector. After a slip of 2 mm, the stiffness reduced to 30 kN / mm. Brittle shear failure of the bolts occurred in all cases at an average load level of 142 kN / shear connector.

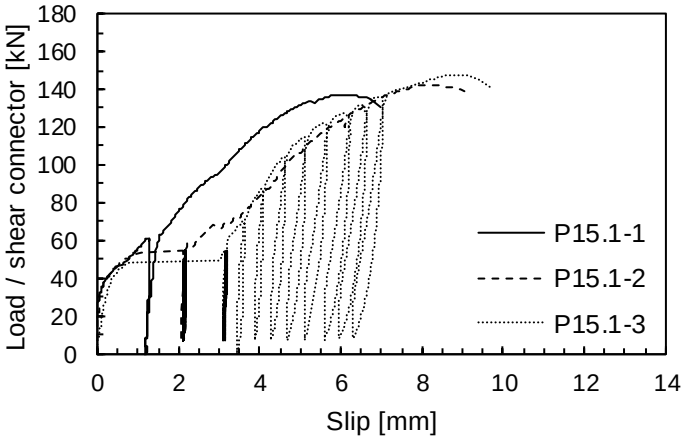

Figure 4.19 Load slip curves of System P15.1

As shown in Figure 4.20 (a), no bearing deformation was observed in the L-profile. However, thread penetration occurred in the bearing surface of the holes in the steel beam (Figure 4.20 (b)).

Figure 4.21 presents the results of the tests with epoxy resin injection bolts. The load-slip curves have three parts: an initial part with a stiffness of 100 kN / mm until the load level of 50 kN, a second part with a stiffness of 30 kN / mm until the load level of 110 kN and a final part with a stiffness of 5 kN / mm until failure. The shear failure of the bolts occurred at an average load level of 131 kN. As the epoxy resin in the bolt holes prevented the slippage of the bolts, the curves overlap despite the varying loading regime. Bolt shear was the only observed damage on the specimens. Figure 4.22 shows a bolt after failure. The resin remained intact during the test. Because of the threaded shape of the resin, the use of a wrench was necessary for the removal of the bolt head from the steel beam.

(a) (b)

Figure 4.20 Observed damages of System P15.1 (a) sheared bolt and no bearing deformation in the L-profile, (b) thread penetration in the flange

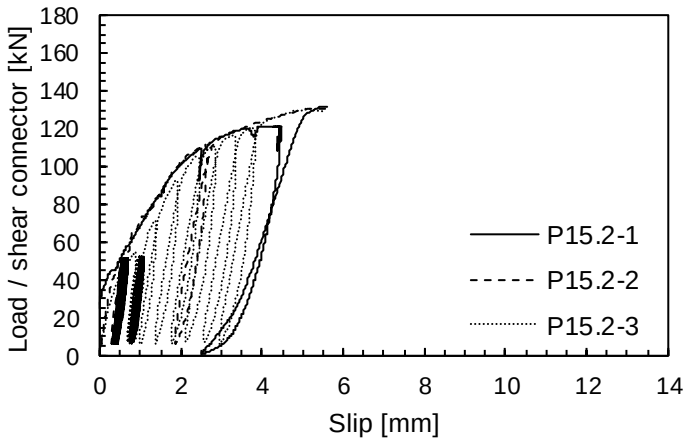

Figure 4.21 Load slip curves of System P15.2

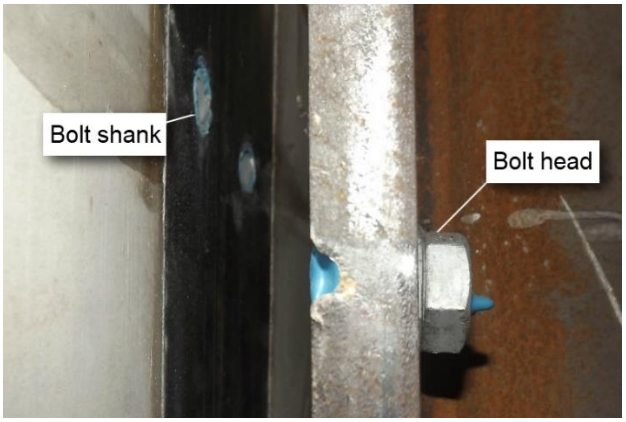

Figure 4.22 Sheared bolt after failure

4.6.4 Test on reused elements

In order to assess the effect of the observed minor damages on the reusability, the most heavily loaded specimens (P3.2-3 and P3.3-3) were reassembled with new bolts and the tests were repeated. The failed bolts were replaced by new bolts from the same batch. This means, black bolts were replaced by identical black bolts and galvanised bolts were replaced by identical galvanised ones. The results of these tests are indicated as P3.2-3R and P3.3-3R in Figure 4.23 (a) and (b), respectively. In the second tests, the failure mode was again bolt shear leading to similar resistance values as in the case of the original tests.

The slip at which the ultimate resistance was reached increased in the case of the reused galvanised specimen. In the non-galvanised specimen the obtained slip was lower than in the case of the original tests. The stiffness of the reused galvanised specimen was relatively low before 6 mm slip was reached when compared to the original specimens. This could be explained by the already existing bearing deformation of the hole of the L-profile. This phenomenon could not be observed in the non-galvanised specimen. These observations can be explained by the different bolt positions inside the bolt hole that have a direct impact on the amount of slip that the bolt can undergo before it becomes in contact with the inner surface of the bolt hole.

Lower friction resistance was observed in the case of the galvanized specimen (P3.2-3R). This can be explained by the flattening of the surface asperities. The obtained shear force and slip values are presented in Table 4.3 together with the results of the original tests.

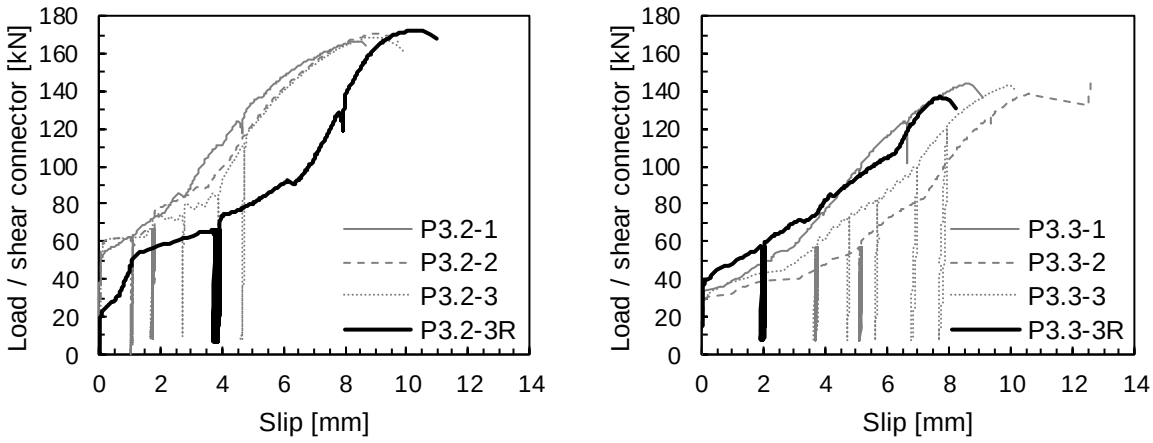

Figure 4.23 Load slip curves of the reused specimens (a) galvanised, (b) non-galvanised

Table 4.3 Results of the reused specimens

Test specimen	Loading regime	Shear resistance [kN]	Slip at max force [mm]	Remark
P3.2-1	LR1	166.2	8.5	
P3.2-2	LR2	170.5	9.1	
P3.2-3	LR3	168.7	8.9	
P3.2-3R	LR1	172.3	10.3	Reused with new galvanised bolts
P3.3-1	LR1	143.9	8.6	
P3.3-2	LR2	138.2	10.6	
P3.3-3	LR3	143.1	10.0	
P3.3-3R	LR1	136.6	7.7	Reused with new black bolts

4.7 Discussion

4.7.1 Load-slip behaviour

The load-slip curves of the shear connections that use preloaded bolts can be divided into three parts:

1. Due to the pre-tensioning, the initial stiffness of the specimens is high (250 – 500 kN / mm).
2. After the friction resistance is overcome, slip occurs and the stiffness is significantly reduced.
3. When the bolt become in contact with the inner surface of the hole, bearing and shear deformation occurs with a stiffness between 15 kN / mm and 20 kN / mm. These values are relatively low compared to traditional welded stud shear connectors, which have a stiffness usually in the range of 40 to 60 kN / mm when applied with profiled sheeting [64].

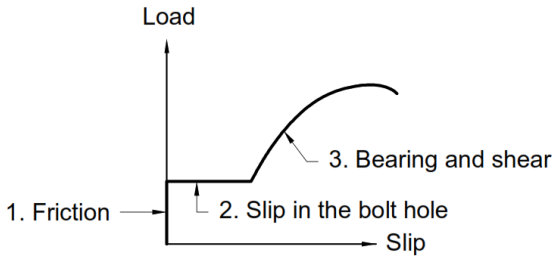

Figure 4.24 Simplified behaviour

The behaviour described above is in accordance with the observations of Lee and Bradford [27].

The second part of the general load-slip behaviour represents the bolt slip inside the bolt hole. The amount of slip before the bolt becomes in contact with the inner surface of the bolt hole is defined by the hole clearance and the position of the bolt inside the hole. Among these two parameters, the position of the bolt is difficult to control because it depends on the construction and installation tolerances. This

is the reason why the three nominally identical specimens within a certain test series had slightly different load-slip curves. The different amount of slip inside the hole caused the observed horizontal offset of the third part (shear and bearing deformation) of the curves. This effect was not removed by the cyclic loading because the cycles were performed after bolt slip had already occurred.

The position of the bolts in the hole does not have an impact on the shear resistance, but it has a significant impact on the slip at which the ultimate capacity is reached (see for example the results of test series P15.1 on Figure 4.19.). Also, the force values that belong to a certain slip have a high variability. These observations indicate that special attention is required for the construction and installation tolerances to reduce this variability. Numerical simulations showed (see chapter 6.3) that the average load-slip curve that correspond to a central bolt position can represent the general behaviour of the composite beam with high accuracy. However, dangerous cases may occur if some of the bolts have lower slip capacity than the others because of their different positions inside the hole. Further probabilistic analyses are recommended to quantify the corresponding risk.

Alternatively, epoxy resin injection bolts can be used because the epoxy resin prevents the bolt slippage; and therefore, the load-slip curves overlap very well with each other (see Figure 4.21).

This behaviour is somewhat different than the one of headed stud connectors. As shown in the DISCCO project [65], usually concrete failure precedes bolt shear failure. This is especially true when the studs are placed in deep metal decking. Pavlović [16] investigated encased bolted shear connectors. He observed both failure due to concrete crushing and failure due to bolt shear, but in his tests some kind of concrete damage always accompanied the bolt shear failure. This could not be observed in the tests presented here due to the large bearing surface of the cast-in cylinder and of the mechanical coupler device. The results obtained the tests presented in this section are similar to the ones obtained by Chen et al. [26] and Lee and Bradford [27] who investigated through bolts similar to System P3. However, they also observed local damage of the concrete at the base of the shear connectors. This leads to the conclusion that the L-profile, the steel cylinder and the mechanical coupler make the tested systems robust and they help preserving the reusability of the concrete deck elements.

4.7.2 Shear resistance

The highest resistance (168 kN) was measured in tests series P3.2 which consisted of the cast-in cylinders and galvanized elements. However, this is the result of the higher material strength of the bolts and not the galvanization, which only provides a zinc coating and does not affect the material strength. The shear failure of the bolts was the governing failure mode in all cases. System P3 produced higher resistances (150 kN on average) than System P15 (137 kN on average).

Table 4.4 summarises the measured shear resistance values (P_{ult}) of all tests in comparison with the calculated shear resistance ($F_{v,Rm}$), which was determined with the formulation given by EN1993-1-8 [66] without applying any partial factors.

Table 4.4 Summary of the measured material properties and shear resistance values

Specimen	Tensile strength $f_{u,m}$ [MPa]	Slab type	Surf. treat class	Preload F_{pc} [kN]	Friction resistance F_s [kN]	Calculated shear resistance $F_{v,Rm}$ [kN]	Measured shear resistance, P_{ult} [kN]	Slip at max. force [mm]
P3.1-1	948.7	Solid	C	100	28	139.5	134.7	7.2
P3.1-2	948.7	Solid	C	100	23	139.5	140.6	10.3
P3.1-3	948.7	Solid	C	100	28	139.5	143.9	7.7
P3.2-1	1045.6	Solid + CF80	B	120	54	153.7	166.2	8.5
P3.2-2	1045.6	Solid + CF80	B	120	56	153.7	170.5	9.1
P3.2-3	1056.6	Solid + CF80	B	120	61	155.3	168.7	8.9
P3.3-1	948.7	Solid + CF80	C	120	32	139.5	143.9	8.6
P3.3-2	948.7	Solid + CF80	C	120	30	139.5	138.2	10.6
P3.3-3	948.7	Solid + CF80	C	120	32	139.5	143.1	10
P15.1-1	967.8*	Solid	C	176	44	142.3	136.7	6.1
P15.1-1	967.8*	Solid	C	176	49	142.3	142.2	8.2
P15.1-1	967.8*	Solid	C	176	46	142.3	147.9	8.8
P15.2-1	892.1*	Solid	C	0	0	131.1	132.1	7.1
P15.2-2	892.1*	Solid	C	0	0	131.1	131.1	5.4
P15.2-3	892.1*	Solid	C	0	0	131.1	130.2	5.1
P3.2-3R	1045.6	Solid + CF80	B	120	27	153.7	172.3	10.4
P3.3-3R	948.7	Solid + CF80	C	120	33	139.5	136.6	7.7

*Calculated from the average measured shear force with Equation (4.3)

$$F_{v,Rm} = 0.6 \cdot f_{u,m} \cdot A_s \quad (4.2)$$

where:

$f_{u,m}$ is the measured tensile strength of the bolts; and

$A_s = 245$ mm^2 is the shear area of a fully threaded M20 bolt.

As there were no tensile tests conducted on the bolts applied in test series P15.1 and P15.2 due to the size limitations of the testing equipment, their tensile strength was calculated from the average shear resistance obtained by the push-out tests by rearranging the previous equation:

$$f_{u,m}^{*} = \frac{P_{ult,m}}{0.6 \cdot A_s} \quad (4.3)$$

When comparing the results of system P3.1 and P3.3 (see Table 4.4) we can observe, that the different levels of pretension did not influence the shear resistance, but it had an influence on the friction resistance. This observation is also in accordance with the findings of Pavlović [16].

4.7.3 Slip capacity

System P3 had in all cases larger slip capacity than System P15. In almost all cases, the load-slip curves showed, that the slip capacity has a high sensitivity on the position of the bolts inside the holes (see section 4.7.1). The only exception was series P15.2 where the epoxy resin was injected into the bolt hole because the resin prevented the slippage inside the hole.

4.7.4 The effect of the solid strip

The specimens where the solid slab was used in combination with profiled steel sheeting behaved similarly to the specimens with fully solid slabs. The solid strip in the shear connection region was sufficient to prevent the profiled sheeting from compromising the shear connection behaviour.

4.7.5 Ductility

Eurocode 4 [18] considers a connector as ductile if the characteristic slip capacity is at least 6 mm. It defines the characteristic slip as the maximum slip measured at the characteristic load level, which is 90% of the failure load in the descending branch of the load-slip curve. Most of the tested configurations had larger deformation capacity than 6 mm, except series P15.2. However, after the maximal load was reached, the specimen failed earlier than the 10% load drop could have happened. Furthermore, contrary to traditional shear connectors where the maximal load is usually reached after 1-2 mm of relative slip, the tested demountable shear connection systems showed monotonic increasing load-slip behaviour. Besides P15.2, each specimen reached its maximum load at a slip level between 6 mm and 10 mm. Only minor descending branch was observed after failure. This means that the Eurocode 4 [18] ductility definition (which is indeed a slip capacity requirement) cannot be applied. Therefore, in this thesis, another ductility definition will be used for the description of the behaviour of the shear connections. A

similar expression will be applied as by Sause and Fahnestock [51] (see Chapter 2.5.2); however, the parameters in the formulation will be defined differently to represent the shear connection behaviour. A ductility parameter D is introduced based on Equation (2.43):

$$D = \frac{\delta_u - \delta_{el}}{\delta_{el}} \tag{4.4}$$

In this formulation, δ_{el} represents the elastic part of the slip. It is taken as the slip where 0.7 P_{Rk} load is first reached [18]. With this definition, D represents the ratio of the inelastic deformation to the elastic one. However, this parameter alone is not sufficient to distinguish between ductile and brittle connectors. For example, in the case of a perfectly rigid connector ($\delta_{el} \approx 0$) that has any nonzero inelastic slip capacity (δ_u - δ_{el} > 0), Equation (4.4) leads to results approaching infinity. Such a connection would not necessarily be ductile if the deformation capacity is low.

Consequently, a shear connection can be considered as ductile only if both the ductility parameter D and the slip capacity δ_u exceed a certain limit:

$$D \geq D_{min} \tag{4.5}$$

$$\delta_u \geq \delta_{u,min} \tag{4.6}$$

The 6 mm criterion of Eurocode 4 [18] for the ductility is indeed a slip capacity requirement:

$$\delta_{u,min} = 6 \text{ mm} \tag{4.7}$$

Traditionally, for headed stud connectors $\delta_{el} \approx 1$ mm and $\delta_u \approx 6$ mm [50], [65]. Based on these values, the REDUCE design guide [67] proposes that D should reach or exceed 5:

$$D_{min} = 5 \tag{4.8}$$

It is important to note that this number is rather conservative. Some headed stud connectors that are normally considered as ductile would not satisfy this criterion. For instance, Oehlers and Bradford [68] give estimates for the proportionality limit δ_p and ultimate slip for welded studs in solid slabs based on the stud diameter: $\delta_p \approx 0.1\ d$, and $\delta_u \approx 0.3\ d$. They assume, that the ultimate resistance P_u is reached at the proportionality limit. Using the Eurocode 4 [18] terminology, the characteristic load is:

$$P_{Rk} = 0.9\ P_u \tag{4.9}$$

The load-slip relation is assumed to be linear for $\delta < \delta_p$. The slip δ_{el} is taken at 0.7 P_{Rk}:

$$\delta_{el} = 0.7 \cdot 0.9 \cdot 0.1 \cdot d = 0.063\ d \tag{4.10}$$

The corresponding ductility parameter is:

$$D = \frac{0.3\,d - 0.063\,d}{0.063\,d} = 3.76 \tag{4.11}$$

These examples illustrate that a single, commonly accepted minimum required ductility parameter D_{min} does not exist; however, generally it is in the range from 3 to 5.

Using these definitions, the ductility parameters were determined for each of the tested shear connections. For this calculation, the minimum obtained resistance and slip values were used. The results of the calculation can be found in the following table.

Table 4.5 Ductility parameters of the tested shear connections

Series	P_u [kN]	0.9 P_u [kN]	0.63 P_u [kN]	δ_{el} [mm]	δ_u [mm]	D [-]
P3.1	135	122	85	4.6	7.2	0.6
P3.2	166	149	105	3.6	8.5	1.4
P3.3	138	124	87	4.6	8.6	0.9
P15.1	137	123	86	2.5	6.1	1.4
P15.2	130	117	82	1.4	5.1	2.6

As one can see, even if the criterion of the minimum required slip capacity given by Equation (4.6) is satisfied in most of the cases (δ_u > 6 mm), the obtained ductility parameters are always less than 5, which means that the criterion of the ductility parameter given by Equation (4.5) is not satisfied in any of the cases. As a result, using the categorisation presented in Figure 2.27, all of the investigated shear connections are considered as "flexible-brittle" connections.

4.7.6 Friction resistance and surface treatment

In the load-slip curves, the first loss of stiffness indicate the point where the friction resistance (F_s) was overcome. This point is the end of the first part of the general load-slip curve showed in Figure 4.24. The friction coefficient could be calculated using the following equations:

$$F_s = F_{pc} \cdot \mu \tag{4.12}$$

Or, alternatively:

$$\mu = F_s / F_{pc} \tag{4.13}$$

where F_s is the friction resistance, F_{pc} is the pre-tensioning force and μ is the friction coefficient.

Table 4.6 summarises the average measured friction resistance and the calculated friction coefficient values. The tests showed that the specimens with no surface finish had a friction coefficient of 0.26, while the galvanized specimens had 0.48. However, after re-assembly of the failed specimens, the friction coefficient of the galvanized specimens was reduced to 0.23. There was no change in the case

of the specimens with no surface finish (see Table 4.6). This reduction of friction coefficient could be explained by the flattening of the surface asperities during the first test.

Table 4.6 Preload and friction resistance

Series	Preload [kN]	Friction resistance [kN]	Friction coefficient [-]	Suface treatment class	Friction coefficient given by EN1090 [-]
P3.1	100	26	0.26	C	0.30
P3.2	120	57	0.48	B	0.40
P3.2R	120	27	0.23	B	0.40
P3.3	120	31	0.26	C	0.30
P3.3R	120	33	0.27	C	0.30
P15.1	176	46	0.26	C	0.30

The following figure shows the comparison of the results obtained by test series P3.2 and P3.3. These two test series were nominally identical. The only difference between them was the different surface treatment. The black curves indicate the results obtained by the galvanised specimens (P3.2) and the grey curves indicate the non-galvanised ones. We can observe two major differences: the first is the higher shear resistance and the second is the higher friction resistance of the galvanised specimens. As discussed in section 4.7.2, the higher shear resistance is due to the higher material strength of the galvanised bolts. As the applied pretension forces were identical in both cases (see Table 4.6), the difference in the friction resistance originates from the different surface treatments.

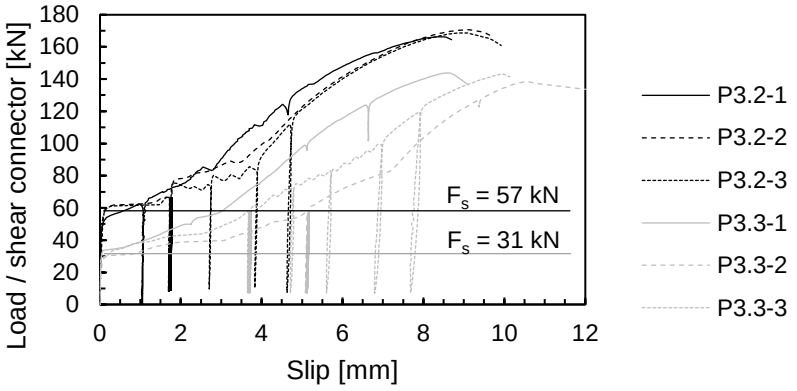

Figure 4.25 Comparison of galvanised (P3.2) and non-galvanised (P3.3) specimens

4.7.7 Demountability and reusability

In load regime 1 (LR1), the specimens were loaded until 500 kN (except P15.2-1, which was loaded until 1000 kN), then unloaded, and the four upper bolts were removed. The successful removal of these bolts proved the demountability of the tested systems. Specimens P3.2-3 and P3.3-3 were re-assembled after failure with new bolts. Afterwards, they were loaded until failure. Their second test showed similar

behaviour to their original tests in the means of resistance, stiffness and slip capacity. Because the failure occurred in the bolts and not in the connected members, the developed composite flooring systems are robust and therefore adequate for reuse.

4.7.8 Challenges in design and application

Some factors can make the design and application of demountable shear connections challenging. First, the fabrication and installation process require special care for tolerances. If the tolerances are too small, the construction process can become difficult or even impossible. However, too large tolerances lead to an increase in slip and a reduction in stiffness. In the tested shear connection types ϕ24 holes were applied for M24 bolts. The beam test specimens presented in the following chapter used the same tolerances. This hole size was sufficient to assemble the specimens successfully. The numerical simulations of the beam tests (Chapter 6.3) showed that the mean value of the bolt position (central position) can be used for the numerical modelling. However, further probabilistic analysis is recommended to assess how the different bolt positions could affect the load-bearing capacity of demountable composite beams. Second, the tested shear connections showed lower stiffness than standard welded studs. This can lead to increased deflections when applied in a beam (see Chapter 5). The question of the reduced beam stiffness is investigated in Chapter 8. Third, the observed load-slip behaviour is different from an ideally plastic curve that represents the traditional shear studs. This will have an effect on the definition of the ultimate load bearing capacity of the shear connection. This question in investigated in detail in Chapter 9.

Chapter 5. Beam tests

5.1 General

Based on the experimental observations of the push-out tests, two shear connection variants were selected and were implemented in two, six-meter-long beam test specimens with prefabricated deck elements. This chapter presents the details of the conducted beam tests including the description of the test specimens, the test setup, the measurements, the testing procedure and the results in terms of load-deflection behaviour and observed damages. Parts of the results shown here were presented in [69].

5.2 Beam tests conducted in the DISCCO project

Nellinger [64] conducted two beam tests in the frame of a preceding RFCS project, called DISCCO [65]. His aim was to investigate the load-displacement behaviour of beams with low degrees of shear connection. Both beams were comprised of an IPE 360 steel beam and a 150 mm thick composite slab with ComFlor® 80 [63] metal decking. The beams had a clear span of 6 m and were subjected to a two-point loading. Both beams used headed studs of 19 mm diameter and 125 mm nominal height (Köco SD 19x125) welded through the decking. The schematic view and the cross-section of the beam tests are presented in Figure 5.1 and Figure 5.2, respectively.

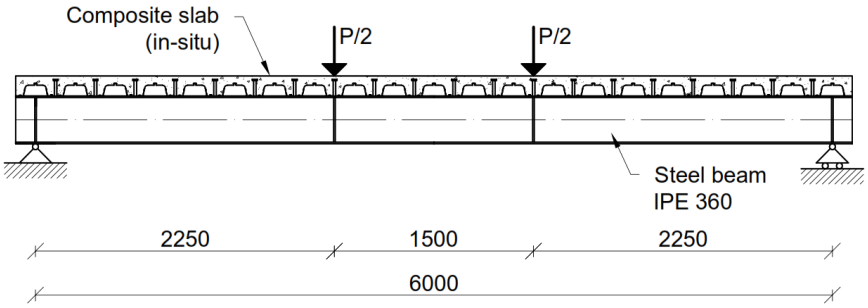

Figure 5.1 Schematic view of Nellinger's beam tests

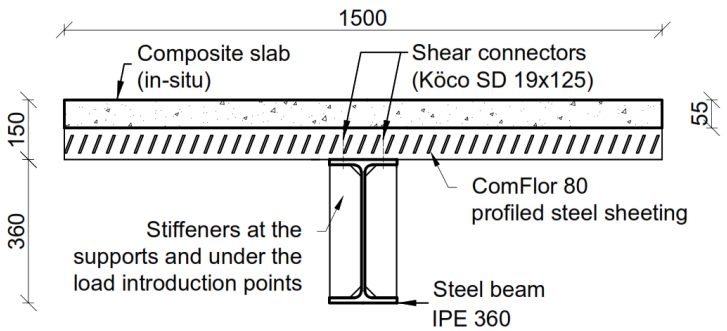

Figure 5.2 Cross-section of Nellinger's beam test (Specimen 2-10)

The two beam tests differed only in the number of shear connectors per rib. In the first test (Specimen 2-09), single stud connectors were applied and in the second test (Specimen 2-10) the connectors were placed in pairs. The longitudinal shear connector spacing was 300 mm in both cases. The parameters of the beam tests conducted by Nellinger [64] are presented in Table 5.1.

Table 5.1 Tested beam configurations of Nellinger

Test No.	Clear span, L	Section	Slab	Shear connectors	η [-]
2-09	6 m	IPE 360 S355 (f_y = 382 MPa)	CF80, d =150 mm C35/45 (f_c = 48.62 MPa)	Köco SD 19x150 (f_u = 550 MPa) (single)	0.22
2-10	6 m	IPE 360 S355 (f_y = 382 MPa)	CF80, d =150 mm C35/45 (f_c = 49.02 MPa)	Köco SD 19x150 (f_u = 550 MPa) (pairs)	0.32

As the demountable shear connections investigated in this thesis are more likely to be placed in pairs, the second beam test specimen of Nellinger [64] (Specimen 2-10) was selected to be a benchmark test when investigating the behaviour of composite beams with demountable shear connections. This test contained 10 pairs of shear connectors placed on the half-length, among which 8 pairs were placed within the shear length (between the support and the load application point. Among the push-out tests conducted by Nellinger [64], test series 3-02 represents the shear connection that he applied in beam test 2-10. The load-slip curve of this connection is presented in the following figure:

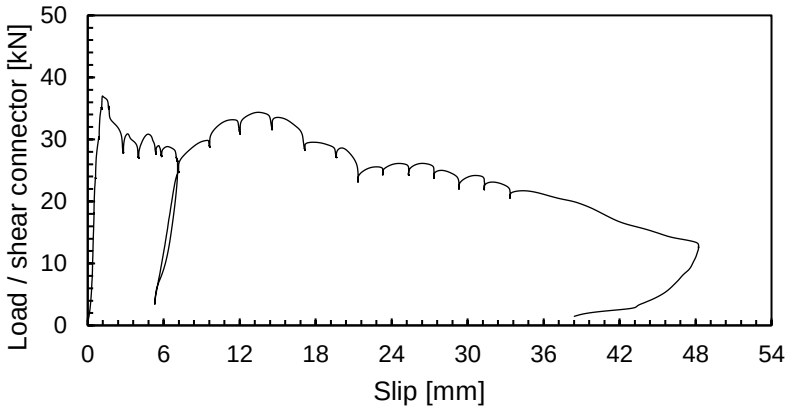

Figure 5.3 Load-slip curve of the shear connection used in Nellinger's beam test (Specimen 2-10)

5.3 Tests specimens with demountable shear connection

Two beam tests have been performed on 6 m span composite beams with demountable shear connectors. The geometrical layout of the tests and the material grade of the steel and the concrete were selected to be similar to the test of Nellinger [64] presented in the previous section. Therefore, it was possible to

make a direct comparison of the results with conventional welded shear connectors. Table 5.1 summarises the tested configurations.

Table 5.2 Tested beam configurations

Test No.	Clear span, *L*	Section	Slab	Shear connection type	Distribution of shear connectors
B7	6 m	IPE 360 S355	CF80 d =150 mm C35/45	P3.3 Friction bolts in cast in cylinders	Uniform along the length placed in pairs with 600 mm spacing
B8	6 m	IPE 360 S355	CF80 d =150 mm C35/45	P15.1 Coupled bolts	Uniform along the length placed in pairs with 600 mm spacing

Each specimen comprised of a 6.3 m long IPE 360 steel beam with a grade of S355 and two pre-fabricated composite slab elements with a depth of 150 mm and a width of 790 mm using ComFlor® 80 [63] metal decking. The beams were subjected to two-point loads so that a defined zone of the beam was subjected to constant shear. Figure 5.4 shows the schematic view of the beam tests.

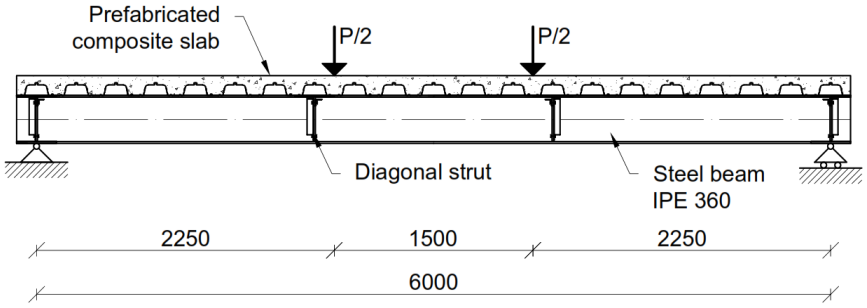

Figure 5.4 Schematic view of the beam tests

The total width of the specimens was 1600 mm. This width corresponds to the effective width defined by Eurocode 4 [18]:

$$b_{eff} = b_0 + \sum b_{ei} = b_0 + 2 \cdot \frac{L}{8} = 100\ mm\ +\ 2 \cdot \frac{6000\ mm}{8} = 1600\ mm \tag{5.1}$$

The shear connectors were placed in pairs with a transversal spacing (b_0) of 100 mm and a longitudinal spacing of 600 mm. The slab elements were stabilised with diagonal struts so that no tension force arose in the shear connectors from the self-weight of the composite slabs. The diagonal struts were not connected to the slabs by any mechanical connectors. They only provided vertical support to deck elements; therefore, they did not influence the longitudinal flexural behaviour. Figure 5.5 shows the cross-section of the tested beams, Figure 5.6 shows the diagonal struts before positioning the second deck element of specimen B8 and Figure 5.7 shows beam test specimen B7 from below before the testing was commenced.

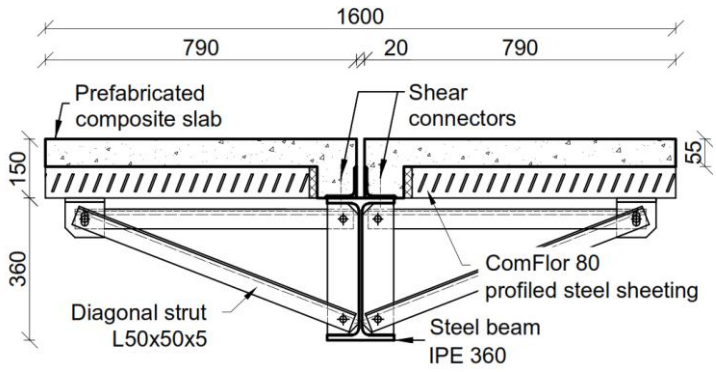

Figure 5.5 Cross-section of the tested beams (a) plan, (b) photo

Figure 5.6 Beam during assembly and diagonal struts before positioning the deck element

Figure 5.7 Beam specimen B7 from below before test conduction

The beams were designed for a 37% nominal degree of shear connection. This value was calculated using the following equation:

$$\eta = \frac{P_{R,6} \cdot n_{sc}}{N_{c,f}} \tag{5.2}$$

where n_{sc} is the number of shear connectors provided within the length between points of zero and maximum moment, $N_{c,f}$ is the compression resistance of the effective area of the concrete slab acting compositely with the steel section, and $P_{R,6}$ = 91.4 kN is the average shear connector force obtained by the push out test series P3.3 at 6 mm slip.

In Equation (5.2), N_{cf} was calculated using the expected values of the material strengths of the steel and the concrete because the actual material properties were unknown before test conduction. For the steel yield strength, the formulation given by the JCSS Probabilistic Model Code [70] was used:

$$f_{y,exp} = f_{y,sp} \cdot \alpha \cdot exp(-u \cdot v) - C = 394\ MPa \tag{5.3}$$

where:

$f_{y,sp}$ = 355 MPa is the nominal value of the yield strength;

α = 1.05 is a spatial position factor for hot rolled sections;

u = -1.5 is a factor related to the fractile of the distribution used in describing the distance between the nominal value and the mean value;

v = 0.07 is the coefficient of variation; and

C = 20 MPa is s a constant reducing the yield strength as obtained from usual mill tests to the static yield strength.

The concrete strength was calculated using the formulation of Eurocode 2 [49]:

$$f_{cm} = f_{ck} + 8\ MPa = 43\ MPa \tag{5.4}$$

where f_{ck} = 35 MPa is the characteristic cylinder strength of a C35/45 concrete.

The calculated η = 0.37 value corresponds to a uniform spacing of 600 mm in pairs. This degree of shear connection is less than the minimum permitted by Eurocode 4 [39], which is 40%. In the RFCS project DISCCO [65], the degree of shear connection in the beam tests ranged from 25% to 38%.

Specimen B7 used shear connection type P3.3, and specimen B8 used shear connection type P15.1. Both shear connection system utilise friction in the early load stages and bolt bearing afterwards.

Shear connector type P3.3 consists of a cast-in steel cylinder welded to an L-profile located at the edge of the slab, a top plate welded to the cylinder and a pre-tensioned bolt with a grade of 8.8. This connection provides accessibility from the top of the slab through pockets in the concrete.

Shear connector type P15.1 uses an embedded coupler device, an embedded bolt and a bolt placed from below the slab. The coupler is of grade 10.9 and the bolts are of grade 8.8 steel. Figure 5.8 shows photos of the shear connector systems in the slabs before concreting.

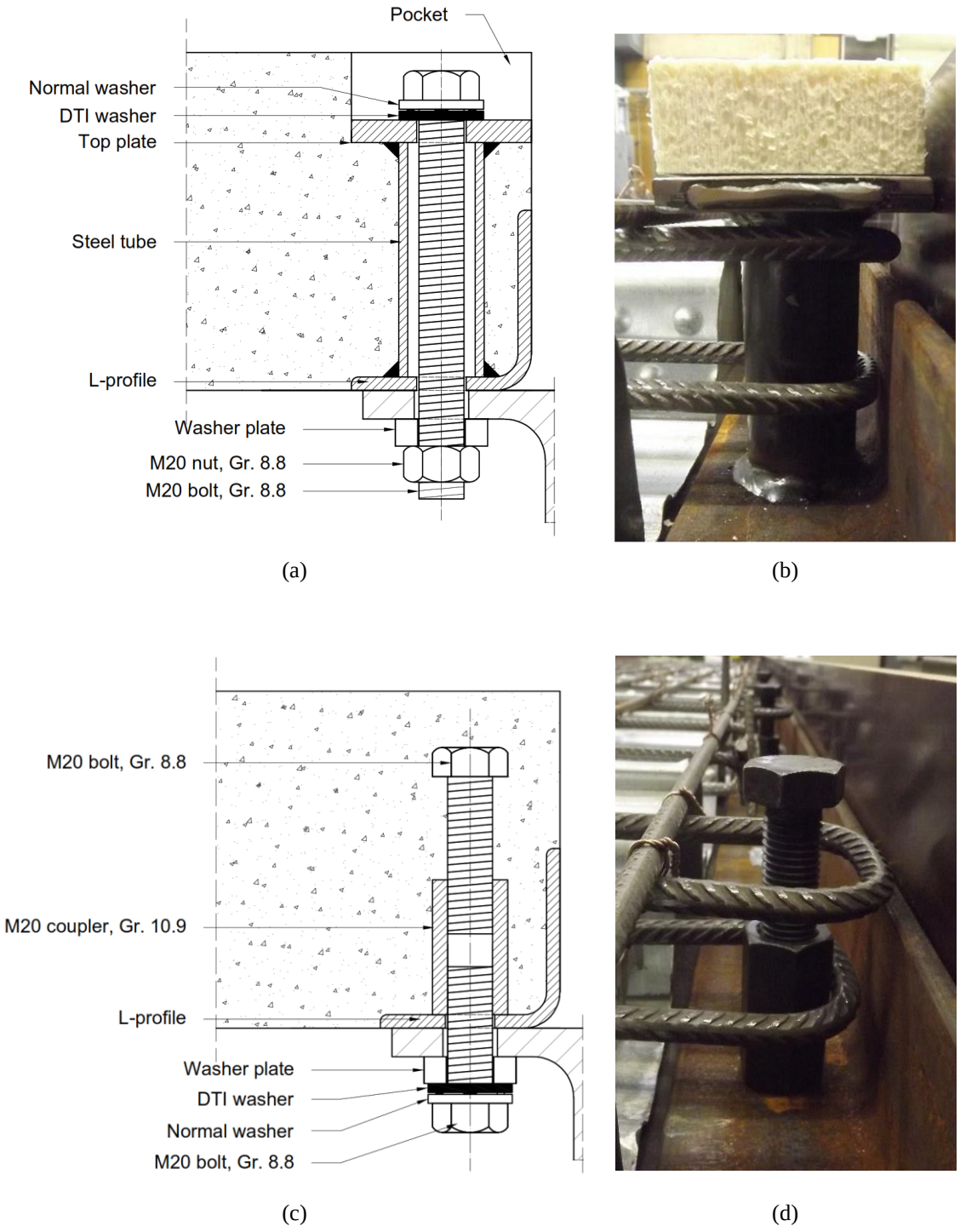

Figure 5.8 Shear connector systems applied in the beam tests: (a) and (b) System P3.3 in beam B7, (c) and (d) System P15.1 in beam B8

5.4 Fabrication and assembly

The formworks for the deck elements were fabricated from plywood placed on standard European pallets. The solid strips were created by placing profiled foam fillers between the base plate of the formwork and the holes under the crests of the profiled steel sheeting. L-profiles with pre-drilled holes were placed between one end of the profiled sheeting and the side wall of the formwork. In specimen B7, expanded polystyrene (EPS) foam blocks were glued to the top plate of the shear connectors in order to create pockets in the concrete (see Figure 5.8). The EPS blocks were removed after the concrete had hardened. In specimen B8, holes were drilled into the base plate of the formwork through the pre-drilled holes of the L-profiles. Then, the mechanical coupler device with the embedded bolt were placed above the holes and dummy bolts were placed from below the base plate of the formwork into the coupler device to keep them in place during concreting. One layer of ϕ8/95/135, B500 B reinforcement mesh were placed on the top of the profiled steel sheeting. Additionally, two layers of ϕ10 U-bars were placed around the shear connectors (see Figure 5.8).

The composite deck elements were fabricated in 6 m long pieces. This means that no transversal joints were applied. However, in practice, it is possible that the application of transversal joints is not avoidable. Lam et al. [71] pointed out that grouted joints can be applied for the transversal connection of the deck elements without compromising the flexural behaviour. Therefore, the tested beams without any transversal joints can represent the behaviour of demountable composite beams adequately.

Both beams were cast on the same day from the same concrete mixture. After the concrete had hardened, the slabs were lifted and placed on the top of the steel beam. For each deck element it was necessary to align 10-10 holes in the steel beam and the concrete at the same time. Due to the L-profiles with pre-drilled holes, low tolerances could be achieved and the hole alignment was successful.

Then, the composite slab elements were fixed to the beam with high-strength bolts through 24 mm diameter pre-drilled holes in the top flange of the beam. The beams were continuously supported along the total length during the assembly. This type of construction corresponds to a propped construction method.

In both cases the bolts were tightened by rotating the bolt head using a pneumatic impact wrench. Direct tension indicator (DTI) washers were applied in accordance with the requirements of EN 1090-2 [39] in order to control the pre-tension force (see Figure 5.9). According to the specifications of the manufacturer of the washers [72], the mean value of the bolt preload that belongs to the flattening of the washers is 150 kN. This is different than the preload during the push-out tests (120 kN for P3.3 and 176 kN for P15.1). This difference can cause between 6.7 - 7.8 kN difference in the resulting friction resistance but it does not affect the shear resistance of the connection (see Chapter 4.7.2 and also the findings of Pavlović [16]).

The assembly of specimen B7 was performed in the following sequence:

1. Lifting the first composite slab element.
2. Inserting bolts into the cast-in cylinders from the top of the slab.
3. Positioning the slab on the top of the beam – when the slab is aligned, all the bolts fit into the holes of the steel beam.
4. Mounting the nuts.
5. Tightening the bolts with hand tools.
6. Repeating step 1-5 with the second slab element.
7. Tightening the bolts with a pneumatic impact wrench in two cycles.
8. Checking the indicator gap of the DTI washer using a feeler gauge.

Specimen B8 was assembled in the following order:

1. Lifting the first composite slab element.
2. Positioning the slab on the top of the beam.
3. Inserting bolts into the coupler embedded in the slab from below the upper flange of the steel beam.
4. Tightening the bolts with hand tools.
5. Repeating step 1-4 with the second slab element.
6. Tightening the bolts with a pneumatic impact wrench in two cycles.
7. Checking the indicator gap of the DTI washer using a feeler gauge.

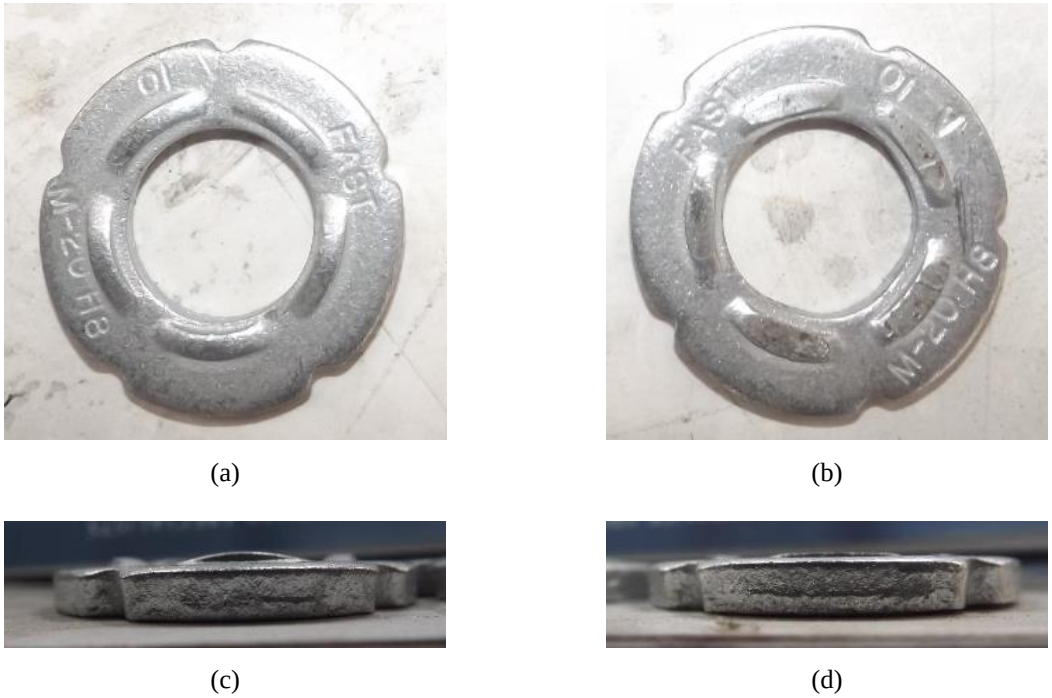

(a) (b)

(c) (d)

Figure 5.9 DTI washers, (a) and (c) before usage, (b) and (d) after usage

5.5 Loading protocol and test conduction

The tests were conducted using a 1000 kN capacity hydraulic jack. Two-point loading was applied to the beam using a testing rig composed of a spreader beam, and two additional beams with steel rods welded on their bottom flange (see Figure 5.11). Steel plates and neoprene layers were applied under the load application rods in order to equilibrate the surface roughness of the concrete and to prevent the local failure of the concrete due to the high concentrated forces. Both the steel and the neoprene layers had a thickness of 10 mm and a width of 100 mm.

The loading protocol consisted of two parts:

First part: 25 cycles as described in EN1994-1-1 [18] for push-out tests

1.1 Loading until the 40% of expected failure load (P_{exp})

1.2 25 cycles between the 5% and the 40% of the expected failure load (1 min / cycle)

Second part: Incremental cyclic loading (loading speed equivalent to 1.2)

2.1 5 cycles between the 5% and the 50% of P_{exp},

2.2 5 cycles between the 5% and the 60% of P_{exp},

2.3 5 cycles between the 5% and the 70% of P_{exp},

2.4 5 cycles between the 5% and the 80% of P_{exp},

2.5 Monotone loading until failure.

The loading was paused for five minutes after each five cycles. The expected failure load was determined using the nonlinear finite element software Abaqus [32]. The cycles were performed using force-controlled mode, while the monotonic loading was applied using displacement-controlled mode. The schematic drawing of the loading protocol is shown in Figure 5.10.

5.6 Measurements

For each specimen, 28 displacement sensors (LVDTs) were applied to measure

(i) The end slip of each composite slab,

(ii) The slip values at the shear connectors,

(iii) The transverse separation of the slabs relative to the beam, and

(iv) The deflection values of the beam in different positions.

The designation and range of the sensors are presented in see Table 5.3. Additionally, one inclinometer was applied on the beam and 10 linear strain gauges (HBM-1-6/120-LY61) [73]: four on the web of the beam, and six on longitudinal reinforcement bars inside the slabs. Furthermore, the travel and the force values of the hydraulic jack were continuously monitored during the tests. Figure 5.11 shows the measurement setup, and Figure 5.12 presents a photo of the test setup.

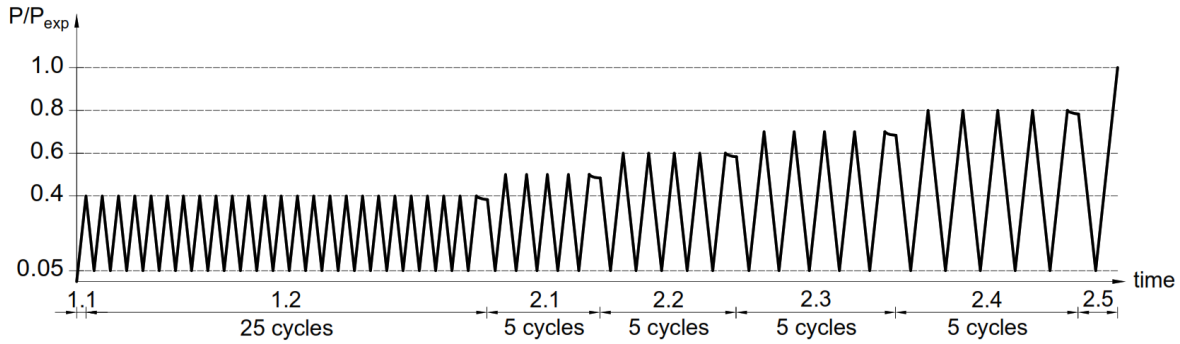

Figure 5.10 Loading protocol

Table 5.3 Applied displacement sensors and inclinometer

#	Position	Measurement	Range [mm]
1	RS-0	Right slab, end slip	20
2	RS-1	Right slab, 1st shear connector slip	20
3	RS-2	Right slab, 2nd shear connector slip	20
4	RS-3	Right slab, 3rd shear connector slip	20
5	RS-4	Right slab, 4th shear connector slip	20
6	RS-5	Right slab, 5th shear connector slip	20
7	RS-6	Right slab, 6th shear connector slip	20
8	RS-7	Right slab, 7th shear connector slip	20
9	RS-8	Right slab, 8th shear connector slip	20
10	RS-9	Right slab, 9th shear connector slip	20
11	RS-10	Right slab, 10th shear connector slip	20
12	RS-11	Right slab, end slip	20
13	LS-0	Left slab, end slip	20
14	LS-1	Left slab, 1st shear connector slip	20
15	LS-3	Left slab, 3rd shear connector slip	20
16	LS-8	Left slab, 8th shear connector slip	20
17	LS-10	Left slab, 10th shear connector slip	20
18	LS-11	Left slab, end slip	20
19	RC-1	Right slab, top, compression	20
20	LC-1	Left slab, top, compression	20
21	BD-0	Supporting beam deflection at 0 mm	50
22	BD-1	Beam deflection at 1125 mm	100
23	BD-2	Beam deflection, load application	100
24	BD-3	Beam deflection, mid-span	100
25	BD-4	Beam deflection, load application	100
26	BD-5	Beam deflection at 4875 mm	100
27	BD-6	Supporting beam deflection at 6000 mm	50
28	RT-1	Right slab, mid-span, transverse separation	50
29	LT-1	Left slab, mid-span, transverse separation	50
30	IN-1	Inclinometer at beam support	

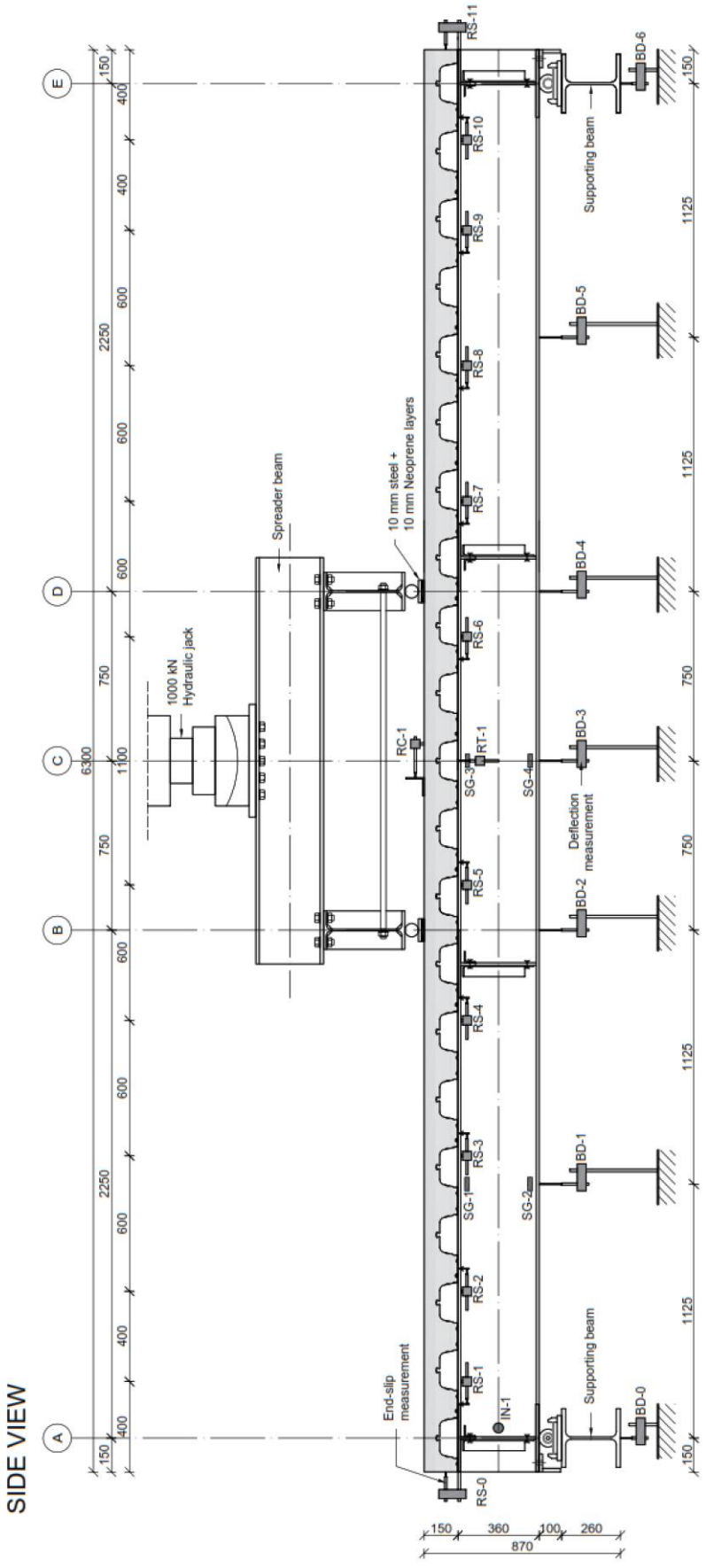

Figure 5.11 Measurement setup

Figure 5.12 The test setup

Additionally, compression tests on concrete cube specimens and uniaxial tensile tests on steel coupon specimens were carried out to obtain information about the properties of the applied materials. According to these tests, the mean values of the concrete cube strength and the steel yield strength were:

$$f_{cu,m} = 64.0\ MPa \tag{5.5}$$

$$f_{y,m} = 381.8\ MPa \tag{5.6}$$

The detailed results of the conducted material tests can be found in 0.

5.7 Disassembly and observed damages

Both beams were loaded up to failure, and the deflection was further increased until ~220 mm (L/27). Figure 5.14 and Figure 5.14 show global photos of the deformation of specimen B7 and B8 under failure conditions. Figure 5.15 shows the specimens after removing them from the testing frame.

Figure 5.13 Specimen B7 under failure conditions

Figure 5.14 Specimen B8 under failure conditions

Figure 5.15 Specimen B7 (right) and B8 (left) after removing them from the testing frame

After the tests, the specimens were disassembled. The disassembly process required less time and effort than in the case of standard composite beams, where welded studs provide the shear connection; and therefore, the separation of the materials requires a large amount of cutting. The concrete slab elements could be separated from the steel beam by using a normal wrench. Hence, the demountability of the specimens was proven.

5.7.1 Beam test B7 with friction bolts in cast in cylinders

Beam test B7 failed at a total load level of 600 kN due to concrete crushing. Cracks appeared above the crests of the profiled sheeting due to tensile stresses arising from bending. The shear connectors did not fail during the tests; however, shear deformation of the bolts and thread penetration in the steel beam were observed. During dismantling all bolts could be removed from the specimen. Figure 5.16 shows the observed damages.

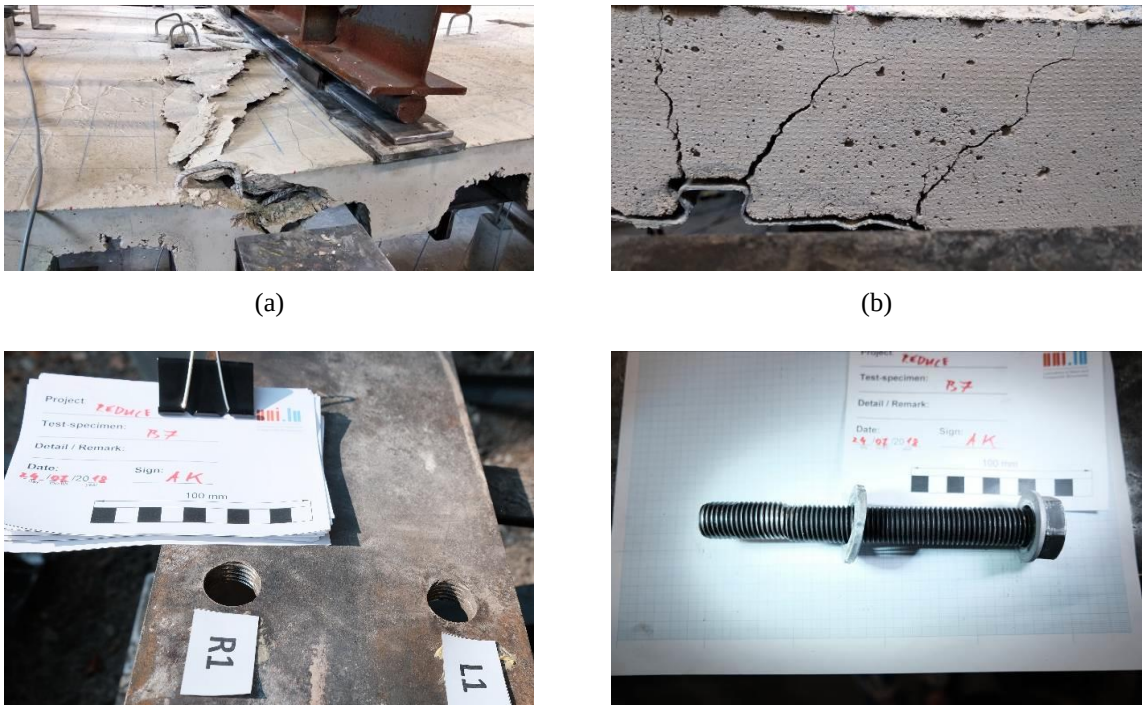

Figure 5.16 Observed damages in specimen B7, (a) concrete crushing, (b) cracks due to bending, (c) thread penetration in the flange, (d) bolt deformation

5.7.2 Beam test B8 with coupled bolts

In the case of specimen B8, the maximum total load was reached at 569 kN. At this load level, the first shear connectors failed. This was followed by the failure of three additional shear connectors as the test was continued and the deformation was further increased. Finally, concrete crushing took place.

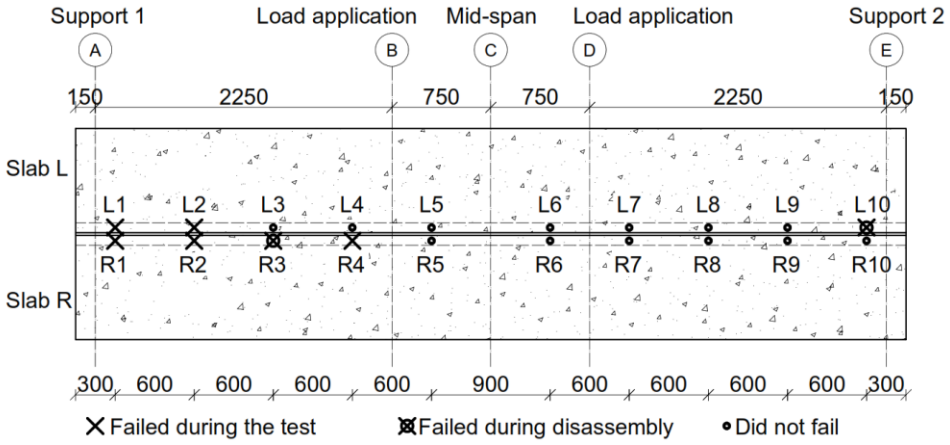

Figure 5.17 Location of the failed bolts

Figure 5.18 Failed bolts after the test

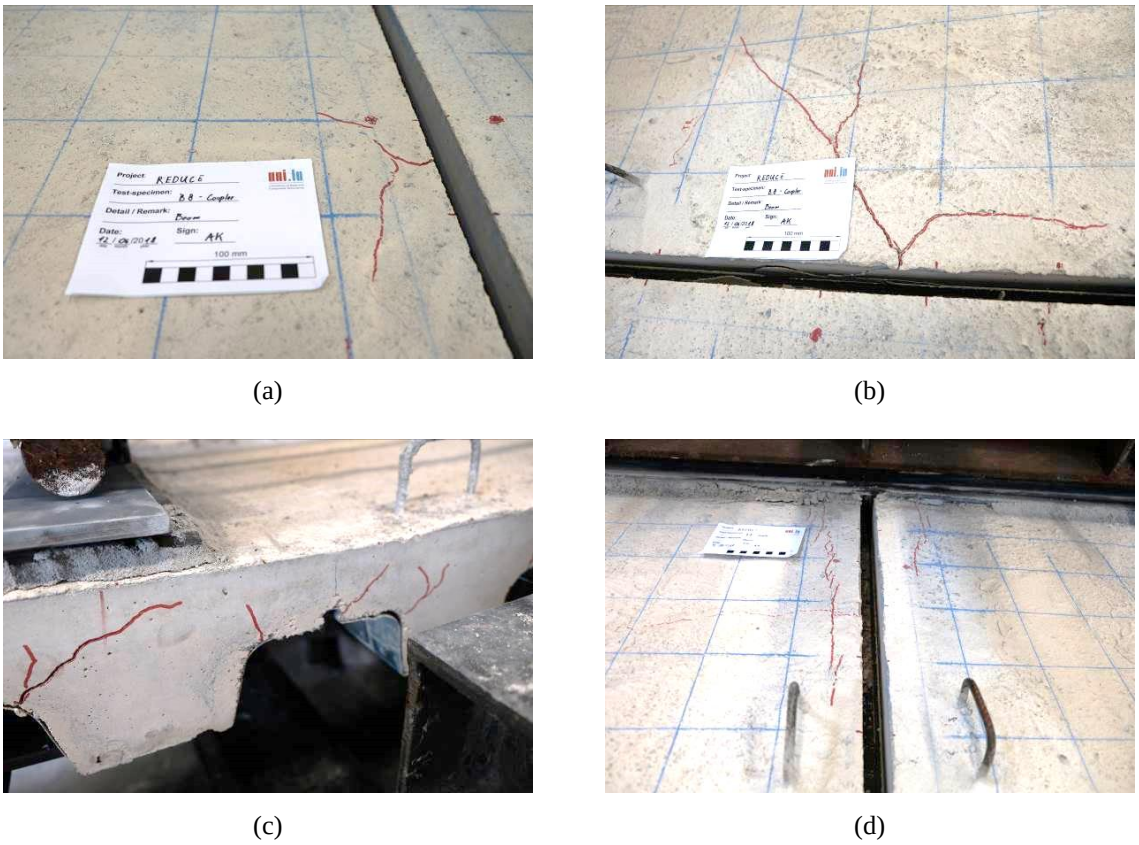

(a) (b)

(c) (d)

Figure 5.19 Cracks on the concrete, (a) cracks around shear connector L1, (b) cracks around shear connector R2, (c) cracks above the crests, (d) longitudinal crack

The failure of the shear connectors occurred in the following order: R1, L1, R2, L2, R4. Two shear connectors (R3, L10) broke during dismantling because they had suffered excessive deformations during the test. The location of the failed bolts in top view is shown in Figure 5.17, and Figure 5.18 shows the failed bolts after the test.

Thread penetration could be observed in the holes of the steel profile similar to the case of test B7. The concrete slab cracked around the outermost shear connectors (see Figure 5.19, a and b) above the crests of the sheeting (Figure 5.19, c) and longitudinally, parallel to the inner edge (Figure 5.19, d).

5.8 Experimental results

This section presents the measured load-deflection curves and the results of the slip measurements.

5.8.1 Load-deflection curves

The measurements started after the assembly of the test setup. Therefore, the self-weight of the composite beam is not included in the measured data. The calculated self-weight deflection is 0.77 mm. The load-deflection curves of specimen B7 and B8 are presented in the following figures.

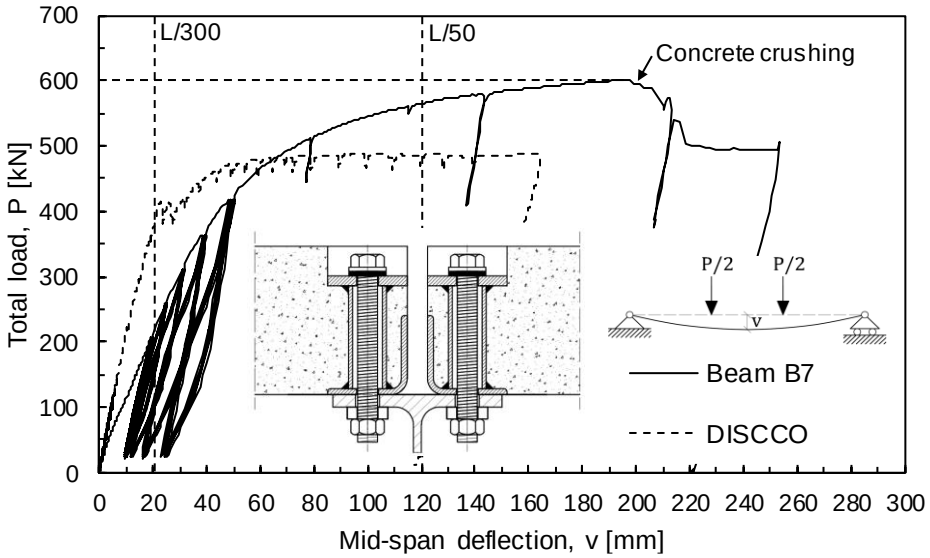

Figure 5.20 Load-deflection curve of specimen B7

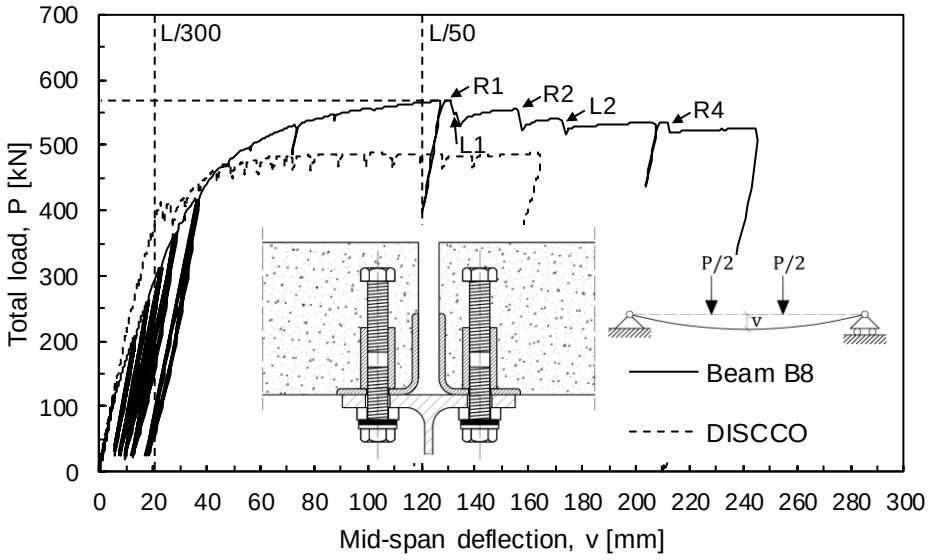

Figure 5.21 Load-deflection curve of specimen B8

Beam test B7 failed at a total load level of 600 kN by concrete crushing. This load level corresponds to a bending moment of 675 kNm. The mid-span deflection at failure was 198 mm (L / 30). After the first cycles of the loading procedure (part 1.2: 25 cycles between 26 kN and 210 kN), the specimen had a residual deflection of 8.2 mm.

The failure of specimen B8 occurred by shear connector failure at a load level of 569 kN. The corresponding bending moment capacity is 640 kNm. At this load level, the deflection of the beam was 133 mm (L / 45). After the first shear connector had failed, the deflection was further increased, and the

failure of the subsequent shear connectors occurred. This mechanism is represented by the stepwise dropping of load on the load-deflection curve.

Both tested beams produced higher resistance than the similar beam tested in the frame of the DISCCO project [65]. The initial stiffness values were compared at the deflection value of 20 mm (L / 300).

The moment-deflection curves are presented in Figure 5.22 and in Figure 5.23. In the figures, the calculated plastic moment capacity in case of full shear connection ($M_{pl,f}$), the plastic moment resistance of the steel beam ($M_{pl,a}$), the calculated plastic moment capacity ($M_{pl,\eta}$) and the elastic moment resistance of the composite section (M_{El}) are also presented. The plastic moment capacity ($M_{pl,\eta}$) was determined using a newly developed algorithm (Method PL1), which is presented in detail in Chapter 9.4.2.

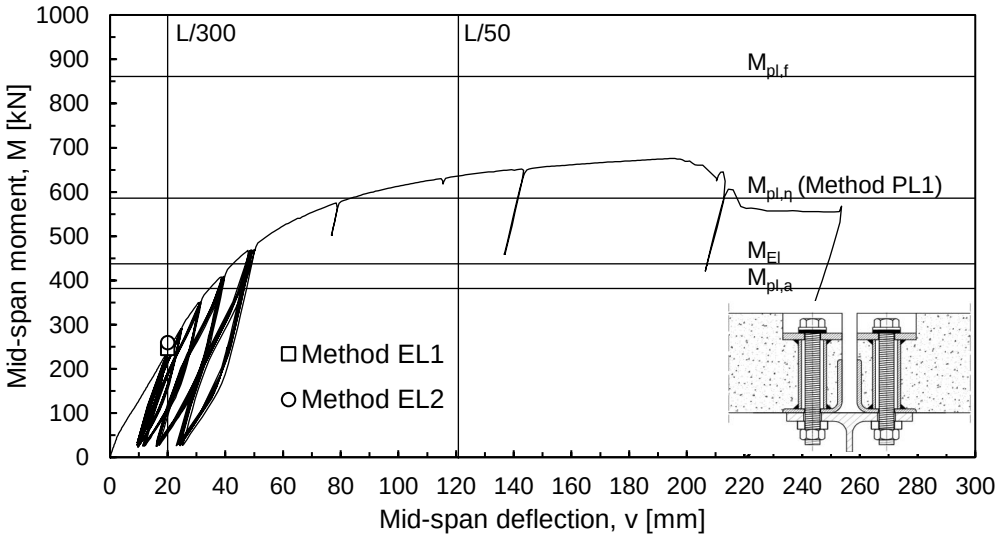

Figure 5.22 Moment-deflection curve of specimen B7

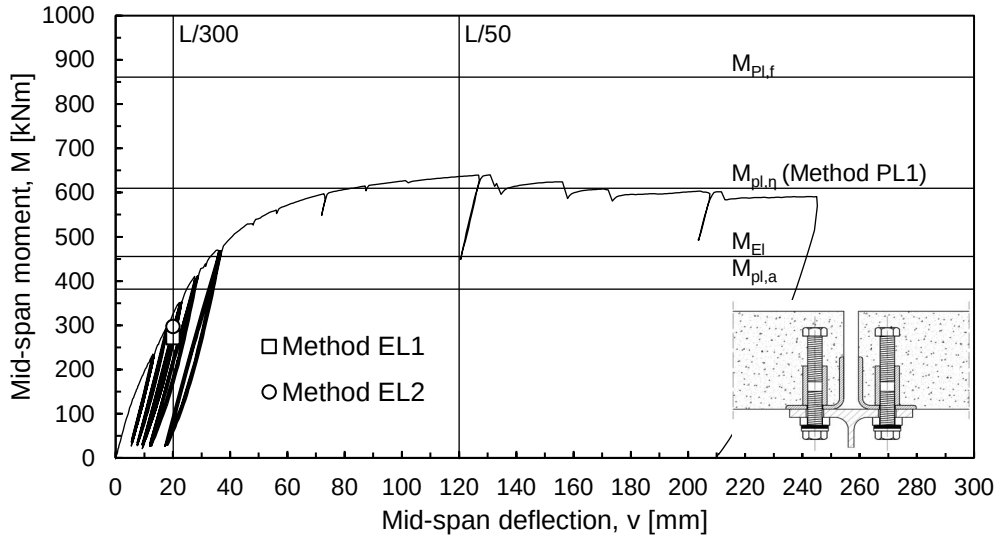

Figure 5.23 Moment-deflection curve of specimen B8

5.8.2 Slip measurements

Figure 5.24 and Figure 5.25 show the results of the end slip measurements. Slip was monitored at both ends of each slab element. The presented end slip values are the mean values of the four measurements.

In the case of specimen B7, the first slip took place at the load level of 50 kN (56.3 kNm). After the first 25 cycles of the loading protocol, the residual slip was 1.46 mm. The end slip was 9 mm when the specimen failed due to concrete crushing. This slip level is in the range where shear connector failure occurred in the push-out tests (c.f. Figure 4.13).

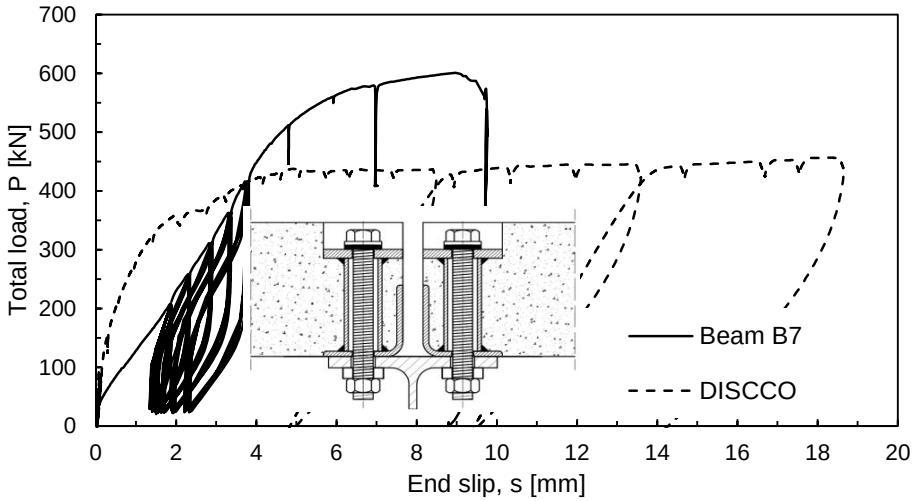

Figure 5.24 Specimen B7: total load vs. average end slip

In the case of specimen B8, the first slip occurred at a load level of 110 kN (123.8 kNm). The end slip at failure was 7.5 mm. At this slip, the two outermost shear connectors (R1 and L1) failed. This slip value is in accordance with the average slip capacity of the shear connector measured in the push-out tests (see Figure 4.19).

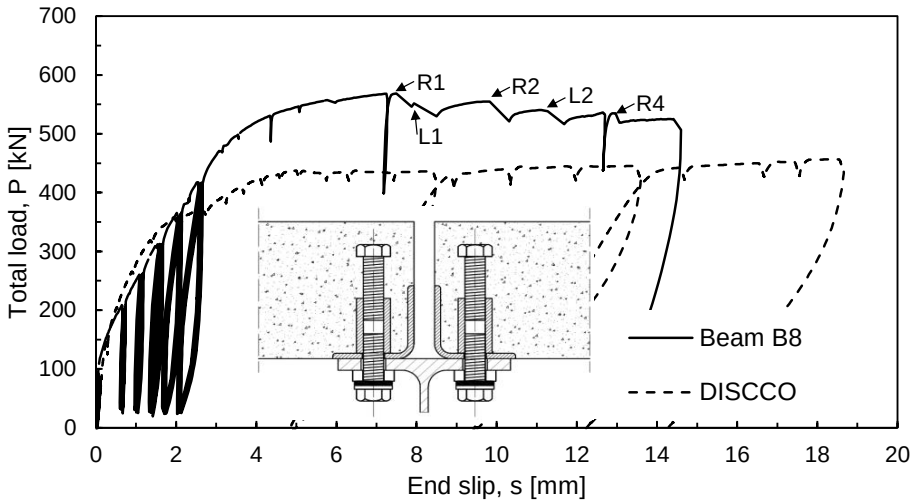

Figure 5.25 Specimen B8: total load vs. average end slip

Figure 5.26 and Figure 5.27 show the slip measurements at each shear connector along the length of the beams at different load levels. The dots represent the measured slip at the individual shear connectors. Cosine functions were also plotted in the figures as an approximation of the slip distribution functions.

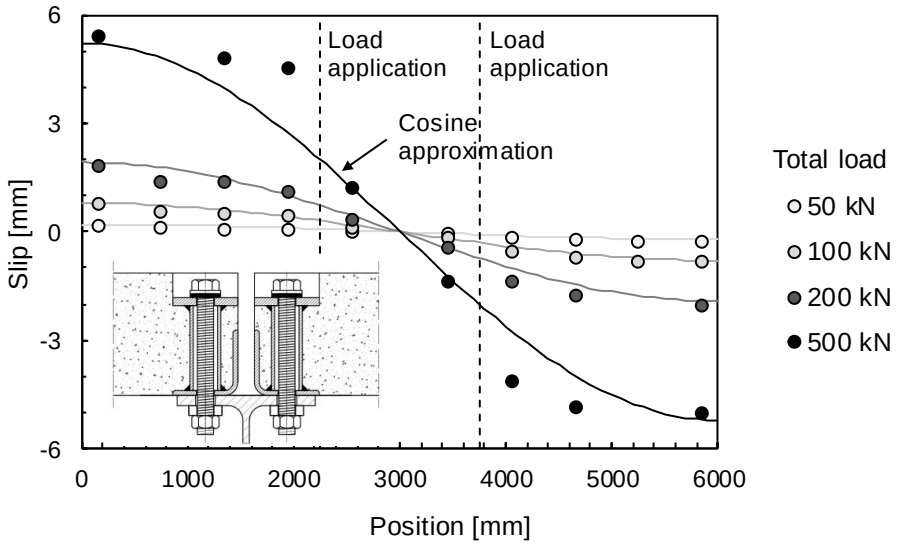

Figure 5.26 Specimen B7: Slip values at different load levels

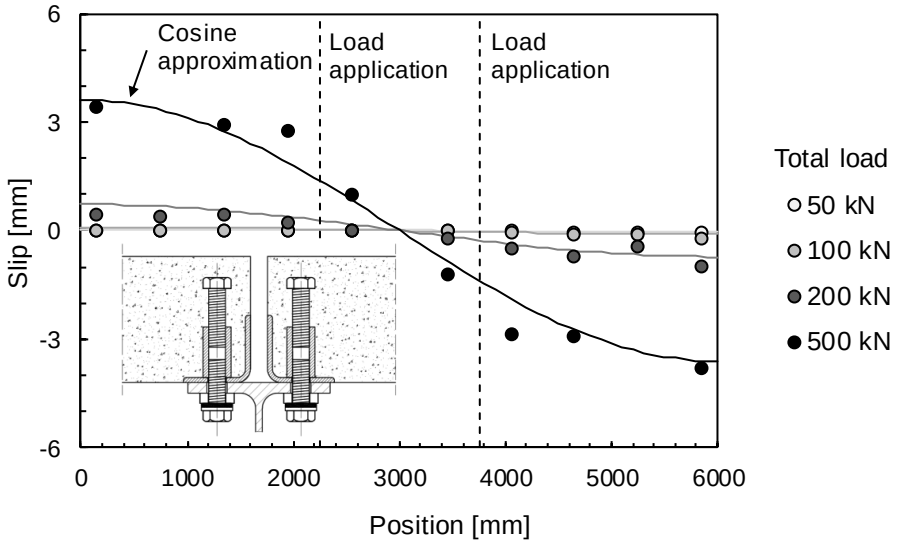

Figure 5.27 Specimen B8: Slip values at different load levels

The end slip was determined at different load levels for both beams. For load levels lower than the elastic limit of the beams ($P < P_{El}$), the end slip was calculated using Equation (8.41). The end slip when the plastic capacity of the beam is reached ($P = P_{Pl,\eta}$) was calculated using Equation (9.4). Between the elastic and the plastic limit load ($P_{El} < P < P_{Pl,\eta}$) linear interpolation was applied. The comparison of the measured and the calculated end slip is presented in Figure 5.28 and Figure 5.29.

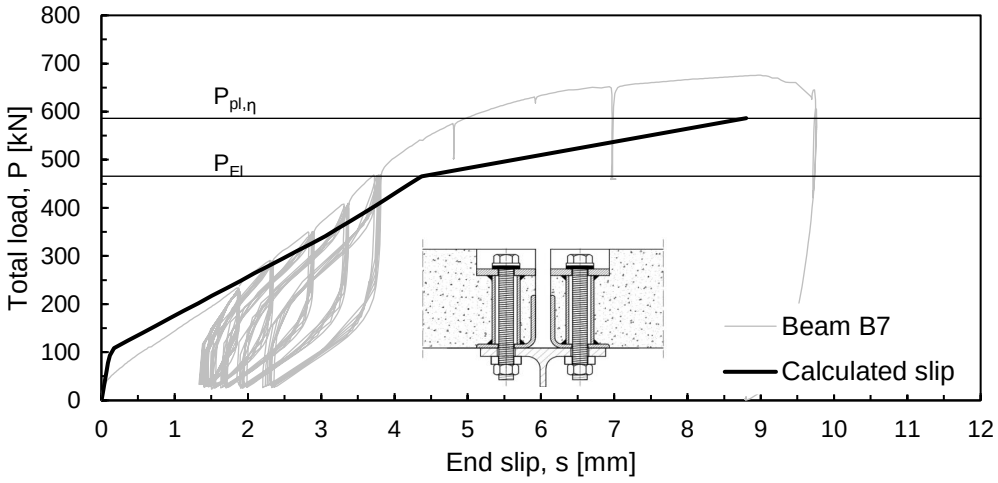

Figure 5.28 Calculated vs. measured end slip (Specimen B7)

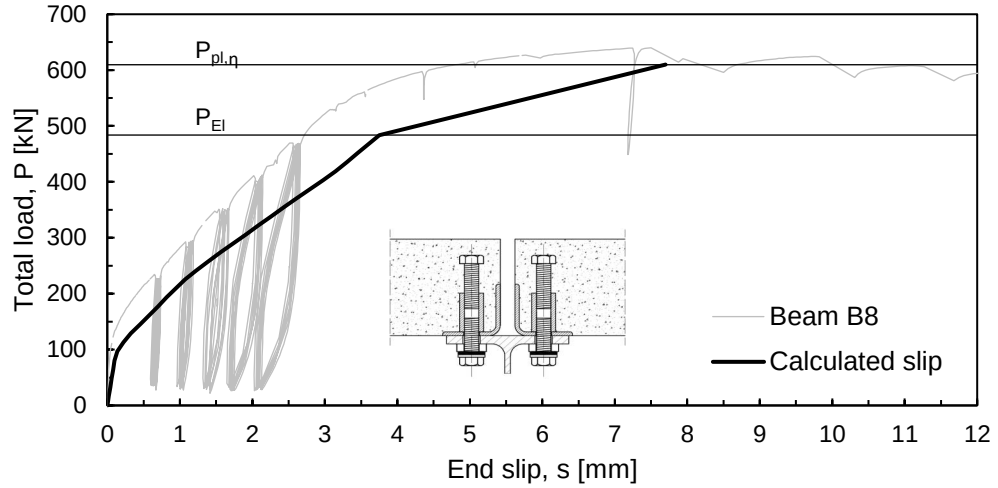

Figure 5.29 Calculated vs. measured end slip (Specimen B8)

5.9 Discussion of the results and observations of the beam tests

5.9.1 Load bearing capacity and degree of shear connection

The stress block method of Eurocode 4 [18] enables to calculate the bending moment capacity of the composite section with partial shear connection based on plastic theory (see Chapter 2.3.2). The method assumes that the developing compression force in the concrete is ηN_{cf}, where η is the degree of shear connection. In the case of the tested specimens, the moment capacity can be calculated from the measured ultimate load with Equation (5.7) but the degree of shear connection is not because the developing compression force is unknown. Using the aforementioned method, it is possible to calculate backwards the degree of shear connection from the measured bending moment capacity (M_{ult}), the calculated bending capacity of the steel beam alone ($M_{pl.a}$) and the calculated bending capacity of the composite section in the case of full shear connection ($M_{pl.f}$). The following table summarises the

determined degree of shear connection for both of the tested specimens and for the beam that was tested within the frame of the DISCCO project [65]. In this table, P_{ult} and M_{ult} also includes the the self-weight of the beams, which means an additional 37 kN force and 28 kNm bending moment to the measured values.

$$M_{ult} = \frac{P_{ult}}{2} \cdot 2.25\ m \tag{5.7}$$

Table 5.4 Load bearing capacity and degree of shear connection of the tested beams

Test No.	Shear connection	P_{ult} [kN]	M_{ult} [kNm]	$M_{pl.a}$ [kNm]	$M_{pl.f}$ [kNm]	η [-]
B7	P3.3	637	703	382	861	0.50
B8	P15.1	606	668	382	861	0.41
DISCCO	Welded stud	494	542	372	825	0.32

5.9.2 Stiffness and degree of interaction

The degree of interaction ψ is governed by the stiffness of the shear connection. If there is no shear connection, the degree of interaction is zero, while in case of a perfectly rigid shear connection its value is one. The load-deflection response of the beams showed some nonlinearities already at the early load stages below reaching L / 300 deflection. The corresponding load values ($P_{L/300}$) are smaller than the load (P_{El}) that corresponds to the elastic limit (see Table 5.5). This, and the lack of visible cracks or damages indicate that these nonlinearities do not originate from the plastification of the cross-section. These slight nonlinearities can be explained by the nonlinear behaviour of the shear connection due to bolt slippage in the bolt holes. Therefore, it was concluded that the beam behaved elastically until at least this deflection level. As the L / 300 deflection also corresponds to the limitation of the serviceability limit state, the stiffness at this point was used for the presented evaluation.

The load level at which the beam would reach this deflection ($P_{L/300}$) was calculated using elastic theory for both extreme cases (ψ = 0 and ψ = 1). The actual degree of interaction was determined using linear interpolation:

$$P_{L/300} = P_{L/300,\psi=0} + (P_{L/300,\psi=1} - P_{L/300,\psi=0}) \cdot \psi \tag{5.8}$$

So, the degree of interaction is:

$$\psi = \frac{P_{L/300} - P_{L/300,\psi=0}}{P_{L/300,\psi=1} - P_{L/300,\psi=0}} \tag{5.9}$$

Table 5.5 summarises the total load at the deflection of L / 300 ($P_{L/300}$) and the corresponding stiffness values ($S_{L/300}$). As one can see, both of the tested demountable composite beams had lower stiffness than

the beam with welded studs tested in the DISCCO project [65]. In the case of welded studs, the degree of interaction is similar to the degree of shear connection (ψ = 0.34 vs. η = 0.33). This is not the case for the demountable beams (B7 and B8), where the degree of interaction is relatively low despite of the higher values of η. This means, that in the design of demountable composite beams special attention is required for the occurring deflections.

Table 5.5 Stiffness Tested beam configurations

Test No.	Shear connection	$P_{L/300}$ [kN]	P_{EI} [kN]	$S_{L/300}$ [kN/mm]	$P_{L/300,\psi=0}$ [kN]	$P_{L/300,\psi=1}$ [kN]	ψ [-]	η [-]
B7	P3.3	210	389	10.50	173	596	0.10	0.50
B8	P15.1	289	405	14.45	173	596	0.27	0.41
DISCCO	Welded stud	319	409	15.95	153	584	0.34	0.33

5.9.3 Fabrication

Prefabricated elements require special attention for tolerances. With the fabrication procedure presented in Chapter 5.4, it was possible to reach sufficiently low tolerances to be able to assemble the specimens. However, it is important to note that the L-profiles applied in specimen B7 were slightly distorted after welding the steel cylinders. A special attention is required during the welding process in order to be able to eliminate this kind of distortion. Otherwise, the distortions need to be corrected before placing the L-profiles inside the formwork.

5.9.4 Disassembly

The demountability and reusability of the tested systems had already been proven during the push-out tests. Therefore, the specimens were not disassembled during the beam tests. After the tests - by when the steel beam, the concrete slab and the shear connectors had all been highly deformed - the specimens were disassembled with standard hand tools. Hence, the demountability was proven again. As it was already mentioned in section 5.9.2, no signs of cracks, damages or plastic deformations were observed before reaching L / 300 deflection, which corresponds to the serviceability limit. This indicates that beams that do not observe loads beyond the serviceability limit state remain reusable.

Chapter 6. Numerical simulations

6.1 General

The conducted experiments were reproduced numerically using the finite element software Abaqus [32].

(i) First, the materials were calibrated based on material testing. The concrete material calibration was based on compression tests. The steel materials were calibrated based on uniaxial tensile tests using the calibration method of Pavlović [16].

(ii) Second, advanced three-dimensional models were developed for the push out tests. The models were validated against the experimental measurements.

(iii) Third, a simplified model representing the beam tests was developed and validated.

(iv) Fourth, parametric studies were conducted on the validated beam test models in order to gain a better understanding of the influences of the different parameters and to assess the accuracy of the developed calculation methods presented in Chapter 8 and Chapter 9.

This chapter describes the developed numerical models as well as their validation against the experimental measurements. The parametric studies are described in Chapter 7.

6.2 Advanced modelling of push-out tests

6.2.1 General

During the push-out tests presented in Chapter 4, no concrete failure happened. The observed damages occurred locally in the vicinity of the shear connectors. Therefore, only this part of the push-out tests was reproduced numerically with the Finite Element software ABAQUS® [32]. This chapter presents the developed finite element models for shear connection systems P3 (friction bolts in cast in cylinders) and P15 (coupled bolts).

6.2.2 Geometry and boundary conditions

The model of System P3 (friction bolts in cast-in cylinders) consisted of an M20 bolt, a part of the flange of the beam, a part of the L-profile, a top plate, a washer plate, a steel cylinder and a part of the concrete between the top plate and the L-profile.

The model of System P15 (coupled bolts) included two M20 bolts coupled with a mechanical coupler device, an L-profile, a part of the flange of the steel beam and a washer plate. Additionally, in P15.2 epoxy resin was placed filling the gap between the lower bolt and the inner surface of the bolt hole.

The geometry of the models is shown in Figure 6.1, and the components of the finite element models are summarised in Table 6.1 and in Table 6.2. The bolts were modelled together with the nuts and washers as one piece. The reinforcement bars were neglected in the model.

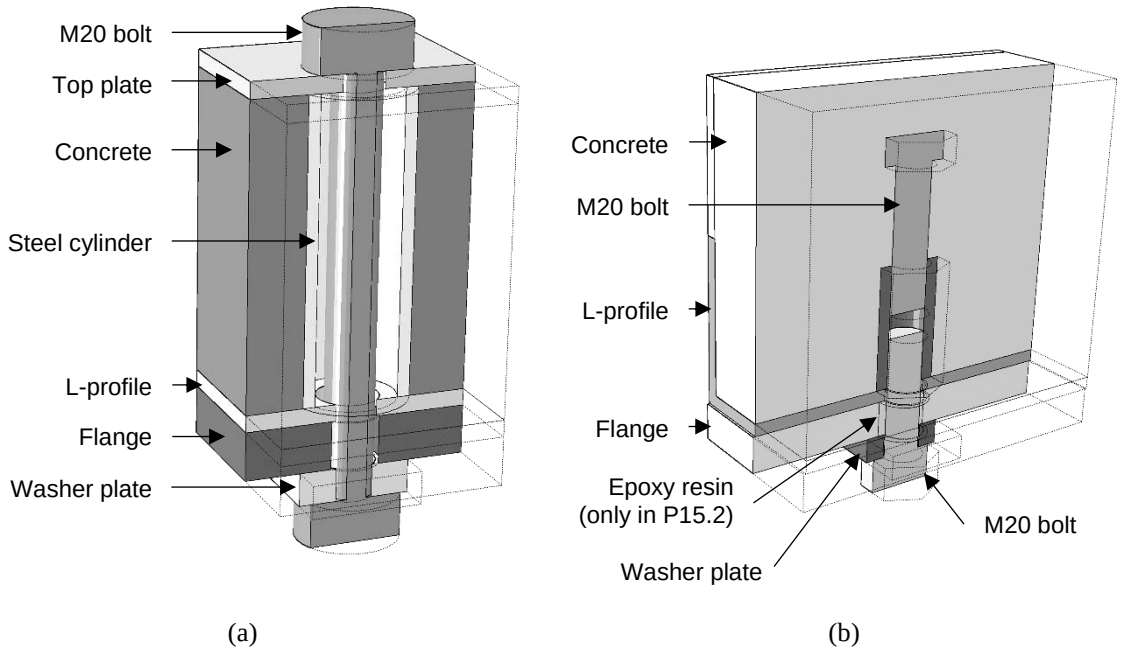

Figure 6.1 Components of the FE model (a) System P3, (b) System P15

Table 6.1 Components of the FE model (P3)

Element	Section	Material	Hole diameter
Bolt with nut and washer	M20, L=149.5	8.8	
Top plate	PL80x80x5	S355	22
Steel cylinder	42.4x4x109	S355	
Leg of the L-profile	80x80x6	S355	22
Flange of the beam	80x80x17.5	S355	24
Washer plate	PL40x40x12	S355	21
Concrete	80x80x109	C45/55	

Table 6.2 Components of the FE model (P15)

Element	Section	Material	Hole diameter
Upper bolt	M20, L=70	8.8	
Coupler	M20, L=60	10.9	
Lower bolt with washer	M20, L=60	8.8	
L-profile	80x80x6	S355	22
Flange of the beam	80x17.5	S355	24 in P15.1 and 26 in P15.2
Washer plate	PL40x40x12	S355	21
Concrete	80x144x160	C45/55	
Epoxy resin*	D=26	SW404	

*only in P15.2

The following boundary conditions were applied:

1. Surfaces at the sides were fixed against translations in normal direction.
2. The steel flange was fixed in vertical direction.
3. Temporary boundary conditions were applied for all individual parts in the initial step while the contacts were formulated.
4. 0.5 mm / sec horizontal movement was applied on the flange of the steel beam to simulate the push-out test procedure.

6.2.3 Contact modelling

For the modelling of the contacts between the elements "General Explicit Contact" was applied. General Contact allows users to define contact between all or multiple areas of the model. These are all defined as a single interaction assuming any part of the model can be in contact with any other part. The interaction was defined as "Hard Contact" in the normal direction, i.e. no penetration of the elements is allowed; and Coulomb friction in the tangential direction with a friction coefficient of 0.26 for the wire brushed steel-to-steel contact surfaces and 0.48 for the galvanised contact surfaces. These values correspond to the ones obtained by the push-out tests.

Tie constrain was applied for those elements that were welded together in reality (top plate, cylinder and L-profile), and for the coupler device and the coupled bolts. This constrains prevents the relative motion between the tied contact surfaces.

6.2.4 Material models

The steel material behaviour was modelled by defining its elastic, inelastic and damage properties. The elastic part of the behaviour is represented by its initial Young's modulus (E_0 = 210 GPa) and its Poisson's ratio ($\nu = 0.3$). Plasticity with isotropic hardening was applied for the modelling of the inelastic behaviour using the true stress – true strain relationship obtained by standard ISO 6892-1:2016 [74] tensile testing (see Annex A.1). Uniaxial tensile tests have been conducted on the L-profiles, on the black bolts applied in push-out test series P3.1 and P3.3 and on the galvanized bolts applied in test series P3.2. No tensile tests were conducted on the bolts applied in test series P15.1 and P15.2, because the lengths of the bolts were not sufficient to be clamped adequately in the testing machine. Therefore, the same material model was applied for test series P15.1 and P15.2 as for P3.1 and P3.3. The following table shows the mean values of the measured yield strength and tensile strength of the applied bolts and the L-profiles.

Table 6.3 Mean values of the measured yield strengths and tensile strengths

Element	Material grade	Corrsponding push-out test	Yield strength, $f_{y,m}$ [MPa]	Tensile strength, $f_{u,m}$ [MPa]
L-profile	S355	P3.1, P3.2, P3.3, P15.1, P15.2	386.6	519.4
Black bolt	8.8	P3.1, P3.3	872.3	948.7
Galvanized bolt	8.8	P3.2	1011.9	1045.6

For the modelling of the steel behaviour, "Damage for ductile metals" were used. The calibration procedure followed the modelling method of Pavlović [16]:

First, the load-displacement curves were extracted from the tensile tests. The engineering stress (σ_i) values were determined as:

$$\sigma_i = F_i/S_0 \tag{6.1}$$

where F_i is the force measured during the tensile tests, and S_0 is the original cross-sectional area.

In order to determine the engineering strains (ε_i), the original gauge length (l_0) needs to be fictitiously reduced to the average necking zone length (l_{loc}). This way the effects of strain localisation can be taken into account:

$$l_i = \begin{cases} l_0, & i < n \\ l_0 + (l_{loc} - l_0)\left(\dfrac{\Delta l_i - \Delta l_n}{\Delta l_r - \Delta l_n}\right)^{\alpha_L}, & i \geq n \end{cases} \tag{6.2}$$

where

l_0 is the original gauge length;

l_{loc} is the average necking zone length;

Δl_i is the elongation at loading stage "i";

Δl_n is the elongation at the onset of necking;

Δl_r is the elongation at rupture; and

$\alpha_L = 0.5$ is the strain localisation rate factor.

The engineering strains can be than calculated as:

$$\varepsilon_i = \begin{cases} \Delta l_i/l_i & i < n \\ \varepsilon_{i-1} + \dfrac{\Delta l_i - \Delta l_{i-1}}{l_i}, & i \geq n \end{cases} \tag{6.3}$$

The true strain (ε'_i) and true stress (σ'_i) values can be calculated with the following formulations:

$$\varepsilon'_i = \ln(1 + \varepsilon_i) \tag{6.4}$$

$$\sigma'_i = \sigma_i(1 + \varepsilon_i) \tag{6.5}$$

The true stress values determined by Equation (6.5) show the damaged material response. We need the undamaged material response because the damage will be implemented by the damage parameter (D) and not by the stress-strain relationship. The undamaged material response is defined by the following equation:

$$\underline{\sigma_i'} = \begin{cases} \sigma_i', & i < n \\ \sigma_n(1+\varepsilon_i), & i \geq n \end{cases} \tag{6.6}$$

where σ_n is the engineering strain at the onset of necking.

The true plastic strains can be determined from the total true strains:

$$\varepsilon_{pl,i}' = \varepsilon_i' - \frac{\sigma_i'}{E} \tag{6.7}$$

The following figure shows the obtained stress-strain diagrams for the investigated black bolts:

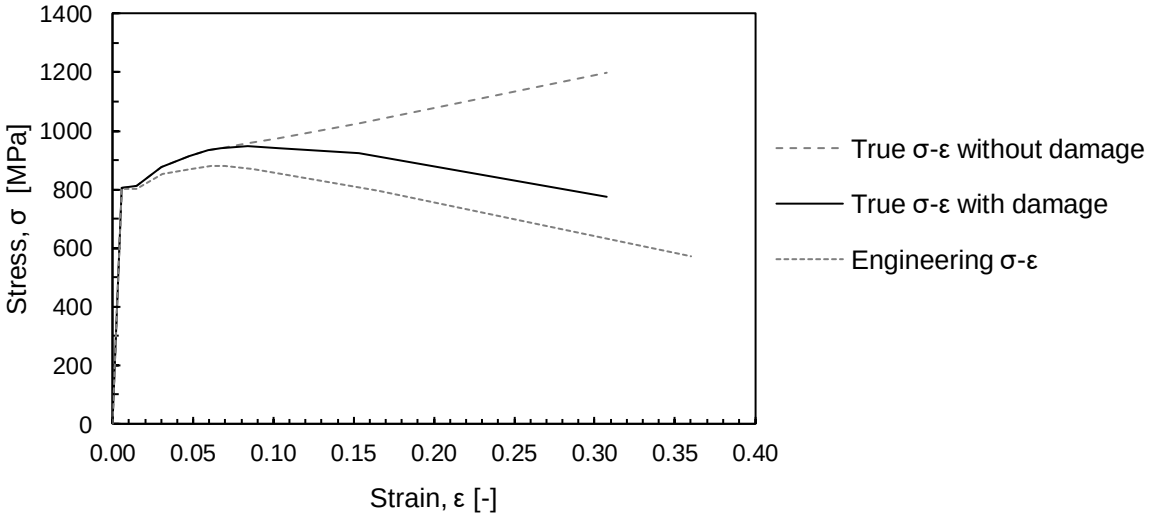

Figure 6.2 Stress strain relationship of a ductile material undergoing damage

The damage parameter (D) is a dimensionless variable representing the difference between the damaged and undamaged response (Equation (6.8)). Its value is 0 before necking occurs and is 1 at fracture.

$$D = 1 - \left(\sigma_i' - \underline{\sigma_i'}\right)\alpha_D \tag{6.8}$$

In the previous equation $\alpha_D = 1.5$ is the damage eccentricity factor. In Abaqus [32], the damage evolution law is described in a tabular form, where the damage parameter (D) is given as the function of the equivalent plastic displacement $\underline{u_{pl,i}}$. Its values can be obtained from the plastic strains in the necking zone with the following equation:

$$\underline{u_{pl,i}} = \underline{u_{pl,f}} \cdot \frac{\varepsilon_{pl,i}' - \varepsilon_{pl,n}'}{\varepsilon_{pl,f}' - \varepsilon_{pl,n}'} \tag{6.9}$$

where:

$u_{pl,f}$ is the equivalent plastic displacement at fracture determined by Equation (6.10);

$\varepsilon'_{pl,i}$ is the true plastic strain at load stage "*i*";

$\varepsilon'_{pl,n}$ is the true plastic strain at the onset of necking; and

$\varepsilon'_{pl,f}$ is the true plastic strain at fracture.

$$\underline{u_{pl,f}} = \lambda_S L_{char}(\varepsilon'_{pl,f} - \varepsilon'_{pl,n}) \tag{6.10}$$

where:

λ_S is the finite element size factor determined by Equation (6.11); and

L_{char} is the characteristic element length determined by Equation (6.12).

$$\lambda_S = \sqrt[3]{L_R/L_E} \tag{6.11}$$

where:

L_R is the element size for a refined mesh density that could be considered as a reference mesh, here its value was taken as 1.5 mm; and

L_E is the element size for the actual mesh density

The characteristic element length was taken as:

$$L_{char} = \lambda_E L_E \tag{6.12}$$

where λ_E is the element type factor. The following table summarises the applied parameters:

Table 6.4 Parameters for ductile damage model

Element	Material grade	l_0 [mm]	l_{loc} [mm]	α_L [-]	α_D [-]	$\varepsilon'_{pl,n}$ [-]	$\varepsilon'_{pl,f}$ [-]	λ_E [-]	λ_S [-]	L_E [mm]	L_{char} [mm]
L-profile	S355	90.2	25	0.5	1.5	0.126	0.336	3.1	0.630	6	18.6
Black bolt	8.8	57.7	10	0.3	1.5	0.053	0.302	3.1	0.794	3	9.3
Galvanized bolt	8.8	57.7	10	0.3	1.5	0.046	0.265	3.1	0.794	3	9.3

Additionally, the equivalent plastic strain at the onset of damage $\underline{\varepsilon'_{0,pl}}$ was defined based on the triaxiality and the uniaxial plastic strain at the onset of damage $\varepsilon'_{pl,n}$:

$$\underline{\varepsilon'_{0,pl}} = \varepsilon'_{pl,n} \cdot e^{-\beta \cdot (\Theta - 1/3)} \tag{6.13}$$

where β = 1.5 is a material parameter [16], and Θ is the stress triaxiality. For uniaxial tension its value is 1/3. Using Equation (6.13), the following values were obtained for the equivalent plastic strain at the onset of damage as the function of the triaxiality:

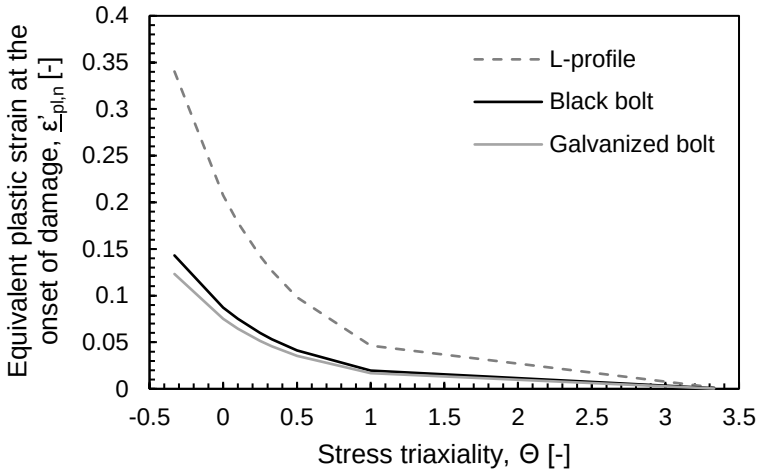

Figure 6.3 Equivalent plastic strain at the onset of damage as the function of stress triaxiality

Figure 6.4 shows the steel coupon specimens that were used for the calibration of the material models and their numerically reproduction.

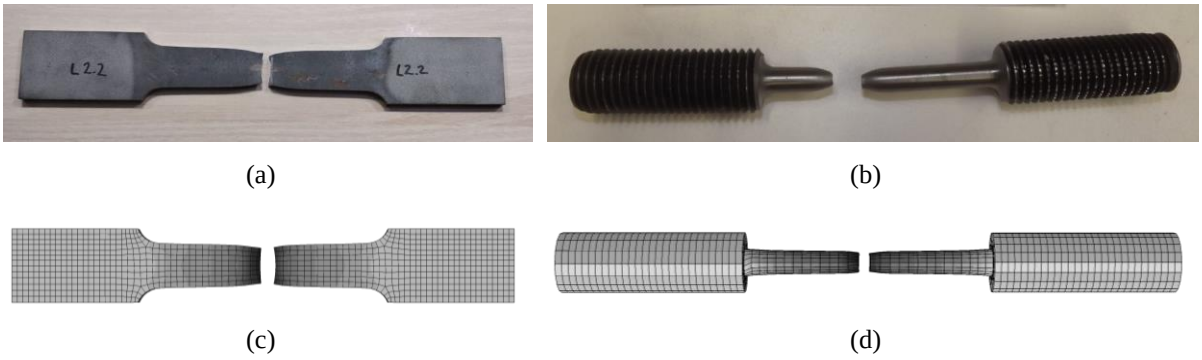

Figure 6.4 (a) and (b) photos, (c) and (d) numerical models of the steel coupon specimens

No concrete damage was observed during the experiments, so it was sufficient to describe the concrete behaviour with its elastic properties: E = 33.4 GPa and ν = 0.2. The epoxy resin was modelled using a Young's modulus of E = 7.6 GPa and a Poisson's ratio of 0.01 [75].

6.2.5 Finite elements and mesh

Every part was modelled using 8-node reduced integration brick elements (C3D8R). The mesh size varied from 1.5 mm to 6 mm. Figure 6.5 shows the applied finite element mesh.

6.2.6 Load steps and solving technique

Although the three nominally identical specimens within the same test series were loaded differently during the push out tests (see chapter 4.5), no effects of the different loading regimes on the load-slip behaviour could be identified. Therefore, the different loading regimes were not implemented in the numerical simulations.

The load was applied in two steps:

1. Application of the pre-tension force to the bolts as a thermal contraction using a predefined filed of an artificial temperature difference and an artificial thermal expansion coefficient.
2. Defining a constant velocity of 0.5 mm / sec in the vertical direction on a reference point coupled with the flange of the beam. This was applied through 100 seconds resulting in 50 mm total displacement.

The solution was found using dynamic explicit solver technique.

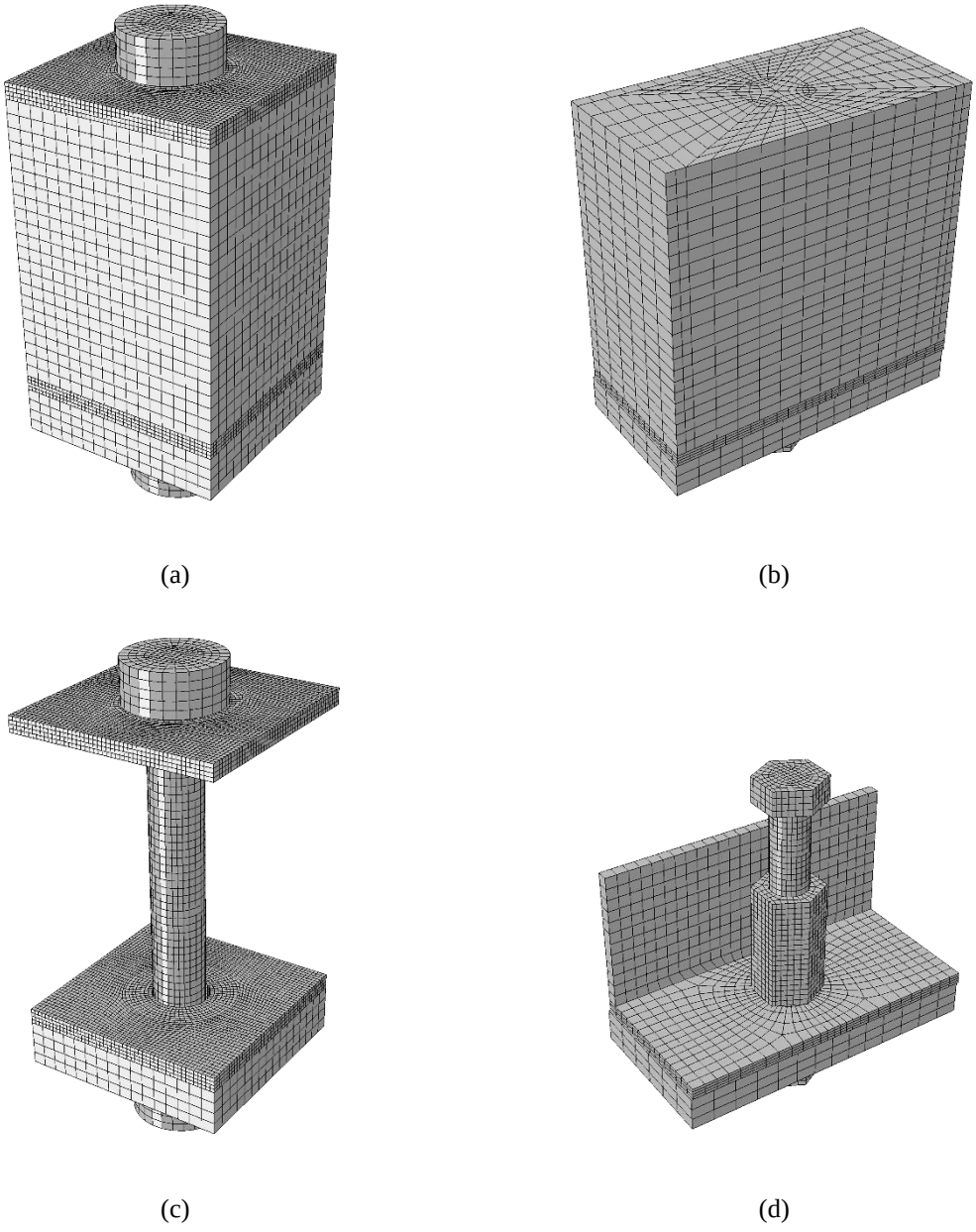

(a) (b)

(c) (d)

Figure 6.5 Finite element mesh (a) and (c) P3 with and without concrete, (b) and (d) P15 with and without concrete

6.2.7 Validation

Figure 6.6 shows the numerical model of specimen P3.3 under failure conditions. As one can see, both the observed bolt shear failure and the bearing deformation of the L-profile (Figure 6.7) could be reproduced numerically.

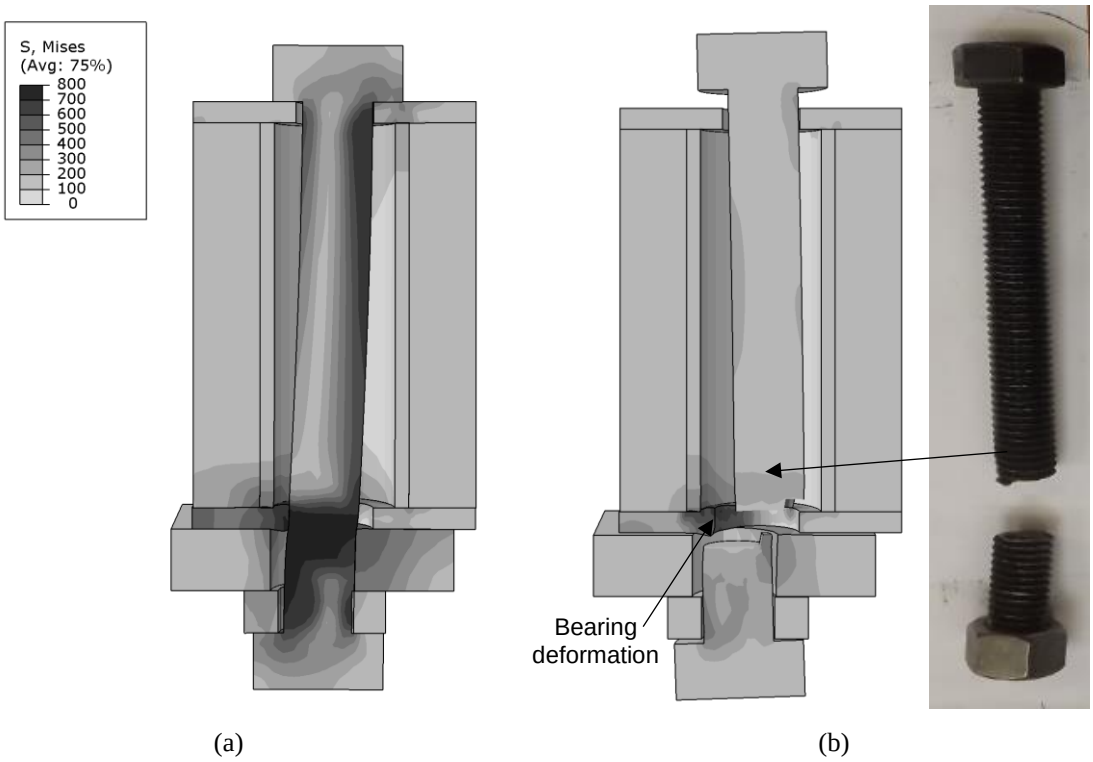

Figure 6.6 Numerical model of specimen P3.3 (a) before failure, (b) after failure

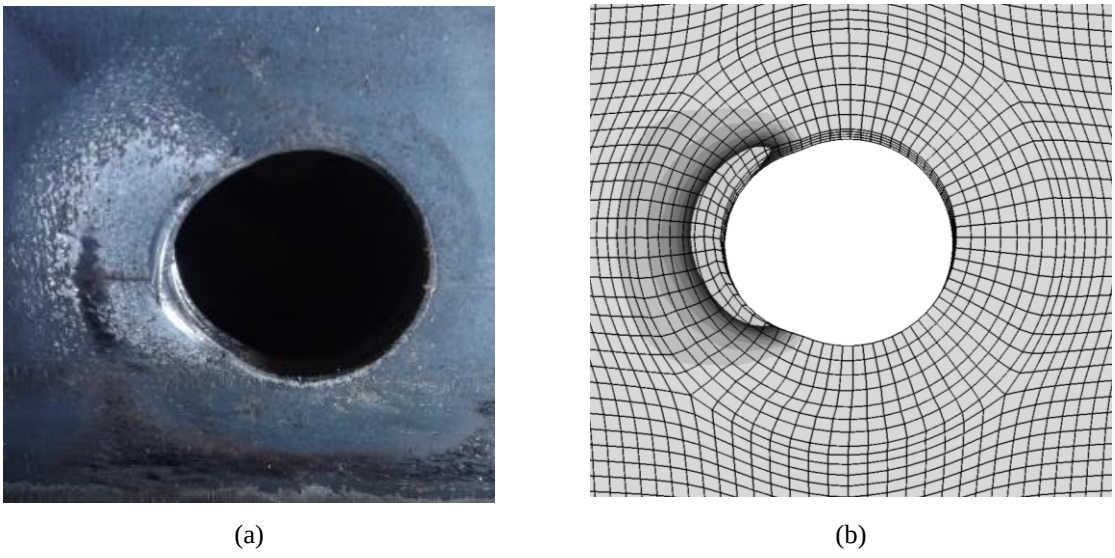

Figure 6.7 Bearing deformation of the L-profile (a) photo, (b) FE simulation

Figure 6.8 shows the numerical model of specimen P15.1 before and after failure.

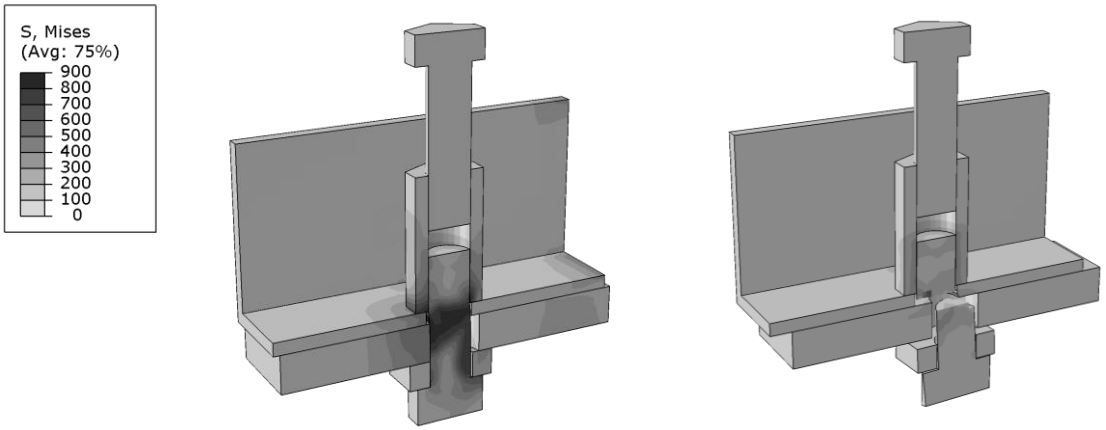

(a) (b)

Figure 6.8 Numerical model of specimen P15.1 (a) before failure, (b) after failure

The comparison of the experimentally and the numerically obtained load slip curves is presented in Figure 6.9. The developed numerical model could capture the general behaviour of the shear connections. The numerically obtained load-slip curves show the three distinct parts that had been previously observed in the push-out tests: first, no slip because of the friction, second bolt slip in the hole, and third, shear and bearing deformation. The only exception is system P15.2, where the bolt slip in the hole is prevented by the epoxy resin injection. In terms of resistance, stiffness and deformation capacity, the model could capture the behaviour of system P3 with an acceptable accuracy. However, in the case of system P15, the numerical model shows a higher stiffness during shear deformation than the experiment. As a result, the deformation capacity is underestimated. One possible explanation for this could be a locking phenomenon. Another explanation could be the tie constrain between the coupler device and the bolts. The tie constrain prevents any relative displacement between the connected surfaces, so the model does not account for the small gap between the threads of the bolts and the coupler that is present in the reality. Nevertheless, the general behaviour as well as the shear resistance could be captured accurately.

System P3: Friction bolts in cast-in cylinders

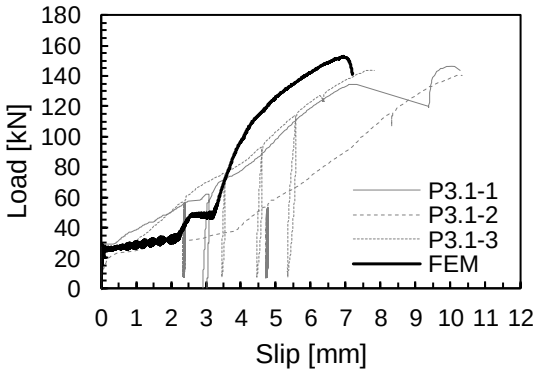

(a) System P3 with solid slab

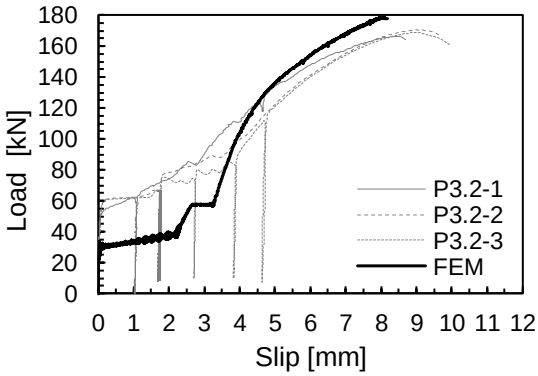

(b) System P3 with CF80 + galvanization

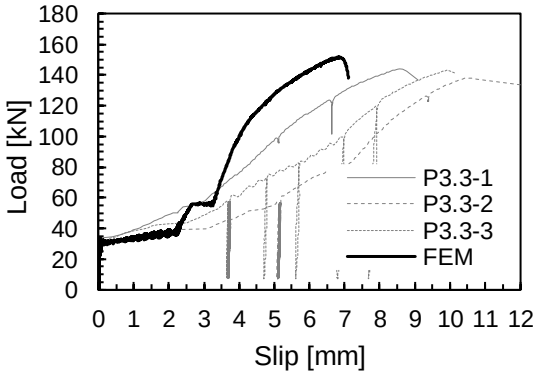

(c) System P3 with CF80

System P15: Coupled bolts

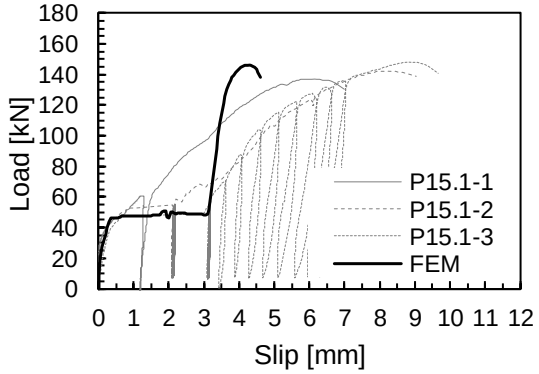

(d) System P15 with solid slab

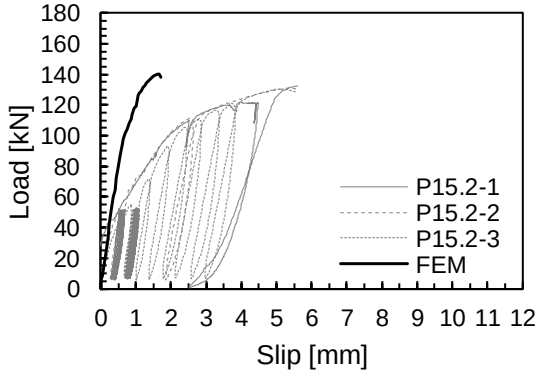

(e) System P15 with solid slab and epoxy resin

Figure 6.9 Comparison of the experimentally and the numerically obtained load-slip curves

6.3 Modelling of beam tests

6.3.1 General

The investigated beams were reproduced numerically using the commercial software Abaqus [32]. This chapter presents the development and validation of the numerical models.

6.3.2 Geometry and boundary conditions

The cross-section of the tested beams is presented in Figure 6.10. The model consisted of an IPE360 steel beam with a length of 6 m and a 1.58 m wide concrete slab. The longitudinal gap between the slab elements and the rounding of the steel beam were neglected. Due to the transversal orientation of the ribs and the profiled sheeting, these parts do not contribute to the longitudinal flexural capacity of the composite section. Consequently, these parts could also be neglected in the numerical model.

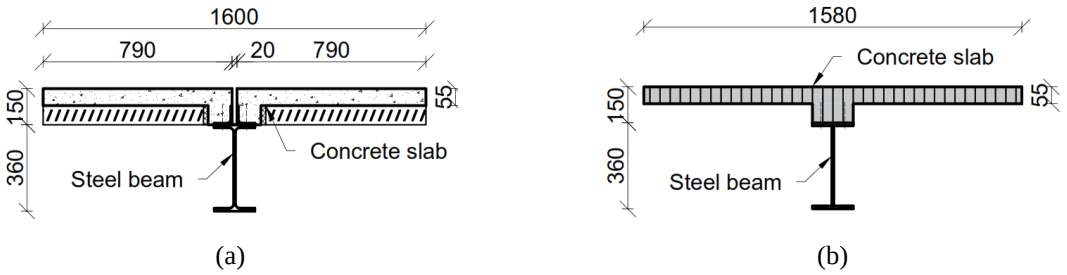

Figure 6.10 Cross-section of the tested beams, (a) plan, (b) FE model

The beam was modelled as a simply supported beam with the help of two reference points at the two ends of the beam. Pinned support was applied on one end of the beam: the vertical and the horizontal displacements were restrained as well as the rotation around the axis of the beam. On the other end, a roller support was applied similarly to the pinned support but allowing for the horizontal displacement in the axial direction. A reference point was created above the geometrical centre of the beam. This point was connected to the surface of the concrete at the two loading positions using continuum distributing coupling. The loading was applied using a prescribed displacement on the reference point.

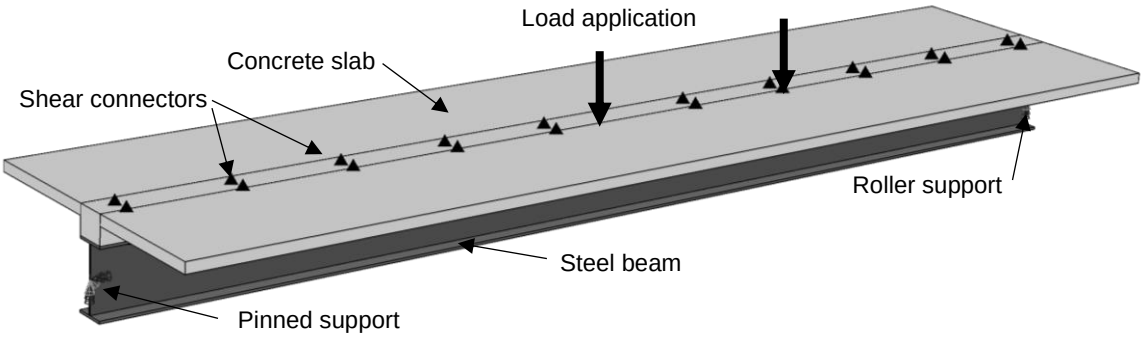

Figure 6.11 Components and boundary conditions and components of the FE model

6.3.3 Material models

The implemented stress-strain curve of the S355 steel material is presented in Figure 6.12. The yield strength was taken as f_y = 381.8 MPa, and the tensile strengths as f_u = 467.7 MPa. The Young's modulus was E = 188.5 GPa. These values are taken as the mean values of the properties measured during the uniaxial tensile tests (see Annex A.1.4). The hardening part was modelled using the 1/100 of the initial Young's modulus [76]. For the ultimate strain, the measured ε_u = 0.35 value was implemented.

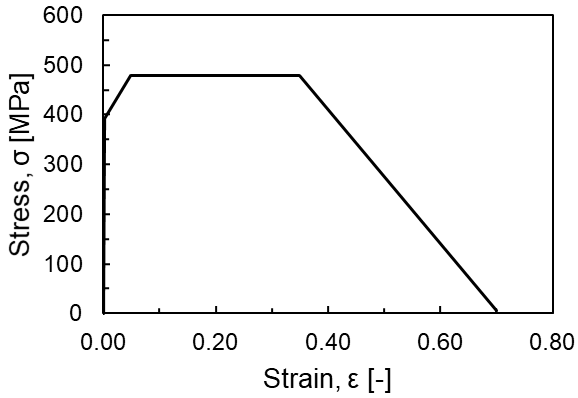

Figure 6.12 The implemented stress-strain curve of the steel material

Concrete damaged plasticity model (CDP) was used for the description of the material behaviour of the concrete. The effects of creep and shrinkage were not taken into account during the analyses. The concrete strength was determined using standard cube tests at the day of testing. The mean value of the compressive strength was $f_{cu,m}$ = 64 MPa (see Annex A.2). The cylinder strength of the concrete was estimated using Equation (6.14) given by the commercial finite element software Atena [77]:

$$f_c = 0.85\, f_{cu,m} = 54.41\ MPa \tag{6.14}$$

Where $f_{cu,m}$ is the mean value of the measured cube strengths.

The tensile strength was determined using equation (6.15) given by CEB-FIP Model Code 2010 [78] :

$$f_t = \left(f_{cu,m}\right)^{2/3} = 4.80\ MPa \tag{6.15}$$

The initial elastic modulus was determined using equation (6.16) given by CEB-FIP Model Code 2010 [78]:

$$E_{cm} = \left(6000 - 15.5 f_{cu,m}\right)\sqrt{f_{cu,m}} = 40066\ MPa \tag{6.16}$$

For the description of the nonlinear stress-strain relationship, the formulation given by EN1992-1-1 [49] was used (Figure 6.13):

$$\frac{\sigma}{f_c} = \frac{k\eta - \eta^2}{1 + (k-2)\eta} \tag{6.17}$$

where:

- $\eta = \varepsilon_c / \varepsilon_{c1}$,
- ε_{c1} is the strain at peak stress, and
- $k = 1.05 \cdot E_{cm} \cdot \varepsilon_{c1} / f_c$.

The descending branch of the curve was described by a linear relationship.

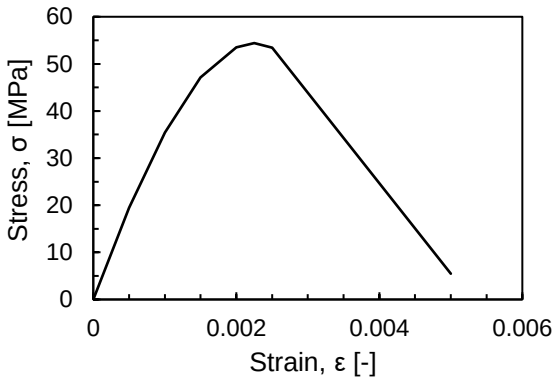

Figure 6.13 Concrete compressive stress-strain relationship

The concrete compression damage parameter was defined as:

$$D_c = 1 - f_c / \sigma_c \tag{6.18}$$

The concrete tensile behaviour was described using the proposal of CEB-FIP Model Code 2010 [78] (see Figure 6.14).

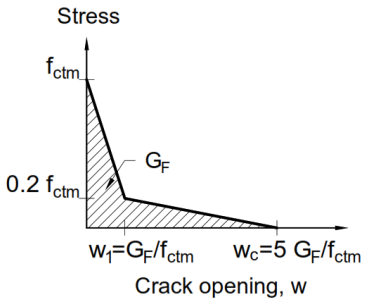

Figure 6.14 Concrete tension law

The specific fracture energy G_F represents the area under the stress-crack relationship. For the determination of its value the following equation was used [78]:

$$G_F = 73 \cdot \frac{f_c^{0.18}}{1000} = 0.14988\ N/mm \tag{6.19}$$

The concrete tension damage parameter was defined as:

$$D_t = 1 - f_t/\sigma_t \tag{6.20}$$

The concrete damaged plasticity model of Abaqus [32] requires the definition of the following parameters:

1) The dilation angle was taken as ψ = 36° as recommended by Pavlović [16].
2) The flow potential eccentricity was set to be ε = 0.1 recommended by Abaqus [32].
3) The ratio of the biaxial and uniaxial compressive strength was taken as $\sigma_{b0} / \sigma_{c0}$ = 1.20 as given by CEB-FIP Model Code 2010 [78].
4) For the ratio of the second stress invariant on the tensile meridian K = 2/3 was used [32].
5) Finally, the viscosity parameter was defined as μ = 0.001 [79].

The following table summarises the plasticity parameters for the CDP model:

Table 6.5 Concrete damaged plasticity model parameters

ψ	ε	$\sigma_{b0} / \sigma_{c0}$	K	μ
36°	0.1	1.20	0.6667	0.001

The shear connectors were modelled using point based, mesh-independent fastener elements. The behaviour of the shear connectors could be described with the "Slot + Align" connection type. The "Slot" connection type provides a connection, where node *b* stays on the line defined by the orientation of node *a* and the initial position of node *b* [32]. This connection type allows to define a nonlinear spring law to describe the load-displacement behaviour of node *b* relative to node *a*. The "Align" connection type ensures that the three local directions are aligned. The application of this type of connection is important, otherwise the direction of the nonlinear spring would not follow the deflection of the beam. The following figure shows the theoretical model that describe the connection behaviour.

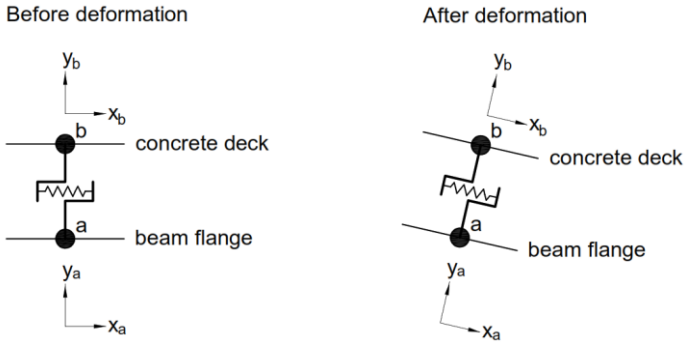

Figure 6.15 Theoretical model of the "Slot + Align" type connection

Although, the bolt position can vary inside the hole, it was assumed that the application of the average load-slip curves obtained by the push-out tests can represent the global behaviour of the experiments accurately due to the fact that each experiment used 20 bolts (presumably placed randomly inside the holes) to connect the slab elements to the steel beam. This was proven by the successful validation of the numerical model against the experimental measurements and observations (see Chapter 6.3.6). Therefore, the nonlinear spring behaviour was described by the average load-slip curves:

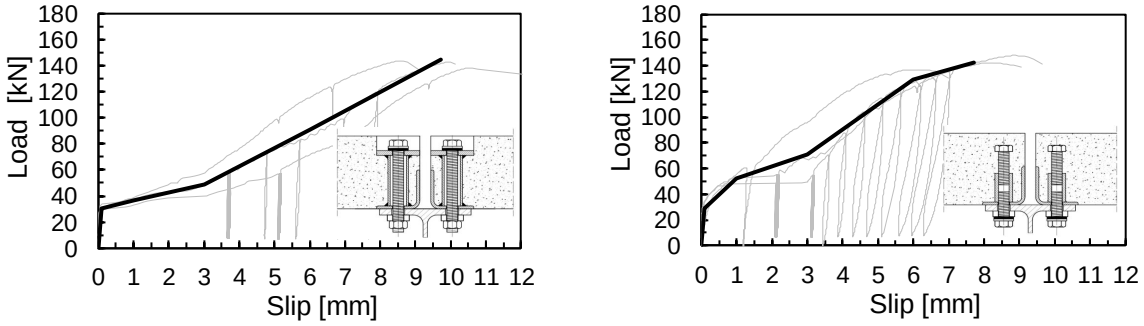

Figure 6.16 Average load slip curves (a) System P3.3, (b) System P15.1

In order to model shear connection failure, an artificial linear descending branch was added (dashed line in the figure below) to the load-slip curves presented in the previous figure:

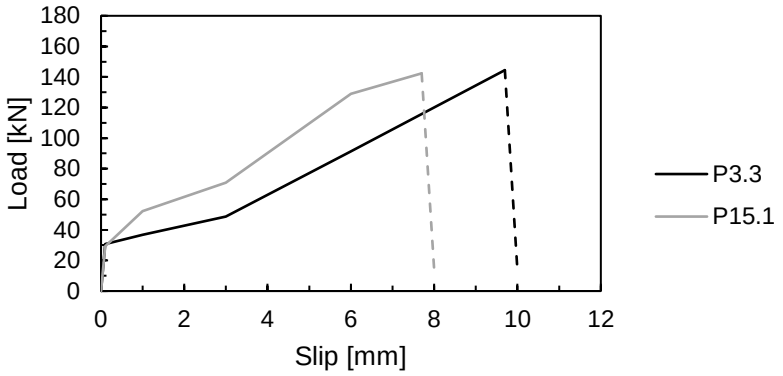

Figure 6.17 Descending branch to model shear connector failure

6.3.4 Finite elements and mesh

The steel beam and the concrete slab were modelled with 4-node, reduced integration shell elements (S4R) with 5 integration points through the thickness. The solid strip of the concrete slab above the steel beam was modelled using a different shell thickness (see Figure 6.10, b). The global mesh density was 50 mm.

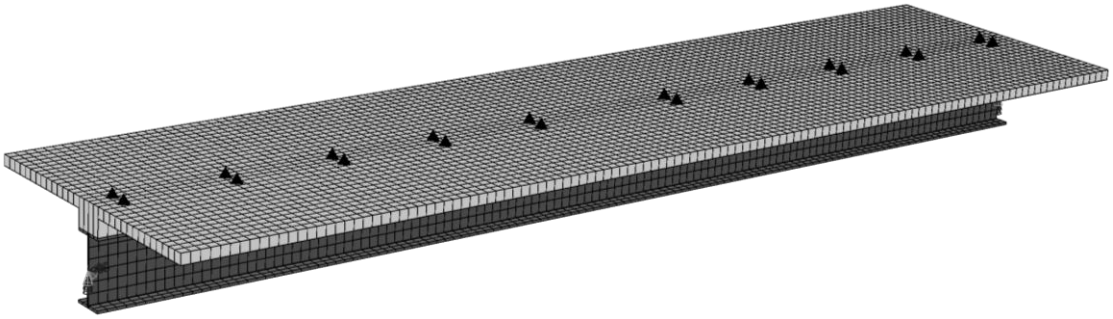

Figure 6.18 Applied finite element mesh

6.3.5 Solving technique

The load was applied in one step using a 180 mm prescribed displacement on the reference point coupled with the top surface of the concrete slab. The maximum increment size was chosen to be 0.05. This value corresponds to a maximum of 9 mm vertical displacement in each step in order to capture the nonlinear behaviour accurately. The analysis was conducted using a quasi-static full Newton solution technique with a direct equation solver method. The beams were continuously supported during the installation of the deck elements and the shear connectors (see section 5.4). This corresponds to a propped construction method, which means that the steel beam and the concrete deck carry all the applied loads together as a composite section. The numerical model was prepared accordingly: the steel beam and the concrete deck were connected together before applying any loads.

The failure load was obtained at the point where the numerical model stopped converging. The lack of convergence could originate from four different factors:

1) Too large stresses at the load introduction points. This mode was sorted out by coupling the reference point to a sufficiently large surface (100 mm x 100 mm) at the top of the concrete slab.
2) The shear connectors reach their slip capacity. This is why the descending branch was added to the load slip curves (see Figure 6.17) to intentionally cause convergence problems when the slip capacity is reached.
3) Loss of stiffness due to concrete crushing. This happens when the concrete damage parameter reaches the value of 1 ($D = 1$).
4) The steel beam is fully plastic.

6.3.6 Validation

The obtained numerical results were compared to the experimental observations.

Both simulations finally stopped due to failure of the shear connection (point 2 in the list presented in section 6.3.5). This is in accordance with the experimental observations in the case of specimen B8, where also shear connection failure happened. Specimen B7 failed due to concrete crushing during the

experiment but the shear connectors did not broke finally. However, at this point the shear connectors at the end of the beam were highly deformed and were close to failure (see Figure 5.16, d). This is also supported by the slip measurements, which showed that the end slip at failure was 9 mm (see Figure 5.24). This is close to the mean value (9.7 mm) of the ultimate slip obtained by the push out tests. In other words, the concrete crushing due to high deformation and the failure of the outermost shear connectors occurred more-or-less at the same load level. In the experiment, concrete crushing occurred first, while having highly deformed shear connectors, and in the numerical simulation shear connector failure occurred first while the concrete was highly damaged (see Figure 6.25).

The comparison of the experimentally and numerically obtained results showed a sufficiently accurate correlation in the means of load-deflection curves (see Figure 6.19 and Figure 6.20), the end slip (Figure 6.21 and Figure 6.22), the slip distribution (Figure 6.23 and Figure 6.24) and the observed damages (Figure 6.25 and Figure 6.26). The following figures show the experimentally and numerically obtained load-deflection curves. The numerical model was able to capture the general behaviour of the composite beam as well as its ultimate load bearing capacity.

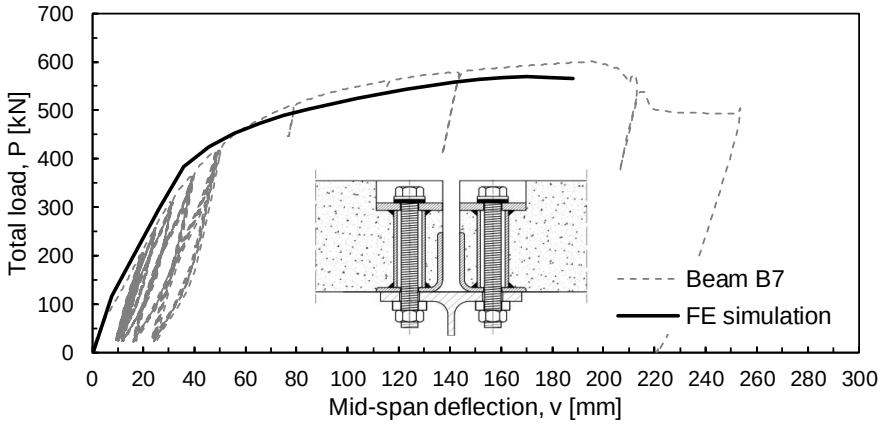

Figure 6.19 Comparison of numerical and experimental load-deflection curves of specimen B7

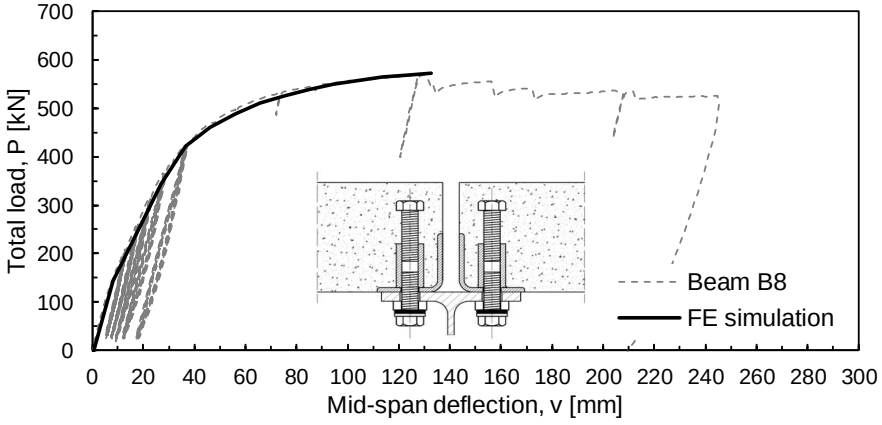

Figure 6.20 Comparison of numerical and experimental load-deflection curves of specimen B8

The next figures show the experimentally and numerically obtained end slip. As one can see, the difference between the two curves are greater than in the case of the load-deflection curves. This difference can originate from different factors. First, the average load-slip curves are implemented in the numerical model assuming central position of all bolts. In reality, the individual bolt positions may differ from this position. Second, the numerical model is perfectly symmetric, while in the laboratory experiment one side of the beam observed greater slips. In the presented experimental end slip curves the curves represent the average end slip measured at four points (at the two ends of the two deck elements). Despite of the differences, the numerically obtained curves show a relatively good correlation with the experimental measurements, and the ultimate load and slip could be well captured.

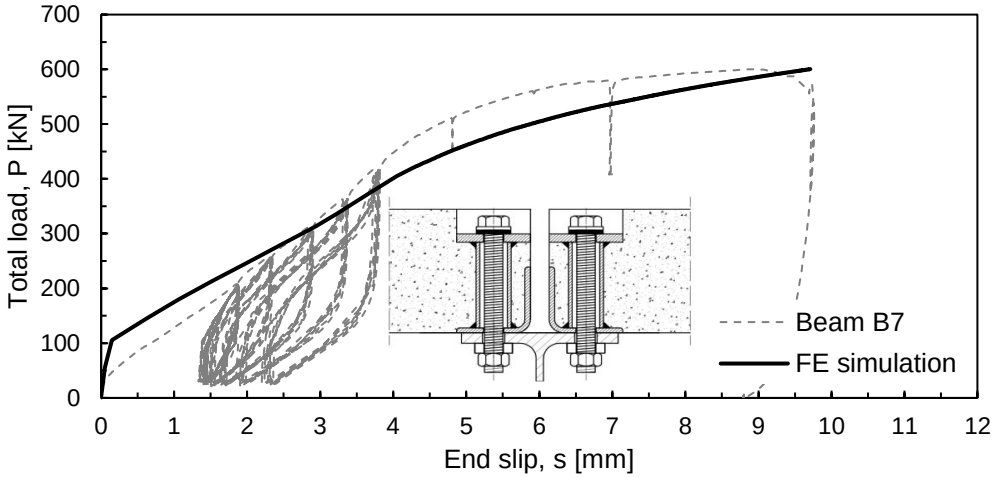

Figure 6.21 Comparison of numerical and experimental load vs. end slip curves of specimen B7

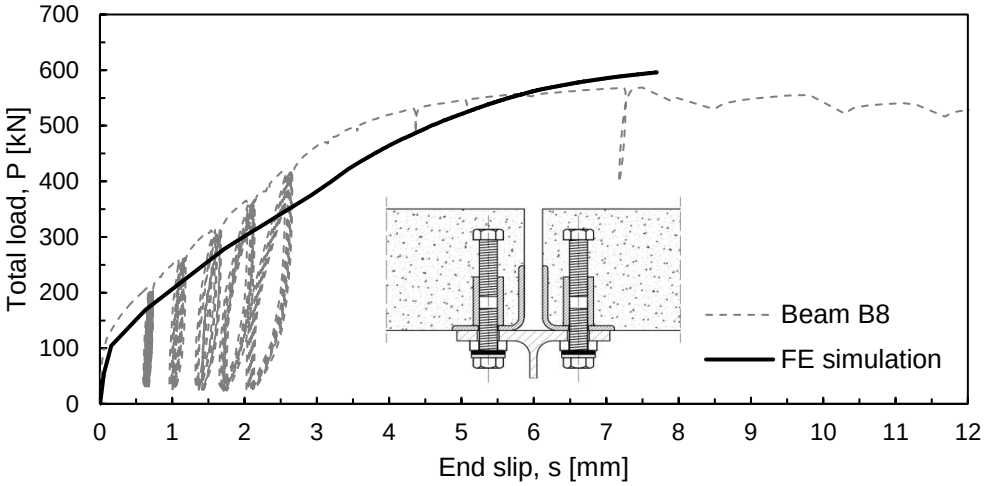

Figure 6.22 Comparison of numerical and experimental load vs. end slip curves of specimen B8

The following figures show the obtained slip distributions together with cosine functions fitted to the experimentally and numerically obtained end slip values. The comparison was made at a 500 kN load level, because some of the intermediate slip measuring devices (LVDTs) stopped functioning at high

deformation levels. Until at least 500 kN they functioned properly. At this load level the numerical simulation produced higher slip values as the experimental measurements (see also Figure 6.21 and Figure 6.22). Theoretically, a cosine slip distribution corresponds to a sinusoidal loading and a linear elastic shear connection. In the tests, the two-point loading was applied and highly nonlinear shear connection. Nevertheless, the assumed cosine slip distribution that is later used in the elastic (Chapter 8) and plastic calculations (Chapter 9) can describe the slip distribution function relatively accurately, even if it does not correspond to the actual loading situation.

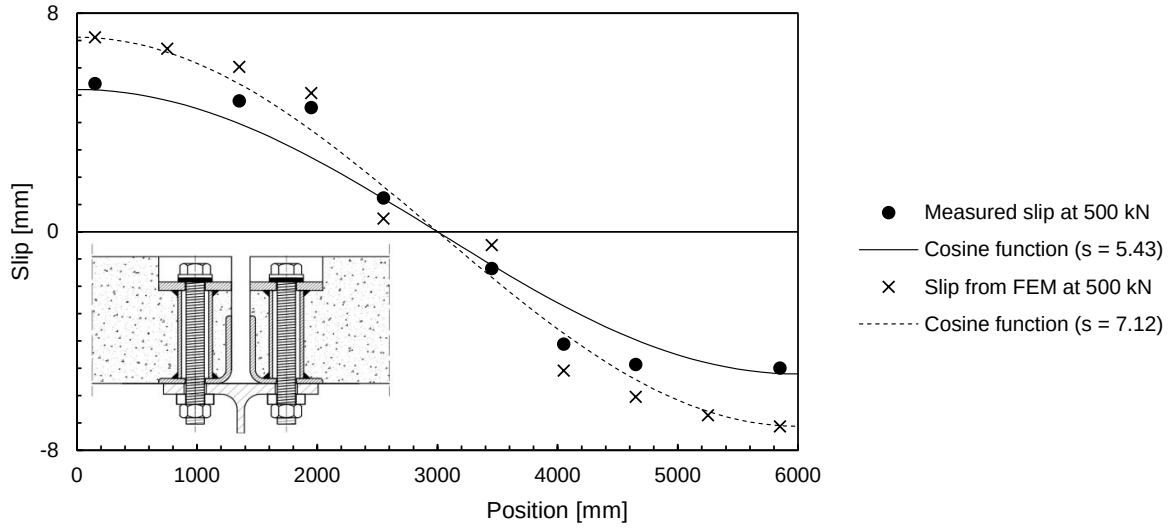

Figure 6.23 Comparison of numerical and experimental slip distributions of specimen B7

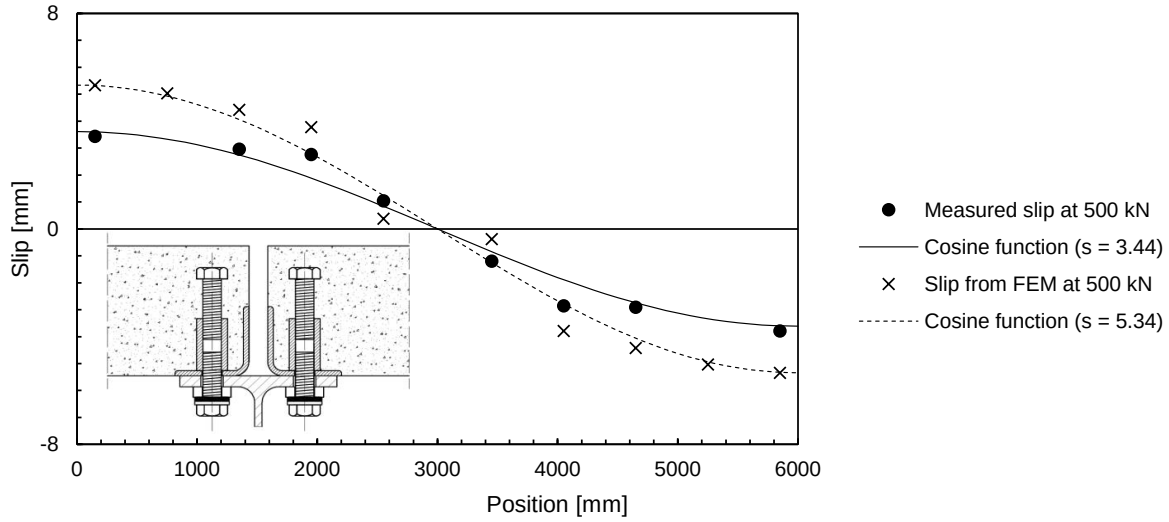

Figure 6.24 Comparison of numerical and experimental slip distributions of specimen B8

The following figure shows the concrete compression damage taken from the numerical model of beam test B7. In the figure, the dark areas show the highly damaged parts of the concrete. As one can see, the

value of the damage parameter near the load introduction points is close to one, which corresponds to the total loss of stiffness. This is in accordance with the experimental observation, where concrete crushing occurred near to the load introduction point.

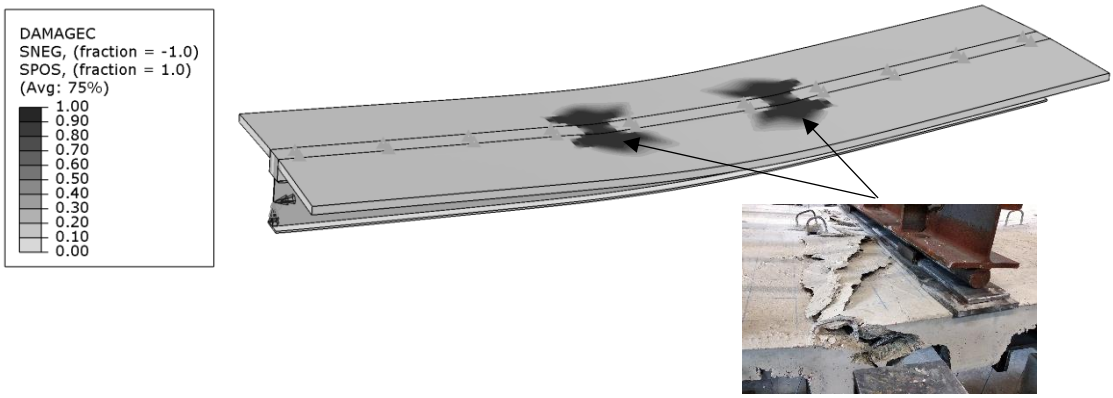

Figure 6.25 Concrete compression damage (beam B7)

The following figure shows the concrete tension damage for the numerical model of the test specimen B7. In the figure, the dark regions show the places where concrete cracking occurs. The numerical model could reproduce the cracks around the shear connectors, the longitudinal cracks at the axes where the shear connectors were placed as well as the cracks at the side of the beam due to bending.

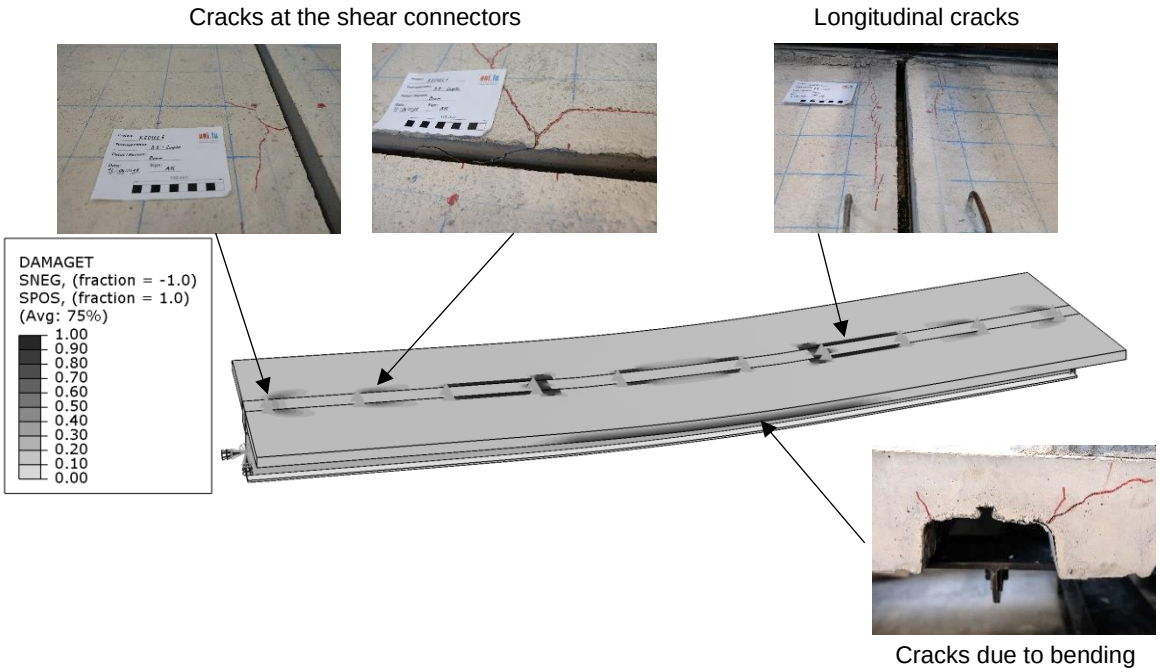

Figure 6.26 Concrete tension damage (beam B8)

Based on these observations, it was concluded that the developed numerical model is capable of capturing the general behaviour of the investigated demountable composite beams with high accuracy. The validated numerical model can be used for extending the experimental study with virtual experiments.

Chapter 7. Parametric studies

7.1 General

The experimental investigations were extended by virtual experiments in the form of parametric studies with the help of the validated numerical models of the beam tests. A certain number of parametric studies on demountable composite beams have already been performed by Jung [80] using similar numerical models as presented in this thesis. It was found that the shear connection distribution has an important effect on the stiffness and on the moment resistance of demountable composite beams. Higher resistance and stiffness values were obtained when the shear connectors were placed according to the elastic shear flow than in the case of equidistant spacing. It was also found that the slip distribution function can be approximated by a cosine function despite.

The studies performed within the frame of this thesis complement the previous studies by extending the range of the investigated parameters. This chapter presents the investigated parameters, an extract of the results and the conclusions that were drawn from the performed simulations. Parts of these results were already presented in [81].

7.2 Investigated parameters

A total of 112 numerical simulations were performed on shell models of composite beams with different parameters. The numerical models were prepared on the basis of the validated model presented in Chapter 6.3. The conducted parametric studies can be divided into two parts.

7.2.1 Parametric study PS-1

The purpose of this study was to investigate the effects of different parameters on the load-deflection behaviour. Thirty four simulations were conducted on 6 m long beams with the same geometry and loading (two-point loads) as in the case of the conducted beam tests. This way it was possible to make a direct comparison between the simulations and the experimental measurements. The following parameters were investigated in this study:

1) Type of shear connection
2) Steel grade
3) Concrete strength
4) Shear connection distribution

The material behaviour of the steel and the concrete was modelled in the same manner as presented in Chapter 6.3. Where the same materials were applied as in the conducted beam tests (S355 for steel and C45/55 for concrete), the material properties were modelled with their experimentally measured values. In those simulations where the material grade was different than the tested ones, the expected values of the material properties were used. More information is given about the investigated material properties in Chapter 7.3.

The following table shows the investigated parameters of parametric study PS-1:

Table 7.1 Investigated parameters (PS-1)

Parameter	Designation	Value of the parameter
Loading	-	2-point load
Beam length	6	6 m
Steel profile	E36	IPE 360
Steel grade	S2	S275
	S3	S355
	S4	S460
Concrete grade	C20	C20/25
	C25	C25/30
	C45	C45/55
Material properties	M	Measured / expected values
Shear connector distribution	DP1	600 mm uniform spacing
	DE1	300 mm on L/6, then 975 mm
Shear connection	P0	Welded stud connector
	P3.3	Friction bolt in cast in cylinders
	P15.1	Coupled bolts
	P15.2	Coupled bolts with epoxy resin injection

7.2.2 Parametric study PS-2

Seventy eight additional simulations were performed for the assessment of the accuracy of the developed analytical equations that describe the elastic behaviour (Chapter 8.5) and the developed calculation method for the plastic moment resistance of demountable composite beams (Chapter 9.4). The 78 simulations included 39 simulations where the material properties were taken into account with their measured / expected values, and 39 simulations where their design values were used. More information is given about the investigated material properties in Chapter 7.3. In these simulations, the loading was applied as a uniformly distributed load.

The differences in the models of PS-2 compared to the models of PS-1 are the following:

(i) The loading was applied as a uniformly distributed load in PS-2, while in PS-1 it two-point loading was applied.

(ii) In PS-2, the effect of steel hardening was neglected; and therefore, a bilinear stress-strain curve (linear elastic – perfectly plastic) was applied in order to use the same material model in the numerical and in the analytic calculations (see Chapter 7.3).

Beams with different lengths, steel profiles, shear connector distributions, shear connection types and material properties were investigated. The concrete slab was modelled using the effective width given

by Eurocode 4 [18] (see Equation (5.1)) in all cases. Table 7.2 shows the analysed range of parameters and Figure 7.1 shows the applied naming conventions.

Table 7.2 Investigated parameters PS-2

Parameter	Designation	Value of the parameter
Loading	-	Uniformly distributed
Beam length	6	6 m
	8	8.1 m
	16	16.2 m
Steel profile	E27	IPE 270
	E36	IPE 360
	E45	IPE 450
	E60	IPE 600
Steel grade	S3	S355
Concrete grade	C20	C20/25
	C45	C45/55
Material properties	M	Measured / expected values
	D	Desing values
Shear connector distribution	DP1	600 mm uniform spacing
	DP2	300 mm uniform spacing
Shear connection	P0	Welded stud connector
	P3.3	Friction bolt in cast in cylinders
	P15.1	Coupled bolts

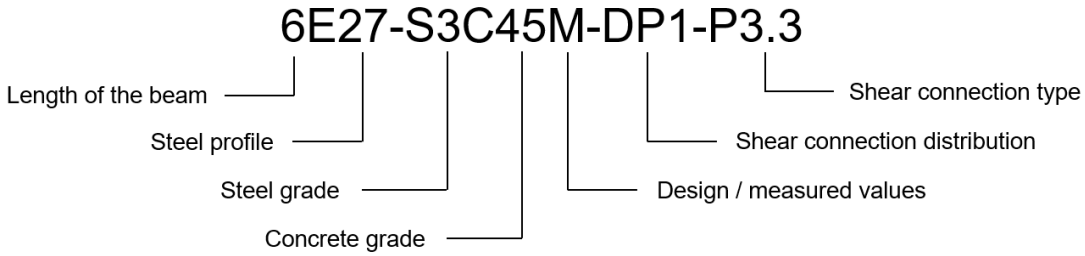

Figure 7.1 Naming conventions for parametric studies

7.3 Material models

For the assessment of the developed calculation methods presented in Chapter 8 and Chapter 9, the material properties were taken into account with their measured / expected values to simulate the real behaviour as accurately as possible. This means, when the same materials were investigated as in the real beam tests presented in Chapter 5 (C45/55 for the concrete and S355 for the steel), the

experimentally measured material properties were used. The results of the material tests are presented in 0. When the material grade differed from the ones applied in the experiments, their expected (most probable) values were used.

The expected value of the concrete cylinder strength was calculated using the formulation given by EN1992-1-1 [49]:

$$f_{cm} = f_{ck} + 8\ MPa \tag{7.1}$$

The expected value of the steel yield strength was calculated with the help of the formulation given by the JCSS Probabilistic Model Code [70]:

$$f_{ym} = f_{y,sp} \cdot \alpha \cdot exp(-u \cdot v) - C \tag{7.2}$$

where:

$f_{y,sp}$ is the nominal value of the yield strength;

α = 1.05 is a spatial position factor for hot rolled sections;

u = -1.5 is a factor related to the fractile of the distribution used in describing the distance between the nominal value and the mean value;

v = 0.07 is the coefficient of variation; and

C = 20 MPa is s a constant reducing the yield strength as obtained from usual mill tests to the static yield strength.

The developed calculation methods presented in Chapter 8 and Chapter 9 are meant to facilitate the design process of composite beams with nonlinear shear connection. In practice, it is quite probable that the structural engineer will use the design values of the material properties when investigating the ultimate design resistance of a composite beam. Therefore, additionally to the simulations using the measured / expected values, the same simulations were performed using the design values of the material properties as well.

The design value of the concrete strength (f_{cd}) was calculated as:

$$f_{cd} = \frac{f_{ck}}{\gamma_c} \tag{7.3}$$

Where f_{ck} denotes the characteristic cylinder strength and γ_C = 1.5 is the partial factor for the resistance of concrete sections given by EN1992-1-1 [49].

The design yield strength was calculated as:

$$f_{yd} = \frac{f_{y,sp}}{\gamma_{M0}} \tag{7.4}$$

Where $f_{y,sp}$ is the nominal value of the yield strength and $\gamma_{M0} = 1.0$ is the partial factor for resistance of steel cross-sections recommended by EN1993-1-1 [8].

The following table summarises the implemented cylinder strength values for the concrete and yield strength values for the steel. The numbers in the table marked with an asterisk are measured material properties. All of the other values were calculated using Equations (7.1) - (7.4).

Table 7.3 Analysed material grades

Concrete	**C20/25**	**C25/30**	**C45/55**
f_{cm} [MPa]	28	33	54*
f_{cd} [MPa]	13.33	16.67	30
Steel	**S275**	**S355**	**S460**
f_{ym} [MPa]	301	391*	516
f_{yd} [MPa]	275	355	460

* measured values

The same constitutive models were applied for the material modelling as presented in Chapter 6.3.3., with the implementation of the values presented in Table 7.3. However, the steel hardening was neglected in the numerical models of parametric study PS-2; and therefore, a linear elastic, perfectly plastic constitutive law was used (Figure 7.2). For the ultimate strain, the measured $\varepsilon_u = 0.35$ value was used in all cases but this strain level was never reached during the simulations. The strain at yield ε_y was obtained as the ratio of the yield strength (f_{ym} or f_{yd}) to the Young's modulus (E).

$$\varepsilon_y = \frac{f_y}{E} \tag{7.5}$$

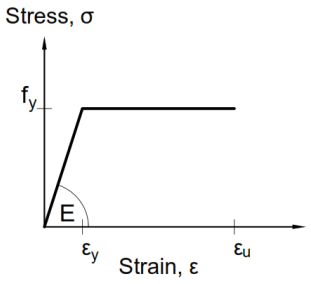

Figure 7.2 Bilinear constitutive model of steel

7.4 Shear connections

The shear connectors were modelled as point based fasteners as presented in Chapter 6.3.3. When the materials were modelled with their measured / expected values, the average load-slip curves were used for the description of the nonlinear shear connection behaviour (Figure 7.3). Traditional welded stud

connections in solids slabs were also investigated (shear connection type P0). Its load-slip curve was taken from [24].

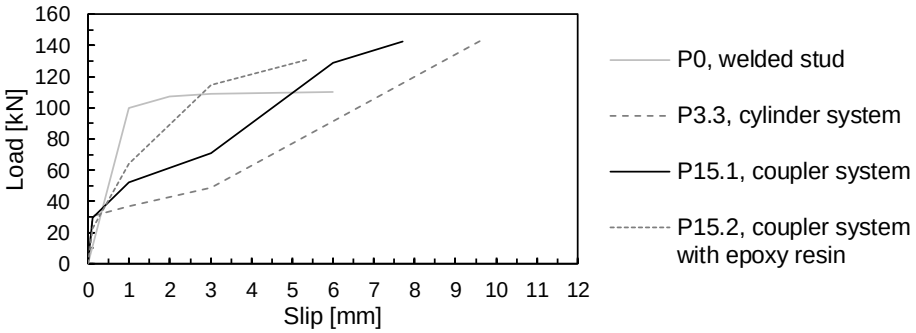

Figure 7.3 Average load-slip curves of the shear connections

When the materials were modelled with their design values, the shear connection behaviour was also modelled with the design load-slip curves. The design curves were created using the proposals of Eurocode 4 [18]. First, the load-slip curve with the minimum failure load was selected from the push out test results (Chapter 4.6). Then, the load values of the curve were reduced by 10% in order to obtain the characteristic curve. Afterwards, the load values were divided by γ_V = 1.25 [18] to get the design curve.

$$P_{Rd} = \frac{P_{Rk}}{\gamma_V} = \frac{0.9\ P_{min}}{\gamma_V} \tag{7.6}$$

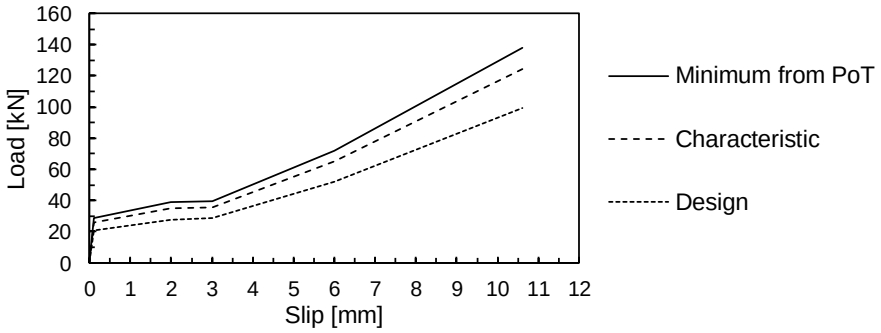

Figure 7.4 Minimum, characteristic and design load slip curves

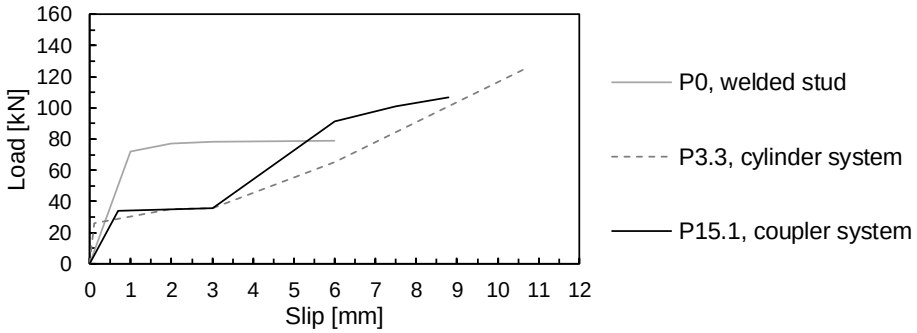

Figure 7.5 Design load slip curves of the shear connections

7.5 Results and discussions of parametric study PS-1

In this section, an extract of the results of the parametric studies is presented and summarised. The details of all simulations and the corresponding results are presented in Annex B.

7.5.1 Influence of the type of the shear connection

Figure 7.6 shows the moment-deflection curves of beams with different shear connector types. Each beams were 6 m long beams with an IPE360 steel profile made of S355 material. The shear connectors were distributed uniformly in pairs with a longitudinal spacing of 600 mm. The concrete slab used CF80 profiled decking and had a total depth of 150 mm and a width of 1600 mm, which corresponds to the effective width given by Eurocode 4 [18]. The beams differed only in the applied type of shear connection.

Each beam failed due to shear connection failure. The stiffness of each specimen was similar at the early load stages (below 150 kN of total load). After this point, the stiffness of the specimens with pre-tensioned shear connectors (P3.3 and P15.1) decreased. This is due to the bolt slippage in the bolt hole (the quasi horizontal part of the load slip-curve). As a result, the mid-span deflections of these specimens were higher than in the case of the specimens with epoxy resin injection (P15.2) and with welded studs (P0). Concerning the ultimate loads, every specimen failed between the total load levels of 560 kN and 600 kN.

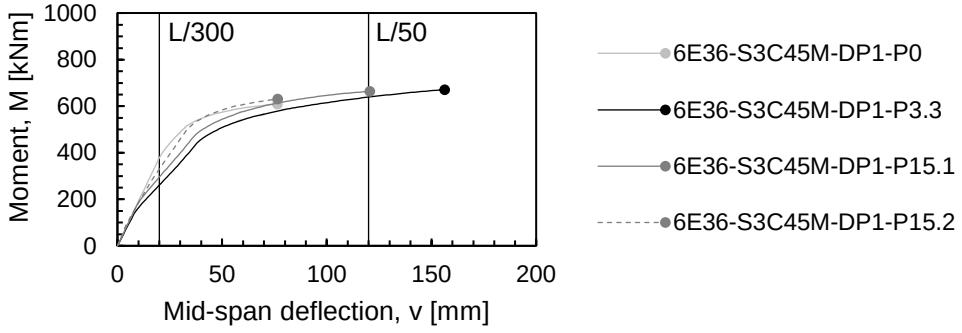

Figure 7.6 Moment-deflection curves of identical beams with different types of shear connection

Figure 7.7 shows the slip distribution of beams with different types of shear connection under failure conditions. In each cases, the highest slip was measured at the outermost shear connectors. As all the beams failed due to shear connection failure, the end-slip was equal to the slip capacity of the shear connectors in each cases. The end-slip at failure in descending order were 9.7 mm for P3.3, 7.7 mm for P15.1, 6 mm for P0 and 5.4 mm for P15.2. The corresponding deflection values at failure follow the same order (Figure 7.6). Only the beams with shear connection type P3.3 and P15.1 could reach L / 50 (120 mm) deflection, which is a generally accepted ductility criterion for beams.

The slip distribution of each type can be described with a monotonic decreasing curve until the middle of the beam. Figure 7.8 shows the corresponding shear connector forces.

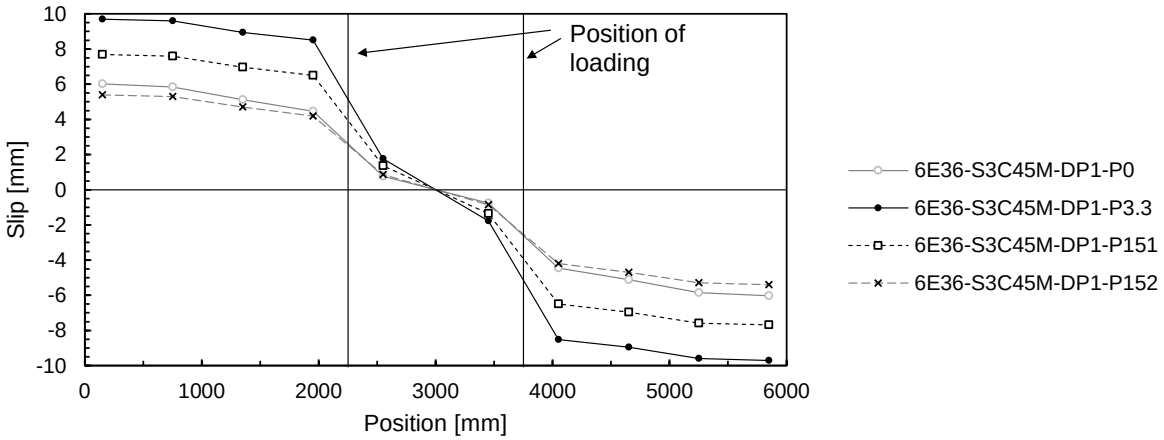

Figure 7.7 Slip distribution of beams with different types of shear connection

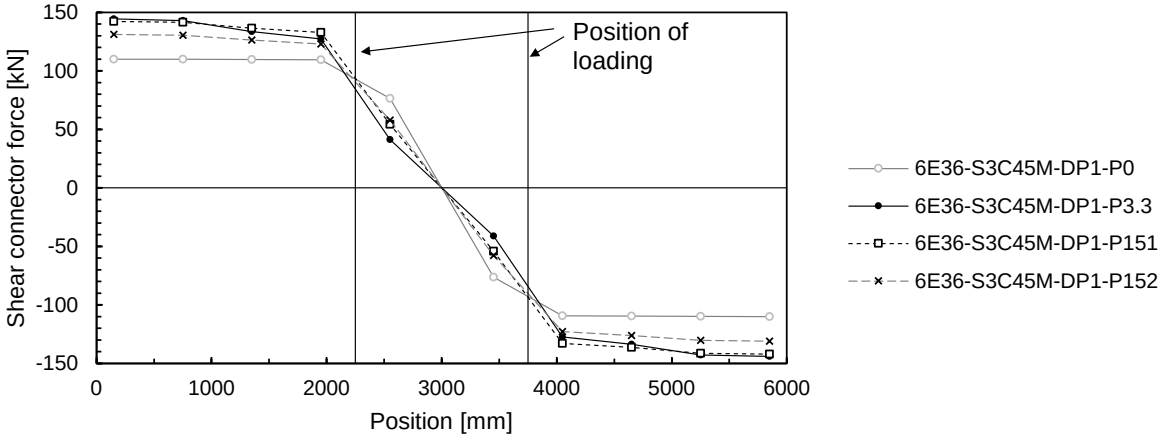

Figure 7.8 Shear connector forces of beams with different types of shear connection

As one can see, the shear connector forces have a more-or-less constant value between the supports and the position of the concentrated loads. This corresponds to the constant vertical shear diagram in this region. The vertical shear diagram between the applied concentrated forces is theoretically zero.

However, shear connectors placed in this area also underwent some slip and; and therefore, could develop a certain amount of shear force. These forces are usually neglected when determining the arising compression force of the concrete.

The method presented in Chapter 9.4.2 (Method PL1) is based on the assumption of a cosine shaped slip distribution function. The more the slip distribution function differs from a cosine shape, the less accurate the method will become. As it was already mentioned and presented in Figure 7.7, the slip distribution functions do not resemble a cosine function in these cases but to a more-or-less constant curve between the load application points and the supports. Nonetheless, the method was used for the calculation of the plastic moment resistance of the tested beams. Table 7.4 shows the comparison of the numerically and analytically obtained results.

Table 7.4 Comparison of analytically and numerically obtained moment results

Shear connection	P_{ult} **[kN]**	N_c **[kN]**	M_{ult} **[kNm]**	$N_{c.calc}$ **[kN]**	$M_{pl.\eta}$ **[kNm]**	$N_{c.calc}/N_c$ **[-]**	$M_{pl.\eta}/M_{ult}$ **[kNm]**
P0	564	1031	609	872	637	0.85	1.05
P3.3	584	1179	657	814	627	0.69	0.95
P15.1	591	1214	664	925	647	0.76	0.97
P15.2	561	1137	631	929	647	0.82	1.03

Where:

P_{ult} is the numerically obtained maximum total load;

N_c is the compression force of the concrete calculated as the sum of the shear connector forces;

M_{ult} is the numerically obtained moment resistance;

$N_{c.calc}$ is the analytically obtained concrete compression force determined by Equation (9.2);

$M_{pl.\eta}$ is the analytically obtained moment resistance determined according to the procedure described in Chapter 9.4.2.

This comparison shows, that even if the slip distribution function is far from being a cosine function for this loading situation, the analytical method can predict the moment resistance with relatively high accuracy. In the case of shear connection P0 and P15.2, the analytical method (Method PL1) overestimated the moment capacity. This is due to the fact that these beams failed at relatively low deflection levels (see Figure 7.6), and the beam could not develop the assumed plastic stress distribution (see Figure 7.9).

The discrepancy between the calculated and numerically determined concrete compression force values is relatively large (31% for P3.3), but the maximum difference in the analytically and numerically obtained moment resistance values is only 5%. For uniformly loaded beams, which has a slip distribution closer to a cosine function this difference becomes even smaller (see Chapter 7.6 and Chapter 9.4.2).

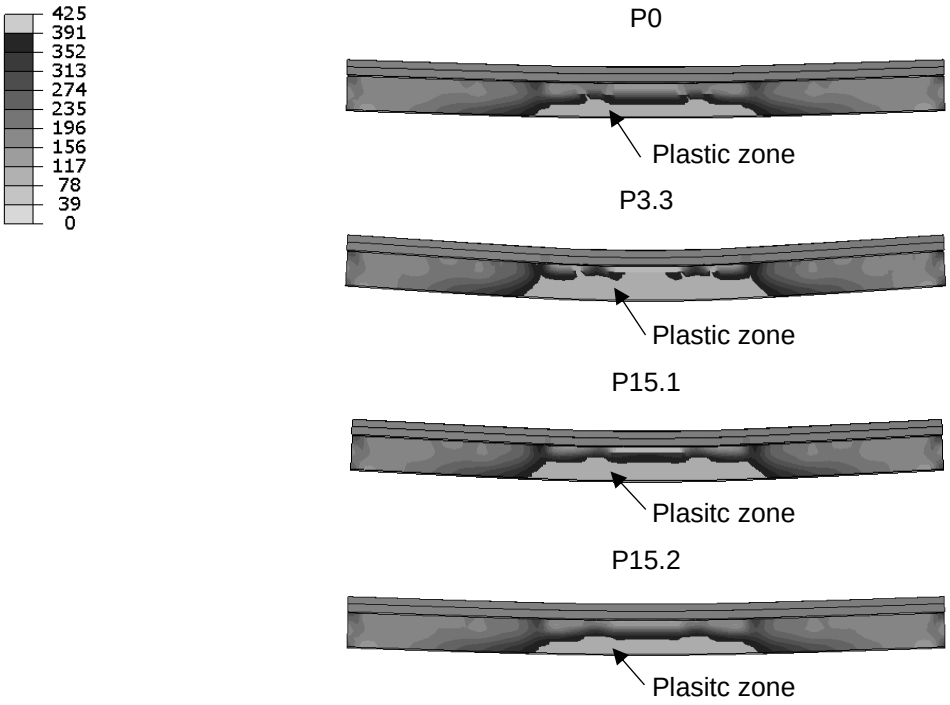

Figure 7.9 Von-Mises stresses in [MPa] under failure conditions

7.5.2 Influence of the steel grade

The following figure shows the influence of the different steel grades. Each of the beams failed due to shear connector failure. The figure clearly shows that the steel grade has a great influence on the behaviour. The ultimate load of the specimens with S275, S355 and S460 steel were 513 kN, 596 kN and 691 kN respectively. This shows a linear relationship between the yield strength and the resistance.

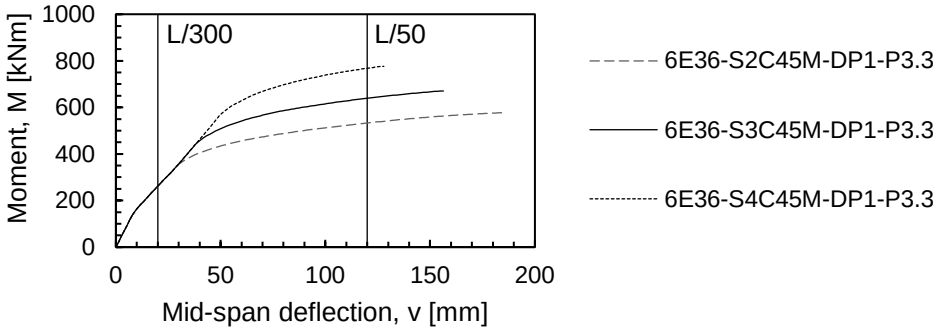

Figure 7.10 Moment-deflection curves of identical beams with different steel grades

Figure 7.11 shows the obtained slip distributions under failure conditions. As all beams failed finally due to bolt shear failure, the end slip always corresponds to the slip capacity of the applied shear connector (9.7 mm for P3.3). A certain difference can be observed in the curves: the slip measured at the 4th shear connector measured from the support, which is closest to the load application was 9.1 mm for S275, 8.5 mm for S355 and 7.8 mm for S460 steel beams. This is due to the fact that the plastic zone

is larger when the steel grade is lower (see Figure 7.12) and this has a direct influence on the slip distribution (see Figure 9.3).

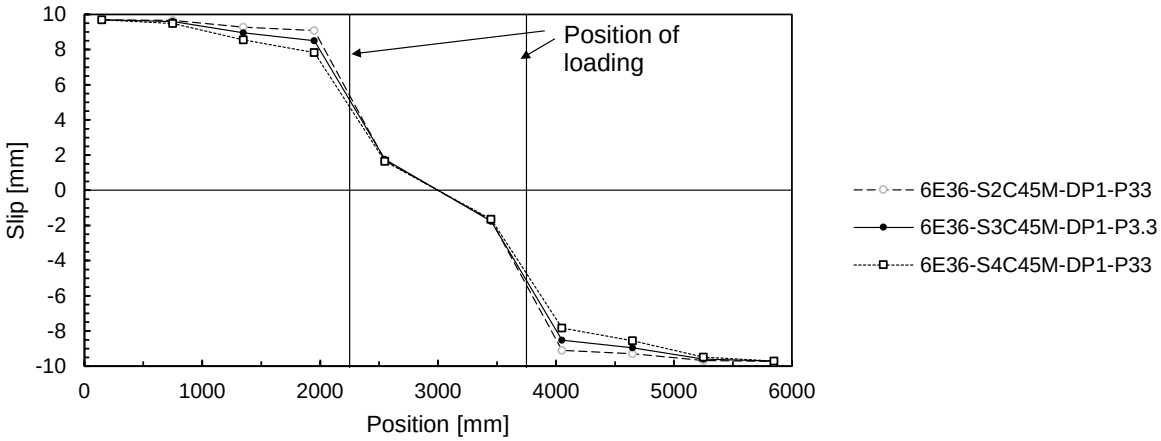

Figure 7.11 Slip distribution curves of identical beams with different steel grades

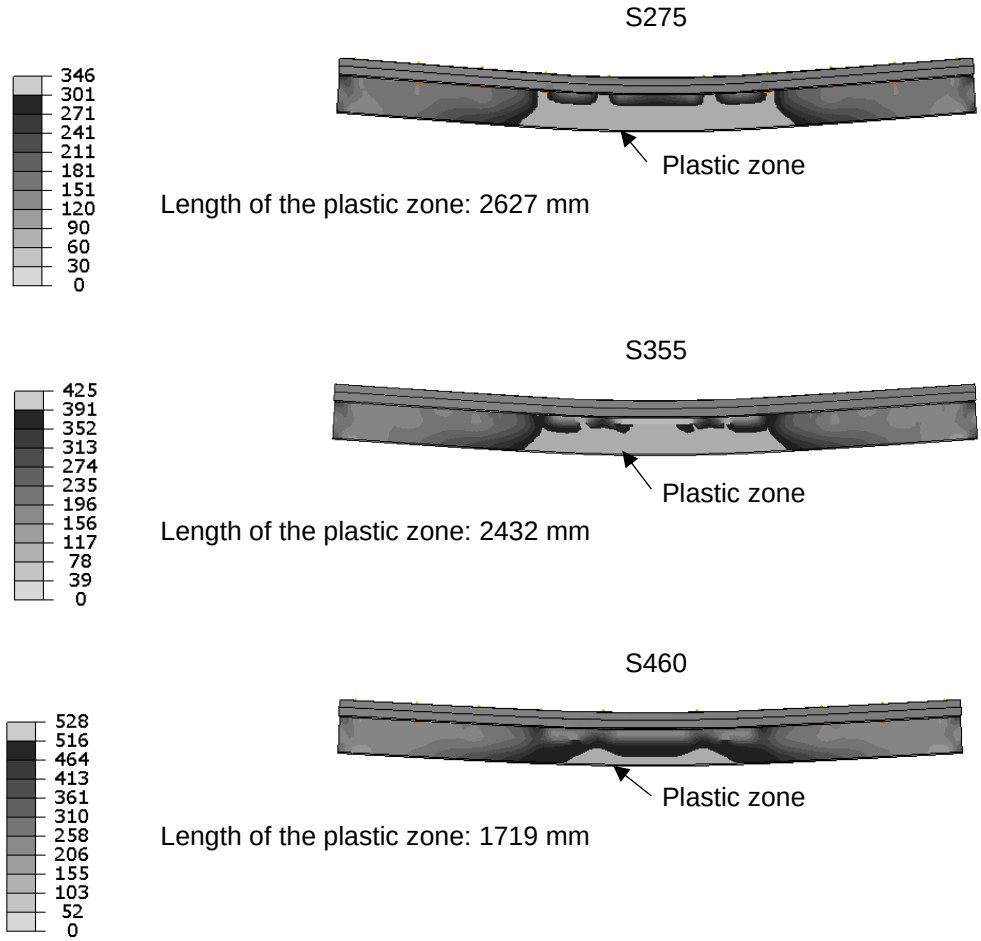

Figure 7.12 Von-Mises stresses in [MPa] for identical beams with different steel grades

The highest concrete damage belongs to the beam where S275 steel is applied.,Less concrete damage can be observed when the steel grade is higher:

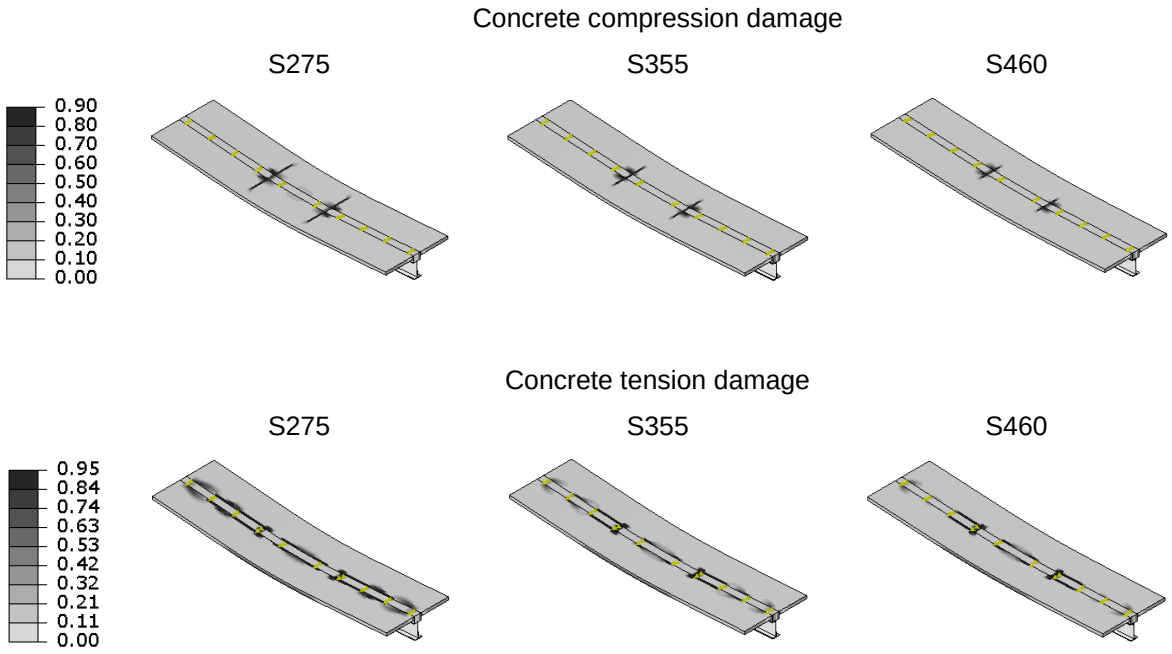

Figure 7.13 Concrete damage for identical beams with different steel grades under failure conditions

7.5.3 Influence of the concrete strength

Identical, 6 m long composite beams with different concrete grades were analysed. The beams used IPE 360 steel profile with a grade of S355. Shear connectors of type P15.1 were applied placed uniformly in pairs with a longitudinal spacing of 600 mm. As shown in Figure 7.14, the influence of the concrete grade on the general behaviour is very low. The moment-deflection curves of the beams are very similar in each cases. However, when we examine the concrete damage (Figure 7.15 - Figure 7.17), we find that the difference in the concrete damage is significant. The beams with C25/35 and C45/55 concrete failed due to bolt shear failure at 7.5 mm end slip, while the beam with C20/55 concrete failed due to the crushing of the concrete while having an end slip of 7.2 mm.

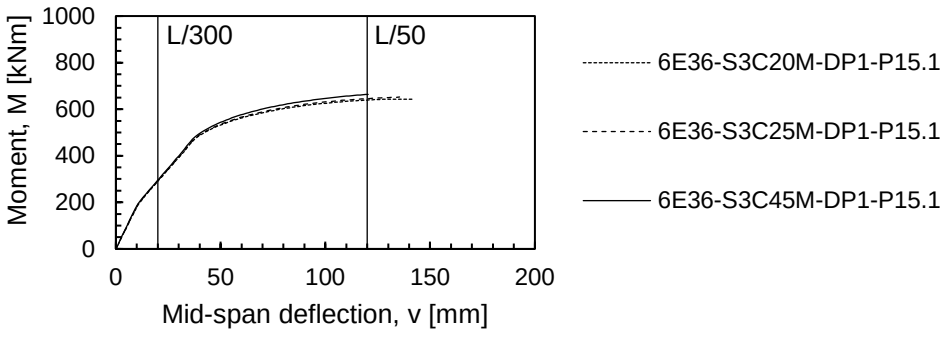

Figure 7.14 Moment-deflection curves of identical beams with different concrete grades

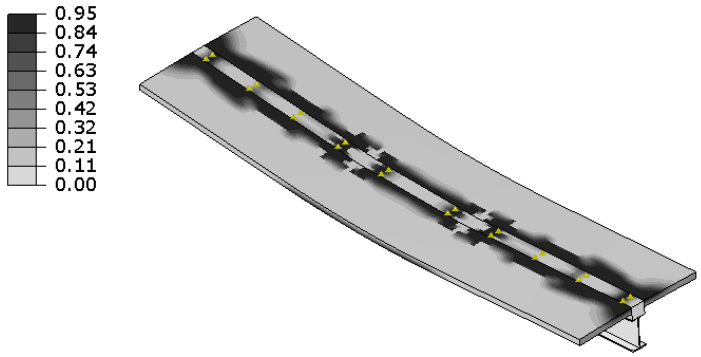

Figure 7.15 Concrete tension damage of a 6 m long composite beam with C20/25 concrete under failure conditions (concrete failure)

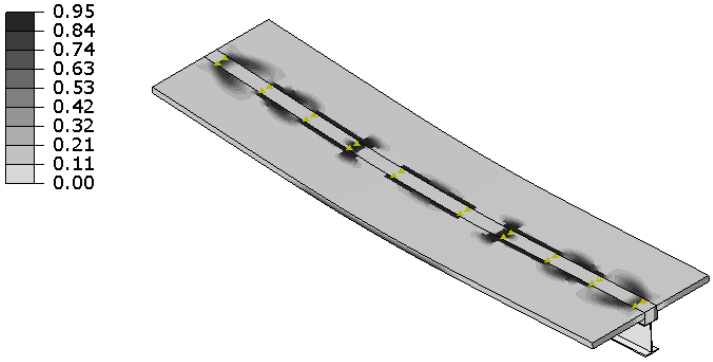

Figure 7.16 Concrete tension damage of a 6 m long composite beam with C25/35 concrete under failure conditions (shear connection failure)

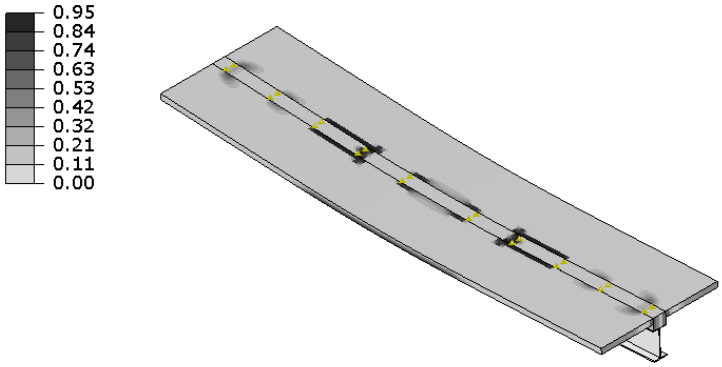

Figure 7.17 Concrete tension damage of a 6 m long composite beam with C45/55 concrete under failure conditions (shear connection failure)

7.5.4 Influence of the distribution of the shear connectors

In shear connector layout DE1 and DP1 the number of shear connectors were almost identical:10 pairs on the half-length in DP1, and 11 pairs in DE1. Figure 7.18 and Figure 7.19 show, that by placing more shear connectors near to the supports the stiffness of the composite beam increases; however, this effect is relatively small. When comparing the slip distributions and the shear connector forces (Figure 7.20 - Figure 7.27), we observe, that the slip and force values are similar in both of the two different shear connector arrangements. However, small differences can be identified. For instance, with non-uniformly placed shear connectors, the largest slip does not necessarily occur at the end of the beam (see Figure 7.22 and Figure 7.26). This is can be explained as follows: the beam was subjected to a two-point loading, which corresponds to a constant shear force diagram between the supports and the load application points. Because of this, the largest slip occurs where the shear connectors are placed less frequently.

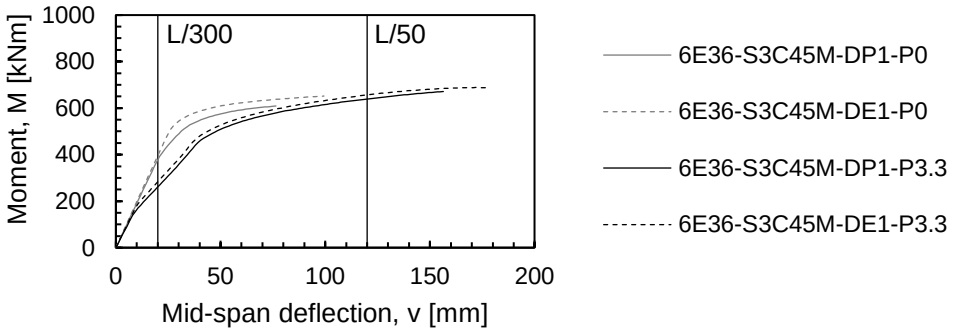

Figure 7.18 Comparison of the moment deflection curves of identical beams with shear connection distribution DE1 and DP1 (P0 and P3.3)

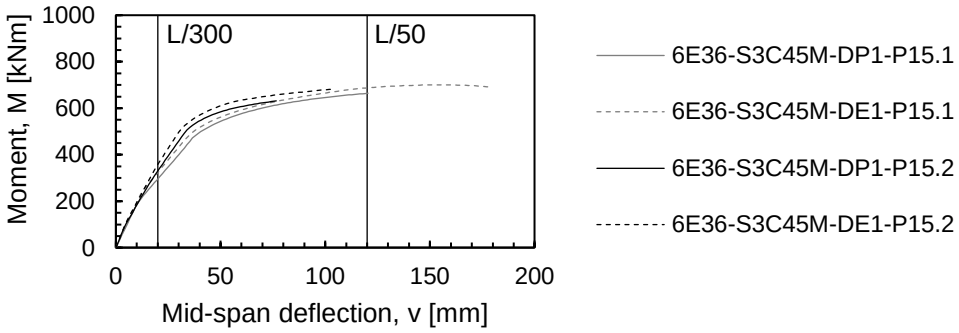

Figure 7.19 Comparison of the moment deflection curves of identical beams with shear connection distribution DE1 and DP1 (P15.1 and P15.2)

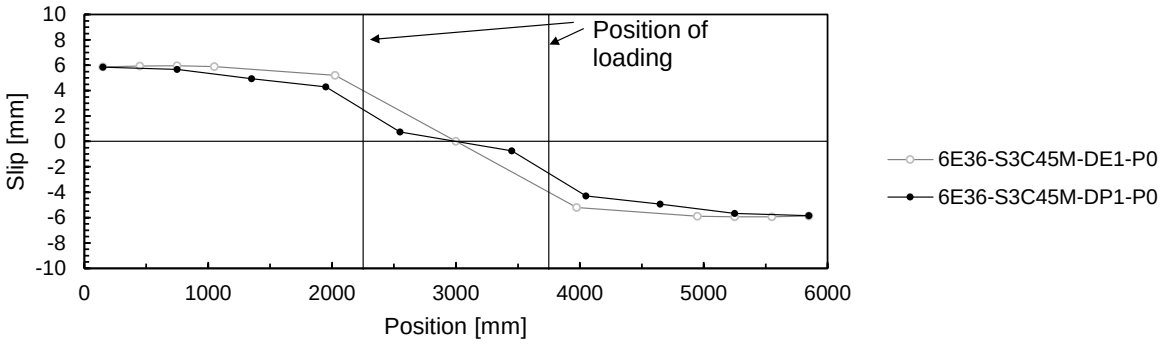

Figure 7.20 Slip distribution of identical beams with different shear connector distribution (P0)

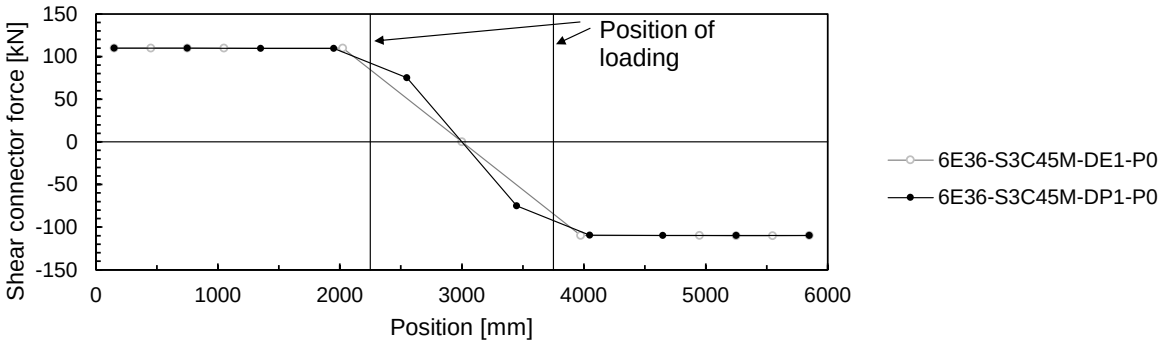

Figure 7.21 Shear connector forces of beams with different shear connector distribution (P0)

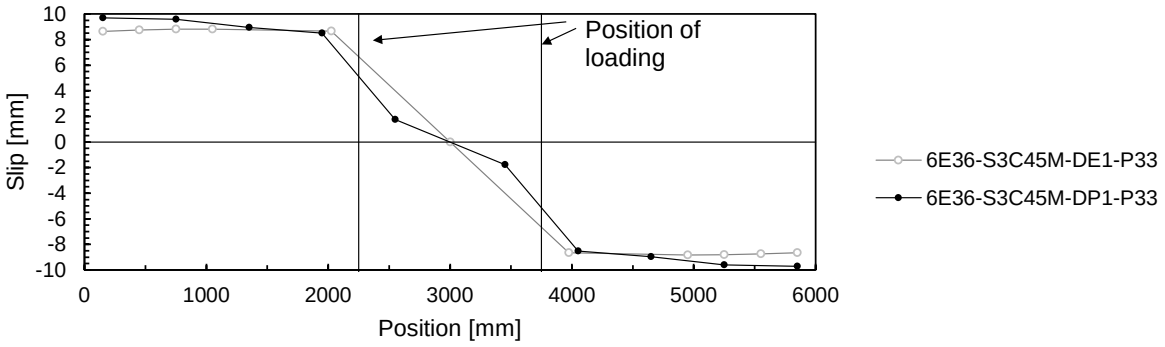

Figure 7.22 Slip distribution of identical beams with different shear connector distribution (P3.3)

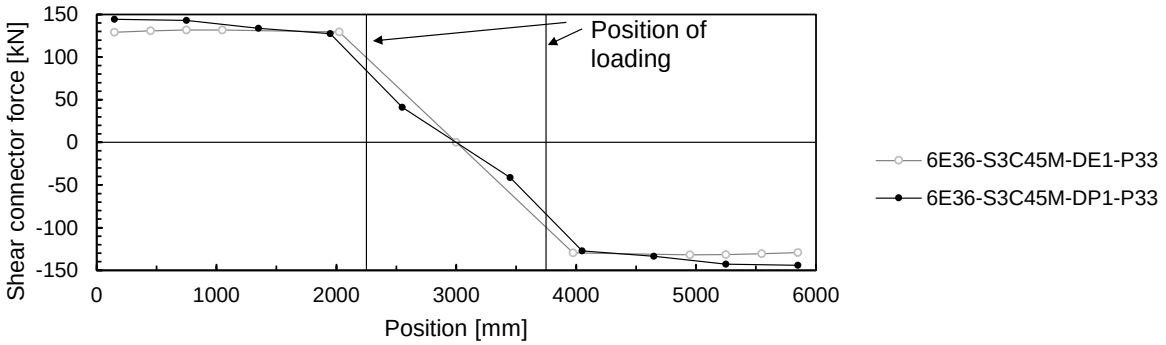

Figure 7.23 Shear connector forces of beams with different shear connector distribution (P3.3)

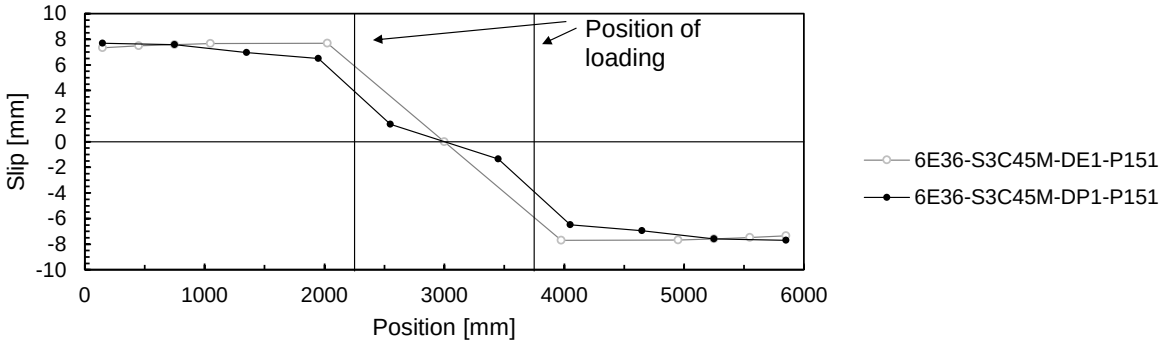

Figure 7.24 Slip distribution of identical beams with different shear connector distribution (P15.1)

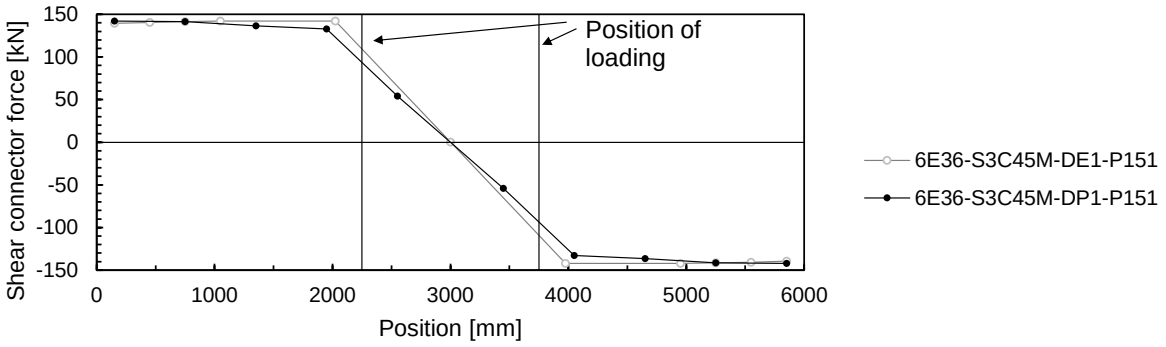

Figure 7.25 Shear connector forces of beams with different shear connector distribution (15.1)

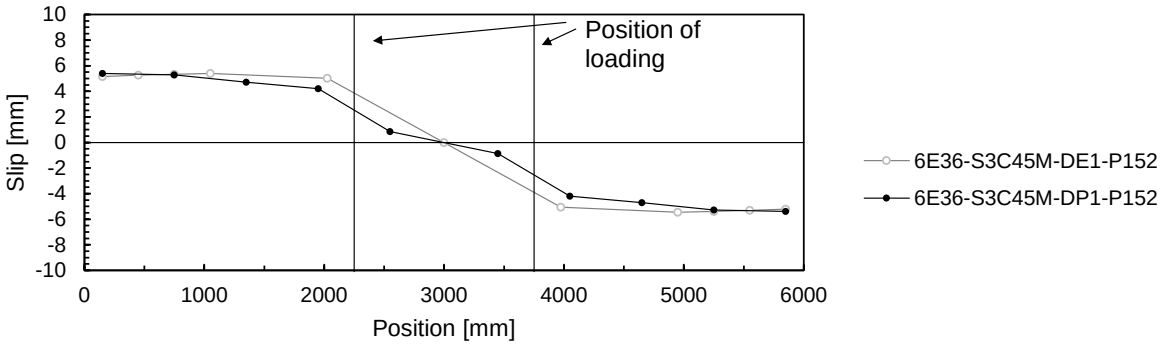

Figure 7.26 Slip distribution of identical beams with different shear connector distribution (P15.2)

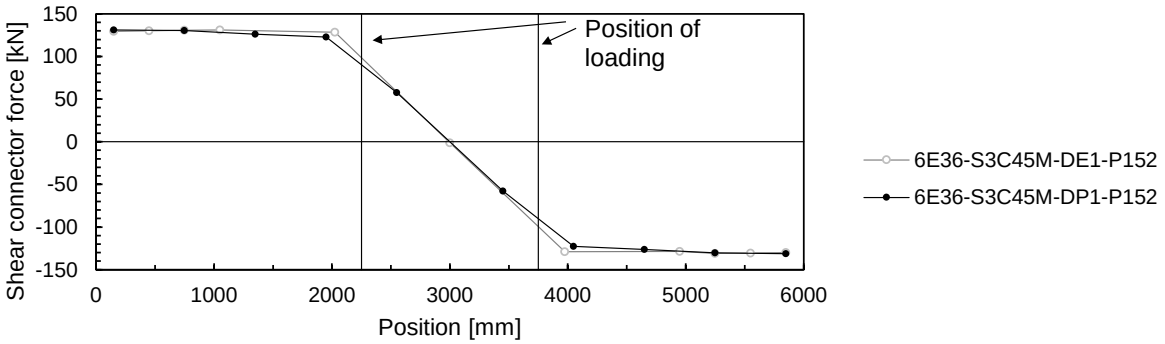

Figure 7.27 Shear connector forces of beams with different shear connector distribution (P15.2)

7.6 Results and discussions of parametric study PS-2

The main purpose of parametric study PS-2 was to assess the accuracy of the developed calculation methods that are presented in Chapter 8 and in Chapter 9. The details of the numerical models and the results (moment-deflection curves, ultimate moment resistance and slip distributions) are presented in Annex B.2. Figure 7.1 presents the applied naming conventions.

7.6.1 Slip distribution

The application of the developed calculation methods (Method PL1 and PL2) for the plastic moment resistance (see Chapter 9) requires to assume a certain slip distribution function. Therefore, besides the general load-deflection behaviour, the ultimate moment capacity and the end slip at failure (presented in Annex B.2) one of the most important outcomes of the presented parametric study is the slip distribution along the length. The following figures show the obtained slip values relative to the end slip at every shear connector along the halt length under failure conditions (either shear connector failure or concrete failure). The figures show those 39 beams that were modelled with the measured / expected values of the material properties (see Chapter 7.3) because they can represent the real behaviour more

accurately than the other 39 beams, which were modelled with their design values. The results of those beams are presented in Annex B.2.

In the figures, the obtained slip values are connected with lines in order to see the slip distribution function. In Chapter 9, it is proposed to approximate the slip distribution with a cosine function; therefore, a cosine curve is also plotted on the figures.

In the figures, we can observe that the slip distribution can vary based on the type of shear connection as well as the distribution of the shear connectors. Shear connection distribution DP1 represent an equidistant spacing of 600 mm and DP2 represents and equidistant spacing of 300 mm. In all cases the largest slip belongs to the outermost shear connectors, i.e. always the end slip is the largest slip value.

In general, the slip distribution is closer to a cosine function in those cases where the shear connector spacing (DP1) is 600 mm than in the cases with 300 mm spacing (DP2). This can be explained by the fact that beams with distribution DP2 fail generally at much higher deflection levels than beams with distribution DP1 (see Annex B.2). Higher levels of deflection result in higher plastic strains, which have a direct effect on the slip distribution (see Figure 9.3). As long as the plastic strains are relatively low, the slip distribution resembles more to the elastic slip distribution, which is usually approximated by a cosine function (for instance [43] and [44]).

A cosine function seems to be a reasonable approximation anyway, as it is easy to use and can describe the slip distribution relatively well even if it does not take the increased slip due to plastification of the section into account. Neglecting this increased slip in calculation methods PL1 and PL2 is on the "safe side" because it only means that we take a lower concrete compression force into account and finally we obtain a lower moment capacity. Nevertheless, the applicability of methods PL1 and PL2 is not necessarily limited to a cosine function but other functions can also be used.

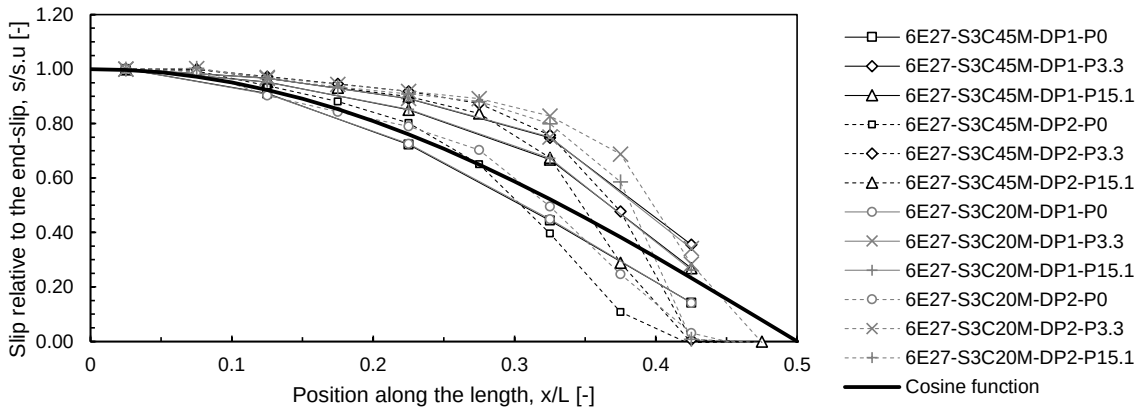

Figure 7.28 Slip distribution of 6 m long beams with IPE270

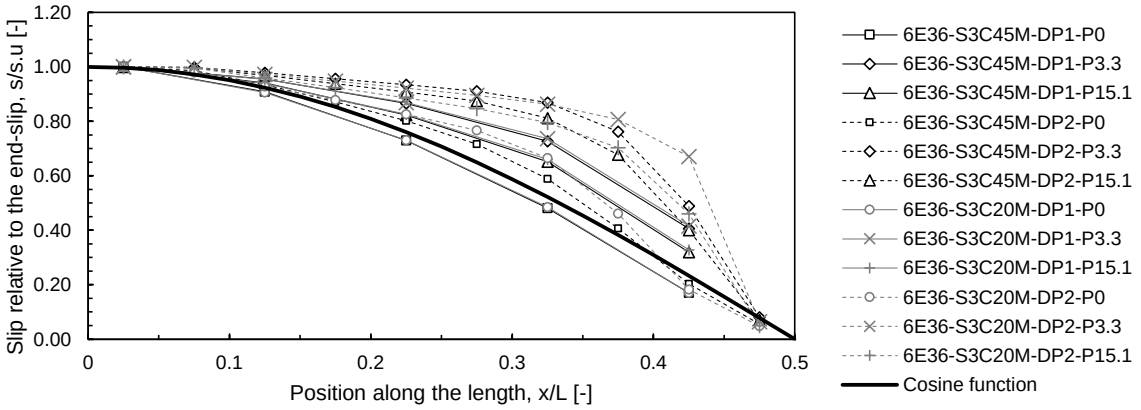

Figure 7.29 Slip distribution of 6 m long beams with IPE360

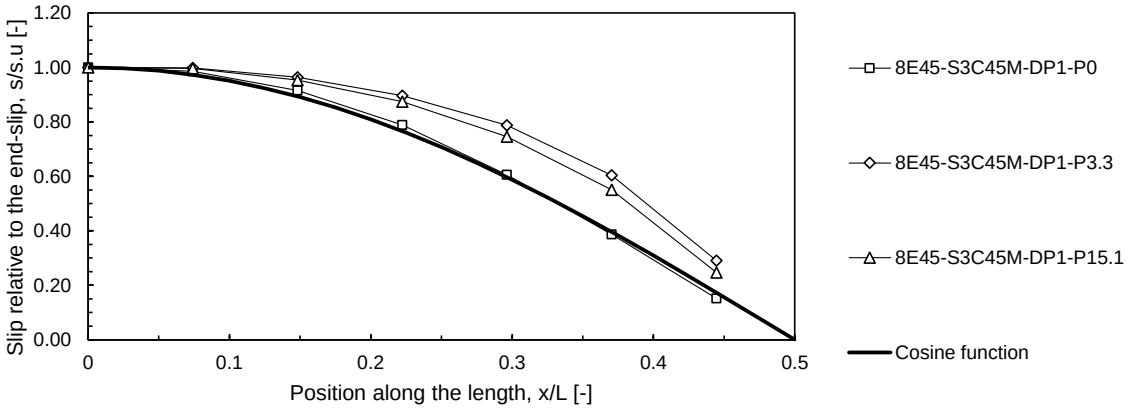

Figure 7.30 Slip distribution of 8.1 m long beams with IPE450

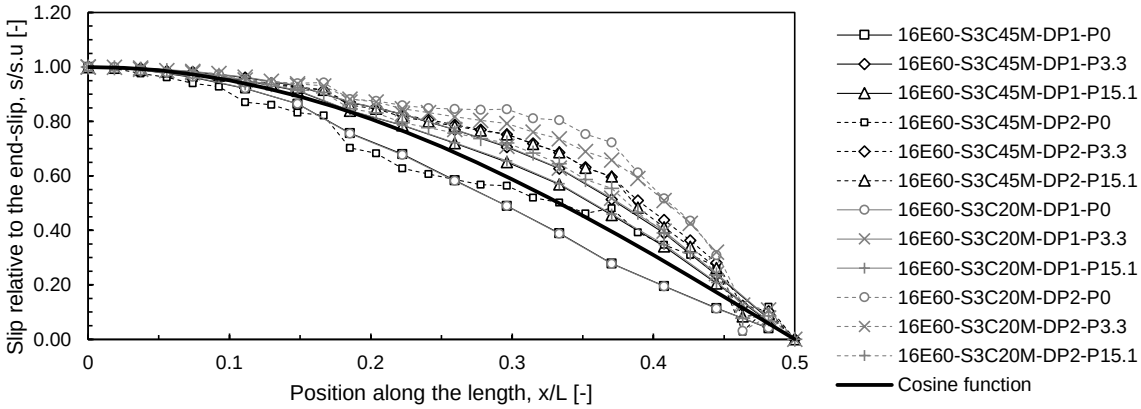

Figure 7.31 Slip distribution of 16.2 m long beams with IPE600

7.6.2 Comparison of results with the analytical methods

The developed calculation methods are presented in Chapter 8 and in Chapter 9. Their practical applications are presented in Annex F. This chapter presents the moment-deflection curves in comparison with the results obtained by the developed analytical calculations for eight beams (two beams for each type of steel profile) from parametric study PS-2.

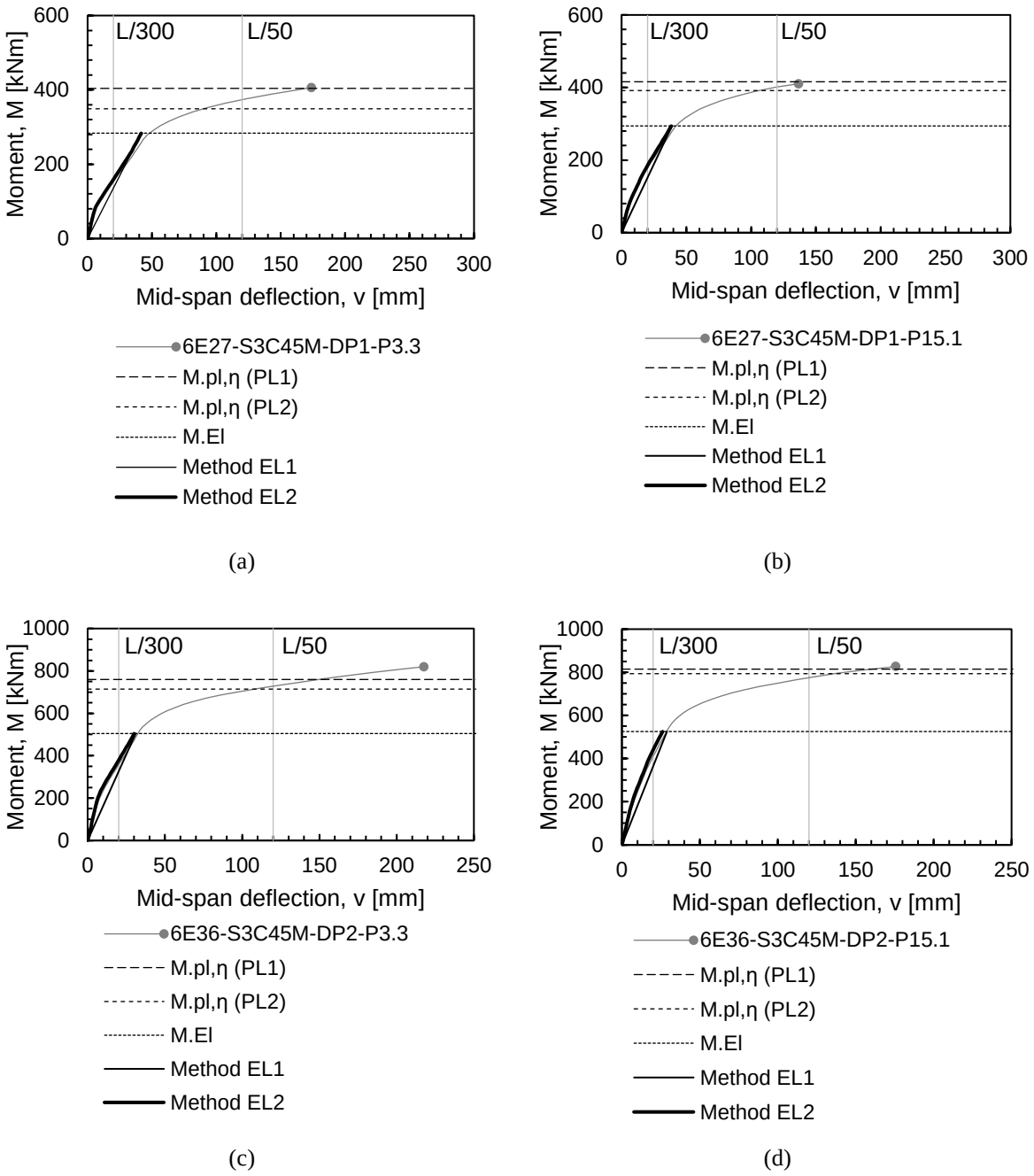

Figure 7.32 Comparison of analytically and numerically obtained results (Part 1)

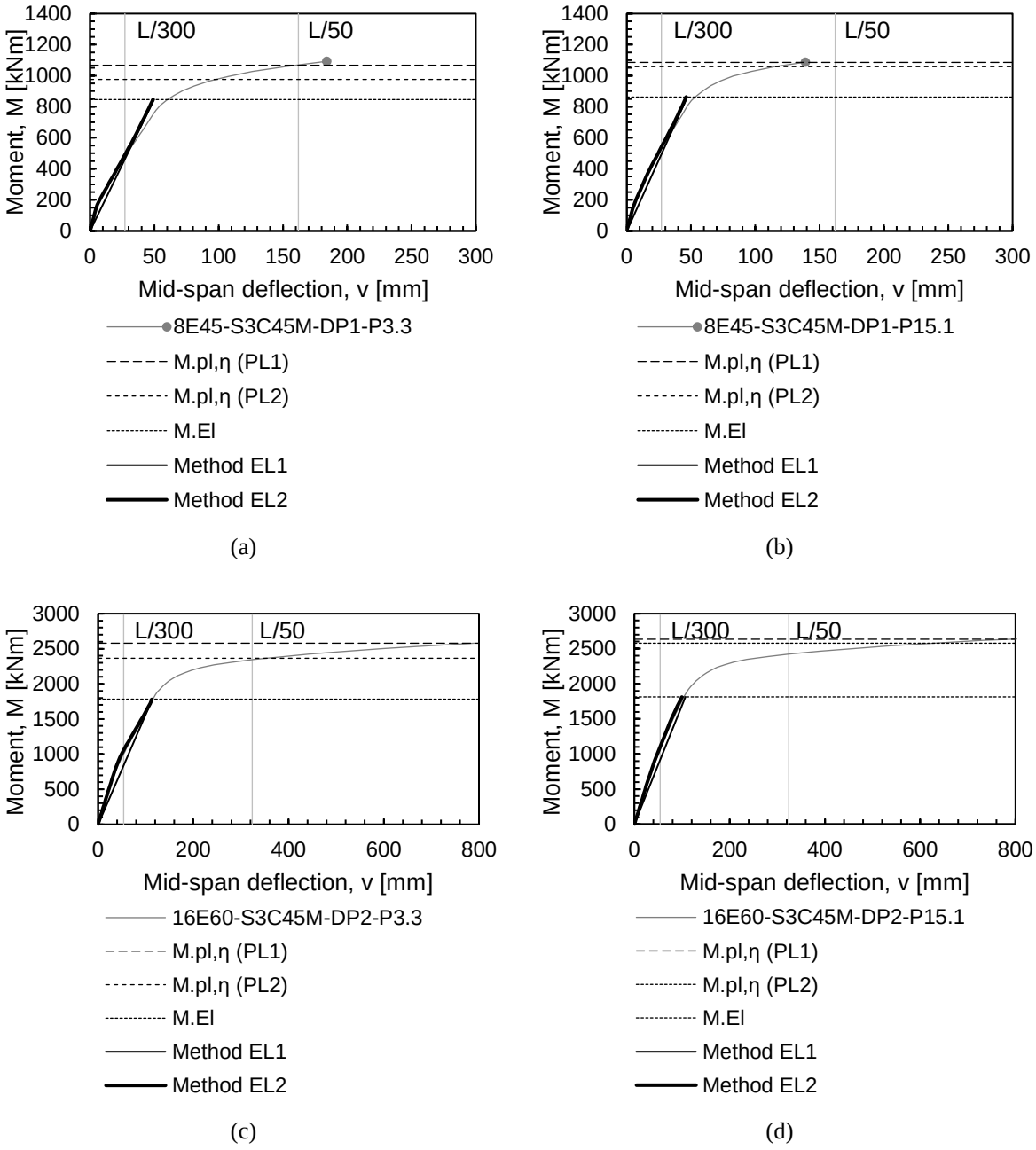

Figure 7.33 Comparison of analytically and numerically obtained results (Part 2)

As one can see, the results obtained by numerical simulations and by analytical calculations are in a good agreement. This is especially true for Method EL2 and Method PL1.

7.7 Conclusions

Based on the performed simulations the following conclusions could be drawn:

1) The resistance of the composite beams with demountable shear connections were similar to or higher than the one with welded studs.
2) Beams with pretensioned bolts had lower bending stiffness due to the bolt slippage in the bolt hole. Similar observations were made during the experimental investigations presented in Chapter 5.8.
3) Among the investigated parameters the highest influence belonged to the yield strength of the steel. Beams with a higher steel grade had a higher moment capacity and a lower concrete damage. Lower steel grades resulted in higher slips at around the load application points due to the plastification of the section.
4) The non-ductile behaviour of the shear connection did not have an effect on the ductility of the composite beam. The beams failed beyond an L / 50 deflection level, which is a generally accepted ductility criterion. However, the shear connection, which had lower deformation capacity (P0 and P15.2) had a negative effect on the ductility. This means that for the ductility of a composite beam the final deformation capacity of the shear connection is more important than the ductility of the shear connection.
5) Low degree of shear connection has a negative effect on the ductility of composite beams because the shear connection failure occurs at lower deflection levels.
6) Beams subjected to a symmetric two-point loading (PS-1) had a slip distribution at failure, which was more-or-less constant on the shear length. The plastic moment capacity of these beams could be determined relatively accurately using Method PL1. The greatest difference in the numerically and analytically obtained moment resistance values was 5%.
7) The slip distribution of beams subjected to a uniformly distributed load (PS-2) could be described with a monotonic decreasing curve. The use of a cosine function for the approximation of the slip distribution seems to be reasonable.
8) The concrete grade did not have a significant influence on the general load-deflection behaviour, but the deck elements with lower grade concrete underwent a higher concrete damage. Therefore, from a reusability point of view, higher grade concrete (C45/55) is recommended.
9) The comparison of the results obtained by numerical simulations and the developed calculation methods presented in Chapter 8 and in Chapter 9 showed a good agreement. This is especially true for Method EL2 and for Method PL1.

Chapter 8. Elastic behaviour of composite beams

8.1 General

Understanding the elastic behaviour of a composite beam is essential for the assessment of its serviceability performance. This can include the calculation of the deflection, the end slip and the stresses for a given load. This chapter covers the following topics:

1) Basic equations of composite beams
2) Equations of the second moment of area for different types of shear connection
3) Calculation of the end slip
4) The elastic deflection calculation for prismatic and non-prismatic composite beams
5) Long-term effects
6) Calculation of the location of the elastic neutral axes for different types of shear connection
7) Calculation of normal stresses from bending

An iterative procedure was developed for the calculation of the elastic properties of composite beams with nonlinear shear connection (Method EL2). This method is presented in chapter 8.5.

The derivations presented in this chapter are reduced in length. The complete derivations can be found in Annex C.

8.2 Scope of the calculation method

The presented calculation method considers the determination of the second moment of area, the deflections and the elastic stresses of steel-concrete composite beams. Stability phenomena are not considered. It is applicable if the following conditions are satisfied:

(i) The beam is simply supported and subjected to a positive bending moment.
(ii) The concrete deck is placed above the steel section (i.e. downstand composite beams).
(iii) The steel beam can be hot-rolled or fabricated (Class 1, 2 or 3).
(iv) The concrete deck can be solid or with profiled decking.
(v) The section is symmetric to the vertical axis.
(vi) The shear connection is distributed uniformly along the length.
(vii) The slip distribution function can be approximated with a cosine function.
(viii) The load-slip behaviour of the shear connection can be described with a monotonic increasing curve.

8.3 Assumptions

The forthcoming derivations are based on the following assumptions:

(i) The beam in consideration is a Euler-Bernoulli beam, i.e. the cross-sections originally plane and perpendicular to the axis of the beam remain plane and perpendicular to the axis of the beam after deformation.

(ii) Only small displacements are considered.

(iii) The steel and the concrete can be considered as linear elastic isotropic materials.

(iv) There is no separation between the steel beam and the concrete slab.

(v) There is no cracking of the concrete.

(vi) The curvature of the steel and the concrete is the same at any section.

8.4 Fundamentals

8.4.1 Basic equations

The basic equations presented here were already presented in the international literature by several researchers, for instance by Hoischen [41], Hanswille [43], [82] and by Lawson et al. [44]. Nevertheless, they are re-presented in this section because they are fundamental for understanding the new method presented in Chapter 8.5.

In order to determine the second moment of area $I_{y,eff}$ of the composite section, first consider the equilibrium equations of the composite section due to an externally applied moment $M_y(x)$ As a result of the composite action, a compression force $F_{x,c}(x)$ acts in the concrete slab and a tension force $F_{x,a}(x)$ in the steel beam (see Figure 8.1).

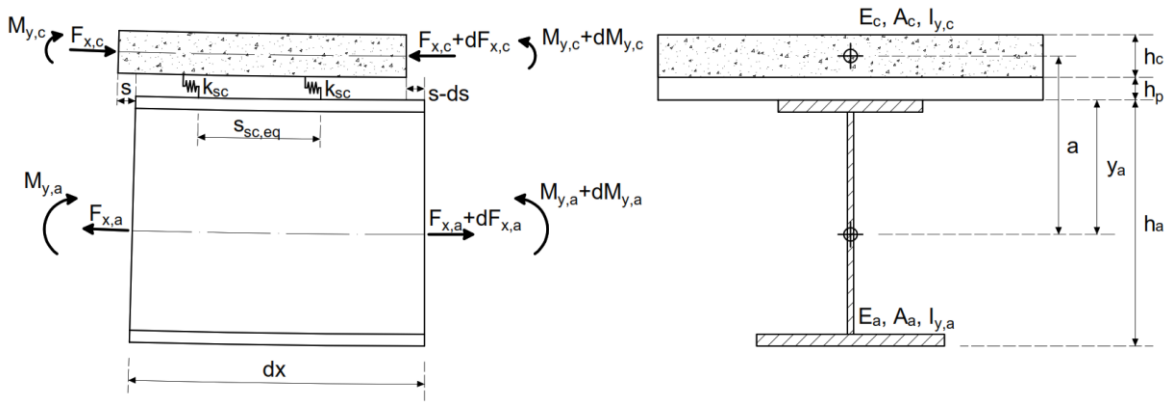

Figure 8.1 Theoretical model and cross-sectional forces of a composite beam with flexible shear connection

If there is no externally applied normal force, the magnitudes of these forces are equal. This will be denoted as $F_x(x)$ in the forthcoming.

$$\left|F_{x,a}(x)\right| = \left|F_{x,c}(x)\right| = F_x(x) \tag{8.1}$$

The externally applied moment $M_y(x)$ is equilibrated by the moment resisted by the slab $M_{y,c}(x)$, the moment resisted by the steel beam $M_{y,a}(x)$ and the moment generated by the pair of the normal forces $F_x(x)$:

$$M_y(x) = M_{y,c}(x) + M_{y,a}(x) + F_x(x) \cdot a \tag{8.2}$$

where a is the distance between the centroidal axes of the slab and the steel beam.

The curvature of the slab and the steel beam is the same at any sections:

$$\frac{M_{y,c}(x)}{E_c I_{y,c}} = \frac{M_{y,a}(x)}{E_a I_{y,a}} = \frac{M_y(x)}{E_a I_{y,eff}} = \kappa(x) \tag{8.3}$$

The modular ratio expresses the ratio of the modulus of elasticity of the steel and of the concrete:

$$n = E_a / E_c \tag{8.4}$$

Using equation (8.3) in equation (8.2), we can express the second moment of area as:

$$I_{y,eff} = \frac{I_{y,c}}{n} + I_{y,a} + \frac{F(x) \cdot a}{E_a \kappa(x)} \tag{8.5}$$

The rate of change of slip $ds(x)/dx$ is determined by the strain difference between the steel and the concrete at their contact surface:

$$\frac{ds(x)}{dx} = \varepsilon_{x,a}(z,x) - \varepsilon_{x,c}(z,x) \tag{8.6}$$

The moment equation of a composite section can be expressed as:

$$M_y(x) = -\frac{ds(x)}{dx} \cdot \frac{E_a I_{y,eff}}{a} + \frac{F_x(x) I_{y,eff}}{a} \left(\frac{A_c + nA_a}{A_c A_a}\right) \tag{8.7}$$

The complete derivation can be found in Annex C, equations (C.32) - (C.46).

8.4.2 Second moment of area

The second moment of area is one of the most important properties of a section. Among others, it is used for the calculation of the deflections and the stresses. Although some of the derivations presented in this chapter have already been presented in the international literature by [43] and [44] in a similar way, they are re-presented here because they are fundamental for the understanding of the equations presented in Chapter 8.5.

No shear connection

If there is no shear connection, there is no compression force in the concrete from composite action:

$$F(x) = 0 \tag{8.8}$$

Using this in equation (8.5), the second moment of area will be the sum of the second moment of area of the steel and of the concrete divided by the modular ratio. The concrete contribution is often neglected:

$$I_{y,eff} = \frac{I_{y,c}}{n} + I_{y,a} + \frac{F_x(x) \cdot a}{E_a \kappa(x)} = \frac{I_{y,c}}{n} + I_{y,a} \approx I_{y,a} \tag{8.9}$$

Rigid shear connection

In order to determine the second moment of area, we use equation (8.5):

$$I_{y,eff} = \frac{I_{y,c}}{n} + I_{y,a} + \frac{F_x(x) \cdot a}{E_a \kappa(x)}$$

with:

$$E_a \kappa(x) = M_y(x)/I_{y,eff}$$

$$I_{y,eff} = \frac{I_{y,c}}{n} + I_{y,a} + \frac{F_x(x) \cdot a \cdot I_{y,eff}}{M_y(x)} \tag{8.10}$$

In the case of rigid shear connection, there is no slip between the slab and the steel beam:

$$s(x) = 0, \text{ and} \tag{8.11}$$

$$\frac{ds(x)}{dx} = 0 \tag{8.12}$$

So, equation (8.7) becomes:

$$M_y(x) = \frac{F_x(x) I_{y,eff}}{a} \left(\frac{A_c + nA_a}{A_c A_a} \right) \tag{8.13}$$

By substituting equation (8.13) into equation (8.10) we obtain the effective second moment of area of a composite beam with rigid shear connection:

$$I_{y,eff} = I_{y,a} + \frac{I_{y,c}}{n} + \frac{A_c A_a}{A_c + nA_a} \cdot a^2 \tag{8.14}$$

The complete derivation can be found in Annex C, equations (C.50) - (C.54).

Flexible (linear elastic) shear connection (Method EL1)

In the case of flexible shear connection, the exact solution of the slip distribution, the compression force in the concrete and the longitudinal shear force requires the solution of the differential equation of the composite beam; and therefore a rather complex task for practical applications (see Chapter 2.2).

As a simplification, generally the slip $s(x)$ is assumed to vary according to a cosine function along the length of the beam (for instance by Hanswille and Schäfer [43] and by Lawson et al. [44]). As a result, the compression force and the bending moment $M_y(x)$ are assumed to vary according to a sine function. This moment diagram corresponds to an external load $q_z(x)$ that is distributed according to a sine function along the length. However, it is still a good approximation for a uniformly loaded beam where the moment diagram is a second order parabola.

The second moment of area can be determined in the same way as in the case of rigid shear connection. The assumed slip function is:

$$s(x) = \bar{s} \cdot \cos\left(\frac{\pi x}{L}\right) \tag{8.15}$$

where $\bar{s}$ is the end slip, L is the span of the beam, and x is the distance along the length of the beam from a support.

Therefore:

$$\frac{ds(x)}{dx} = -\bar{s} \cdot \frac{\pi}{L} \cdot \sin\left(\frac{\pi x}{L}\right) \tag{8.16}$$

The shear connector forces $P_{sc}(x)$ are not considered in discrete points, but over a unit length:

$$P_{sc}(x) = s(x) \cdot \frac{k_{sc}}{s_{sc,eq}} = \bar{s} \cdot \cos\left(\frac{\pi x}{L}\right) \cdot \frac{k_{sc}}{s_{sc,eq}} \tag{8.17}$$

where k_{sc} is the stiffness of the shear connectors, and $s_{sc,eq}$ is the equivalent longitudinal spacing. The compression force in the slab $F_x(x)$ can be determined from the integral of the shear connector forces:

$$F_x(x) = \int_0^x P_{sc}(x)\, dx = \bar{s} \cdot \frac{k_{sc}}{s_{sc,eq}} \int_0^x \cos\left(\frac{\pi x}{L}\right) dx =$$

$$F_x(x) = \bar{s} \cdot \frac{k_{sc}}{s_{sc,eq}} \cdot \frac{L}{\pi} \cdot \sin\left(\frac{\pi x}{L}\right) \tag{8.18}$$

Using equations (8.16) and (8.18), equation (8.7) becomes:

$$M_y(x) = \bar{s} \cdot \sin\left(\frac{\pi x}{L}\right) \cdot \frac{I_{y,eff}}{a}\left(E_a \cdot \frac{\pi}{L} + \frac{k_{sc}}{s_{sc,eq}} \cdot \frac{L}{\pi}\left(\frac{A_c + nA_a}{A_c A_a}\right)\right) \tag{8.19}$$

By substituting equations (8.19) and (8.18) into equation (8.10) we obtain the effective second moment of area of composite beams with flexible shear connectors:

$$I_{y,eff} = I_{y,a} + \frac{I_{y,c}}{n} + \frac{A_c/n}{1 + \frac{A_c}{nA_a} + \left(\frac{E_a}{k_{sc}/s_{sc,eq}}\right)\left(\frac{\pi}{L}\right)^2\left(\frac{A_c}{n}\right)} \cdot a^2 \tag{8.20}$$

The end slip as the function of the mid-span moment $\bar{M}$ is:

$$\bar{s} = \frac{\bar{M} \cdot a}{I_{y,eff}\left(E_a \cdot \frac{\pi}{L} + \frac{k_{sc}}{s_{sc,eq}} \cdot \frac{L}{\pi}\left(\frac{A_c + nA_a}{A_c A_a}\right)\right)} \tag{8.21}$$

Or, by introducing an auxiliary parameter S_k:

$$S_k = \frac{a}{\frac{E_a}{\left(\frac{k_{sc}}{s_{sc,eq}}\right)\left(\frac{L}{\pi}\right)^2} + \frac{A_c + nA_a}{A_c A_a}} \tag{8.22}$$

$$\bar{s} = \bar{M}\frac{S_k}{I_{y,eff}}\frac{s_{sc,eq}}{k_{sc}}\frac{\pi}{L} \tag{8.23}$$

Alternatively, the mid-span moment that belongs to a certain the end slip is:

$$\bar{M} = \bar{s}\frac{I_{y,eff}}{S_k}\frac{k_{sc}}{s_{sc,eq}}\frac{L}{\pi} \tag{8.24}$$

The complete derivation can be found in Annex C, equations (C.55) - (C.60).

An example of the practical application of this calculation is presented in Annex F.3.

8.4.3 Elastic deflection determination

The elastic deflection of a composite beam can be determined as the double integral of the curvature function.

$$\kappa(x) = \frac{M(x)}{E_a I_{y,eff}} \tag{8.25}$$

When the beam in consideration is prismatic, i.e. the cross-section is uniform along the length, the well-known formulations can be used for the calculation of the deflections. These formulations are summarised here for the basic load cases.

For a point load P at mid-span:

$$\bar{w} = \frac{PL^3}{48 \cdot E_a I_{y,eff}} \tag{8.26}$$

For symmetric two-point loads acting at a distance e measured from the supports:

$$\bar{w} = \frac{Pe}{24 \cdot E_a I_{y,eff}} \cdot (3L^2 - 4e^2) \tag{8.27}$$

For uniformly distributed load:

$$\bar{w} = \frac{5}{384} \cdot \frac{qL^4}{E_a I_{y,eff}} \tag{8.28}$$

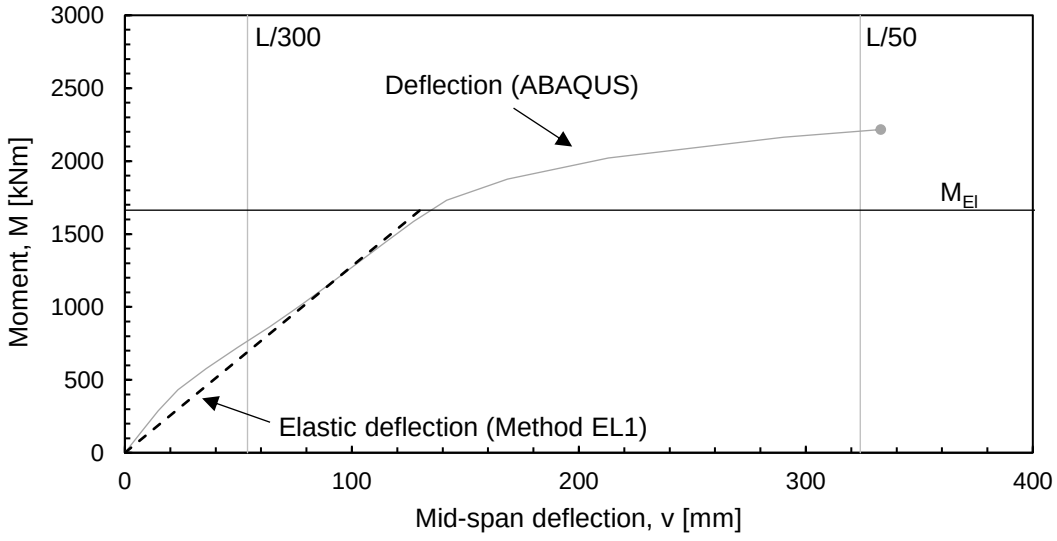

Figure 8.2 Comparison of the numerically and analytically obtained deflections

Figure 8.2 shows the comparison of the analytically and numerically determined deflections of a composite beams analysed in the frame of the parametric studies presented in Chapter 7. The beam was denoted as 16E60-S3C20M-DP1-P3.3, which corresponds to a 16.2 m long composite beam with an IPE 600 section made of S355 steel and C20/25 concrete deck. It uses shear connectors of type P3.3 distributed uniformly in pairs with a longitudinal spacing of 300 mm. The deflection was calculated using Equation (8.28), and the second moment of area was determined using Equation (8.20).

8.4.4 Location of the neutral axes

The concrete slab and the steel beam have their own elastic neutral axes:

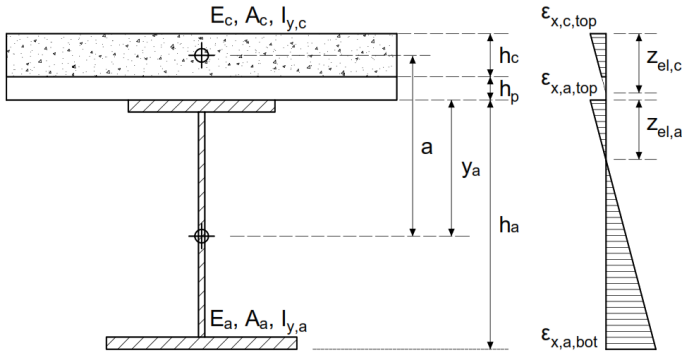

Figure 8.3 Strain diagram of a composite section with flexible shear connection

Elastic neutral axes in the case of no shear connection

If there is no shear connection, each element has its neutral axis in its centroidal axis. Using the notations of the Figure 8.3, this means:

$$z_{el,c} = h_c/2 \tag{8.29}$$

$$z_{el,a} = y_a \tag{8.30}$$

where $z_{el,c}$ is the distance between the neutral axis of the concrete and its extreme fibre in compression, and $z_{el,a}$ is the distance between the neutral axis of the steel beam and its extreme fibre in compression.

Elastic neutral axes in the case of rigid shear connection

If the connection between the slab and the steel beam is rigid, their neutral axes coincide:

$$z_{el,c} = h_c + h_p + z_{el,a} \tag{8.31}$$

Elastic neutral axes in the case of flexible shear connection

In the case of a flexible shear connection, the location of the elastic neutral axes depends on the stiffness and spacing of the shear connectors. At any section, the concrete is subjected to a bending moment $M_{y,c}(x)$ and a compression force $F_x(x)$. The corresponding strains are presented in Figure 8.4.

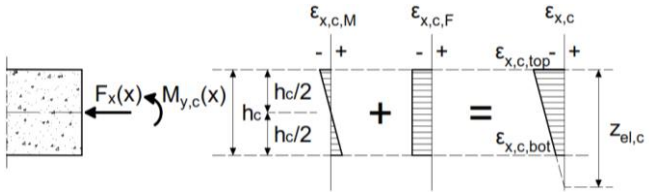

Figure 8.4 Strains in the slab

Similarly, at any section, the steel beam is subjected to a bending moment $M_{y,a}(x)$ and a tension force $F_x(x)$. The corresponding strains are presented in Figure 8.5.

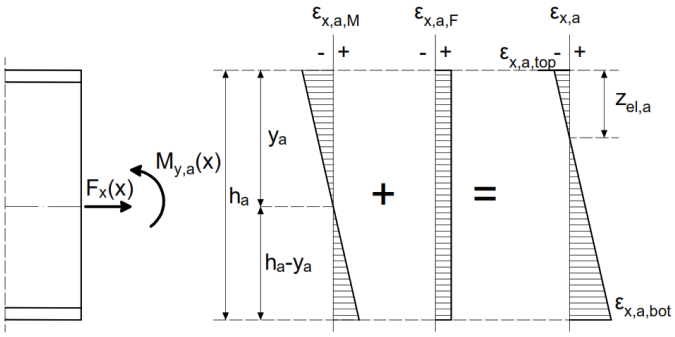

Figure 8.5 Strains in the beam

Based on these strain diagrams, the location of the neutral axes can be written as the function of the shear connection stiffness and spacing:

$$z_{el,c} = \frac{h_c}{2} + \frac{n \cdot S_k}{A_c} \tag{8.32}$$

$$z_{el,a} = y_s - \frac{S_k}{A_a} \tag{8.33}$$

where S_k is an auxiliary parameter given by Equation (8.22).

The complete derivations can be found in Annex C, equations (C.70) - (C.86).

8.5 Composite beams with nonlinear shear connection (Method EL2)

8.5.1 Second moment of area for nonlinear connection

EN1994-1-1 [18], A.3 proposes that the shear connector stiffness k_{sc} may be taken as:

$$k_{sc} = 0.7P_{Rk}/s \tag{8.34}$$

where:

P_{Rk}: is the characteristic resistance of the shear connector;

s: is the slip, determined from push tests in accordance with EN1994-1-1 [18], Annex B, at a load of 0.7 P_{Rk}.

It is important to note that the above equation refers mainly to welded studs that have a more-or-less ideal bi-linear elastic-plastic behaviour, where the load level of 0.7 P_{Rk} fells into the elastic part. The tested demountable shear connectors behave differently than the welded studs. Although several different variants have been tested, one common property of the different results was the highly nonlinear load-slip behaviour (see Figure 4.24). The behaviour of the pre-tensioned shear connectors can be divided into three distinct parts:

1) First, the shear connections behave rigidly until the friction resistance is overcome.
2) Second, bolt slip occurs inside the bolt hole.
3) Finally, the third part is the shear deformation of the bolts.

Generally, the load level of 0.7 P_{Rk} fells into the third part of the load-slip curve. As a result, the stiffness at this point cannot represent the stiffness of the shear connectors accurately for all load levels. Indeed, the actual stiffness depends on the acting load on the shear connector, which is different for all shear connectors along the length. Maintaining the assumption of a cosine slip function, the slip at each shear connector can be determined with Equation (8.15). If the slip of the connector is known, the secant stiffness $k_{sc,i}$ of each shear connector can be determined from the load-slip curve (see Figure 8.6).

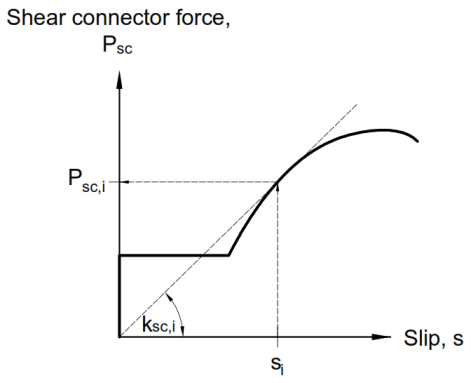

Figure 8.6 Secant stiffness depending on the occurring slip

$$k_{sc,i} = \frac{P_{sc,i}}{s_i} \tag{8.35}$$

The individual shear connector forces over a unit length can be expressed as:

$$P_{sc,i}(x) = s(x) \cdot \frac{k_{sc,i}}{s_{sc,eq}} = \bar{s} \cdot cos\left(\frac{\pi x}{L}\right) \cdot \frac{k_{sc,i}}{s_{sc,eq}} \tag{8.36}$$

Strictly speaking, the cosine slip distribution in the previous equation corresponds to a sinusoidal loading and a linear elastic shear connection. The conducted parametric studies show (Chapter 7), that it is still a reasonable approximation for uniformly distributed loading and nonlinear shear connection. However, it is important to note that the more the moment diagram differs from a sinusoidal curve the less accurate this approximation will become.

Because this function is non-continuous over the length, the compression force in the concrete slab will become the sum of the integrals of the parts where the function is continuous:

$$F_x(x_m) = \sum_{i=1}^{m} \int_{\frac{(i-1)L}{2n_p}}^{\frac{i \cdot L}{2n_p}} P_{sc,i}(x)dx = \bar{s} \sum_{i=1}^{m} \frac{k_{sc,i}}{s_{sc,eq}} \frac{L}{\pi} \cdot \left[\sin\left(\frac{i\pi}{2n_p}\right) - \sin\left(\frac{(i-1)\pi}{2n_p}\right)\right] \tag{8.37}$$

where m is the number of shear connectors (or pairs of shear connectors) and x_m is the distance from the support until the section in consideration. Using the previous formula, Equation (8.7) becomes:

$$\begin{aligned} M_y(x_m) = \bar{s} \cdot \frac{\pi}{L} \cdot \frac{E_a I_{y,eff,m}}{a} \sin\left(\frac{m\pi}{2n_p}\right) + \\ + \bar{s} \sum_{i=1}^{m} \frac{k_{sc,i}}{s_{sc,eq}} \frac{L}{\pi} \cdot \left[\sin\left(\frac{i\pi}{2n_p}\right) - \sin\left(\frac{(i-1)\pi}{2n_p}\right)\right] \frac{I_{y,eff,m}}{a} \left(\frac{A_c + nA_a}{A_c A_a}\right) \end{aligned} \tag{8.38}$$

The second moment of area can be expressed similarly as using equations (C.87) - (C.92).

$$I_{y,eff,m} = I_{y,a} + \frac{I_{y,c}}{n} + \frac{a^2}{\frac{E_a \sin\left(\frac{m\pi}{2n_p}\right)}{\frac{\pi}{L} \cdot \frac{}{\sum_{i=1}^{m} \frac{k_{sc,i}}{s_{sc,eq}} \frac{L}{\pi} \cdot \left[\sin\left(\frac{i\pi}{2n_p}\right) - \sin\left(\frac{(i-1)\pi}{2n_p}\right)\right]}} + \left(\frac{A_c + nA_a}{A_c A_a}\right)} \tag{8.39}$$

This equations shows that the second moment of area is not constant nor continuous over the length, but it takes a certain value at every shear connector.

The second moment of area at midspan is:

$$I_{y,eff,n_p} = I_{y,a} + \frac{I_{y,c}}{n} + \frac{a^2}{\frac{\pi}{L} \cdot \frac{E_a}{\sum_{i=1}^{n_p} \frac{k_{sc,i}}{s_{sc,eq}} \frac{L}{\pi} \cdot \left[\sin\left(\frac{i\pi}{2n_p}\right) - \sin\left(\frac{(i-1)\pi}{2n_p}\right)\right]} + \left(\frac{A_c + nA_a}{A_c A_a}\right)} \tag{8.40}$$

where n_p is the number of shear connectors (or pairs of shear connectors) over the shear length.

These derivations commenced with the assumption that the slip at every shear connector is known, i.e. the end slip is known. However, the occurring the end slip depends on the load level. Its value can be expressed based on the the mid-span moment and the effective second moment of area at mid-span:

$$\bar{s} = \frac{\bar{M} \cdot a}{I_{y,eff,n_p}\left(\frac{\pi}{L} \cdot E_a + \sum_{i=1}^{n_p} \frac{k_{sc,i}}{s_{sc,eq}} \frac{L}{\pi} \cdot \left[\sin\left(\frac{i\pi}{2n_p}\right) - \sin\left(\frac{(i-1)\pi}{2n_p}\right)\right] \left(\frac{A_c + nA_a}{A_c A_a}\right)\right)} \tag{8.41}$$

As one may notice, the end slip depends on the shear connector stiffness values and vice-versa. In other words these values are interdependent. The solution for this issue is an iterative procedure:

1) At the beginning of the calculation, the value of the end slip is unknown; therefore, it is necessary to assume any value between zero and the maximum possible end slip defined by the load-slip curve
2) Then, the secant stiffness of the shear connectors can be determined by equation (8.35).
3) Afterwards, the second moment of area at mid-span can be calculated by equation (8.40).
4) The end slip can be calculated by equation (8.41).
5) The calculated end slip needs to be compared to the initial assumption.
6) If the discrepancy between the two end slips is greater than 1%, the initial assumption needs to be updated with the calculated end slip and all the steps need to be repeated.
7) When the discrepancy between the two end slip values is less than 1%, the second moment of area can be determined at each shear connector by equation (8.39).
8) Due to the different bending stiffness values, the beam cannot be considered to be prismatic anymore. For the calculation of the deflections, the deflection increments need to be calculated first. This is presented in chapter 8.5.2.
9) The total deflection will be the sum of the defection increments (equation (8.43)).

The error in the end slip (the difference between the assumed end slip and the calculated one) decreases with each iteration. Figure 8.7 shows how the error decreases with the iterations with the help of four examples. The flowchart of the iterative procedure is presented in Figure 8.8.

The complete derivations of the equation presented in this chapter can be found in Annex C, equations (C.87) - (C.94). An example of the practical application of this calculation method is presented in Annex F.4.

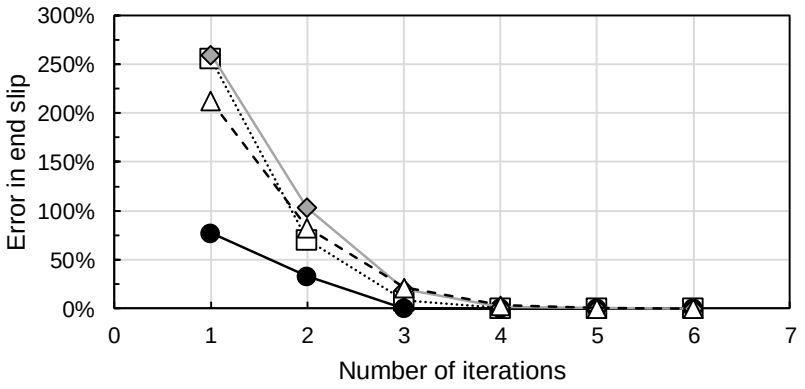

Figure 8.7 Error in end slip vs. the number of iterations

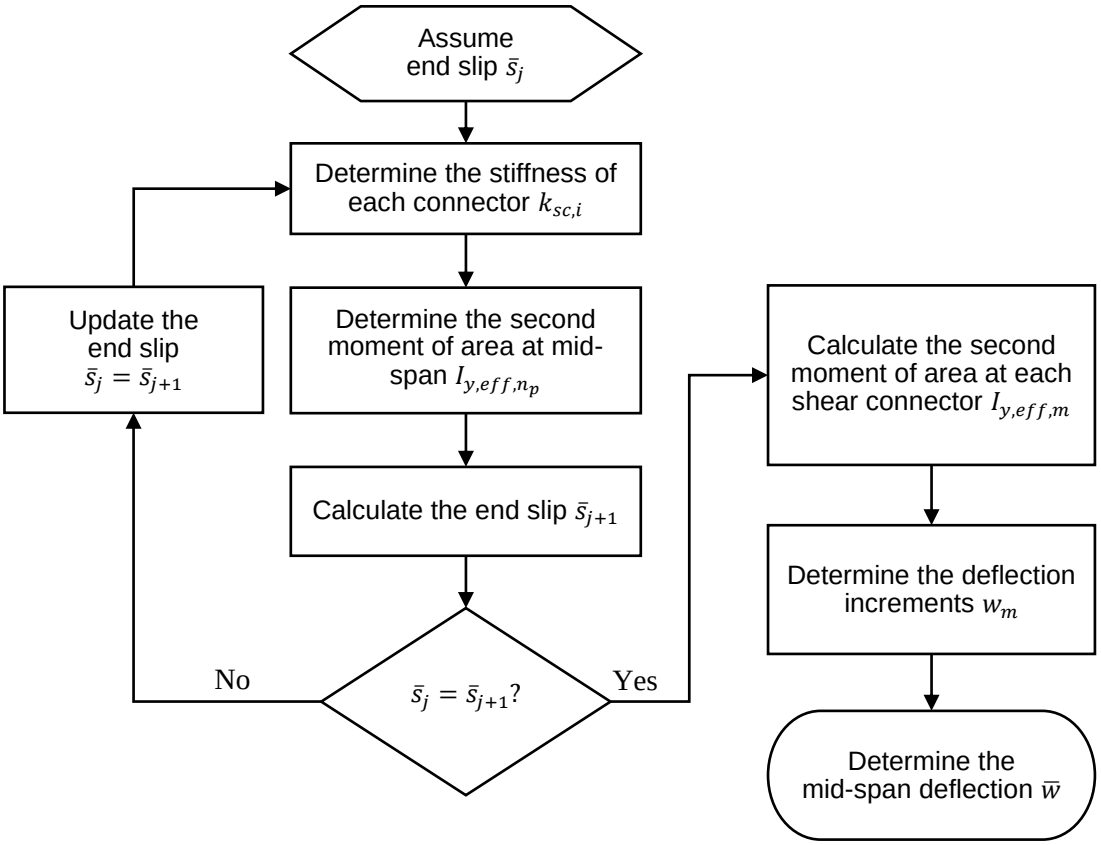

Figure 8.8 Iterative procedure for the determination of the elastic deflection

8.5.2 Elastic deflection of beams with nonlinear shear connection

As it was described in the previous section, when shear connectors with nonlinear load-slip curves are applied, the second moment of area is not uniform along the length, but it has certain values between the sections of each shear connector. Therefore, the beam cannot be considered as a prismatic beam.

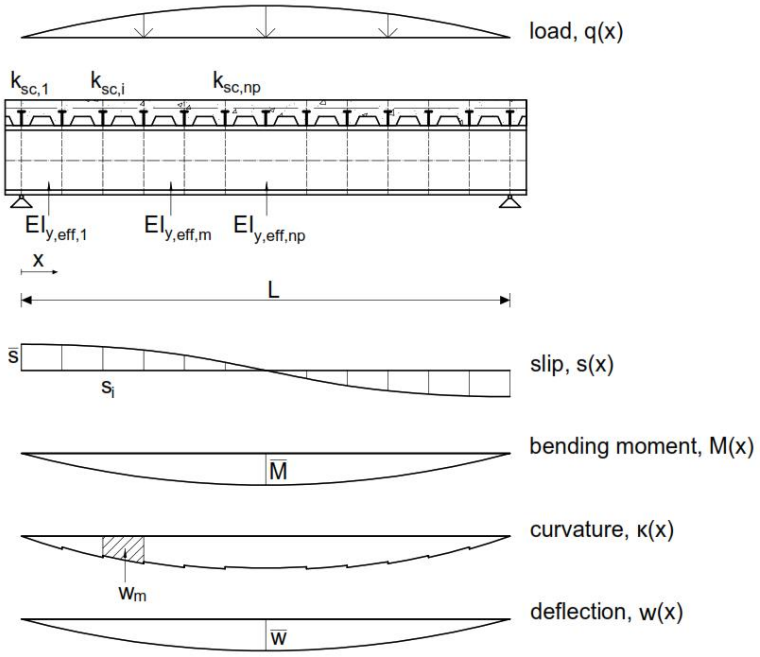

Figure 8.9 Loading, slip, moment, curvature and deflection diagram of a composite beam with nonlinear shear connection

The function of the curvature is not continuous because of the different second moment of area values along the length:

$$\kappa_m(x_m) = \frac{M(x_m)}{E_a I_{y,eff,m}} \tag{8.42}$$

As a result, the deflection at mid-span $\overline{w}$ will be the sum of the integral of the parts where the previous function is continuous:

$$\overline{w} = \sum_{m=1}^{n_p} \iint_{\frac{(m-1)L}{2n_p}}^{\frac{m \cdot L}{2n_p}} \kappa_m(x) dx^2 = \sum_{m=1}^{n_p} w_m \tag{8.43}$$

The previous integral (equation (8.43)) was solved for basic load cases.

For a point load *P* at mid-span:

$$w_m = \frac{P/2}{E_a I_{y,eff,m}} \cdot \left[\frac{L^2}{8}(A-B) + \frac{1}{6}(B^3 - A^3)\right] \tag{8.44}$$

Where the variables *A* and *B* denote the integration boundaries of the section in consideration:

$$A = \frac{m \cdot L}{2n_p}$$

$$B = \frac{(m-1)L}{2n_p}$$

For symmetric 2-point loads acting at a distance *e* measured from the supports:

$$w_m = \frac{P}{E_a I_{y,eff,m}} \cdot \left[\frac{L^2}{8}(A-B) + \frac{1}{6}(B^3 - A^3)\right] \tag{8.45}$$

for $0 < A < e$, and

$$w_m = \frac{P \cdot e}{2\, E_a I_{y,eff,m}} \cdot [L(A-B) + (B^2 - A^2)] \tag{8.46}$$

for $e < A < L/2$

For uniformly distributed load:

$$w_m = \frac{q}{24 E_a I_{y,eff,m}} \cdot [L^3(A-B) + 2L(B^3 - A^3) + A^4 - B^4] \tag{8.47}$$

The uniformly distributed load can be approximated with a sinusoidal load. This means that the second order parabola shaped moment diagram will be approximated with a sinusoidal one:

$$M_y(x) = \bar{M} \sin\left(\frac{\pi x}{L}\right) \tag{8.48}$$

Then, the deflection increments are:

$$w_m = \frac{\bar{M}}{E_a I_{y,eff,m}} \left(\frac{L}{\pi}\right)^2 \left[sin\left(\frac{A\pi}{L}\right) - sin\left(\frac{B\pi}{L}\right)\right] \tag{8.49}$$

The following figure shows the comparison between the numerically determined deflections and the deflections calculated using the presented iterative procedure for a 16 m long composite beam, which was earlier used for the comparison presented in Figure 8.2:

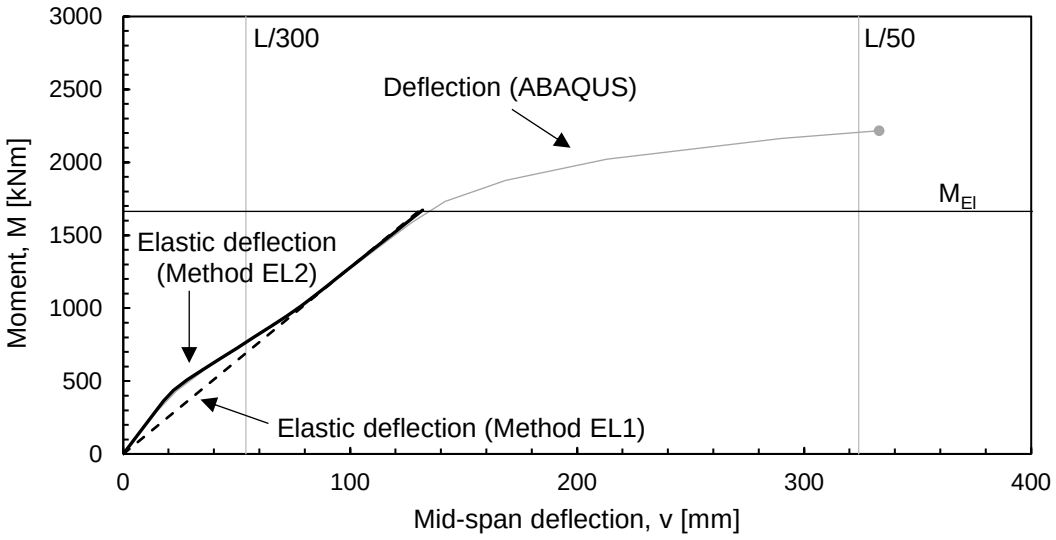

Figure 8.10 Comparison of the numerically and analytically determined deflections

8.5.3 Long-term effects on the deflection

Eurocode 4 [18] accounts for long-term effects such as creep and shrinkage with a modified modular ratio:

$$n_L = n_0(1 + \psi_L \varphi_t) \tag{8.50}$$

Where:

n_0 is the modular ratio E_a / E_{cm} for short term loading;

E_{cm} is the secant modulus of elasticity of the concrete for short-term loading according to EN1992-1-1 [49];

φ_t is the creep coefficient according to EN1992-1-1 [49] depending on the age t of the concrete at the moment considered and at the age t_0 at loading;

ψ_L is the creep multiplier depending on the type of loading (ψ_L = 1.1 for permanent loads and ψ_L = 0.55 for primary and secondary effects).

As a result, the composite beam stiffness $EI_{y,eff}$ is lower for long-term loads than it is for short-term loads. Usually, the deflections are determined for long-term loads (w_{lt}) and for short-term loads (w_{st}) separately, and then the final deflection (w_{tot}) can be calculated as their sum:

$$w_{tot} = w_{lt} + w_{st} \tag{8.51}$$

This calculation causes no problem when a flexible or a rigid shear connection is used,. However, in the case of nonlinear shear connection, the actual stiffness of each shear connector depends on the occurring slip and the load level. This means that by the time the short-term loads are applied to the structure, the

shear connectors have already undergone some slip due to the long-term loads. In order to take this effect into account, the following calculation method is proposed:

1) Determine the deflection due to long-term loads w_{lt} with the long-term modular ratio n_L.
2) Check the occurring slip s_i at each shear connector.
3) At every shear connector offset the origin of the load-slip curve to the actual load-slip values ($P_{sc,i}$; s_i). (see Figure 8.11)
4) Determine the deflection due to short-term loads w_{st} with the short-term modular ratio n_0 and the modified load slip curves.
5) The total deflection can be calculated by Equation (8.51).

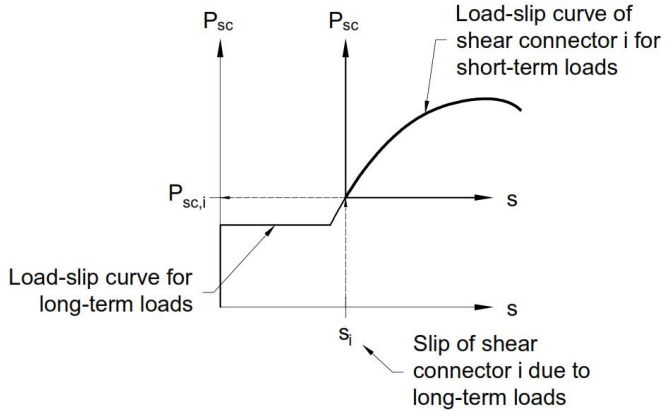

Figure 8.11 Offset of the load-slip diagram for the calculation of short-term deflections

8.5.4 Elastic neutral axes in the case of nonlinear shear connection

When deriving the equations for the location of the elastic neutral axes, it is necessary to divide the beams into sections at each shear connector because each shear connector has a different secant stiffness. As a result, the location of the neutral axes will not be constant along the length but will change at every shear connector. At shear connector number *m*:

$$z_{el,c,m} = \frac{h_c}{2} + \frac{n \cdot S_{k,m}}{A_c} \tag{8.52}$$

$$z_{el,a,m} = y_s - \frac{S_{k,m}}{A_a} \tag{8.53}$$

Where $S_{k,m}$ is the auxiliary parameter at location *m*:

$$S_{k,m} = \frac{a}{\frac{E_a}{\sum_{i=1}^{m} \frac{k_{sc,i}}{s_{sc,eq}} \cdot \left[\sin\left(\frac{i\pi}{2n_p}\right) - \sin\left(\frac{(i-1)\pi}{2n_p}\right)\right] \left(\frac{L}{\pi}\right)^2} + \frac{A_c + nA_a}{A_c A_a}} \tag{8.54}$$

The derivations of equations (8.52) - (8.54) was done using equations (8.37) - (8.39) in a similar way as presented in Annex C by equations (C.70) - (C.86).

8.5.5 Elastic stresses from bending

When a composite section is designed elastically, a stress verification should be performed proving that the stresses everywhere in the section in the corresponding limit state are below the elastic limit stresses (see Chapter 2.3.3). The stresses are usually determined with the help of the well-known formulae of structural mechanics using the cross-sectional properties of a homogenised cross-section:

Normal stress in the concrete: $$\sigma_{x,c}(x,z) = \frac{M_y(x)}{n \cdot I_{y,eff}(x)} \cdot z_c(x) \tag{8.55}$$

Normal stress in the steel: $$\sigma_{x,a}(x,z) = \frac{M_y(x)}{I_{y,eff}(x)} \cdot z_a(x) \tag{8.56}$$

The derivation of these equations are presented in Annex C by equations (C.47) - (C.49).

It is important to note that in the previous formulae, both the second moment of area and the location of the neutral axes depend on the position along the length if a nonlinear shear connection is applied. These parameters are constant in the case of rigid or flexible shear connection.

Chapter 9. Plastic moment resistance of composite beams

9.1 General

The calculation method that is suitable for the determination of the plastic moment resistance of a composite beam is largely influenced by the behaviour of the shear connection. This chapter presents the calculation methods for composite beams with rigid-ductile and rigid-brittle shear connections. A new calculation method is also presented in Chapter 9.4.2 for the calculation of the plastic moment resistance of composite beams with flexible or nonlinear shear connection, and a simplified procedure is proposed in Chapter 9.4.3.

9.2 Composite beams with rigid-ductile shear connection

For the determination of the plastic moment resistance M_{Rd} of composite beams with ductile shear connectors, the approach given by Eurocode 4 [18] is based on the equilibrium and moment equations that correspond to the plastic stress distribution. The approach assumes full plasticity, i.e. everywhere in the section the stresses are equal to their plastic limit stresses and all the shear connectors undergo plastic deformations. Where the shear connector behaviour can be described by an ideal rigid-plastic load-slip curve this approach is convenient to use because the longitudinal shear force will be the same (P_{Rd}) at every shear connector along the length. The developing compression force in the concrete equals to the sum of the shear connector forces between the critical sections. As every shear connector develops the same shear force, the compression force in the concrete can be determined by multiplying the shear connector resistance with the number of shear connectors between the critical sections (equation (2.35)). The same principles apply for full and for partial shear connection as well. This approach was already presented in detail in Chapter 2.3.2. It is important to note that the use of this approach might lead to unconservative design when not rigid-ductile, but flexible ductile connectors are used.

9.3 Composite beams with rigid-brittle shear connection

In the case of rigid shear connection, the redistribution of the shear forces is not possible; therefore, the slip must be kept small (≈0). This leads to a shear connector distribution that follows the elastic shear flow in the elastic zone (where $M_E \leq M_{el}$) of the beam. In the plastic zone of the beam (where $M_{el} < M_E \leq M_{pl}$), additional shear connectors are required because the longitudinal shear force will increase due to the plastification of the members (see Figure 9.1). The longitudinal shear force in the plastic zone ($v_{L,p}$) can be calculated from the difference between the compression force of the concrete at the sections where the elastic moment resistance M_{el} is reached and the position of the maximum bending moment $M_{E,max}$ divided by the length between these sections (L_p) [82]:

$$v_L = \frac{N_{c,pl} - N_{c,el}}{L_p} \tag{9.1}$$

The determination of the normal force $N_{c,pl}$ in the plastic zone requires an iterative procedure, which needs to consider the occurring strains.

Alternatively, Eurocode 4 [18] proposes a linear interpolation, which was already presented in Chapter 2.3.4.

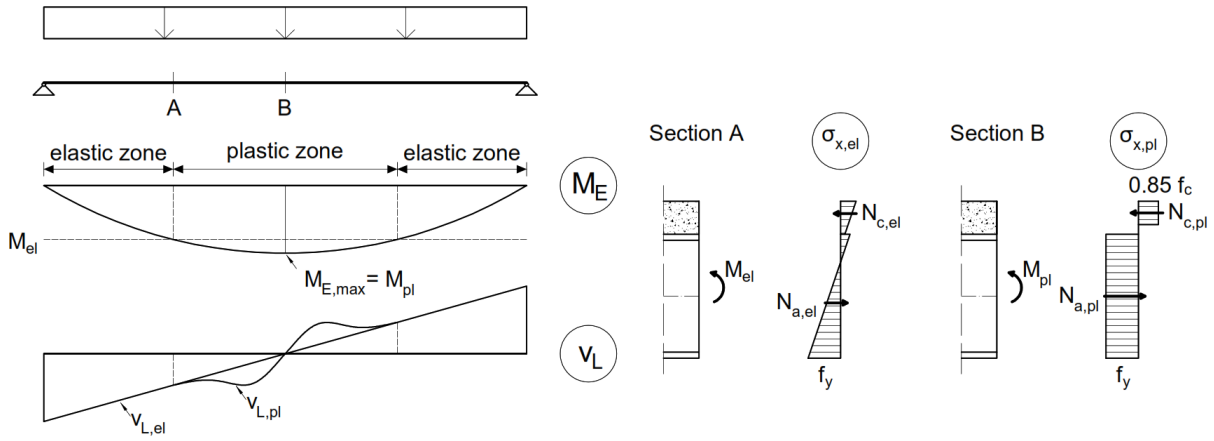

Figure 9.1 Longitudinal shear flow and the normal stress diagrams in the elastic and plastic limit state

9.4 Composite beams with flexible or nonlinear shear connection

9.4.1 Fundamental behaviour

When flexible shear connectors are applied, a relative slip occurs at the steel-concrete interface. Consequently, some sort of redistribution of the longitudinal shear is possible depending on the flexibility and the deformation capacity of the connection.

In order to be able to calculate the moment capacity of a composite beam it is essential to know the developing compression force in the concrete slab. This force depends on the shear force that the shear connectors can transfer. However, given that the load-slip behaviour is a flexible one, the force will be different in each shear connector depending on the occurring slip. The compression force in the concrete deck will be then the sum of the shear connector forces. Consequently, it is necessary to know the value of the occurring slip at each shear connector along the length at the load level where the plastic moment resistance is reached. The slip originates from the relative strain difference between the bottom fibre of the concrete deck and the top fibre of the steel beam. For a simply supported beam with flexible shear connectors and linear load-slip curve, it is usually assumed that the slip distribution along the length follows the shape of the integral of the moment diagram as long as the beam is in elastic state [83]. As a simplification, some researchers [43], [44] assume a cosine shaped slip distribution along the length. Theoretically, this would correspond to a sinusoidal moment diagram but it is also a reasonable approximation for uniformly loaded beams with a second order moment diagram.

Beyond the elastic limit ($M_E > M_{el,R}$), further elastic deformations occur and plastic strains start to develop. A plastic zone starts to form at the location of the maximum bending moment.

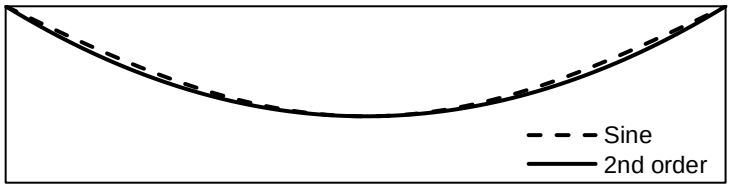

Figure 9.2 Comparison of a sinusoidal curve and a second order parabola

This is not limited to a discrete section but it has a certain length that includes all the sections where the acting moment is higher than the elastic moment resistance (c.f. Figure 9.1). This part of the beam will be referred to as the "plastic zone". The sections outside this region remain in elastic state. The slip due to plastic deformation is constant in the elastic part of the beam [52]. The total slip can be determined as the sum of the slips due to elastic and plastic deformations (see Figure 9.3). In the figure below, the slip distribution curve is schematic but not in scale.

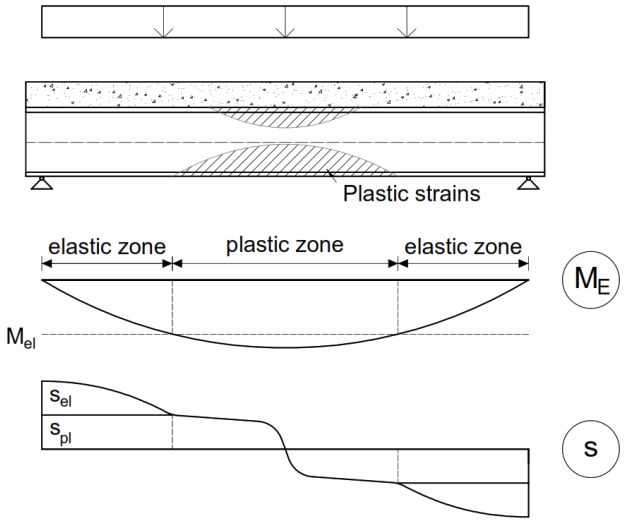

Figure 9.3 Slips due to elastic and plastic deformations

Nonetheless, the evaluation of the occurring slip is a complex task, as the slip due plastic deformation is difficult to quantify. It depends on several different factors, such as:

1) the length of the plastic zone,
2) the material behaviour,
3) the location of the neutral axes,
4) the loading situation,
5) the load-slip behaviour of the connectors, and
6) the number of shear connectors.

Without the use of a non-linear finite element simulation, this information is hardly obtainable.

9.4.2 New plastic calculation method for nonlinear shear connections (Method PL1)

In order to overcome the issues presented in the previous section, herein a new approach is proposed, which can be used for the determination of the plastic moment resistance of composite beams with flexible and with nonlinear shear connection.

The presented method is applicable if the following conditions and assumptions are satisfied:

(i) The beam is simply supported and subjected to a positive bending moment.
(ii) The concrete deck is placed above the steel section (i.e. downstand composite beams).
(iii) The steel section is Class 1 or 2 according to EN1993-1-1 [8].
(iv) The steel beam can be hot-rolled or fabricated.
(v) The concrete deck can be solid or with profiled decking.
(vi) The section is symmetric to the vertical axis.
(vii) The shear connection is distributed uniformly along the length.
(viii) The load-slip behaviour of the shear connection can be described with a monotonic increasing curve.
(ix) The curvature of the composite beam under failure conditions is large enough to enable the assumption of a plastic stress distribution in the cross-section.

Among the aforementioned conditions and assumptions, (ix) is difficult to quantify without the help of a numerical analysis. Nonetheless, the design method of Eurocode 4 [18] assumes that this condition is satisfied when the requirements for the minimum degree of shear connection are met.

It is important to note that the minimum degree of shear connection rules were developed based on studies on headed studs that had a slip capacity at least 6 mm. The calculation method presented here is not limited to shear connectors that have a larger slip capacity than 6 mm. However, a higher degree of shear connection is required when shear connectors with low slip capacity (< 6 mm) are applied. The exact definition of the minimum required degree of shear connection is out of the scope of this thesis; and therefore, the application of this procedure for beams with shear connectors that have a lower slip capacity than 6 mm is not recommended as long as a reliable definition for the minimum degree of shear connection is not established.

It is also important to point out that the development of this procedure was made based on simply supported beams subjected to uniformly distributed loading. The more the bending moment diagram differs from a sinusoidal shape, the less accurate this procedure will become.

If all the presented conditions are satisfied, the plastic moment resistance can be determined in the following way: First, it is necessary to assume:

1) a certain value for the end slip $\bar{s}$ when the plastic moment capacity is reached, and
2) a certain slip distribution function along the length $s(x)$.

With these assumptions, the occurring slip s_i can be estimated at each shear connector row and therefore the shear connector forces $P_{sc,i}$ can be determined with the help of their load-slip curve. The sum of these forces will be then the compression force in the concrete deck (equation (9.2)).

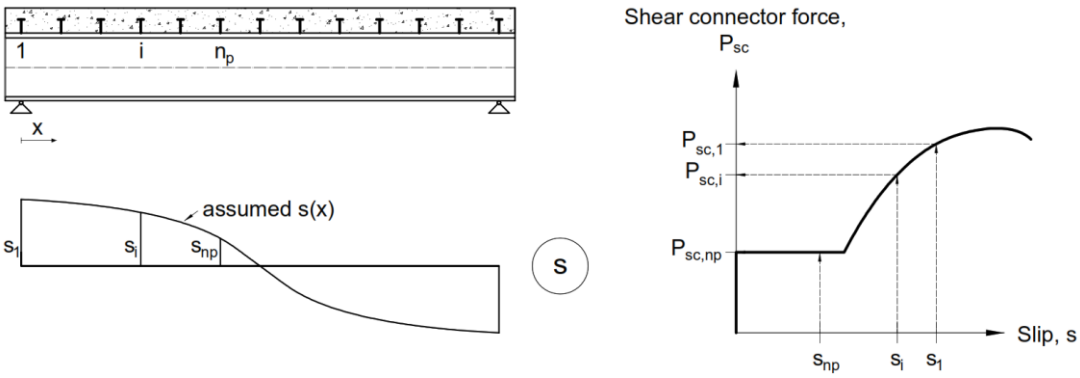

Figure 9.4 Determination of shear force from the slip distribution with the help of the load-slip curve

$$N_c = n_r \sum_{i=1}^{n_p} P_{sc,i} \tag{9.2}$$

where:

n_r is the number of shear connectors in a row, and

n_p is the number of shear connector rows placed within the critical length

Knowing the compression force N_c in the concrete, the plastic stress distribution can be determined. The moment resistance $M_{pl,\eta}$ can be calculated from the equilibrium and moment equations using the Eurocode 4 [18] approach for partial shear connection.

The presented algorithm is summarised in Figure 9.5.

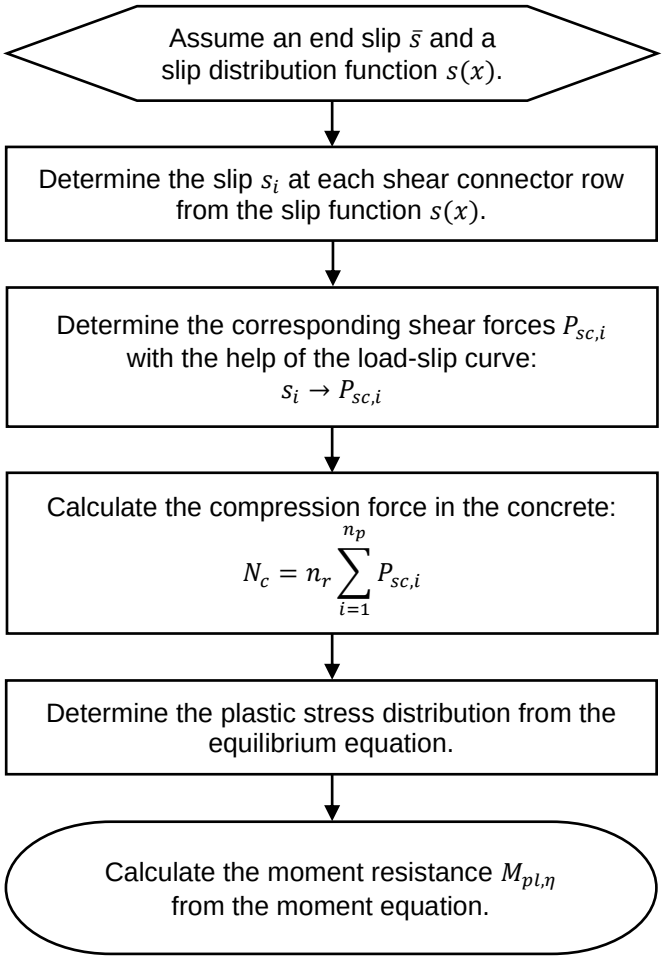

Figure 9.5 Algorithm for the determination of the plastic moment resistance of composite beams with non-ductile shear connection (Method PL1)

The accuracy of the algorithm depends on the initially assumed end slip and slip distribution function. As presented in Chapter 2.7 and 9.4.1, the approximation of the occurring end slip is complicated at the ultimate limit state. However, experimental and numerical investigations show that the following assumptions are reasonable:

(i) The end slip can be approximated by equation (9.4).

(ii) The slip distribution can be described by a cosine function (equation (9.3)) similarly to the elastic calculations [80].

$$s(x) = \bar{s} \cdot \cos\left(\frac{\pi \cdot x}{L}\right) \tag{9.3}$$

The approximation of the end-slip when the plastic moment capacity is reached is not recommended by Eggert's [58] or Johnson and Molenstra's [57] formulae, which were presented in Chapter 2.7 because they were developed for headed stud connectors. Therefore, herein a new approximation is presented based on Bärtschi's [52] proposal that was presented in section 2.7.5. However, instead of using the degree of shear connection η for the interpolation, it is now proposed to use the degree of interaction ψ.

This is based on the fact that at $\eta = 1$ we do not necessarily know the occurring end slip, while at the theoretical case of $\psi = 1$ (perfectly rigid shear connection) we know that no slip occurs. The end slip to be taken into account when determining the developing shear connector forces is:

$$\bar{s} = \min\begin{Bmatrix} \delta_u \\ s_{ult,0} \cdot (1-\psi) \end{Bmatrix} \tag{9.4}$$

where:

δ_u is the slip capacity of the shear connection;

$s_{ult,0}$ is the end slip when the moment capacity is reached in the case of no shear connection determined by equation (2.55)); amd

ψ is the degree of interaction determined by equation (9.5):

$$\psi = \frac{I_{y,eff} - \left(I_{y,a} + \frac{I_{y,c}}{n}\right)}{I_{y,rigid} - \left(I_{y,a} + \frac{I_{y,c}}{n}\right)} \tag{9.5}$$

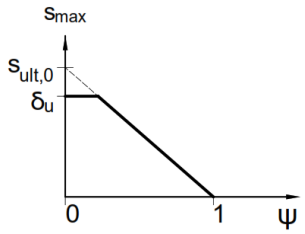

Figure 9.6 Linear interpolation of the end slip based on the degree of shear interaction

The following figure shows the comparison of the numerically and analytically determined plastic moment resistance of the same composite beam that was used for the illustration of the accuracy of the analytically determined deflections (Figure 8.2 and Figure 8.10):

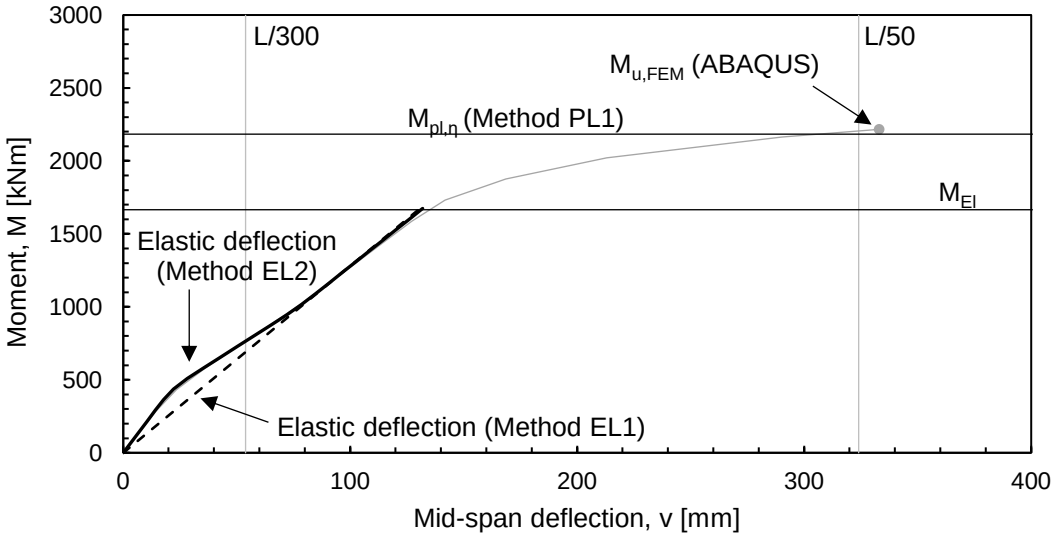

Figure 9.7 Comparison of the numerically and analytically obtained plastic moment resistance values

Using this algorithm, the plastic moment resistance $M_{pl,\eta}$ was determined for the composite beams, which were simulated in the frame of the parametric study PS-2 presented in Annex B.2. The comparison of the analytically and numerically obtained resistance $M_{u,FEM}$ values can be found in Annex D, and are presented in Figure 9.8. The resistance model uncertainty parameters were determined for each cases:

$$\theta_i = \frac{M_{u,FEM,i}}{M_{pl,\eta,i}} \tag{9.6}$$

The mean value of the model uncertainties:

$$\mu_\theta = \frac{1}{n} \cdot \sum_{i=1}^{n} \theta_i = 1.010 \tag{9.7}$$

The standard deviation:

$$\sigma_\theta = \frac{1}{n} \cdot \sum_{i=1}^{n} (\theta_i - \mu_\theta)^2 = 0.037 \tag{9.8}$$

The coefficient of variation:

$$V_\theta = \frac{\sigma_\theta}{\mu_\theta} = 0.037 \tag{9.9}$$

These values indicate that the developed calculation method is in a good agreement with the numerical simulations.

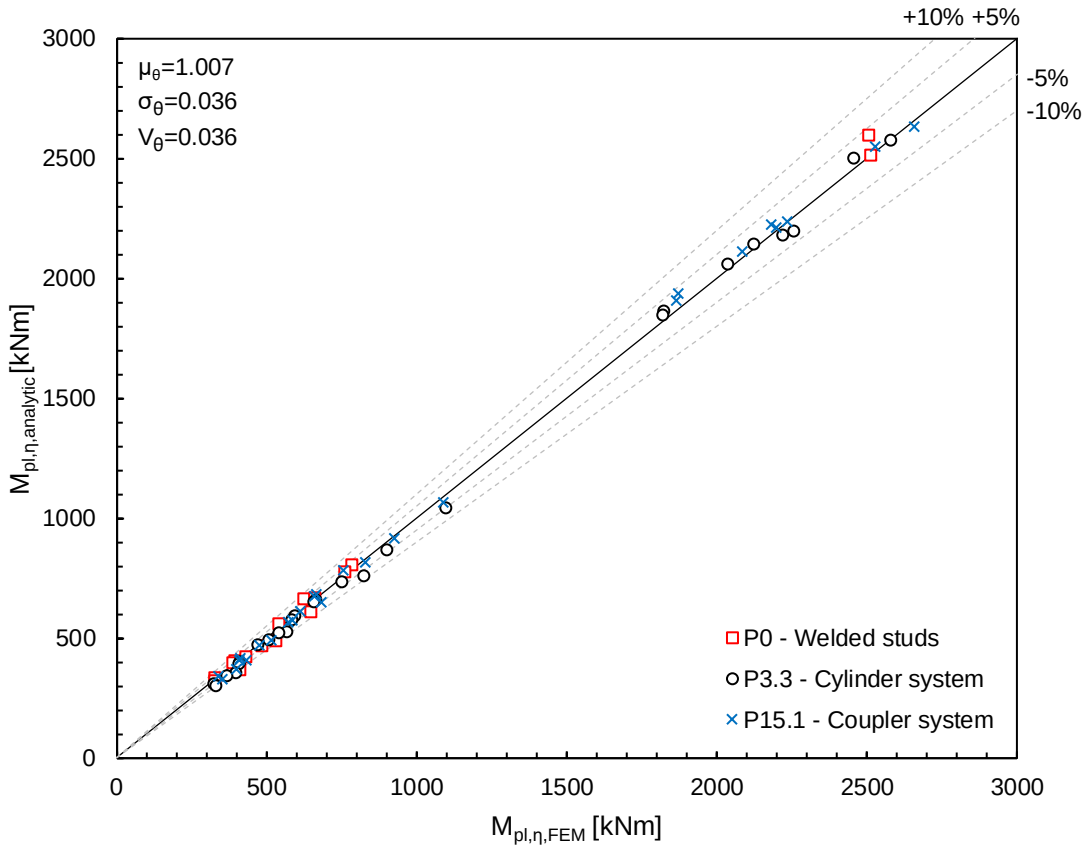

Figure 9.8 Comparison of the analytically and numerically obtained resistance values

An example of the practical application of this method is presented in Annex F.5.

9.4.3 Simplified plastic calculation method (Method PL2)

The previously presented method (Method PL1) requires the individual shear connector forces to be determined in each calculation. This chapter proposes a simplification by defining the average shear connector force as the effective shear connection resistance $P_{R,eff}$, and introducing a parameter k_{flex} that represents the ratio of $P_{R,eff}$ to the shear force in the last shear connector $\bar{P}$:

$$P_{R,eff} = \frac{\sum_{i=1}^{n_p} P_{sc,i}}{n_p} \tag{9.10}$$

$$k_{flex} = \frac{P_{R,eff}}{\bar{P}} \tag{9.11}$$

The factor k_{flex} depends on:

1) the load-slip curve of the shear connection,
2) the number of shear connector rows on the critical length,
3) the distribution of the shear connectors,
4) the assumed end slip, and
5) the slip distribution function.

The procedure presented in the previous section can be simplified if we apply the following assumptions:

(i) The end slip is exactly 6 mm when the plastic moment resistance is reached.
(ii) The slip distribution can be described by a cosine function.
(iii) The shear connectors are placed equidistantly.

With the previous assumptions, k_{flex} only depends on the number of shear connector rows n_p on the critical length and the type of the shear connection. The value of k_{flex} was calculated using the load-slip curves of the tested demountable shear connectors presented in Chapter 4 (see Figure 9.9). Shear connection type P15.2 was excluded as it did not have a 6 mm deformation capacity.

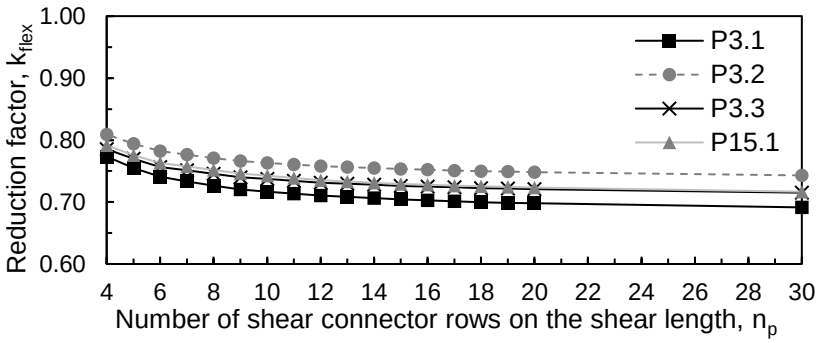

Figure 9.9 Reduction factor k_{flex} depending on the number of shear connector rows

As one can see, the more shear connector rows we have, the lower the value of k_{flex} is. However, the difference in the values of k_{flex} between 4 rows and 30 rows is relatively small. For the tested shear connections, its value varies between 0.69 to 0.81.

As a simplification, it is proposed to use the number that corresponds to $n_p = 6$. This means, that when determining the average shear connector force P_{Reff} we assume that only six pairs of shear connectors are placed on the critical length. The advantage of this simplification is that k_{flex} now only depends on the load-slip curve, i.e. it became a shear connection specific parameter. For shear connection type P3.3 its value is $k_{flex} = 0.756$, and for P15.1 it is $k_{flex} = 0.762$. Once this parameter is known, the algorithm presented in Figure 9.5 becomes simpler. The effective shear connector resistance can be determined as:

$$P_{R,eff} = k_{flex} \cdot P_{R,6} \tag{9.12}$$

where $P_{R,6}$ is the shear connector resistance at 6 mm slip. The compression force N_c in the concrete can be calculated by multiplying the number of shear connectors on the critical length by the effective shear connector resistance (c.f. Equation (2.35))

$$N_c = n \cdot P_{R,eff} \leq N_{c,f} \tag{9.13}$$

After this point, the calculation procedure is analogous to the Eurocode 4 [18] method for the determination of the plastic moment resistance of sections with partial shear connection (see Chapter 2.3.2). The plastic stress distribution and the location of the neutral axes can be determined from the equilibrium equations; and the moment resistance $M_{pl,\eta}$ from the moment equation. The flowchart of the simplified calculation method is presented in Figure 9.11.

The following figure shows the comparison of the analytically and numerically obtained results of the beam that was used for the previous comparisons presented in Figure 8.2, Figure 8.10 and Figure 9.7:

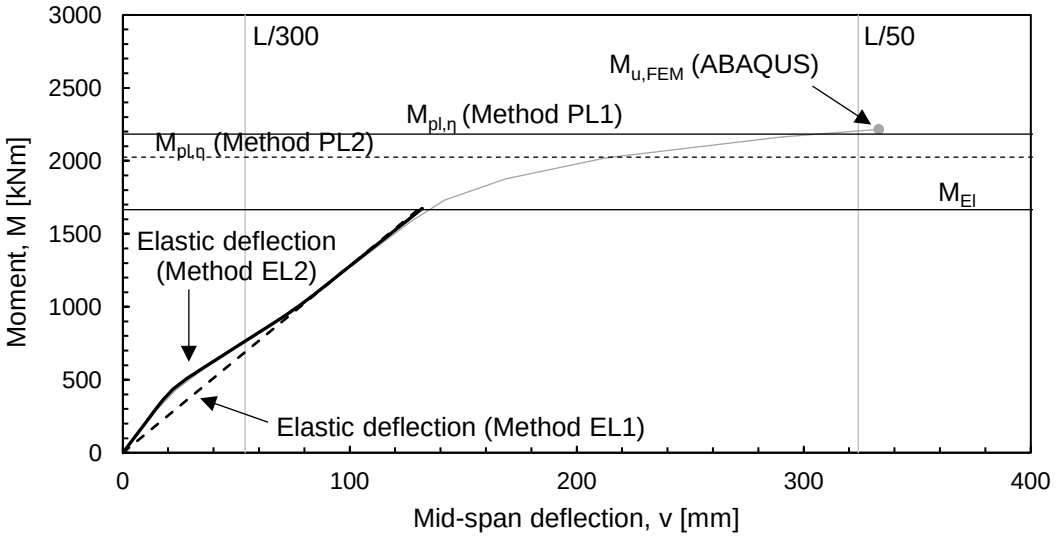

Figure 9.10 Comparison of the numerically and analytically obtained plastic moment resistance values

Similarly to Section 9.4.2, the calculated moment resistance values were compared to the numerically obtained ones (Annex E). The corresponding statistical parameters are summarised in the following table, and the comparison of the experimentally and numerically obtained resistance values is presented in Figure 9.12.

Table 9.1 Statistical parameters of the model uncertainties

Parameter	Notation	Value
Mean value	μ_θ	1.052
Standard deviation	σ_θ	0.063
Coefficient of variaton	V_θ	0.060

Although the simplified method (Method PL2) produces more conservative results than the method presented in the previous section (Method PL1), it was concluded that the simplified calculation method is applicable for the determination of the plastic moment resistance of composite beams with demountable shear connection. An example of the practical application of this method is presented in Annex F.6.

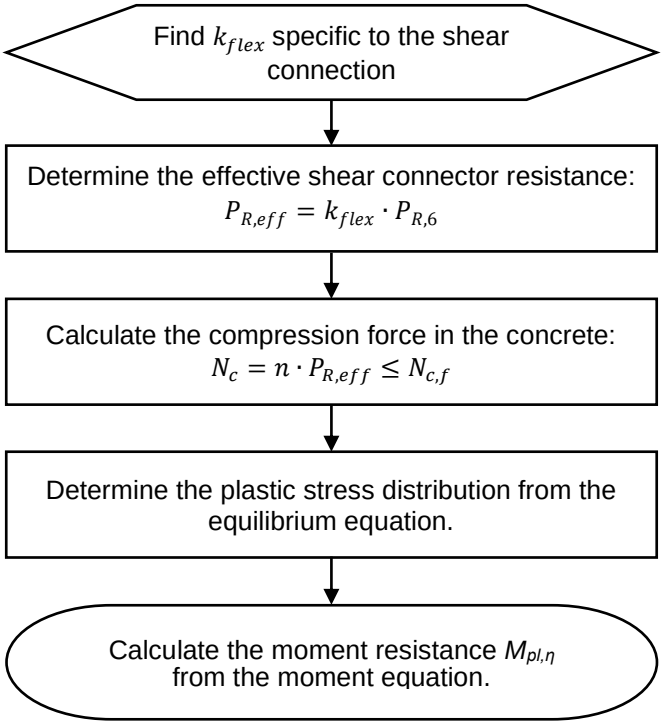

Figure 9.11 Simplified algorithm for the determination of the plastic moment resistance of composite beams with non-ductile shear connection (Method PL-2)

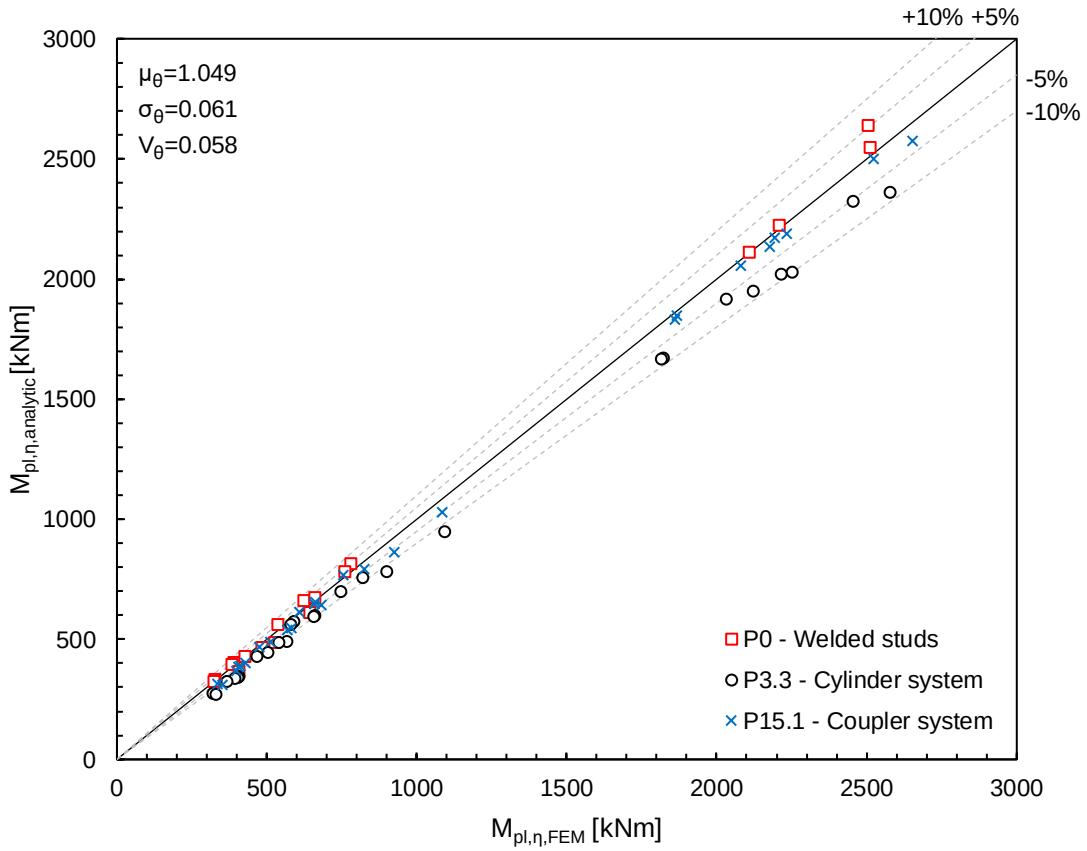

Figure 9.12 Comparison of the analytically and numerically obtained resistance values

9.5 Summary

In this chapter reviewed the calculation methods for the plastic moment resistance of composite beams with partial shear connection. This was done for different types of shear connection (rigid-ductile, rigid-brittle and flexible). For beams with flexible or non-linear shear connections a new calculation method and its simplified version were proposed in Chapter 9.4.2 and Chapter 9.4.3, respectively. It was shown, that the proposed calculation methods could reproduce the numerically obtained moment resistance values with a high accuracy within the range of the tested parameters.

The application of these methods are limited to the cases where all of the following conditions are fulfilled:

(i) The beam is simply supported and subjected to a positive bending moment.
(ii) The concrete deck is placed above the steel section (i.e. downstand composite beams).
(iii) The steel section is Class 1 or 2 according to EN1993-1-1 [8].
(iv) The steel beam can be hot-rolled or fabricated.
(v) The concrete deck can be solid or with profiled decking.
(vi) The section is symmetric to the vertical axis.
(vii) The shear connection is distributed uniformly along the length.

(viii) The load-slip behaviour of the shear connection can be described with a monotonic increasing curve.

(ix) The curvature of the composite beam under failure conditions is large enough to enable the assumption of a plastic stress distribution in the cross-section.

Among the aforementioned conditions (ix) is difficult to quantify, so at this point, it is recommended to limit the application of the presented methods to cases where the minimum degree of shear connection requirement of Eurocode 4 [18] is satisfied and the shear connection has a slip capacity that exceeds 6 mm. Further development is needed for the quantification of the minimum degree of shear connection requirements for different types of shear connections to ensure that the assumed plastic stress distribution can develop in the cross-section.

The development of the presented methods based on uniformly loaded beams and it assumed a cosine slip distribution function. It is important to point out that different loading situations will result in different slip distribution functions. The more the slip distribution differs from a cosine shape the less accurate the presented methods will become. Nonetheless, the methods can be applied with different slip distribution functions based on the same principles as presented in this chapter. Further research is required to find slip distribution functions for different loading situations that can represent the real behaviour more accurately.

The presented methods are based on the assumption that the greatest slip occurs at the end of the beam. This was supported by the parametric studies conducted on uniformly loaded beams (see Chapter 7.6). However, it is possible that such cases exist where this assumption is not valid anymore due to the increased slips at the plastic zone of the beam (Figure 9.13). The exact identification of these cases are recommended to be the subject of further research.

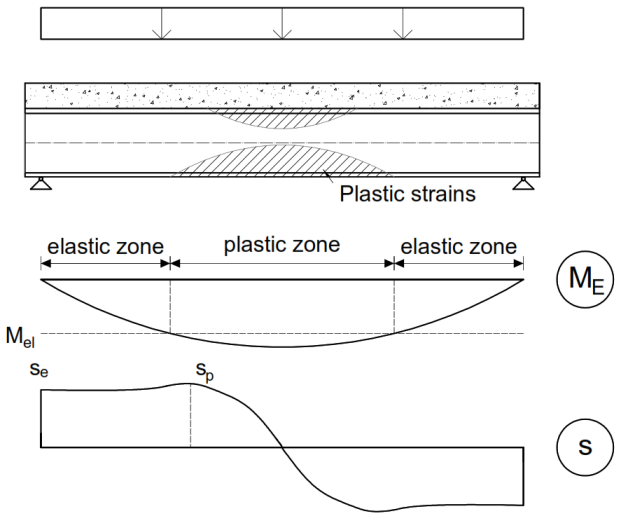

Figure 9.13 A slip distribution where the slip at the edge of the plastic zone exceeds the end slip

Chapter 10. Conclusions and outlook

10.1 General

The work carried out throughout the thesis focused on the behaviour of demountable composite beams in order to facilitate the integration of steel-concrete composite construction into the concept of circular economy. There are several hindrances in the way of reuse when considering traditional composite structures. One of them is the method the current construction practice applies for connecting the concrete deck to the steel beam. The traditionally applied welded studs are advantageous in the terms of structural performance; however, they do not provide the ability of dismounting. In order to overcome this issue, different types of shear connection types were investigated that use bolted connections. The structural solutions were investigated using experimental structural testing; and the laboratory experiments were complemented by numerical simulations. The experimental research included push-out tests for the assessment of the shear connection behaviour; and full scale beam tests for the evaluation of the structural performance of demountable composite beams. The investigation showed that the behaviour of demountable composite beams differs from the behaviour of the non-demountable traditional solution. Analytical equations were derived for the description of the elastic behaviour and a new calculation method was proposed for the determination of the plastic moment resistance of composite beams with demountable shear connection. This chapter presents the main conclusions that were drawn based on the conducted research.

10.2 Demountable shear connections and composite beams

The tested demountable shear connections behaved differently than welded studs. They did not show a ductile behaviour; and their load-slip curve could not be described by an ideal rigid-plastic curve but a rather linear elastic one. The more accurate description is a multilinear curve that has three distinct parts (see Figure 4.24):

1) an almost vertical, rigid part until the friction resistance is overcome,
2) an almost horizontal part, which shows the bolt slippage in the bolt hole, and
3) a nonlinear part, which represents the shear and bearing deformation before the failure occurs.

The four parameters that have the highest influence on the load-slip behaviour are the bolt shear resistance, the level of pretension, the surface treatment (i.e. the friction coefficient) and the diameter of the bolt hole.

The failure occurred due to the shearing of the bolt in all of the conducted push-out tests. The failure of the concrete was prevented by the large bearing surfaces of the tested connectors. The demountable shear connections produced in all cases similar or higher resistance values than welded studs, but the corresponding stiffness values were significantly lower. The observed slip capacities were generally between 6 mm and 12 mm.

Demountable composite beams behave similarly to traditional non-demountable beams with welded stud connectors. The tested demountable composite beams produced higher resistance values than a comparable composite beam with welded studs tested in a preceding research project called DISCCO [65]. However, the reduced stiffness of the shear connection resulted in a lower bending stiffness. Furthermore, the nonlinear behaviour of the shear connection caused a nonlinear load-deflection response already in the elastic phase.

10.3 Elastic behaviour of demountable composite beams

The elastic response of demountable composite beams can be calculated by using the cross-sectional properties of a homogenised section. For the calculation of the elastic normal stresses from bending, or for the calculation of the elastic moment resistance M_{el}, the location of the elastic neutral axis needs to be known. When non-rigid shear connection is applied, the concrete and steel members have their own elastic neutral axes.

Analytical equations were derived for the calculation of the effective second moment of area, and for the determination of the location of the neutral axes of the composite beams with flexible (Chapter 8.4) and with nonlinear shear connections (Chapter 8.5).

An iterative procedure was developed (Chapter 8.5) for the calculation of the elastic deflections of composite beams with nonlinear shear connection. With the developed iterative method, the elastic deflections can be determined with a similar accuracy by using spreadsheet calculations as by using nonlinear finite element simulations.

10.3.1 Beams with flexible shear connection

The second moment of area of composite beams with flexible shear connection can be determined using equation (8.20). According to EN1994-1-1 [18] the stiffness of the shear connection may be taken as $k_{sc} = 0.7\ P_{Rk}\ /\ s$ (see equation (8.34)). This is a reasonable approximation for welded stud connectors as well as for demountable shear connectors.

The location of the elastic neutral axes can be determined by equations (8.32) and (8.33).

10.3.2 Beams with nonlinear shear connection

Demountable shear connections can be more accurately described by multilinear load-slip curves. Then, the shear connectors can be taken into account with their secant stiffness values in the calculations. The secant stiffness $k_{sc,i}$ of each connector depends on the occurring slip, which depends on the load level. This results in different second moment of area values $I_{y,eff,m}$ along the length, which also depend on the load level. An analytical equation was derived for the determination of the second moment of area at every shear connector along the length. At shear connector m, $I_{y,eff,m}$ can be determined by equation (8.39):

$$I_{y,eff,m} = I_{y,a} + \frac{I_{y,c}}{n} + \frac{a^2}{\frac{\pi}{L} \cdot \frac{E_a \sin\left(\frac{m\pi}{2n_p}\right)}{\sum_{i=1}^{m} \frac{k_{sc,i}}{s_{sc,eq}} \frac{L}{\pi} \cdot \left[\sin\left(\frac{i\pi}{2n_p}\right) - \sin\left(\frac{(i-1)\pi}{2n_p}\right)\right]} + \left(\frac{A_c + nA_a}{A_c A_a}\right)}$$

An analytical equation was derived to describe the relationship between the end slip $\bar{s}$ and the bending moment at mid-span $\bar{M}$ (equation (8.41)). For this equation, it is necessary to know the different shear connector stiffness values $k_{sc,i}$, which depend on the end slip. This means, that end slip and the stiffness of the shear connectors are interdependent. The solution for this problem is an iterative procedure that was presented in Chapter 8.5.1.

The occurring deflection can be calculated as the double integral of the curvature function, but due to the different $I_{y,eff,m}$ values along the length, the curvature function is not continuous. Therefore, the deflection at midspan can be calculated as the sum of the integral of the parts where the curvature function is continuous (equation (8.43)). The integral was solved for basic load cases such as: one-point load at mid-span, symmetric two-point loads, a uniformly distributed load and a sinusoidal load. The formulations are presented in Chapter 8.5.2. The location of the elastic neutral axes can be determined by equations (8.52) and (8.53).

10.4 Plastic moment resistance

10.4.1 General

The general behaviour of the tested shear connections is significantly different than the behaviour of welded studs. As a result, the basic assumptions of Eurocode 4 [18] for the determination of the plastic moment resistance of composite beams with partial shear connection are not valid anymore. The code therefore does not enable the use of equidistant shear connector spacing and the design needs to be conducted using a fully elastic analysis. This would the make the use of demountable shear connections complicated and uneconomic. In the face of these issues, the probability of the practical application of demountable and reusable composite structures would be very low. On the other hand, experiments (Chapter 5) and numerical simulations (Chapter 6 and Chapter 7) show that composite beams can develop plasticity even if non-ductile shear connection is applied. In order to overcome these issues, a new calculation method was developed that enables the extension of the code for demountable shear connection. In this way, the benefits of composite construction can be maintained while providing the possibility of reuse.

10.4.2 New calculation method for the plastic moment resistance (Method PL1)

A calculation method was developed (Chapter 9.4.2) that enables the calculation of the developing compression force in the concrete based on the individual shear connector forces. These forces depend on the load-slip behaviour, the number of shear connectors and the distribution of the shear connectors. The method requires assumptions for the shape of the slip function and the value of the occurring end

slip. The slip function can be approximated with a cosine function Equation (9.3)), and the occurring end slip can be estimated based on the degree of interaction Equation (9.4)). It was shown (Figure 9.8) that the plastic moment resistance $M_{pl,\eta}$ can be determined with a high accuracy using the previous assumptions.

10.4.3 Simplified calculation method for demountable composite beams (Method PL2)

Based on the developed calculation method a simplified method was proposed (Chapter 9.4.3) by defining an effective shear resistance $P_{R,eff}$ for the investigated shear connections. Once $P_{R,eff}$ is known, the calculation method is analogous to the current Eurocode 4 [18] design procedure. It was shown (Figure 9.12), that the simplified method is also able to produce plastic moment resistance $M_{pl,\eta}$ values with acceptable accuracy.

10.5 Further research

10.5.1 Further parametric studies and beam tests

The presented calculation method for the calculation of the plastic moment resistance of composite beams was evaluated based on a comparison against a certain set of numerical simulations with a certain set of parameters. Strictly speaking, the scope of its application is limited to cases which fall into the range of the investigated parameters. Further research is required for the extension of the scope of application by conducting additional parametric studies and laboratory experiments on full-scale composite beams.

10.5.2 End slip calculation

The method uses an approximation of the occurring end slip that can be taken into account during the calculations. The proposed approximation uses a linear interpolation according to the degree of interaction. One limit of the interpolation is where there is no shear connection (i.e. the degree of interaction is $\psi = 0$). At this point the occurring end slip is given by an approximation proposed by Baertschi [52]. Within the range of the conducted simulations this approximation gives reasonable results; however generally, the estimation of the end slip after the section is beyond its elastic limit still remains relatively uncertain; and therefore, this topic requires further investigation.

10.5.3 Minimum degree of shear connection

The numerical simulations showed that the investigated demountable composite beams could develop plasticity, and they could reach $M_{pl,\eta}$ even if their degree of shear connection was below the minimum required by the Eurocode 4 [18]. This shows that the minimum degree of shear connection rules may need to be redefined for demountable shear connections.

It is possible to use the developed calculation method for shear connections that have a lower slip capacity than 6 mm, but further development is needed for the quantification of the minimum degree of

shear connection requirements for different types of shear connections to ensure that the assumed plastic stress distribution can develop in the cross-section.

In the meantime, it is possible to design demountable composite beams using the developed numerical model presented in Chapter 6.3.

10.5.4 Slip functions for different loading situation

The assumed cosine function for the description of the slip distribution works well for uniformly loaded simply supported beams. However, the loading situation can have a significant influence on its shape. Further research is required to identify the scope of applicability of the cosine function beyond the uniformly loaded beams; and other slip functions may need to be found for the description of the slip distribution due to different loading situations.

10.5.5 Further parametric studies on shear connections

The developed numerical model presented in Chapter 6.2 allows to extend the research with further parametric studies by creating new load-slip curves that can be implemented in the shell model of the beams. The presented methods are based on the assumption that the greatest slip occurs at the end of the beam. This was supported by the parametric studies conducted on uniformly loaded beams (see Chapter 7.6). However, it is possible that such cases exist where this assumption is not valid anymore due to the increased slips at the plastic zone of the beam (Figure 9.13). The exact identification of these cases are recommended to be the subject of further research.

Acknowledgements

The research leading to these results is a part of a common project of Steel Construction Institute, University of Luxembourg, University of Bradford, Lindab, Tata Steel, Bouwen met Staal, Delft University of Technology and AEC3. The project has received funding from the Research Fund for Coal and Steel under grant agreement No 710040.

The numerical simulations presented in this thesis were carried out using the HPC facilities of the University of Luxembourg, https://hpc.uni.lu.

List of papers related to the thesis

Within the frame of the thesis, the following publications were made until the day of publication of the thesis:

1. A. Kozma, C. Odenbreit, M. V. Braun, M. Veljkovic and M. Nijgh, “Push-out tests on demountable shear connectors of steel-concrete composite structures,” in *Proceedings of the 12th International Conference on Advances in Steel-Concrete Composite Structures*, Valencia, 2018.
2. C. Odenbreit and A. Kozma, “Dismountable flooring systems for multiple use, ”*SBE19 Brussels, BAMB-CIRCPAPATCH, IOP Conf.Series: Earth and Environmental Science 225* (2019) 012028, doi:10.1088/1755-1315/225/1/012028, 2019.
3. A. Kozma, C. Odenbreit, M. V. Braun, M. Veljkovic and M. Nijgh, “Push-out tests on demountable shear connectors of steel-concrete composite structures,” *Structures*, vol. 21, pp. 45-54; https://doi.org/10.1016/j.istruc.2019.05.011, October 2019.
4. C. Odenbreit, A. Kozma and M.V. Braun, “Characterisation Of Demountable Shear Connector Systems In Composite Beams,” in *Proceedings of the 9th International Conference on Steel and Aluminium Structures*, 2019, Bradford, UK
5. C. Odenreit and A. Kozma, “Parametric study on non-ductile demountable shear connectors,” in *Proceedings of the 14th Nordic Steel Construcion Conference, September 18-20, 2019, ,* Copenhagen, Denmark, 2019.
6. European Commission, Directorate-General for Research and Innovation., “Reuse and demountability using steel structures and the circular economy (REDUCE) Final report, Project No. 710040,,” Brussels, 2020

The following paper was accepted for publication:

7. C. Odenbreit and A. Kozma; Demountable and reusable construction system for steel-concrete composite structures, *The Seventh International Symposium on Life-Cycle Civil Engineering*, October 27-30, 2020, Shanghai

References

[1] M. F. Ashby, D. F. Balas and J. S. Coral, Materials and sustainable development, Oxford: Butterworth-Heinemann, 2016, pp. 211-241.

[2] P. Crowther, “Design for disassembly - themes and principles,” *RAIA/BDP Environment Design Guide*, 2005.

[3] B. Burgan and M. Sansom, “Sustainable steel construction,” *Journal of constructional stell research*, November 2006.

[4] M. Ghyoot, L. Devlieger, L. Billiet and A. Warnier, Déconstruction et réemploi, Comment faire circuler les éléments de construction, Bruxelles: Presses polytechniques universitaires romandes (PPUR), ISBN 978-2289152391, 2018.

[5] International Energy Agency (IEA), Global Alliance for Building and Construction, 2018 Global Status Report, United Nations, ISBN 978-92-807-3729-5, 2018.

[6] L. Jaillon and C. S. Poon, “Life cycle design and prefabrication in buildings: A review and case studies in Hong Kong,” *Automation in construction*, vol. 39, pp. 195-202, 2014.

[7] World Steel Assosiation, Steel in the circular economy - A life cycle perspective, World Steel Assosiation, ISBN 978-2-930096-80-7, 2015.

[8] EN1993-1-1, Eurocode 3: Design of steel structures - Part 1-1: General rules and rules for buildings, 2005.

[9] L. N. Dallam, “High Strength Bolt Shear Connectors - Pushout Tests,” *ACI Journal*, pp. 767-769, 1968.

[10] W. Marshall, H. Nelson and H. K. Banerjee, “An experimental study of the use of high strength friction-grip bolts as shear connectors in composite beams,” *The Structural Engineer*, vol. 49, no. 4, pp. 171-178, 1971.

[11] D. Dedic and F. Klaiber, “High-strength bolts as shear connectors in rehabilitation work,” *Concrete International*, vol. 6, no. 7, pp. 41-46, 1984.

[12] G. Sedlacek, B. Hoffmeister, H. Trumpf, B. Kühn, J. Stötzel, O. Hechler, H. Stangenberg, D. Bitar and Y. Galéa, “Composite bridge design for small and medium spans. Final Report,” European Commission - Technical Steel Resarch, Contract No 7210-PR/0113, Luxembourg, 2003.

[13] B. A. Schaap, Methods to develop composite action in non-composite bridge floor systems, MSc thesis, Austin, Texas, 2004.

[14] G. Kwon, B. Hungerford, H. Kayir, B. Schaap, Y. K. Ju, R. Klingner and M. Engelhardt, "Strengthening existing non-composite steel bridge girders using post-installed shear connectors," Center for Transportation Research, The University of Texas at Austin, Austin, 2007.

[15] G. Kwon, M. D. Engelhardt and R. E. Klingner, "Behavior of post-installed shear connectors under static and fatigue loading," *Journal of Constructional Steel Research,* vol. 66, no. 4, pp. 532-541, 2010.

[16] M. Pavlović, Resistance of Bolted Shear Connectors in prefabricated steel-concrete composite decks. PhD thesis, Belgrade: University of Belgrade, 2013.

[17] M. Moynihan and J. Allwood, "Viability and performance of demountable composite connectors," *Journal of Constructional Steel Research,* vol. 99, pp. 47-56, 2014.

[18] EN1994-1-1, *Eurocode 4: Design of composite steel and concrete structures - Part 1-1: General rules and rules for buildings,* 2004.

[19] D. Lam and X. Dai, "Demountable shear connectors for sustainable composite construction," in *Advances in Structural Engineering and Mechanics (ASEM13)*, Jeju, 2013.

[20] X. H. Dai, D. Lam and E. Saveri, "Effect of concrete strength and stud collar size to shear capacity of demountable shear connectors," *Journal of Structural Engineering,* vol. 141, no. 11, 2015.

[21] N. Rehman, D. Lam, X. Dai and A. F. Ashour, "Experimental study on demountable shear connectors in composite slabs with profiled decking," *Journal of Constructional Steel Research,* pp. 178-189, 2016.

[22] J. Wang, J. Guo, L. Jia, S. Chen and Y. Dong, "Push-out tests of demountable headed stud shear connectors in steel- UHPC composite structures," *Composite Structures,* vol. 170, pp. 69-79, 2017.

[23] K. Roik and K. E. Bürkner, "Reibwert zwischen Stahlgurter und aufgespannten Betonfertigteilen," *Der Bauingenieur,* vol. 53, pp. 37-41, 1978.

[24] J. Becker, Beitrag zur Auslegung der Verdübelung von Verbundträgern des Hochbaus unter ruhender und nichtruhender Belastung, Fachgebiet Stahlbau, Kiaserslautern: University of Kaiserslautern, 1997.

[25] A. Thiele, Verbundträger im Hochbau, In: Stahlhochbau., Vieweg+Teubner Verlag, 1986.

[26] Y. T. Chen, Y. Zhao, J. S. West and S. Wallbridge, "Behaviour of steel – precast composite girders with through-bolt shear connectors under static loading," *Journal of Constructional Steel Research,* vol. 103, pp. 168-178, 2014.

[27] S. Lee and M. Bradford, "Sustainable composite beams with deconstructable bolted shear connectors," in *Research and Applications in Structural Engineering, Mechanics and Computation (ASEM13)*, Jeju, 2013.

[28] A. Ataei, M. A. Bradford and X. Liu, "Sustainable Composite Beams and Joints With Deconstructable Bolted Shear," in *23rd Australasian Conference on the Mechanics of Structures and Materials (ACMSM23)*, Byron Bay, 2014.

[29] A. Ataei, M. A. Bradford, R. H. Valipour and X. Liu, "Experimental study of sustainable high strength steel flush end plate beam-to-column composite joints with deconstructable bolted shear connectors," *Engineering structures,* vol. 123, pp. 124-140, September 2016.

[30] X. Liu, M. A. Bradford, Q.-J. Chen and H. Ban, "Finite element modelling of steel-concrete composite beams with high-strength friction-grip bolt shear connectors," *Finite elements in analysis and design,* vol. 108, pp. 54-65, 2016.

[31] X. Liu, M. A. Bradford and A. Ataei, "Flexural performance of innovative sustainable composite steel-concrete beams," *Engineering Structures,* vol. 130, pp. 282-296, 2017.

[32] *SIMULIA User Assistance*, "Abaqus, © Dassault Systèmes Simulia," Abaqus Corp. All rights Reserv. Provid. RI, USA, 2017.

[33] A. A. Bagon, "A new type of urban brdige, prefabricated and demountable," in *Demountable concrete structures, a challange for precast concrete, Proceedings of the international symposium*, H. W. Reinhardt and J. J. Bouvy, Eds., Rotterdam, The Netherlands, Delft University Press, 1985, pp. 293-305.

[34] H. Ban, B. Uy, S. W. Pathirana, I. Henderson, O. Mirza and X. Zhu, "Time-dependent behaviour of composite beams with blind bolts under sustained loads," *Journal of Constructional Steel Research,* vol. 112, pp. 196-207, 2015.

[35] S. W. Pathirana, B. Uy, O. Mirza and X. Zhu, "Flexural behaviour of composite steel-concrete beams utilising blind bolt shear connectors," *Engineering Structures,* vol. 114, pp. 181-194, 2016.

[36] B. Uy, V. Patel, D. Li and F. Aslani, “Behaviour and Design of Connections for Demountable Steel and Composite Structures,” *Structures,* vol. 9, pp. 1-12, 2017.

[37] A. S. H. Suwaed and T. L. Karavasilis, “Experimental evaluation of a novel demountable shear connector for accelerated repair or replacement of precast steel-concrete composite bridges,” in *EUROSTEEL 2017,* Copenhagen, 2017.

[38] E. Feidaki and G. Vasdravellis, “Horizontal push out tests on a steel-yielding demountable shear connector,” in *Proceedings of the 12th International Conference on Advances in Steel-Concrete Composite Structures,* Valencia, 2018.

[39] EN 1090-2, *Execution of steel structures and aluminium structures - Part 2: Technical requirements for steel structures,* 2008.

[40] BS 5400-5: 1979, British Standard, Steel concrete and composite bridges - Part 5: Code of practice for design of composite bridges.

[41] A. Hoischen, “Verbundträger mit elastischer und unterbrochener Verdübelung,” *Der Bauingenieur,* vol. 29, no. 7, pp. 214-244, 1954.

[42] D. Zhou, M. Pahn és W. Kurz, „Beitrag zur Berechnung von Verbundträgern mit elastischem Verbund - Genaue Methode und ein Näherungsverfahren,” *Stahlbau,* %1. kötet83, %1. szám4, pp. 278-288, 2014.

[43] G. Hanswille and M. Schäfer, “Simplified method for the determination of the infulence of flexibility of shear connection on deflections of composite beams and slim-floor systems (in German),” *Stahlbau,* vol. 76, no. 11, pp. 845-854, November 2007.

[44] R. M. Lawson, D. Lam, S. Nellinger and E. S. Aggelopoulos, “Serviceability performance of steel-concrete composite beams,” *Proceedings of the Institution of Civil Engineers - Structures and Buildings,* pp. 98-114, 2017.

[45] K. E. Bürkner, Elasto-plastische berechnung von nachgiebig verduebelten verbundtragwerken. Finite-Element-berechnungen und versuche, Bochum: Institut für Konstruktiven Ingenieurbau Ruhr-Universität Bochum, 1981.

[46] W. Kurz, M. Kludka, R. Friedland és P.-L. Geiß, Adhesive as a Permanent Shear Connection for Composite Beams, Chapter C.3, Wiley-VCH Verlag GmbH & Co. KGaA, 2018.

[47] R. P. Johnson, Designers' Guide to Eurocode 4: Design of Composite Steel and Concrete Structures EN1994-1-1, 2 ed., Croydon: CPI Group (UK) Ltd, 2012.

[48] EN1990, “Eurocode - Basis of structuraldesign,” 2002.

[49] EN1992-1-1, “Eurocode 2: Design of concretestructures - Part 1-1: General rules and rules for buildings,” 2004.

[50] SC4.T3, EN1994-1-1, Annex B2, Background document, 2018.

[51] R. Sause and L. A. Fahnestock, “Strength and ductility of HPS-100W I-girders in negative flexure,” *Journal of Bridge Engineering,* pp. 318-323, September/October 2001.

[52] R. Bärtschi, Load-bearing behaviour of composite beams in low degrees of partial shear connection. PhD Thesis, Zürich: ETH Zürich Research Collection, 2005.

[53] A. G. Romero, Numerical parametric study on minimum degree of shear connection in steel-concrete composite beams, MSc Thesis, Luxembourg: University of Luxembourg, 2019.

[54] CEN-TC250-SC4.T3, Development of design procedures for shear connectors used with modern forms of profiled sheeting, EN1994-1-1, 6.6.1.1, Minimum degree of shear connection, Final draft, 2018.

[55] D. J. Oehlers and M. A. Bradford, Composite steel and concrete structural members, Fundamental behaviour, Oxford: Elsevier Science Ltd, 1995.

[56] J. M. Aribert, “Analyse et formulation pratique de l'influence de la nuance de l'acier du profilé sur le degré minimum de connexion partielle d'une poutre mixte,” *Construction Métallique,* vol. 3, pp. 39-55, 1997.

[57] R. P. Johnson and N. Molenstra, “Partial shear connection in composite beams for buildings,” *Proceedings of the Instituion of Civil Engineers , Part 2,* vol. 91, pp. 679-704, 1991.

[58] F. Eggert, Einfluss der Verdübelung auf das Trag- und Verformungsverhalten von Verbundträgern mit und ohne Profilblech, PhD Thesis, Stuttgart: University of Stuttgart, 2018.

[59] Wegertseder, “Schrauben-lexikon.de,” Wegertseder GmbH, 2019. [Online]. Available: https://www.schrauben-lexikon.de/norm/DIN_6334.asp.

[60] F. Yang, Y. Liu, Z. Jiang and H. Xin, “Shear performance of a novel demountable steel-concrete bolted connector under static push-out tests,” *Engineering Structures,* vol. 160, pp. 133-146, 2018.

[61] A. Kozma, C. Odenbreit, M. V. Braun, M. Veljkovic and M. Nijgh, “Push-out tests on demountable shear connectors of steel-concrete composite structures,” in *Proceedings of the*

12th International Conference on Advances in Steel-Concrete Composite Structures, Valencia, 2018.

[62] A. Kozma, C. Odenbreit, M. V. Braun, M. Veljkovic and M. Nijgh, "Push-out tests on demountable shear connectors of steel-concrete composite structures," *Structures*, vol. 21, pp. 45-54; https://doi.org/10.1016/j.istruc.2019.05.011, October 2019.

[63] Tata Steel UK Limited, "ComFlor® manual," www.tatasteelconstruction.com, London, 2017.

[64] S. Nellinger, On the behaviour of shear stud connections in composite beams with deep decking, PhD Dissertation, Luxembourg: University of Luxembourg, 2015.

[65] European Commission, Directorate-General for Research and Innovation, "Development of improved shear connection rules in composite beams (DISCCO), Final Report, Project No. RFCS-CT-2012-00030," Brussels, 2017.

[66] EN1993-1-8, *Eurocode 3: Design of steelstructures - Part 1-8: Design of joints*, 2005.

[67] European Commission, Directorate-General for Research and Innovation., "Reuse and demountability using steel structures and the circular economy (REDUCE), Final report, Project No. 710040,," Brussels, 2020.

[68] D. J. Oehlers and M. A. Bradford, Elementary behaviour of composite steel & concrete structural members, Oxford: Butterworth-Heinemann, 1999.

[69] C. Odenbreit and A. Kozma, "Dismountable flooring systems for multiple use," *SBE19 Brussels, BAMB-CIRCPAPATCH, IOP Conf.Series: Earth and Environmental Science 225 (2019) 012028,* doi:10.1088/1755-1315/225/1/012028, 2019.

[70] Joint Committee on Structural Safety (JCSS), Probabilistic model code, Part 3 - Material Properties, 2002, ISBN 978-3-909386-79-6.

[71] D. Lam, J. Yang, X. Dai, T. Sheehan and K. Zhou, "Development of composite floor system for a circular economy," in *Advances in Structural Engineering and Mechanics (ASEM19)*, Jeju Island, Korea, September 17-21, 2019, 2019.

[72] TurnaSure LLC, Instruction Manual for installing Preloaded (HSFG) Bolting with TurnaSure direct tension indicators CE marked EN 14399-9, Langhorne, PA 19047 U.S.A.: TurnaSure LLC., 2011.

[73] Hottinger Baldwin Messtechnik GmbH, "Strain Gauge PDF Catalog," [Online]. Available: https://www.hbm.com/en/2073/strain-gauge-pdf-catalog/.

[74] International Organization for Standardization (ISO), Metallic materials — Tensile testing — Part 1: Method of test at room temperature, 2016.

[75] M. P. Nijgh, H. Xin and M. Veljkovic, “Non-linear hybrid homogenization method for steel-reinforced resin,” *Construction and Building Materials,* vol. 182, pp. 324-333, 2018.

[76] S. Ádány, E. Dulácska, D. László, F. Sándor and H. László, Acélszerkezetek - Tervezés az Eurocode alapján, Általános eljárások, Budaörs: Business Media Magyarország Kft., 2010, ISBN 963 86129 5 9.

[77] V. Cervenka, L. Jendele and J. Cervenka, ATENA Program documentation - Part 1 Theory., Prague, 2013.

[78] International Federation for Structural concrete (fib), CEB-FIP Model Code 2010, Lausanne, ISBN 978-2-88394-105-2, 2010.

[79] A. Demir, H. Ozturk, K. Edip, M. Stojmanovksa and A. Bogdanovic, “Effect of viscosity parameter on the numerical simulation of reinforced concrete deep beam behaviour,” *The Online Journal of Science and Technology,* vol. 8, no. 3, pp. 50-56, 2018.

[80] S. Jung, The effects of dismountable shear connectors on the structural behaviour of composite beams, Luxembourg: University of Luxembourg, 2019.

[81] C. Odenreit and A. Kozma, “Parametric study on non-ductile demountable shear connectors,” in *Proceedings of the 14th Nordic Steel Construcion Conference, September 18-20, 2019,* , Copenhagen, Denmark, 2019.

[82] G. Hanswille, M. Schäfer and M. Bergmann, Verbundtragwerke aus Stahl und Beton - Bemessung und Konstruktion - Kommentar zur EN 1994-1-1, in Kuhlmann, U.: Stahlbaukalender 2018, Berlin: WILEY-VCH/Ernst & Sohn Verlag, 2018.

[83] M. V. Leskelä, Shear connections in composite flexural members of steel and concrete, vol. 138, Mem Martins: European Convention for Constructional Steelwork (ECCS), 2017.

Annex A Complementary experiments

A.1 Steel tensile tests

A.1.1 General

In order to obtain information about the properties of the applied steel materials, standard ISO 6892-1:2016 [74] uniaxial tensile tests were conducted on the bolts, the L-profiles and steel beams used in the laboratory experiments. This chapter presents the results of the tensile tests.

ISO 6892-1:2016 [74] defines the yield strength (R_{eH}) as:

$$R_{eH} = F_y/S_0 \tag{A.1}$$

where F_y is the peak load prior to the first decrease in force and S_0 is the original cross-sectional area of the test piece.

The tensile strength (R_m) is defined as:

$$R_m = F_m/S_0 \tag{A.2}$$

where F_m is the maximum force.

The percentage elongation at fracture, (A) is:

$$A = \frac{L_u - L_0}{L_0} \cdot 100 \tag{A.3}$$

where L_0 is the original gauge length and L_u is the final gauge length after fracture.

The percentage reduction of area (Z) is:

$$Z = \frac{S_u - S_0}{S_0} \cdot 100 \tag{A.4}$$

where S_u is the minimum cross-sectional area after fracture.

A.1.2 Tensile tests on bolts

Coupon specimens were fabricated from the bolts applied in push-out test series P3 and in beam tests B7. The geometry of the steel coupons is presented in the following figure:

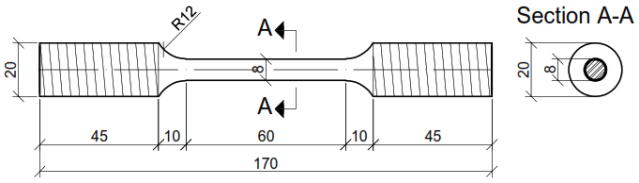

Figure A.1 Steel coupon test specimen of bolts (M20)

The following figure shows the coupon specimens after failure. The detailed results can be found in Table A.2.

Figure A.2 Steel coupon specimens after failure

Table A.1 Summary of the tensile tests on bolts (M20)

Tensile test series	Number of tests	Measured average tensile strength $f_{u,m}$ [MPa]	Corresponding test series
BL	4	948.7	P3.1, P3.3, B7
GV	4	1045.6	P3.2

Table A.2 Results of the tensile tests on bolts (M20)

#	1	2	3	4	5	6	7	8
Specimen	BL1	BL2	BL3	BL4	GV1	GV2	GV3	GV4
Diameter, d_1 [mm]	M20	M20	M20	M20	M20	M20	M20	M20
Grade	8.8	8.8	8.8	8.8	8.8	8.8	8.8	8.8
Length, L_t [mm]	170.1	170.0	170.2	170.2	170.4	170.1	170.1	170.1
Neck diameter, d_0 [mm]	8.035	8.019	8.049	8.035	8.109	7.975	8.135	8.080
Cross-sectional area, S_0 [mm2]	50.71	50.50	50.88	50.71	51.64	49.95	51.98	51.28
Neck length, L_0 [mm]	57.74	57.50	57.85	57.64	57.70	57.85	57.60	57.60
Yield load, F_y [kN]	44.2	44.5	44.0	44.2	52.1	50.0	52.6	52.6
Failure load, F_m [kN]	48.2	47.9	48.1	48.2	54.0	52.0	54.0	54.2
Yield strength, R_{eH} [MPa]	871.7	881.1	864.7	871.7	1008.8	1001.0	1012.0	1025.8
Tensile strength, R_m [MPa]	950.6	948.4	945.3	950.6	1045.6	1041.0	1038.9	1057.0
Neck diameter after fracture, d_u [mm]	4.535	4.710	4.850	4.795	4.950	4.835	4.960	4.850
Area after fracture, S_u [mm^2]	16.15	17.42	18.47	18.06	19.24	18.36	19.32	18.47
Neck length after fracture, L_u [mm]	65.47	65.57	65.06	65.18	64.38	64.40	64.08	63.73
Percentage elongation at fracture, A [%]	11.74	12.31	10.93	11.47	10.15	9.93	9.87	9.33
Percentage reduction area, Z [%]	68.14	65.50	63.69	64.39	62.74	63.24	62.83	63.97
Mean value of the yield strength, μ_{ReH} [MPa]	872.3				1011.9			
Standard deviation of the yield strength, σ_{ReH} [MPa]	6.73				10.38			
Coefficient of variation of the yield strength, V_{ReH} [-]	0.0077				0.0103			
Mean value of the tensile strength, μ_{ReH} [MPa]	948.7				1045.6			
Standard deviation of the tensile strength, σ_{ReH} [MPa]	2.49				8.09			
Coefficient of variation of the tensile strength, V_{ReH} [-]	0.0026				0.0077			

A.1.3 Tensile tests on L-profiles

From the push-out test specimens, three L-profiles that were selected for tensile testing. From each peace three coupon specimens were cut out. The geometry of the steel coupons is presented in the following figure, and the results of the tensile tests are presented in Table A.3.

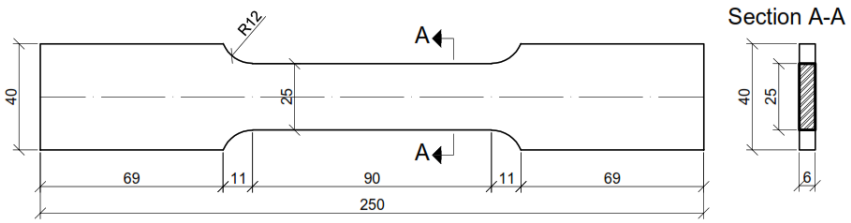

Figure A.3 Geometry of the steel coupon specimen of the L-profiles (L 80x80x6)

Figure A.4 Photo the steel coupon specimens of the L-profiles (L 80x80x6)

Table A.3 Results of the tensile tests on the L-profiles (L 80x80x6)

#	1	2	3	4	5	6	7	8	9
Part	L1.1	L1.2	L1.3	L2.1	L2.2	L2.3	L3.1	L3.2	L3.3
original thickness, a_0 [mm]	6.05	5.97	6.06	6.02	6.08	5.99	6.09	6.11	6.03
Width, b [mm]	40.0	40.0	40.0	39.9	40.0	39.9	40.1	40.0	39.9
Total length, L_{t0} [mm]	250.1	250.4	250.3	250.4	250.0	250.2	250.6	250.2	250.0
Original gauge length, L_0 [mm]	69.2	69.2	69.2	69.2	69.2	69.2	69.2	69.2	69.2
Neck width, b_0 [mm]	25.3	25.0	25.4	25.2	25.1	25.1	25.0	25.0	25.0
Cross-sectional area, S_0 [mm^2]	152.9	149.2	154.2	151.5	152.4	150.6	152.5	152.6	150.9
Parallel length, L_{c0} [mm]	90.1	90.2	90.3	90.3	90.0	90.1	90.3	90.2	90.0
Total length after fracture, L_{tu} [mm]	273.5	275.2	274.1	274.2	274.0	275.2	276.2	274.3	275.7
Gauge length after fracture, L_u [mm]	87.1	88.2	87.4	87.5	87.7	88.4	88.8	87.7	88.9
Neck width after fracture, b_u [mm]	18.5	18.3	18.5	18.3	18.8	18.2	18.3	18.4	18.5
Neck thickness after fracture, a_u [mm]	4.5	4.5	4.7	4.5	4.7	4.5	4.5	4.5	4.5
Cross-sectional area after fracture, S_u [mm^2]	83.0	81.6	86.1	81.5	88.1	81.9	82.8	83.5	82.3
Parallel length after fracture, L_{cu} [mm]	113.5	115.0	114.1	114.1	114.0	115.1	115.9	114.4	115.7
Maximum force, F_m [kN]	80.4	77.1	79.1	77.3	80.2	79.2	78.9	80.1	77.6
Yield strength, R_{eH} [MPa]	392.0	372.0	385.0	369.0	403.0	394.0	391.0	403.0	370.0
Tensile strength, R_m [MPa]	525.9	516.8	513.1	510.2	526.2	525.9	517.4	524.8	514.1
Percentage reduction area, Z [%]:	45.7	45.3	44.2	46.2	42.2	45.6	45.7	45.3	45.5
Percentage elongation at fracture, A [%]:	25.9	27.5	26.3	26.4	26.7	27.7	28.4	26.8	28.5
Mean value of the yield strength, μ_{ReH} [MPa]	383.0			388.7			388.0		
Standard deviation of the yield strength, σ_{ReH} [MPa]	10.1			17.6			16.7		
Coefficient of variation of the yield strength, V_{ReH} [-]	0.0265			0.0453			0.0430		
Mean value of the tensile strength, μ_{ReH} [MPa]	518.6			520.7			518.8		
Standard deviation of the tensile strength, σ_{ReH} [MPa]	6.6			9.2			5.5		
Coefficient of variation of the tensile strength, V_{ReH} [-]	0.0127			0.0176			0.0105		

A.1.4 Tensile tests on the beams

Tensile tests were conducted on steel coupon specimens cut out from the flanges of the beams used in the beam tests. The geometry of the coupons is presented in the following figure, and the results can be found in the following table.

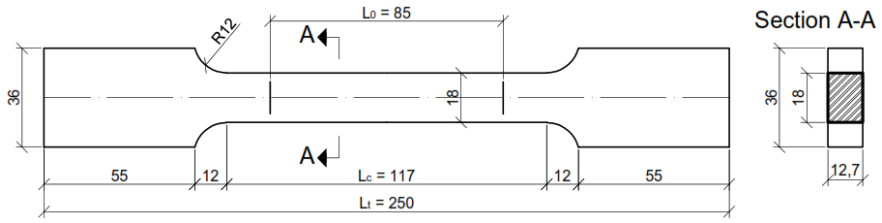

Figure A.5 Geometry of the steel coupon specimen of the beams (IPE 360)

Table A.4 Results of the tensile tests on the beams (IPE 360)

#	1	2	3	4
Part	B1	B2	T1	T2
original thickness, a_0 [mm]	12.90	12.64	12.90	12.98
Width, b [mm]	36.1	36.1	36.1	36.1
Total length, L_{t0} [mm]	250.0	250.1	250.2	250.0
Original gauge length, L_0 [mm]	85.4	85.2	85.0	85.2
Neck width, b_0 [mm]	18.1	18.1	18.2	18.0
Cross-sectional area, S_0 [mm^2]	234.0	228.4	234.5	233.1
Parallel length, L_{c0} [mm]	116.8	116.8	116.8	116.8
Total length after fracture, L_{tu} [mm]	284.6	284.8	286.0	285.7
Gauge length after fracture, L_u [mm]	113.8	113.2	116.5	117.4
Neck width after fracture, b_u [mm]	11.1	10.8	10.9	11.0
Neck thickness after fracture, a_u [mm]	6.8	6.5	7.1	6.9
Neck length after fracture, l_{loc} [mm]	27	26	30	29
Cross-sectional area after fracture, S_u [mm^2]	75.5	70.2	77.4	75.9
Parallel length after fracture, L_{cu} [mm]	151.3	151.5	152.7	152.5
Young's modulus, E [GPa]	197.0	183.0	186.0	188.0
Maximum force, F_m [kN]	111.5	108.6	108.3	108.5
Yield strength, R_{eH} [MPa]	392.0	378.0	375.0	382.0
Tensile strength, R_m [MPa]	476.0	464.0	463.0	464.0
Percentage reduction area, Z [%]	67.7	69.3	67.0	67.4
Percentage elongation at fracture, A [%]	33.3	32.9	37.1	37.8
Mean value of the yield strength, μ_{ReH} [MPa]	381.8			
Standard deviation of the yield strength, σ_{ReH} [MPa]	7.4			
Coefficient of variation of the yield strength, V_{ReH} [-]	0.0194			
Mean value of the tensile strength, μ_{ReH} [MPa]	467.7			
Standard deviation of the tensile strength, σ_{ReH} [MPa]	7.2			
Coefficient of variation of the tensile strength, V_{ReH} [-]	0.0155			

A.2 Concrete compression tests

A.2.1 General

The same concrete grade (C35/45) was ordered for all laboratory experiments. The concrete was cast on three occasions:

1) 28th June, 2017 – for push-out test series P15.1 and P15.2;
2) 25th September, 2017 – for push-out test series P3.1, P3.2 and P3.3;
3) 27th March, 2018 – for beam tests B7 and B8.

Compression tests were conducted on standard cube specimens on 9 different occasions:

Table A.5 Details of the parametric studies PS-1 (part 1)

Test series	Date of casting	Date of testing	Concrete age at testing [days]	Average measured cube strength, $f_{cu,m}$ [MPa]
CC1	28/06/2017	26/07/2017	28	44.33
CC2	28/06/2017	04/08/2017	37	49.12
CC3	28/06/2017	22/08/2017	55	52.43
CC4	28/06/2017	25/08/2017	58	55.81
CC5	25/09/2017	23/10/2017	28	59.39
CC6	25/09/2017	21/11/2017	57	70.65
CC7	27/03/2018	24/04/2018	28	51.47
CC8	27/03/2018	05/06/2018	70	64.88
CC9	27/03/2018	14/06/2018	79	63.13

The next table shows the list of the laboratory experiments and the corresponding cube tests.

Table A.6 List of experiments and the corresponding cube tests (Part 1)

Test	Date of experiment	Date of casting	Concrete age at experiment [days]	Date of cube test	Cube test series	Concrete age at cube test [days]	Concrete cube strength $f_{cu,m}$ [MPa]
P15.2-1	26/07/2017	28/06/2017	51	26/07/2017	CC1	28	44.33
P15.2-2	02/08/2017	28/06/2017	58	04/08/2017	CC2	37	49.12
P15.2-3	09/08/2017	28/06/2017	65	04/08/2017	CC2	37	49.12
P15.1-1	18/08/2017	28/06/2017	74	04/08/2017	CC2	37	49.12
P15.1-2	22/08/2017	28/06/2017	78	22/08/2017	CC3	55	52.43
P15.1-3	24/08/2017	28/06/2017	80	25/08/2017	CC4	58	55.81
P3.1-1	07/11/2017	25/09/2017	43	23/10/2017	CC5	28	59.39
P3.1-2	10/11/2017	25/09/2017	46	23/10/2017	CC5	28	59.39

Table A.7 List of experiments and the corresponding cube tests (Part 2)

Test	Date of experiment	Date of casting	Concrete age at experiment [days]	Date of cube test	Cube test series	Concrete age at cube test [days]	Concrete cube strength $f_{cu,m}$ [MPa]
P3.1-3	14/11/2017	25/09/2017	50	23/10/2017	CC5	28	59.39
P3.3-1	17/11/2017	25/09/2017	53	23/10/2017	CC5	28	59.39
P3.3-2	21/11/2017	25/09/2017	57	21/11/2017	CC6	57	70.65
P3.3-3	24/11/2017	25/09/2017	60	21/11/2017	CC6	57	70.65
P3.2-1	28/11/2017	25/09/2017	64	21/11/2017	CC6	57	70.65
P3.2-2	01/12/2017	25/09/2017	67	21/11/2017	CC6	57	70.65
P3.2-3	05/12/2017	25/09/2017	71	21/11/2017	CC6	57	70.65
P3.3-3R	07/12/2017	25/09/2017	73	21/11/2017	CC6	57	70.65
P3.2-3R	12/12/2017	25/09/2017	78	21/11/2017	CC6	57	70.65
B8	05/06/2018	27/03/2018	70	05/06/2018	CC8	70	64.88
B7	14/06/2018	27/03/2018	79	14/06/2018	CC9	79	63.13

A.2.2 Results of the compression tests

Figure A.6 shows a concrete cube specimen, and the following tables summarise the results of the conducted compression tests.

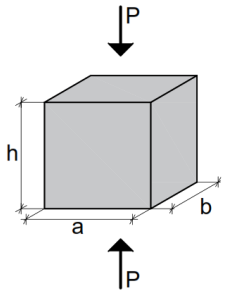

Figure A.6 Concrete cube test specimen

Table A.8 Results of compression test series CC1

Specimen	a [mm]	b [mm]	h [mm]	m [g]	$f_{cu,meas}$ [MPa]
CC1-1	150	149	150	7021	44.51
CC1-2	150	150	150	7078	44.96
CC1-3	149	150	150	7734	43.51
				Mean value:	**44.33**

Table A.9 Results of compression test series CC2

Specimen	a [mm]	b [mm]	h [mm]	m [g]	$f_{cu,meas}$ [MPa]
CC2-1	149	150	150	7808	49.56
CC2-2	151	150	150	7814	49.20
CC2-3	149	149	150	7824	48.62
				Mean value:	**49.12**

Table A.10 Results of compression test series CC3

Specimen	a [mm]	b [mm]	h [mm]	m [g]	$f_{cu,meas}$ [MPa]
CC3-1	149	150	150	7776	52.17
CC3-2	147	149	150	7769	52.40
CC3-3	146	150	150	7713	52.74
				Mean value:	**52.43**

Table A.11 Results of compression test series CC4

Specimen	a [mm]	b [mm]	h [mm]	m [g]	$f_{cu,meas}$ [MPa]
CC4-1	149	150	150	7751	54.57
CC4-2	149	150	150	7721	54.35
CC4-3	149	150	150	7734	55.53
				Mean value:	**55.81**

Table A.12 Results of compression test series CC5 - Cube

Specimen	a [mm]	b [mm]	h [mm]	m [g]	$f_{cu,meas}$ [MPa]
CC5.1-1	149	150	150	8024	61.17
CC5.1-2	150	150	150	7995	57.89
CC5.1-3	150	149	150	7960	59.11
				Mean value:	**59.39**

Table A.13 Results of compression test series CC5 – Cylinder

Specimen	h [mm]	D [mm]	m [g]	$f_{c,meas}$ [MPa]
CC5.2-1-	292	149	12320	54.02
CC5.2-2	294	148	12376	53.52
CC5.2-3	295	150	12460	52.24
			Mean value:	**53.26**

Table A.14 Results of compression test series CC6

Specimen	a [mm]	b [mm]	h [mm]	m [g]	$f_{cu,meas}$ [MPa]
CC6-1	150	150	150	7975	72.71
CC6-2	150	149	149	7969	68.13
CC6-3	150	149	150	7926	71.12
				Mean value:	**70.65**

Table A.15 Results of compression test series CC7

Specimen	a [mm]	b [mm]	h [mm]	m [g]	$f_{cu,meas}$ [MPa]
CC7-1	149	150	150	7804	50.92
CC7-2	150	148	151	7701	51.23
CC7-3	149	150	150	7844	52.23
				Mean value:	**51.47**

Table A.16 Results of compression test series CC8

Specimen	a [mm]	b [mm]	h [mm]	m [g]	$f_{cu,meas}$ [MPa]
CC8-1	149	150	150	7744	61.39
CC8-2	148	149	149	7758	68.12
CC8-3	149	149	150	7739	65.12
				Mean value:	**64.88**

Table A.17 Results of compression test series CC9

Specimen	a [mm]	b [mm]	h [mm]	m [g]	$f_{cu,meas}$ [MPa]
CC9-1	151	150	150	7724	64.27
CC9-2	150	150	150	7750	65.29
CC9-3	150	150	150	7627	59.83
				Mean value:	**63.13**

A.3 Bolt pretension tests

During the push-out tests it was not possible to measure the bolt pretension. So instead, separate experiments were carried out with the following test setup:

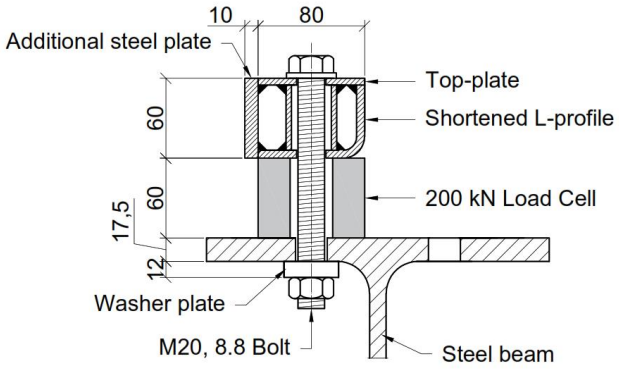

Figure A.7 Geometry of the pretension test

The test setup consisted of the following elements:

1) M20, Gr. 8.8 bolts with 12 mm thick washer plates and 4 mm thick washers (7 black and 3 galvanised)
2) An HE 260B beam identical to one used in the push-out tests
3) A 200 kN load cell
4) L-profile with welded top plate and cylinder
5) Additional plate welded to the L-profile and the top plate

While designing the test setup the aim was to represent the push-out test specimens as accurately as possible. The steel beam was one of the steel beams used in the push-out tests and the bolts, the washers, the L-profile, the top plate were from the same batch as the ones used in the push-out tests. It was necessary to keep the clamping length also the same, so the steel cylinder needed to be shortened because of the addition of the 60 mm high load cell. In this experiment, there was no concrete around the steel cylinder, so the web of the L-profile was welded to the top plate and an additional 10 mm thick steel plate was welded to the top plate as well as the leg of the L-profile. The size of the additional plate was determined such that the resulting normal stiffness is the same as in the case of the push-out test specimen.

Concrete area below the top plate in the push-out tests:

$$A_c = 80\ mm \cdot 80\ mm - \frac{(42.5\ mm)^2 \cdot \pi}{4} = 4981\ mm^2 \tag{A.5}$$

Young's modulus of the concrete:

$$E_c = 33400\ N/mm^2 \tag{A.6}$$

Young's modulus of the steel:

$$E_a = 210000\ N/mm^2 \tag{A.7}$$

The normal stiffness should be the same:

$$E_a A_a = E_c A_c \tag{A.8}$$

Therefore, the required steel area:

$$A_a = \frac{E_c A_c}{E_a} = \frac{33400 \frac{N}{mm^2} \cdot 4981\ mm^2}{210000 \frac{N}{mm^2}} = 792.2\ mm^2 \tag{A.9}$$

This area was composed of the 6 mm thick web and the 10 mm thick additional plate cut to a length of:

$$l = \frac{A_a}{10\ mm + 6\ mm} = 49.5\ mm \tag{A.10}$$

The following figure shows the L-profile, the cylinder, the top plate and the additional welded plate:

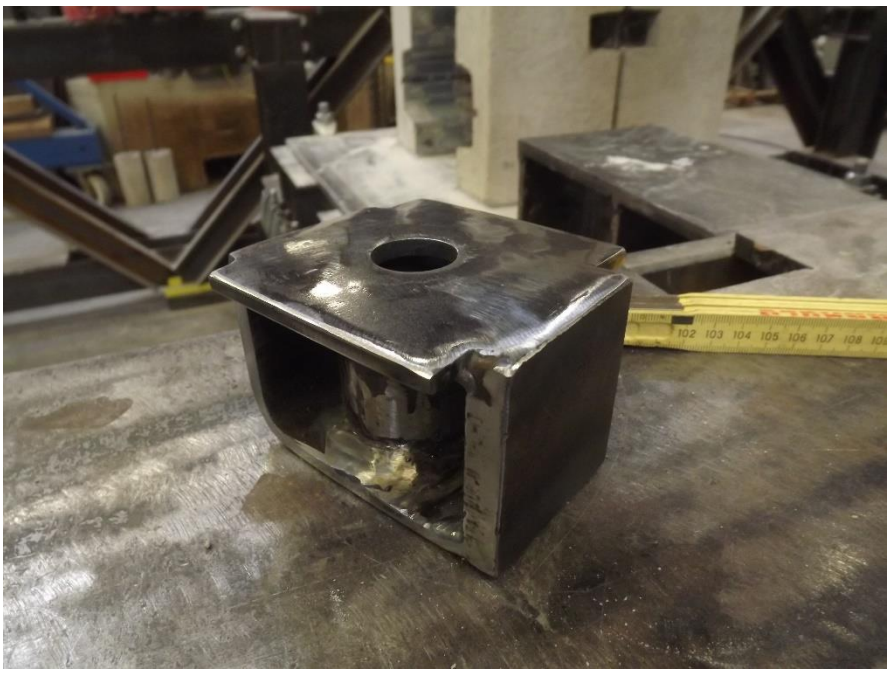

Figure A.8 The L-profile, the cylinder, the top plate and the additional welded plate

Before the experiments the position of the bolts and the nuts were marked with a chalk. During the experiments, the bolts were tightened to a snug tight condition [48], then different amount of rotations were applied on the nuts while the load was continuously measured. The angle of rotation was measured afterwards digitally from the photos taken during the experiments:

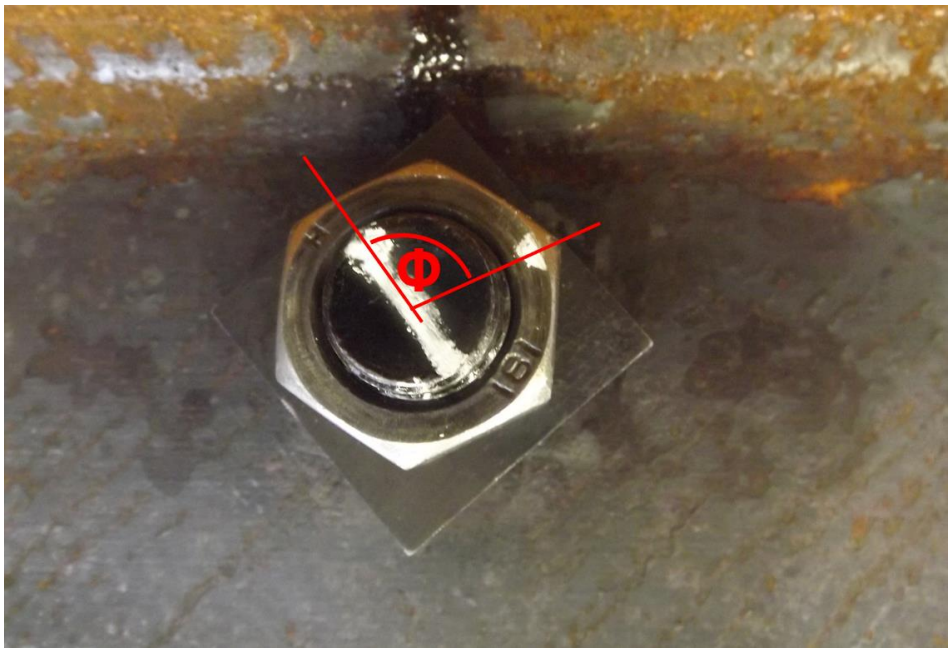

Figure A.9 Rotation measurement

The following table summarises the obtained rotation and force values:

Table A.18 Results of the pretension measurements

#	Rotation [deg]	Force [kN]
1	98	84
2	102	89
3	103	96
4*	115	104
5*	87	95
6*	128	113
7	133	122
8	140	136
9	161	145
10	150	143

*Galvanised bolts

The linear relationship can be observed between the applied rotation and the measured force values. This relationship can be described as:

$$F_{p,c} = \left(C \cdot \frac{\Phi}{360°} \cdot p_b\right) \cdot \frac{1}{l_{clamp}} \cdot E_a \cdot A_s \tag{A.11}$$

Where Φ is the rotation applied on the nut, p_b = 2.5 mm is the pitch of the bolt, l_{clamp} = 153.5 mm is the clamping length, E_a is the Young's modulus of the steel and A_s = 245 mm^2 is the cross-sectional area of the bolt. From the applied rotation, not all of the elongation is applied to the bolt itself, but a certain amount is absorbed by the system (by the compression of the elements and the by the bending of the top plate). Therefore, a dimensionless constant C = 0.39 parameter is introduced that takes into account this effect. The value of this constant was found using the method of least squares so that the experimentally obtained results fit the analytical calculation. This way, the first part of the equation represents the elongation of the bolt, dividing this part with the clamping length we get the normal strain, multiplying this by the Young's modulus we get the normal stress, and finally, we obtain the bolt pretension force by multiplying the stress by the cross-sectional area of the bolt. The following table summarises the obtained results from this calculation:

Table A.19 Comparison of analytically and experimentally obtained results

#	**Rotation [deg]**	**Elongation [mm]**	**Strain [-]**	**Stress [MPa]**	**Calculated force, $F_{p,c,calc}$ [kN]**	**Measured force, $F_{p,c}$ [kN]**	**θ $F_{p,c}/F_{p,c.calc}$ [-]**
1	98	0.2648	0.0017	362.3	89	84	0.95
2	102	0.2756	0.0018	377.1	92	89	0.96
3	103	0.2783	0.0018	380.8	93	96	1.03
4*	115	0.3108	0.0020	425.1	104	104	1.00
5*	87	0.2351	0.0015	321.6	79	95	1.21
6*	128	0.3459	0.0023	473.2	116	113	0.97
7	133	0.3594	0.0023	491.7	120	122	1.01
8	140	0.3783	0.0025	517.6	127	136	1.07
9	161	0.4351	0.0028	595.2	146	145	0.99
10	150	0.4053	0.0026	554.5	136	143	1.05

*Galvanised bolts

The statistical parameters of the uncertainties were determined to evaluate the accuracy of the analytical approach. First, the model uncertainty parameters were determined:

$$\theta_i = \frac{F_{p,c}}{F_{p,c,calc}} \tag{A.12}$$

The mean value of the model uncertainties:

$$\mu_\theta = \frac{1}{n} \cdot \sum_{i=1}^{n} \theta_i = 1.02 \tag{A.13}$$

The standard deviation:

$$\sigma_\theta = \frac{1}{n} \cdot \sum_{i=1}^{n} (\theta_i - \mu_\theta)^2 = 0.076 \tag{A.14}$$

The coefficient of variation:

$$V_\theta = \frac{\sigma_\theta}{\mu_\theta} = 0.074 \tag{A.15}$$

These values show a low uncertainty, and therefore, it was concluded the analytical model can predict the bolt pretension load from the applied rotation with high accuracy. The following figure shows the comparison of the obtained results:

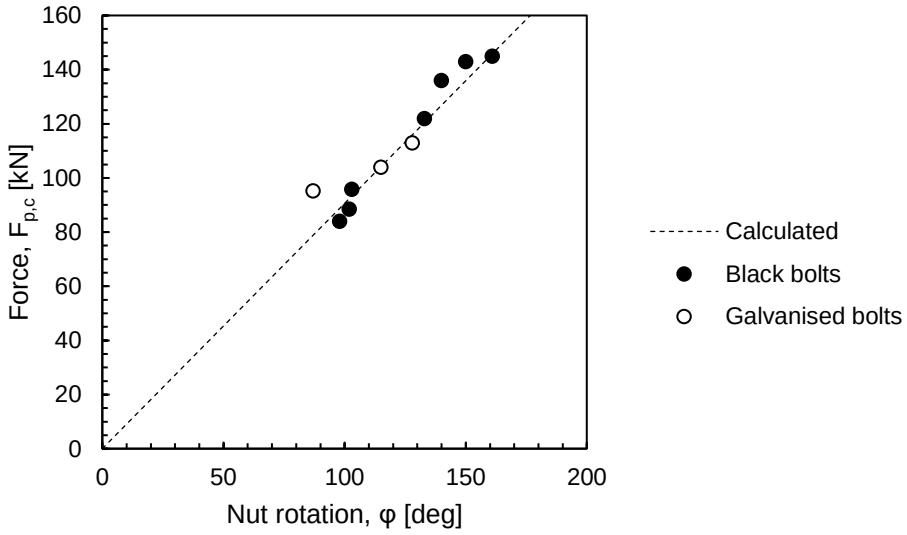

Figure A.10 Comparison of analytically and experimentally obtained results

We can also observe from the previous figure that this method of preloading is not sensitive to the surface treatment because a certain amount rotation always belongs to a certain amount of elongation. This is not the case with the torque method, which depends on other factors besides the surface treatment (amount and type of lubrication, thread damages).

Annex B Parametric studies

B.1 Parametric study PS-1

Table B. and Table B.2 show the investigated parameters of each simulation and the corresponding ultimate moment resistance and end slip values.

Table B.1 Details of the parametric studies PS-1 (part 1)

#	Name	L [m]	Profile	f_y [MPa]	f_c [MPa]	Shear conn.	Dist.	$M_{u,FEM}$ [kNm]	$s_{u,FEM}$ [mm]
1	6E36-S3C45M-DP1-P0	6	IPE 360	391	54	P0	DP1	634	6.0
2	6E36-S3C45M-DP1-P3.3	6	IPE 360	391	54	P3.3	DP1	657	9.7
3	6E36-S3C45M-DP1-P15.1	6	IPE 360	391	54	P15.1	DP1	664	7.7
4	6E36-S3C45M-DP1-P15.2	6	IPE 360	391	54	P15.2	DP1	631	5.4
5	6E36-S3C25M-DP1-P0	6	IPE 360	391	33	P0	DP1	617	6.0
6	6E36-S3C25M-DP1-P3.3	6	IPE 360	391	33	P3.3	DP1	635	9.2
7	6E36-S3C25M-DP1-P15.1	6	IPE 360	391	33	P15.1	DP1	652	7.7
8	6E36-S3C25M-DP1-P15.2	6	IPE 360	391	33	P15.2	DP1	624	5.4
9	6E36-S3C20M-DP1-P0	6	IPE 360	391	28	P0	DP1	615	6.0
10	6E36-S3C20M-DP1-P3.3	6	IPE 360	391	28	P3.3	DP1	628	8.7
11	6E36-S3C20M-DP1-P15.1	6	IPE 360	391	28	P15.1	DP1	643	7.2
12	6E36-S3C20M-DP1-P15.2	6	IPE 360	391	28	P15.2	DP1	623	5.4
13	6E36-S3C45M-DE1-P0	6	IPE 360	391	54	P0	DE1	664	6.0
14	6E36-S3C45M-DE1-P3.3	6	IPE 360	391	54	P3.3	DE1	674	8.8
15	6E36-S3C45M-DE1-P15.1	6	IPE 360	391	54	P15.1	DE1	697	7.7
16	6E36-S3C45M-DE1-P15.2	6	IPE 360	391	54	P15.2	DE1	682	5.4
17	6E36-S3C25M-DE1-P3.3	6	IPE 360	391	33	P3.3	DE1	649	7.3
18	6E36-S3C25M-DE1-P15.1	6	IPE 360	391	33	P15.1	DE1	671	5.3
19	6E36-S3C25M-DE1-P15.2	6	IPE 360	391	33	P15.2	DE1	670	5.4
20	6E36-S3C20M-DE1-P3.3	6	IPE 360	391	28	P3.3	DE1	641	6.6
21	6E36-S3C20M-DE1-P15.1	6	IPE 360	391	28	P15.1	DE1	659	5.0
22	6E36-S3C20M-DE1-P15.2	6	IPE 360	391	28	P15.2	DE1	662	3.4
23	6E36-S4C45M-DP1-P3.3	6	IPE 360	507	54	P3.3	DP1	777	9.7
24	6E36-S4C45M-DP1-P15.1	6	IPE 360	507	54	P15.1	DP1	766	7.7
25	6E36-S4C45M-DP1-P15.2	6	IPE 360	507	54	P15.2	DP1	705	5.4
26	6E36-S4C45M-DE1-P3.3	6	IPE 360	507	54	P3.3	DE1	807	8.8
27	6E36-S4C45M-DE1-P15.1	6	IPE 360	507	54	P15.1	DE1	824	7.7
28	6E36-S4C45M-DE1-P15.2	6	IPE 360	507	54	P15.2	DE1	783	5.4
29	6E36-S2C45M-DP1-P3.3	6	IPE 360	303	54	P3.3	DP1	550	9.7

Table B.2 Details of the parametric studies PS-1 (part 2)

#	Name	L [m]	Profile	f_y [MPa]	f_c [MPa]	Shear conn.	Dist.	$M_{u,FEM}$ [kNm]	$s_{u,FEM}$ [mm]
30	6E36-S2C45M-DP1-P15.1	6	IPE 360	303	54	P15.1	DP1	571	7.7
31	6E36-S2C45M-DP1-P15.2	6	IPE 360	303	54	P15.2	DP1	550	5.4
32	6E36-S2C45M-DE1-P3.3	6	IPE 360	303	54	P3.3	DE1	563	8.8
33	6E36-S2C45M-DE1-P15.1	6	IPE 360	303	54	P15.1	DE1	592	7.7
34	6E36-S2C45M-DE1-P15.2	6	IPE 360	303	54	P15.2	DE1	589	5.4

The moment-deflection curves are presented in Figure B.11 - Figure B.13. In the figures, the dots represent shear connector failure. If no dot is presented at the end of the curve, it means that the failure occurred in a different way: either by concrete crushing or by plastification of the steel section.

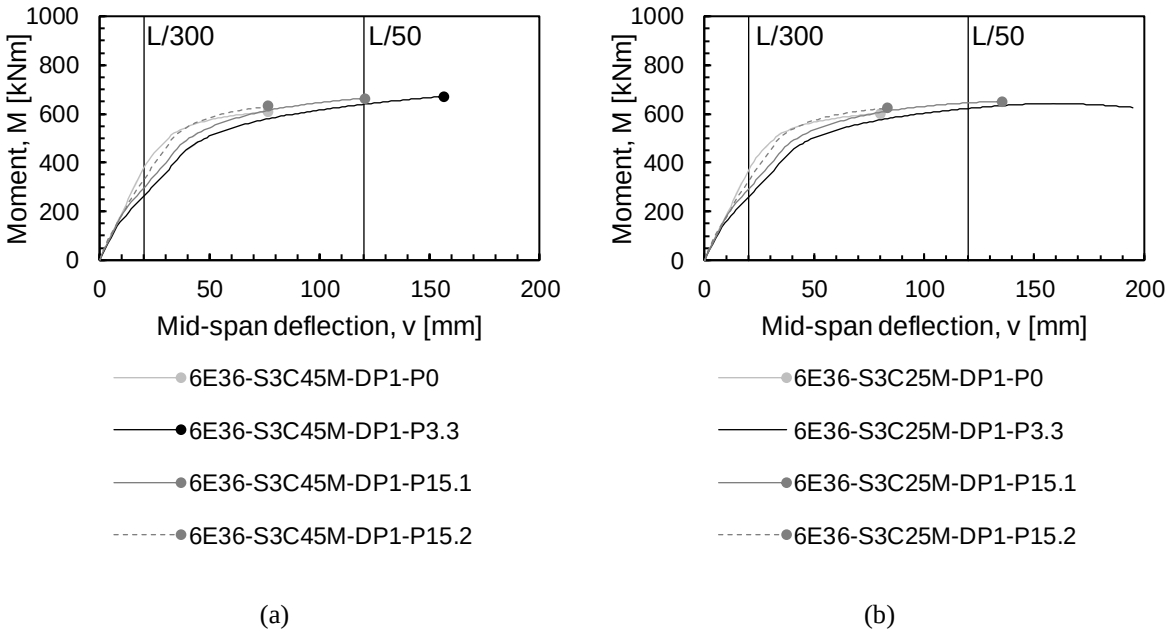

(a) (b)

Figure B.11 Moment deflection curves (a) simulation #1-#4, (b) simulation #5-#8

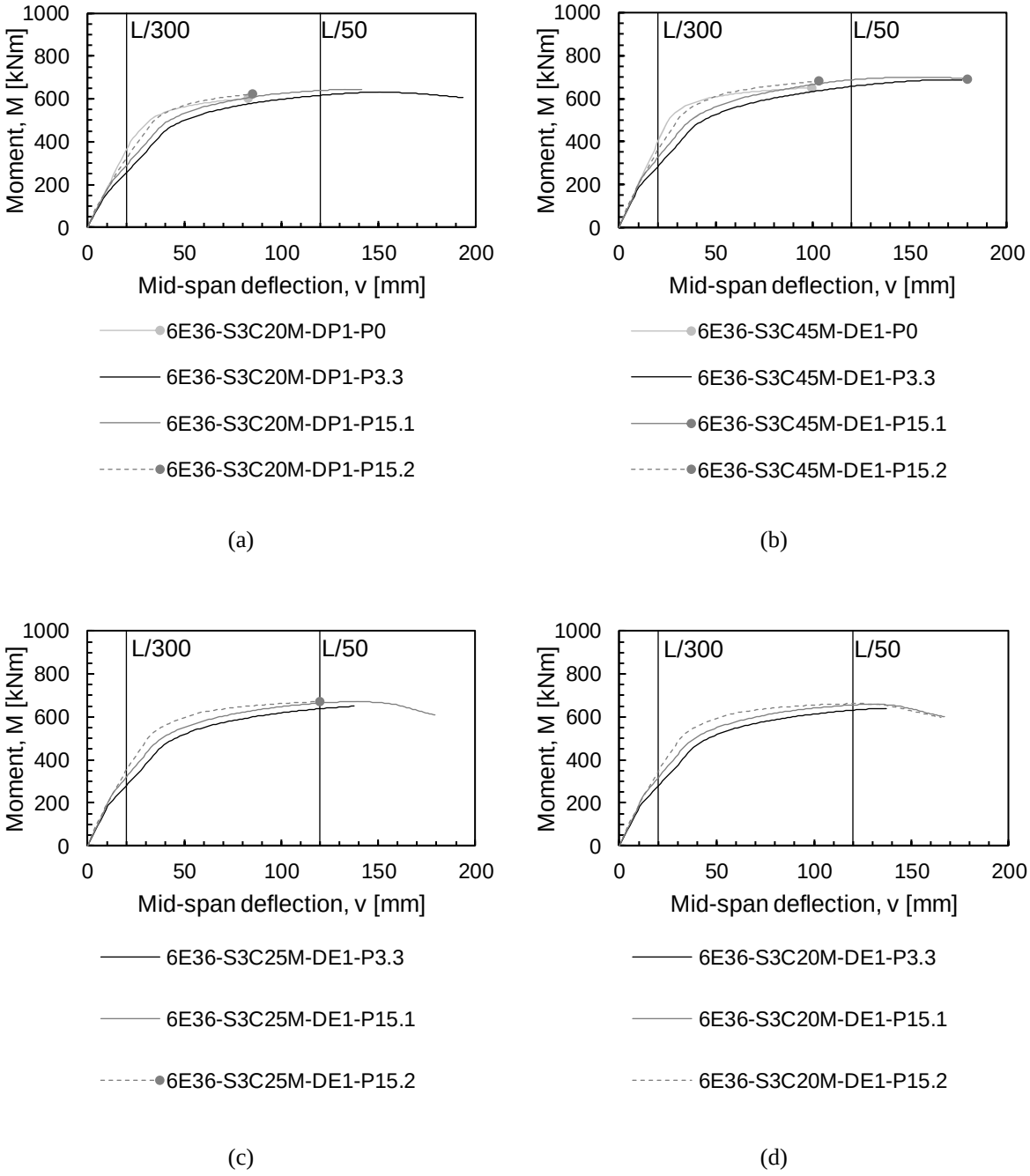

Figure B.12 Moment deflection curves (a) simulation #9-#12, (b) simulation #13-#16, (c) simulation #17-#19, (d) simulation #20-#22

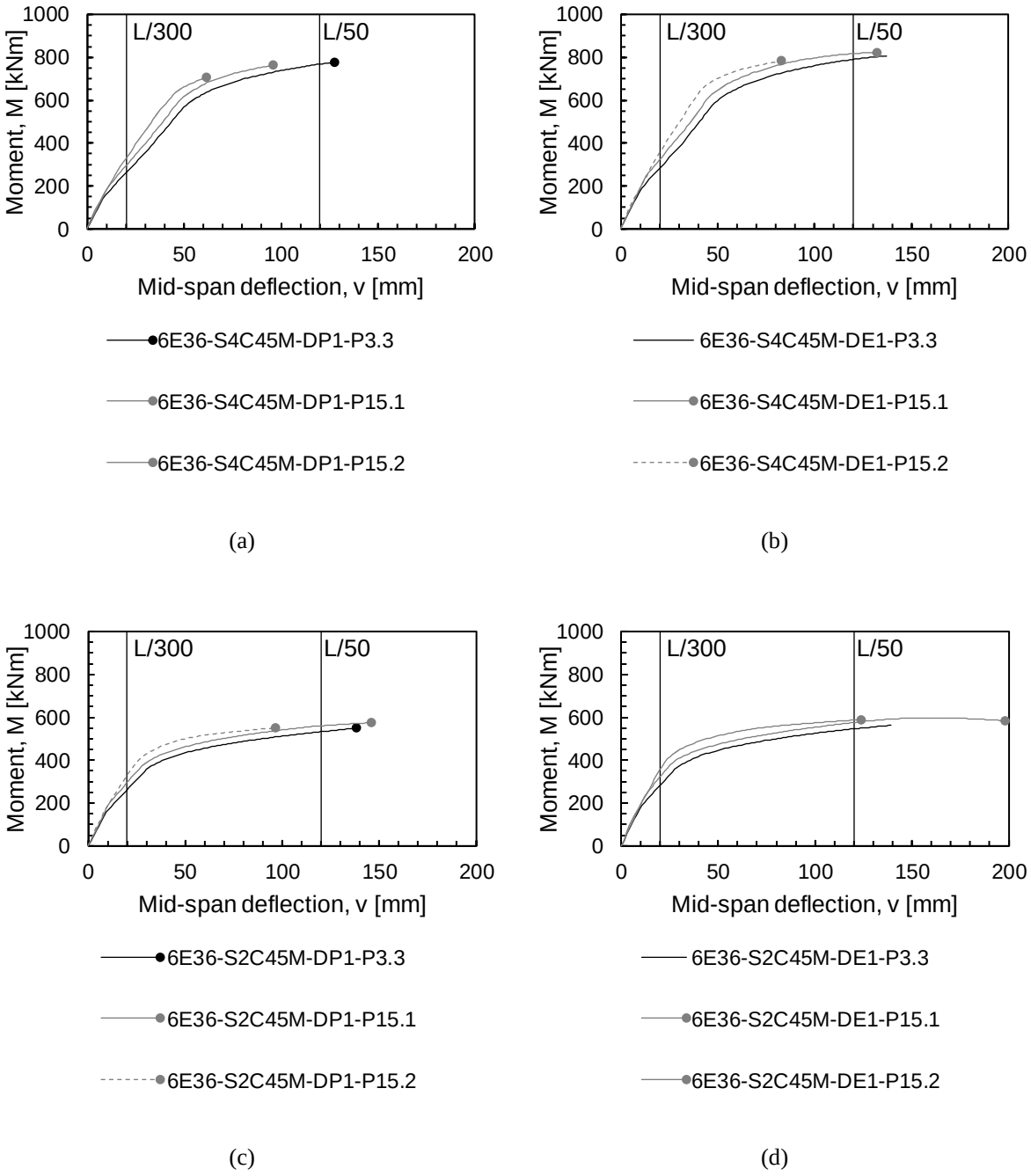

Figure B.13 Moment deflection curves (a) simulation #23-#25, (b) simulation #26-#28, (c) simulation #29-#31, (d) simulation #32-#34

B.2 Parametric study PS-2

Table B.3 - Table B.5 show the investigated parameters of each simulation and the corresponding ultimate moment resistance and end slip values.

Table B.3 Details of the parametric studies PS-2 (part 1)

#	Name	L [m]	Steel grade	Profile	f_y [MPa]	f_c [MPa]	Shear conn.	Dist.	$M_{u,FEM}$ [kNm]	$s_{u,FEM}$ [mm]
35	6E27-S3C45M-DP1-P0	6.0	S355	IPE 270	391	54	P0	DP1	389	6.0
36	6E27-S3C45M-DP1-P3.3	6.0	S355	IPE 270	391	54	P3.3	DP1	406	9.7
37	6E27-S3C45M-DP1-P15.1	6.0	S355	IPE 270	391	54	P15.1	DP1	411	7.7
38	6E27-S3C45M-DP2-P0	6.0	S355	IPE 270	391	54	P0	DP2	526	6.0
39	6E27-S3C45M-DP2-P3.3	6.0	S355	IPE 270	391	54	P3.3	DP2	503	7.8
40	6E27-S3C45M-DP2-P15.1	6.0	S355	IPE 270	391	54	P15.1	DP2	513	5.6
41	6E27-S3C20M-DP1-P0	6.0	S355	IPE 270	391	28	P0	DP1	383	6.0
42	6E27-S3C20M-DP1-P3.3	6.0	S355	IPE 270	391	28	P3.3	DP1	403	9.7
43	6E27-S3C20M-DP1-P15.1	6.0	S355	IPE 270	391	28	P15.1	DP1	407	7.7
44	6E27-S3C20M-DP2-P0	6.0	S355	IPE 270	391	28	P0	DP2	481	3.2
45	6E27-S3C20M-DP2-P3.3	6.0	S355	IPE 270	391	28	P3.3	DP2	466	7.3
46	6E27-S3C20M-DP2-P15.1	6.0	S355	IPE 270	391	28	P15.1	DP2	475	5.3
47	6E36-S3C45M-DP1-P0	6.0	S355	IPE 360	391	54	P0	DP1	625	6.0
48	6E36-S3C45M-DP1-P3.3	6.0	S355	IPE 360	391	54	P3.3	DP1	659	9.7
49	6E36-S3C45M-DP1-P15.1	6.0	S355	IPE 360	391	54	P15.1	DP1	663	7.7
50	6E36-S3C45M-DP2-P0	6.0	S355	IPE 360	391	54	P0	DP2	780	6.0
51	6E36-S3C45M-DP2-P3.3	6.0	S355	IPE 360	391	54	P3.3	DP2	820	9.7
52	6E36-S3C45M-DP2-P15.1	6.0	S355	IPE 360	391	54	P15.1	DP2	827	7.7
53	6E36-S3C20M-DP1-P0	6.0	S355	IPE 360	391	28	P0	DP1	621	6.0
54	6E36-S3C20M-DP1-P3.3	6.0	S355	IPE 360	391	28	P3.3	DP1	654	9.7
55	6E36-S3C20M-DP1-P15.1	6.0	S355	IPE 360	391	28	P15.1	DP1	658	7.7
56	6E36-S3C20M-DP2-P0	6.0	S355	IPE 360	391	28	P0	DP2	758	6.0
57	6E36-S3C20M-DP2-P3.3	6.0	S355	IPE 360	391	28	P3.3	DP2	747	8.4
58	6E36-S3C20M-DP2-P15.1	6.0	S355	IPE 360	391	28	P15.1	DP2	755	5.9
59	8E45-S3C45M-DP1-P0	8.1	S355	IPE 450	391	54	P0	DP1	1026	6.0
60	8E45-S3C45M-DP1-P3.3	8.1	S355	IPE 450	391	54	P3.3	DP1	1092	9.7
61	8E45-S3C45M-DP1-P15.1	8.1	S355	IPE 450	391	54	P15.1	DP1	1087	7.7
62	16E60-S3C45M-DP1-P0	16.2	S355	IPE 600	391	54	P0	DP1	2014	6.0
63	16E60-S3C45M-DP1-P3.3	16.2	S355	IPE 600	391	54	P3.3	DP1	2253	9.7
64	16E60-S3C45M-DP1-P15.1	16.2	S355	IPE 600	391	54	P15.1	DP1	2234	7.7
65	16E60-S3C45M-DP2-P0	16.2	S355	IPE 600	391	54	P0	DP2	2504	2.2
66	16E60-S3C45M-DP2-P3.3	16.2	S355	IPE 600	391	54	P3.3	DP2	2578	8.8
67	16E60-S3C45M-DP2-P15.1	16.2	S355	IPE 600	391	54	P15.1	DP2	2655	6.7
68	16E60-S3C20M-DP1-P0	16.2	S355	IPE 600	391	28	P0	DP1	1980	6.0

Table B.4 Details of the parametric studies PS-2 (part 2)

#	Name	L [m]	Steel grade	Profile	f_y [MPa]	f_c [MPa]	Shear conn.	Dist.	$M_{u,FEM}$ [kNm]	$s_{u,FEM}$ [mm]
69	16E60-S3C20M-DP1-P3.3	16.2	S355	IPE 600	391	28	P3.3	DP1	2216	9.7
70	16E60-S3C20M-DP1-P15.1	16.2	S355	IPE 600	391	28	P15.1	DP1	2197	7.7
71	16E60-S3C20M-DP2-P0	16.2	S355	IPE 600	391	28	P0	DP2	2511	6.0
72	16E60-S3C20M-DP2-P3.3	16.2	S355	IPE 600	391	28	P3.3	DP2	2454	7.9
73	16E60-S3C20M-DP2-P15.1	16.2	S355	IPE 600	391	28	P15.1	DP2	2526	5.9
74	6E27-S3C45D-DP1-P0	6.0	S355	IPE 270	355	30	P0	DP1	325	6.0
75	6E27-S3C45D-DP1-P3.3	6.0	S355	IPE 270	355	30	P3.3	DP1	320	10.6
76	6E27-S3C45D-DP1-P15.1	6.0	S355	IPE 270	355	30	P15.1	DP1	337	8.8
77	6E27-S3C45D-DP2-P0	6.0	S355	IPE 270	355	30	P0	DP2	426	6.0
78	6E27-S3C45D-DP2-P3.3	6.0	S355	IPE 270	355	30	P3.3	DP2	394	9.3
79	6E27-S3C45D-DP2-P15.1	6.0	S355	IPE 270	355	30	P15.1	DP2	429	7.1
80	6E27-S3C20D-DP1-P0	6.0	S355	IPE 270	355	13.33	P0	DP1	322	6.0
81	6E27-S3C20D-DP1-P3.3	6.0	S355	IPE 270	355	13.33	P3.3	DP1	328	10.0
82	6E27-S3C20D-DP1-P15.1	6.0	S355	IPE 270	355	13.33	P15.1	DP1	352	8.8
83	6E27-S3C20D-DP2-P0	6.0	S355	IPE 270	355	13.33	P0	DP2	405	6.0
84	6E27-S3C20D-DP2-P3.3	6.0	S355	IPE 270	355	13.33	P3.3	DP2	364	8.2
85	6E27-S3C20D-DP2-P15.1	6.0	S355	IPE 270	355	13.33	P15.1	DP2	398	6.0
86	6E36-S3C45D-DP1-P0	6.0	S355	IPE 360	355	30	P0	DP1	536	6.0
87	6E36-S3C45D-DP1-P3.3	6.0	S355	IPE 360	355	30	P3.3	DP1	564	10.6
88	6E36-S3C45D-DP1-P15.1	6.0	S355	IPE 360	355	30	P15.1	DP1	583	8.8
89	6E36-S3C45D-DP2-P0	6.0	S355	IPE 360	355	30	P0	DP2	657	6.0
90	6E36-S3C45D-DP2-P3.3	6.0	S355	IPE 360	355	30	P3.3	DP2	589	8.0
91	6E36-S3C45D-DP2-P15.1	6.0	S355	IPE 360	355	30	P15.1	DP2	681	8.4
92	6E36-S3C20D-DP1-P0	6.0	S355	IPE 360	355	13.33	P0	DP1	536	6.0
93	6E36-S3C20D-DP1-P3.3	6.0	S355	IPE 360	355	13.33	P3.3	DP1	538	9.9
94	6E36-S3C20D-DP1-P15.1	6.0	S355	IPE 360	355	13.33	P15.1	DP1	569	8.8
95	6E36-S3C20D-DP2-P0	6.0	S355	IPE 360	355	13.33	P0	DP2	644	6.0
96	6E36-S3C20D-DP2-P3.3	6.0	S355	IPE 360	355	13.33	P3.3	DP2	579	7.7
97	6E36-S3C20D-DP2-P15.1	6.0	S355	IPE 360	355	13.33	P15.1	DP2	610	5.7
98	8E45-S3C45D-DP1-P0	8.1	S355	IPE 450	355	30	P0	DP1	871	6.0
99	8E45-S3C45D-DP1-P3.3	8.1	S355	IPE 450	355	30	P3.3	DP1	898	10.6
100	8E45-S3C45D-DP1-P15.1	8.1	S355	IPE 450	355	30	P15.1	DP1	924	8.8
101	16E60-S3C45D-DP1-P0	16.2	S355	IPE 600	355	30	P0	DP1	1568	6.0
102	16E60-S3C45D-DP1-P3.3	16.2	S355	IPE 600	355	30	P3.3	DP1	1821	10.6
103	16E60-S3C45D-DP1-P15.1	16.2	S355	IPE 600	355	30	P15.1	DP1	1870	8.8
104	16E60-S3C45D-DP2-P0	16.2	S355	IPE 600	355	30	P0	DP2	2208	6.0
105	16E60-S3C45D-DP2-P3.3	16.2	S355	IPE 600	355	30	P3.3	DP2	2120	10.6
106	16E60-S3C45D-DP2-P15.1	16.2	S355	IPE 600	355	30	P15.1	DP2	2178	7.5

Table B.5 Details of the parametric studies PS-2 (part 3)

#	Name	L [m]	Steel grade	Profile	f_y [MPa]	f_c [MPa]	Shear conn.	Dist.	$M_{u,FEM}$ [kNm]	$s_{u,FEM}$ [mm]
107	16E60-S3C20D-DP1-P0	16.2	S355	IPE 600	355	13.33	P0	DP1	1560	6.0
108	16E60-S3C20D-DP1-P3.3	16.2	S355	IPE 600	355	13.33	P3.3	DP1	1815	10.6
109	16E60-S3C20D-DP1-P15.1	16.2	S355	IPE 600	355	13.33	P15.1	DP1	1862	8.8
110	16E60-S3C20D-DP2-P0	16.2	S355	IPE 600	355	13.33	P0	DP2	2109	6.0
111	16E60-S3C20D-DP2-P3.3	16.2	S355	IPE 600	355	13.33	P3.3	DP2	2033	9.4
112	16E60-S3C20D-DP2-P15.1	16.2	S355	IPE 600	355	13.33	P15.1	DP2	2083	6.4

The moment-deflection curves are presented in Figure B.14 - Figure B.17. In the figures, the dots represent shear connector failure. If no dot is presented at the end of the curve, it means that the failure occurred in a different way: either by concrete crushing or by plastification of the steel section. The left and the right figures correspond to the same simulations with expected values (left) and with design values (right).

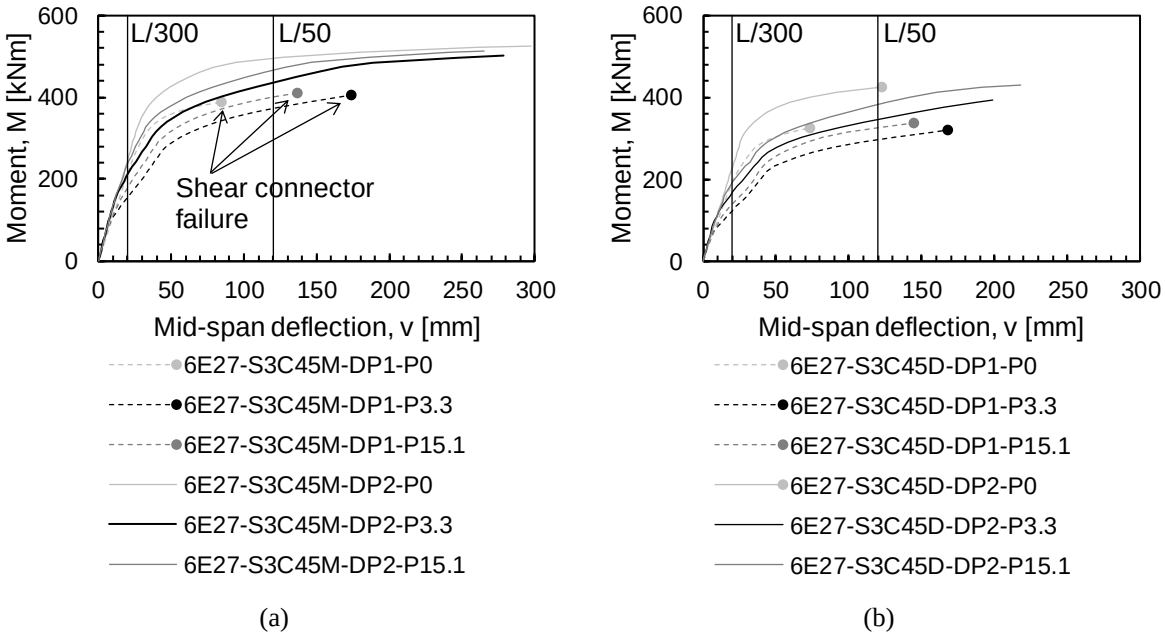

Figure B.14 Moment deflection curves (a) simulation #35-#40, (b) simulation #74-#79

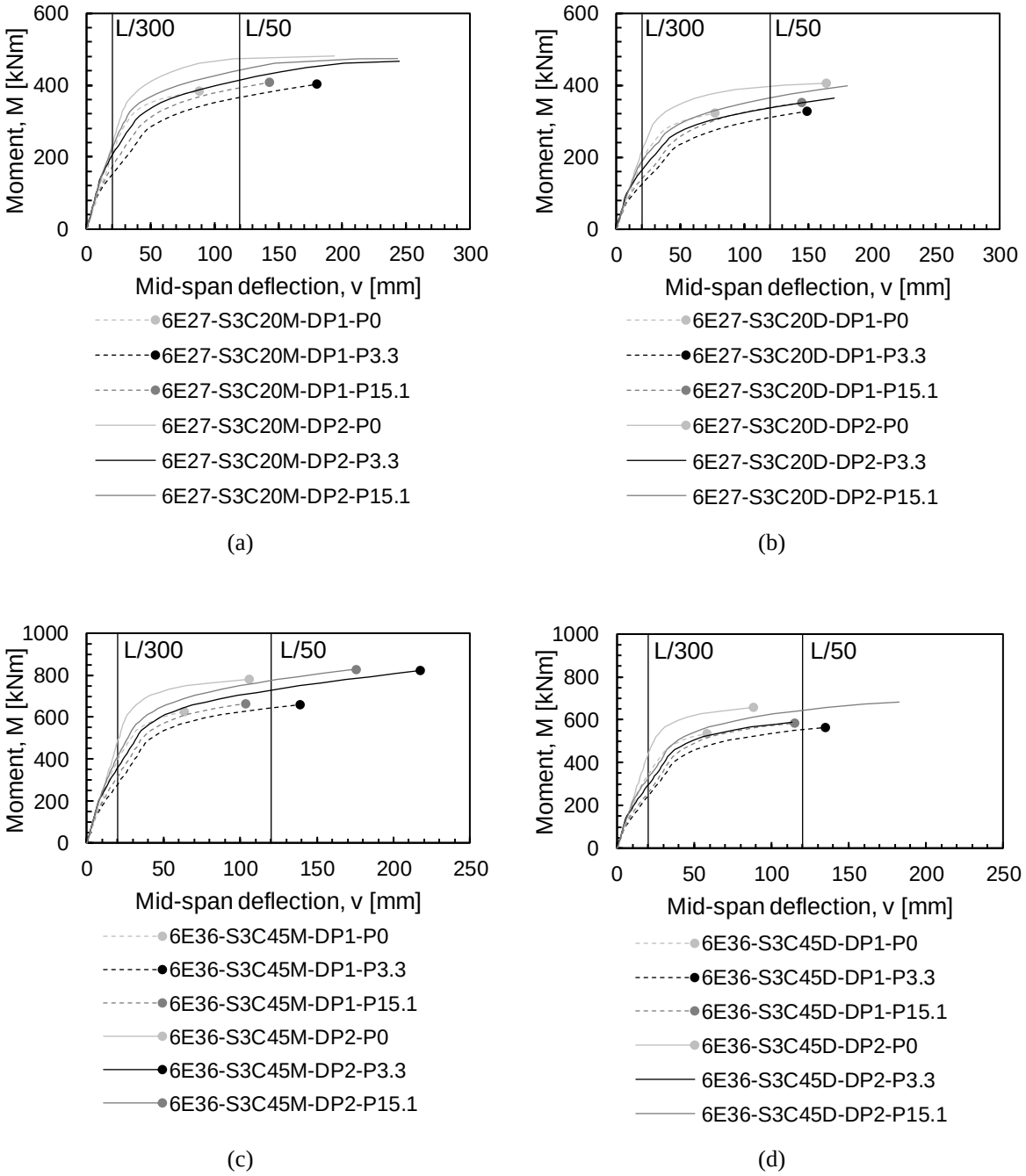

Figure B.15 Moment deflection curves (a) simulation #41-#46, (b) simulation #80-#85, (c) simulation #47-#52, (d) simulation #86-#91

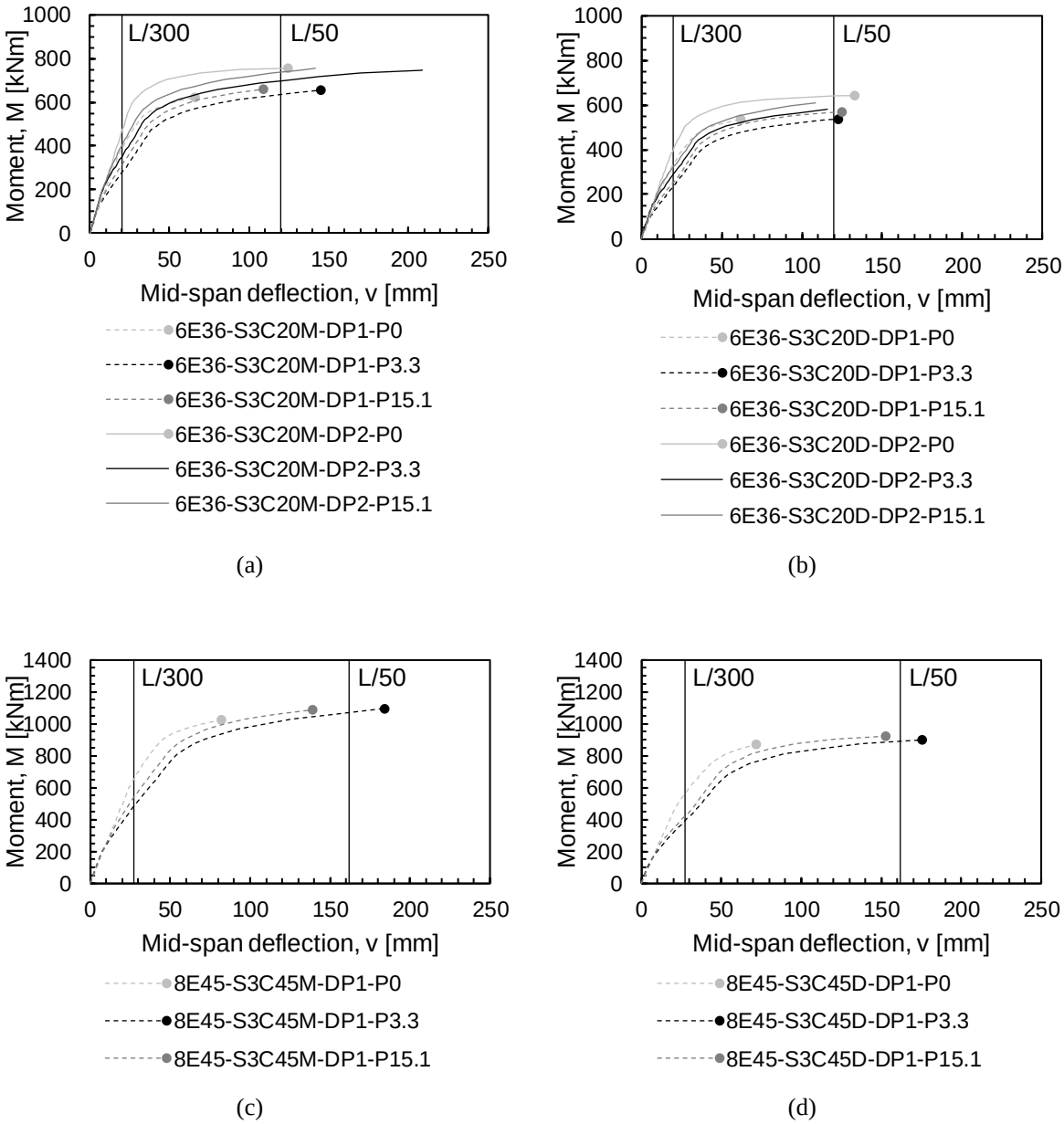

Figure B.16 Moment deflection curves (a) simulation #53-#58, (b) simulation #92-#97, (c) simulation #59-#61, (d) simulation #98-#100

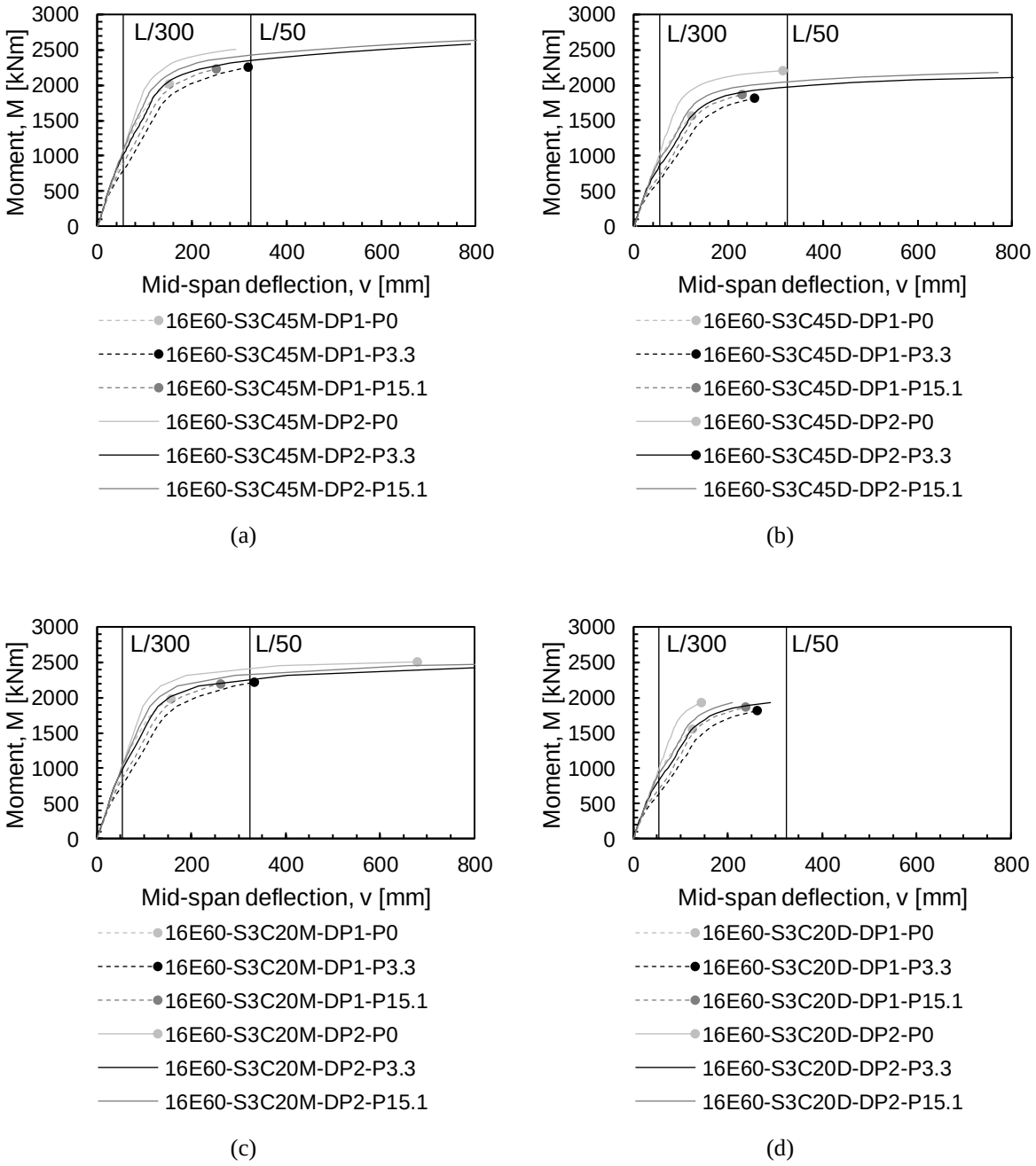

Figure B.17 Moment deflection curves (a) simulation #62-#67, (b) simulation #101-#106, (c) simulation #68-#73, (d) simulation #107-#112

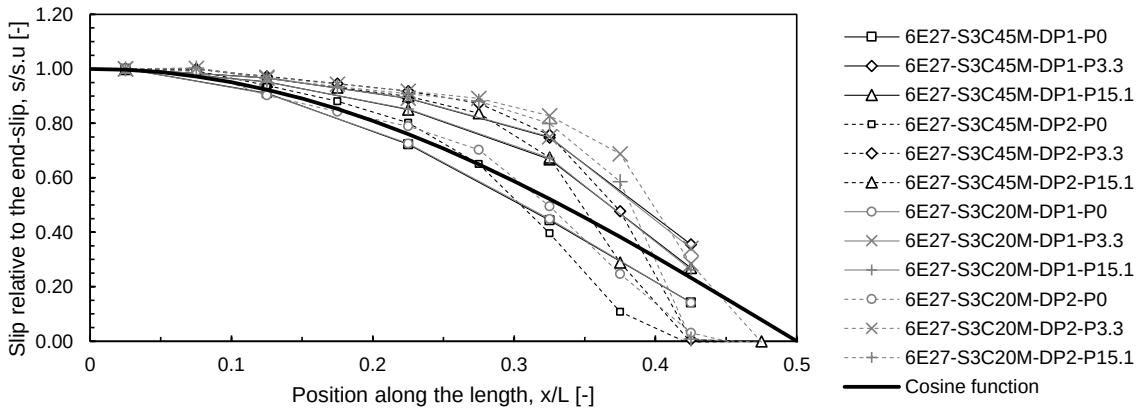

Figure B.18 Slip distribution of 6 m long beams with IPE270

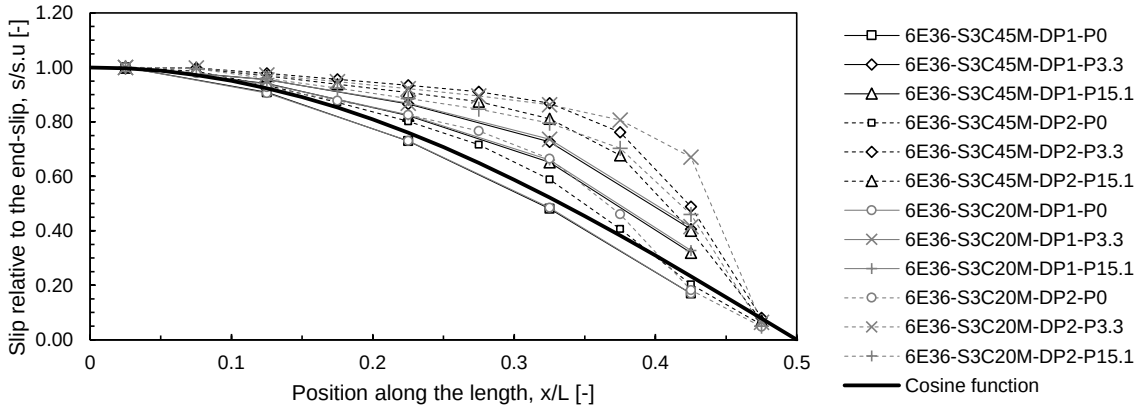

Figure B.19 Slip distribution of 6 m long beams with IPE360

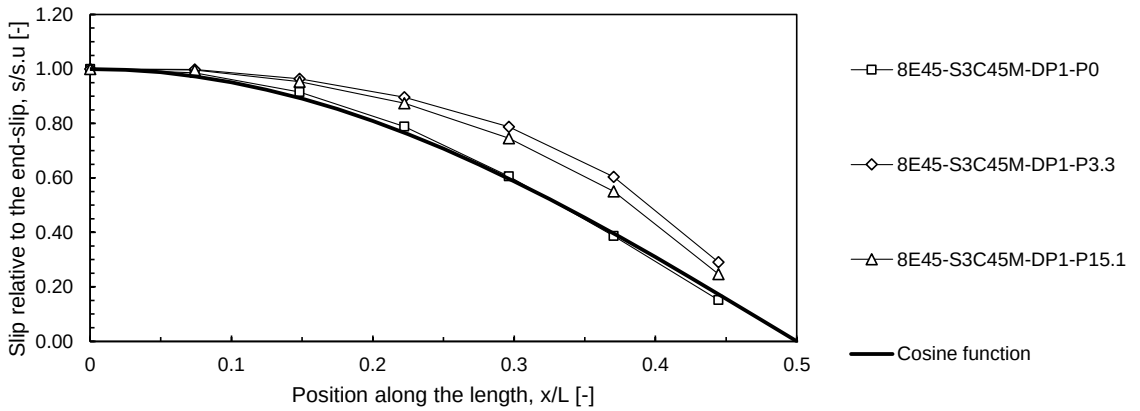

Figure B.20 Slip distribution of 8.1 m long beams with IPE450

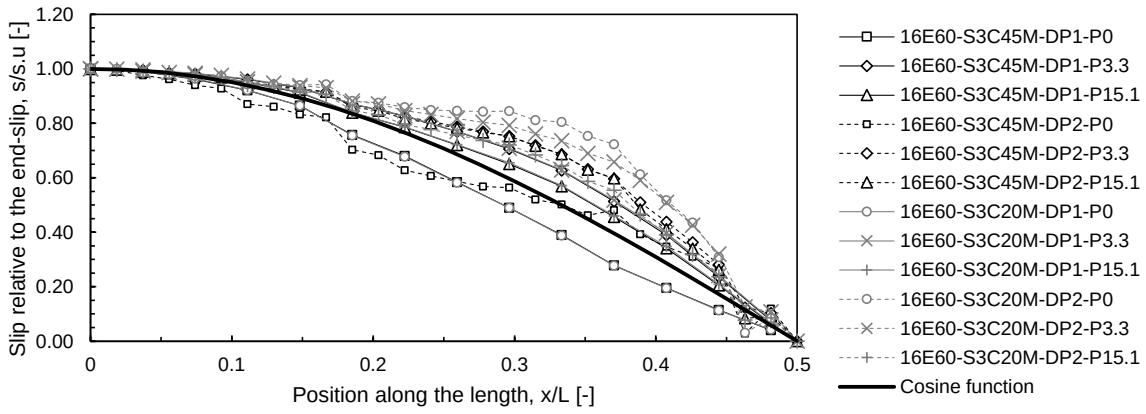

Figure B.21 Slip distribution of 16.2 m long beams with IPE600

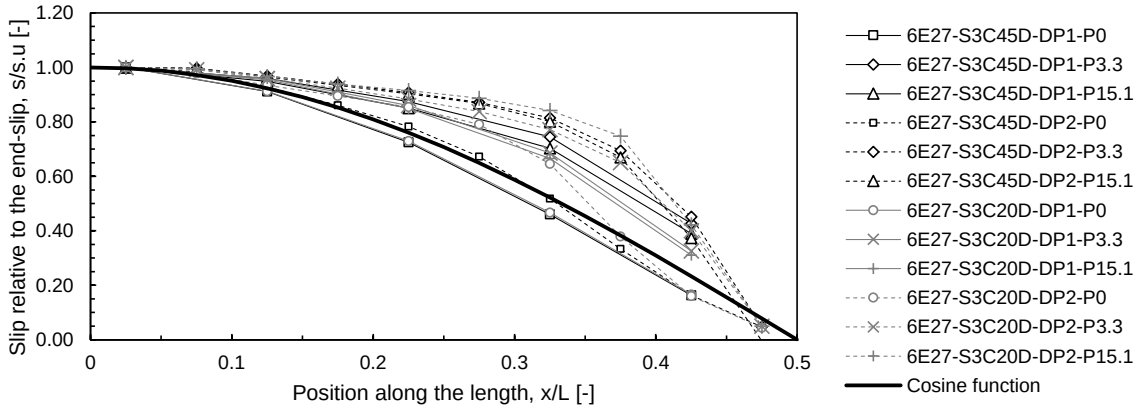

Figure B.22 Slip distribution of 6 m long beams with IPE270 (modelled with design values)

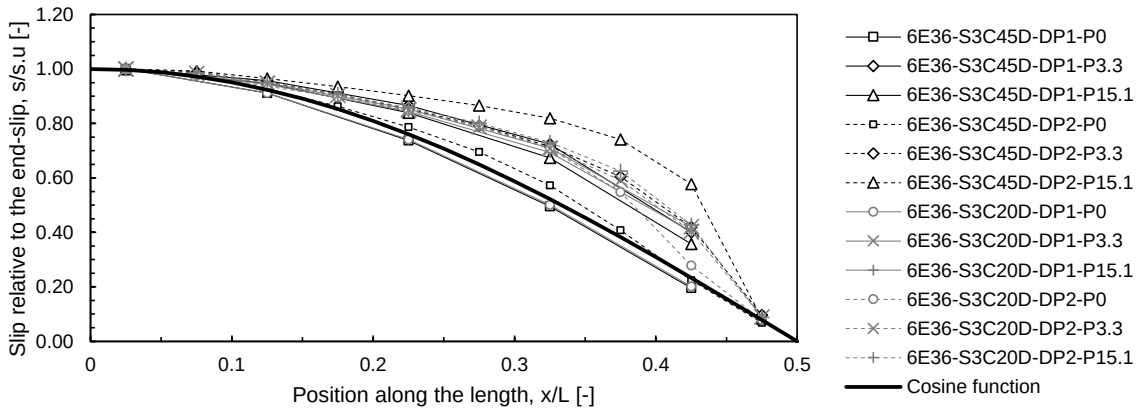

Figure B.23 Slip distribution of 6 m long beams with IPE360 (modelled with design values)

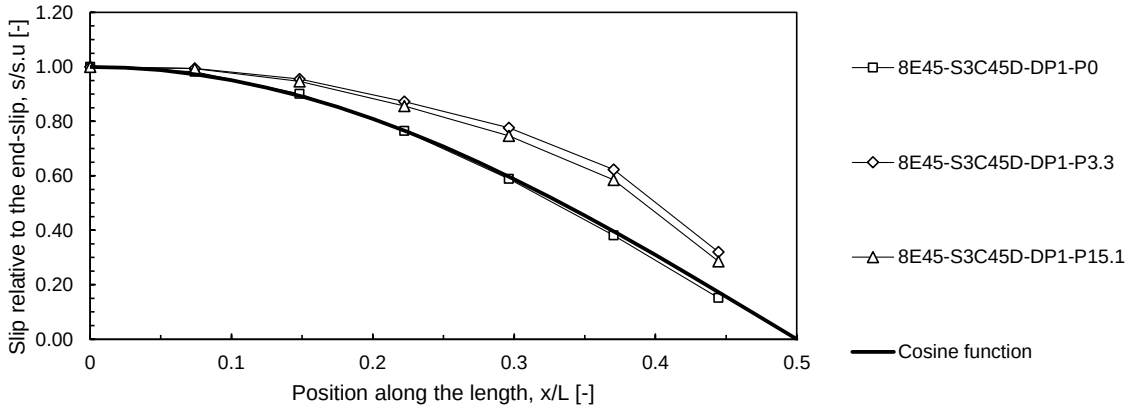

Figure B.24 Slip distribution of 8.1 m long beams with IPE450 (modelled with design values)

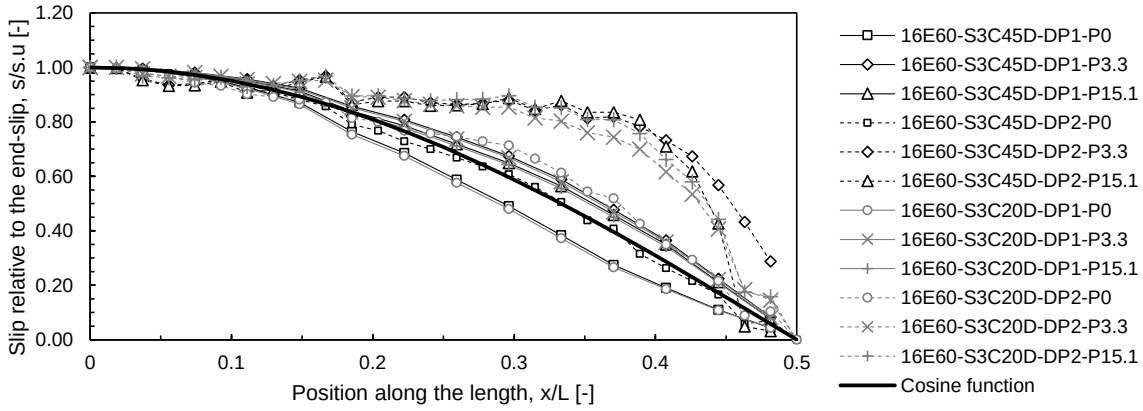

Figure B.25 Slip distribution of 16.2 m long beams with IPE600 (modelled with design values)

Annex C Equations for elastic calculations

C.1 Assumptions

(i) The beam in consideration is as an Euler-Bernoulli beam, i.e. the cross-sections originally plane and perpendicular to the axis of the beam remain plane and perpendicular to the axis of the beam after deformation.

(ii) Only small displacements are considered.

(iii) The material is linear elastic and isotropic.

C.2 Basic material equations – engineering stress and engineering strain

Equations (C.16) and (C.17) present the simplest forms of the engineering stress and the engineering strain:

$$\sigma = F/A \tag{C.16}$$

$$\varepsilon = \Delta l/l_0 \tag{C.17}$$

where σ is the engineering stress, F is the normal force acting on the cross-section and A is the original cross-sectional area, ε is the engineering strain, Δl is the elongation and l_0 is the original length of the element.

Elastic materials do not show any irreversible phenomena due to external loads. In the case of linear elastic isotropic materials the relationship between the stresses are linearly proportional to the strains:

$$\sigma = \sigma_0 + E\varepsilon \tag{C.18}$$

Generally, the initial stresses σ_0 are neglected because they are significantly smaller than the stresses of active loads, so the above equation takes the following form:

$$\sigma = E\varepsilon \tag{C.19}$$

where E is the modulus of elasticity. This equation is referred to as the Hooke's law in standard engineering practice. Using equations (C.16) and (C.19), we obtain the relationship between the strain ε and the normal force F:

$$\varepsilon = \frac{\sigma}{E} = \frac{F}{EA} \tag{C.20}$$

C.3 Basic equations of beam theory

According to the Euler-Bernoulli beam theory the relationship between the deflection and the applied load is:

$$\frac{d^2}{dx^2}\left(EI_y \frac{d^2w(x)}{dx^2}\right) = q_z(x) \tag{C.21}$$

The flexural rigidity EI_y of the beam is often constant along the length, therefore the equation above becomes:

$$EI_y \frac{d^4w(x)}{dx^4} = q_z(x) \tag{C.22}$$

where $w(x)$ is the deflection of the beam and $q(x)$ is the external load.

The rotation $\varphi(x)$ is the first derivative of the deflection:

$$\varphi(x) = \frac{dw(x)}{dx} \tag{C.23}$$

The curvature $\kappa(x)$ is the first derivative of the rotation:

$$\kappa(x) = \frac{d^2w(x)}{dx^2} = \frac{d\varphi(x)}{dx} \tag{C.24}$$

The relationship between the external load $q_z(x)$ and the shear force $V_z(x)$ is:

$$\int q_z(x)\,dx = V_z(x) \tag{C.25}$$

The relationship between the shear force $V_z(x)$ and the bending moment $M_y(x)$ is:

$$\int V_z(x)\,dx = \iint q_z(x)dx^2 = M_y(x) \tag{C.26}$$

or, in another form:

$$\frac{d^2M_y(x)}{dx^2} = \frac{dV_z(x)}{dx} = q_z(x) \tag{C.27}$$

Using equations (C.22) and (C.27) we obtain:

$$M_y(x) = EI_y \frac{d^2w(x)}{dx^2} = EI_y \cdot \kappa(x) \tag{C.28}$$

or:

$$\kappa(x) = \frac{M_y(x)}{EI_y} \tag{C.29}$$

According to the Euler-Bernoulli theory, the neighbouring planar cross-sections have different rotations during pure bending. As a result, the longitudinal fibres that connect them undergo normal strains. The magnitude of these strains $\varepsilon_x(z,x)$ is the product of the difference in rotation between the sections $d\varphi(x)/dx$, and the distance z between the fibre in consideration and the axis of the rotation:

$$\varepsilon_x(z,x) = \frac{d\varphi(x)}{dx} \cdot z = \kappa(x) \cdot z = \frac{M_y(x)}{EI_y} \cdot z \tag{C.30}$$

Using equations (C.19), (C.29) and (C.30), we can express the normal stress $\sigma_x(x,z)$ due to the bending moment as:

$$\sigma_x(x,z) = E \cdot \varepsilon_x(x,z) = E \cdot \kappa(x) \cdot z = E \cdot \frac{M_y(x)}{EI_y} \cdot z = \frac{M_y(x)}{I_y} \cdot z \tag{C.31}$$

C.4 Composite beams with rigid and flexible shear connections

C.4.1 Assumptions

(i) The steel and the concrete can be considered as linear elastic isotropic materials.

(ii) There is no separation between the steel beam and the concrete slab.

(iii) There is no cracking of the concrete.

(iv) The curvature of the steel and the concrete is equal at any section.

C.4.2 Basic equations

In order to determine the second moment of area $I_{y,eff}$ of the composite section, first consider the equilibrium equations of the composite section due to an externally applied moment $M_y(x)$. As a result of the composite action, a compression force $F_{x,c}(x)$ acts in the concrete slab and a tension force $F_{x,a}(x)$ in the steel beam:

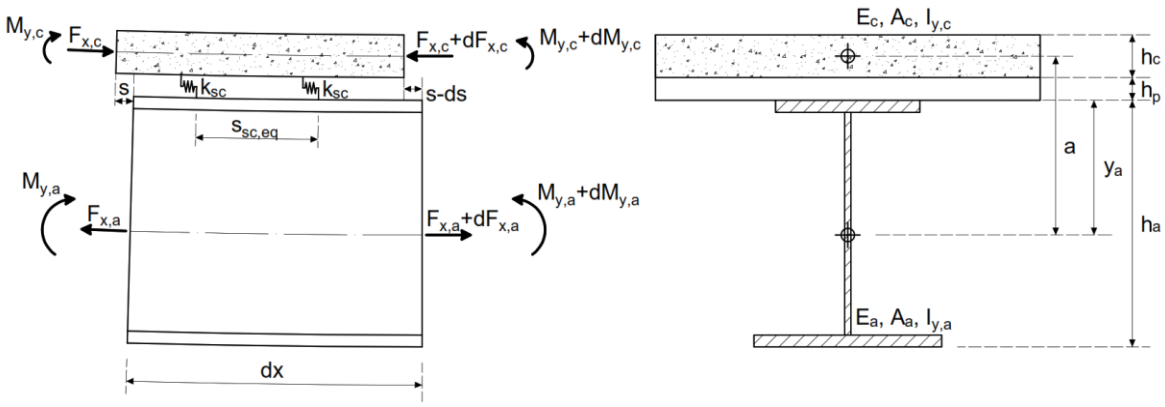

Figure C.1 Theoretical model and cross-sectional forces of a composite beam with flexible shear connection

If there is no externally applied normal force, the magnitudes of these forces are equal. This will be denoted as $F_x(x)$ in the forthcoming.

$$F_{x,a}(x) - F_{x,c}(x) = 0$$

$$\left|F_{x,a}(x)\right| = \left|F_{x,c}(x)\right| = F_x(x) \tag{C.32}$$

The externally applied moment $M_y(x)$ is equilibrated by the moment resisted by the slab $M_{y,c}(x)$, the moment resisted by the steel beam $M_{y,a}(x)$, and the moment generated by the pair of the normal forces $F_x(x)$:

$$M_y(x) = M_{y,c}(x) + M_{y,a}(x) + F_x(x) \cdot a \tag{C.33}$$

where a is the distance between the centroidal axes of the slab and the steel beam. For a typical composite beam, it can be calculated as:

$$a = y_a + h_p + h_c/2 \tag{C.34}$$

where y_a is the distance between the top fibre of the steel beam and its centroidal axis, h_p is the height of the metal decking, and h_c is the depth of the concrete over the metal decking.

The curvature of the slab and the steel beam is the same at any section:

$$\kappa_c(x) = \kappa_a(x) = \kappa(x) \tag{C.35}$$

Using equation (C.29), the previous equation becomes:

$$\frac{M_{y,c}(x)}{E_c I_{y,c}} = \frac{M_{y,a}(x)}{E_a I_{y,a}} = \frac{M_y(x)}{E_a I_{y,eff}} = \kappa(x) \tag{C.36}$$

The modular ratio expresses the ratio of the modulus of elasticity of the steel and of the concrete:

$$n = E_a/E_c \tag{C.37}$$

If we rearrange equation (C.36), we obtain the moment resisted by the concrete:

$$M_{y,c}(x) = \frac{M_y(x)}{E_a I_{y,eff}} E_c I_{y,c} = \frac{M_y(x)}{E_a I_{y,eff}} \cdot \frac{E_a}{n} \cdot I_{y,c} = \frac{M_y(x)}{n \cdot I_{y,eff}} I_{y,c} \tag{C.38}$$

Similarly, the moment resisted by the steel beam is:

$$M_{y,a}(x) = \frac{M_y(x)}{E_a I_{y,eff}} E_a I_{y,a} = \frac{M_y(x)}{I_{y,eff}} I_{y,a} \tag{C.39}$$

Using equation (C.36) in equation (C.33), we can express the second moment of area:

$$M_y(x) = M_{y,c}(x) + M_{y,a}(x) + F_x(x) \cdot a$$

With:

$M_{y,c}(x) = E_c I_{y,c} \kappa(x)$,

$M_{y,a}(x) = E_a I_{y,a} \kappa(x)$, and

$M_y(x) = E_a I_{y,eff} \kappa(x)$; we obtain:

$$E_a I_{y,eff} \kappa(x) = E_c I_{y,c} \kappa(x) + E_a I_{y,a} \kappa(x) + F_x(x) \cdot a$$

With:

$E_c = E_a/n$,

$$E_a I_{y,eff} \kappa(x) = \frac{E_a}{n} I_{y,c} \kappa(x) + E_a I_{y,a} \kappa(x) + F_x(x) \cdot a$$

$$E_a I_{y,eff} \kappa(x) = \left(\frac{I_{y,c}}{n} + I_{y,a}\right) E_a \kappa(x) + F_x(x) \cdot a$$

Dividing both sides by $E_a \kappa(x)$:

$$I_{y,eff} = \frac{I_{y,c}}{n} + I_{y,a} + \frac{F(x) \cdot a}{E_a \kappa(x)} \tag{C.40}$$

The rate of change of slip *ds(x)/dx* is determined by the strain difference between the steel and the concrete at their contact surface i.e. at the top fibre of the steel beam:

$$\frac{ds(x)}{dx} = \varepsilon_{x,a}(z,x) - \varepsilon_{x,c}(z,x) \tag{C.41}$$

The strains in the steel and in the concrete can be calculated as the sum of the strains arising from the normal force and the bending moment. It is important to note that attention needs to be payed to the signs of the strains as the absolute values of the force *F(x)* and the distance *z* is used. Positive sign denotes elongation and negative sign denotes compression. Using equations (C.20) and (C.30), we can obtain the strains at the contact surface:

$$\varepsilon_{x,c}(z,x) = \frac{M_{y,c}(x)}{E_c I_{y,c}} \cdot \left(h_p + \frac{h_c}{2}\right) - \frac{F_x(x)}{E_c A_c} \tag{C.42}$$

$$\varepsilon_{x,a}(z,x) = -\frac{M_{y,a}(x)}{E_a I_{y,a}} \cdot y_a + \frac{F_x(x)}{E_a A_a} \tag{C.43}$$

By substituting equations (C.42) and (C.43) into equation (C.41), the rate of change of slip is:

$$\frac{ds(x)}{dx} = -\frac{M_{y,a}(x)}{E_a I_{y,a}} \cdot y_a - \frac{M_{y,c}(x)}{E_c I_{y,c}} \cdot \left(h_p + \frac{h_c}{2}\right) + \frac{F_x(x)}{E_a A_a} + \frac{F_x(x)}{E_c A_c} \tag{C.44}$$

If we substitute equations (C.37)(8.4) and (C.38) into the equation above, we obtain:

$$\frac{ds(x)}{dx} = -\frac{\frac{M_y(x)}{I_{y,eff}} I_{y,a}}{E_a I_{y,a}} \cdot y_a - \frac{\frac{M_y(x)}{n \cdot I_{y,eff}} I_{y,c}}{E_c I_{y,c}} \cdot \left(h_p + \frac{h_c}{2}\right) + \frac{F_x(x)}{E_a A_a} + \frac{F_x(x)}{E_c A_c}$$

$$\frac{ds(x)}{dx} = -\frac{\frac{M_y(x)}{I_{y,eff}}}{E_a} \cdot y_a - \frac{\frac{M_y(x)}{n \cdot I_{y,eff}}}{E_c} \cdot \left(h_p + \frac{h_c}{2}\right) + \frac{F_x(x)}{E_a A_a} + \frac{F_x(x)}{E_c A_c}$$

With:

$$E_c = E_a / n$$

$$\frac{ds(x)}{dx} = -\frac{\frac{M_y(x)}{I_{y,eff}}}{E_a} \cdot y_a - \frac{\frac{M_y(x)}{n \cdot I_{y,eff}}}{\frac{E_a}{n}} \cdot \left(h_p + \frac{h_c}{2}\right) + \frac{F_x(x)}{E_a A_a} + \frac{F_x(x)}{\frac{E_a}{n} A_c}$$

$$\frac{ds(x)}{dx} = -M_y(x) \cdot \frac{y_a + h_p + \frac{h_c}{2}}{E_a I_{y,eff}} + \frac{F_x(x)}{E_a A_a} + \frac{F_x(x) \cdot n}{E_a A_c}$$

with:

$$a = y_a + h_p + \frac{h_c}{2}$$

$$\frac{ds(x)}{dx} = -M_y(x) \cdot \frac{a}{E_a I_{y,eff}} + \frac{F_x(x)}{E_a}\left(\frac{1}{A_a} + \frac{n}{A_c}\right) \tag{C.45}$$

If we rearrange equation (C.45) for $M_y(x)$, we get:

$$M_y(x) \cdot \frac{a}{E_a I_{y,eff}} = -\frac{ds(x)}{dx} + \frac{F_x(x)}{E_a}\left(\frac{1}{A_a} + \frac{n}{A_c}\right)$$

$$M_y(x) = -\frac{ds(x)}{dx} \cdot \frac{E_a I_{y,eff}}{a} + \frac{F_x(x)}{E_a} \cdot \frac{E_a I_{y,eff}}{a}\left(\frac{1}{A_a} + \frac{n}{A_c}\right)$$

$$M_y(x) = -\frac{ds(x)}{dx} \cdot \frac{E_a I_{y,eff}}{a} + \frac{F_x(x) I_{y,eff}}{a}\left(\frac{A_c + nA_a}{A_c A_a}\right) \tag{C.46}$$

C.5 Elastic normal stresses from bending

The normal stresses from bending can be determined using equation (C.31). Therefore, the normal stress in the concrete from bending can be calculated as:

$$\sigma_{x,c}(z,x) = \frac{M_{y,c}(x)}{I_{y,c}} \cdot z_c \tag{C.47}$$

where z_c is the distance between the fibre in consideration from the centroidal axis of the concrete.

Using equation (C.38), we obtain:

$$\sigma_{x,c}(z,x) = \frac{\frac{M_y(x)}{n \cdot I_{y,eff}} I_{y,c}}{I_{y,c}} \cdot z_c = \frac{M_y(x)}{n \cdot I_{y,eff}} \cdot z_c \tag{C.48}$$

Similarly, using equations (C.31) and (C.39) we can express the normal stress in the steel:

$$\sigma_{x,a}(z,x) = \frac{M_{y,a}(x)}{I_{y,a}} \cdot z_a = \frac{\frac{M_y(x)}{I_{y,eff}} I_{y,a}}{I_{y,a}} \cdot z_a = \frac{M_y(x)}{I_{y,eff}} \cdot z_a \tag{C.49}$$

In the equations above $M_{y,c}(x)$, $M_{y,a}(x)$ and $M_y(x)$ denote the bending moment that acts on the concrete, the steel and the composite section respectively.

C.5.1 Second moment of area for rigid connection

In order to determine the second moment of area, we use equation (C.40):

$$I_{y,eff} = \frac{I_{y,c}}{n} + I_{y,a} + \frac{F_x(x) \cdot a}{E_a \kappa(x)}$$

With:

$$E_a \kappa(x) = M_y(x) / I_{y,eff}$$

$$I_{y,eff} = \frac{I_{y,c}}{n} + I_{y,a} + \frac{F_x(x) \cdot a}{\frac{M_y(x)}{I_{y,eff}}}$$

$$I_{y,eff} = \frac{I_{y,c}}{n} + I_{y,a} + \frac{F_x(x) \cdot a \cdot I_{y,eff}}{M_y(x)} \quad \text{(C.50)}$$

In the case of rigid shear connection, there is no slip between the slab and the steel beam:

$$s(x) = 0 \quad \text{(C.51)}$$

Therefore:

$$\frac{ds(x)}{dx} = 0 \quad \text{(C.52)}$$

So equation (C.46) becomes:

$$M_y(x) = \frac{F_x(x) I_{y,eff}}{a} \left(\frac{A_c + nA_a}{A_c A_a} \right) \quad \text{(C.53)}$$

We obtain the effective second moment of area of composite beams with rigid shear connectors by substituting equation (C.53) into equation (C.50):

$$I_{y,eff} = \frac{I_{y,c}}{n} + I_{y,a} + \frac{F_x(x) \cdot a \cdot I_{y,eff}}{\frac{F_x(x) I_{y,eff}}{a} \left(\frac{A_c + nA_a}{A_c A_a} \right)}$$

$$I_{y,eff} = \frac{I_{y,c}}{n} + I_{y,a} + \frac{a^2}{\left(\frac{A_c + nA_a}{A_c A_a} \right)}$$

$$I_{y,eff} = I_{y,a} + \frac{I_{y,c}}{n} + \frac{A_c A_a}{A_c + nA_a} \cdot a^2 \quad \text{(C.54)}$$

C.5.2 Second moment of area for flexible connection

In the case of flexible shear connection, generally the slip *s(x)* is assumed to vary according to a cosine function along the length of the beam [43], [44]. As a result, the compression force *F(x)* and moment $M_y(x)$ is assumed to vary according to a sine function. This moment diagram corresponds to an external load $q_z(x)$ that is distributed according to a sine function along the length. However, it is still a good approximation for a uniformly loaded beam where the moment diagram is a second order parabola.

The second moment of area can be determined in the same way as in the case of rigid shear connection. The assumed slip function is:

$$s(x) = \bar{s} \cdot \cos\left(\frac{\pi x}{L}\right) \tag{C.55}$$

where $\bar{s}$ is the end slip, *L* is the span of the beam, and *x* is the distance along the length of the beam from a support.

Therefore:

$$\frac{ds(x)}{dx} = -\bar{s} \cdot \frac{\pi}{L} \cdot \sin\left(\frac{\pi x}{L}\right) \tag{C.56}$$

The shear connector forces $P_{sc}(x)$ are not considered in discrete points, but over a unit length:

$$P_{sc}(x) = s(x) \cdot \frac{k_{sc}}{s_{sc,eq}} = \bar{s} \cdot \cos\left(\frac{\pi x}{L}\right) \cdot \frac{k_{sc}}{s_{sc,eq}} \tag{C.57}$$

where k_{sc} is the stiffness of the shear connectors, and $s_{sc,eq}$ is the equivalent longitudinal spacing. The compression force in the slab $F_x(x)$ can be determined from the integral of the shear connector forces:

$$F_x(x) = \int_0^x P_{sc}(x)\, dx = \bar{s} \cdot \frac{k_{sc}}{s_{sc,eq}} \int_0^x \cos\left(\frac{\pi x}{L}\right)\, dx =$$

$$F_x(x) = \bar{s} \cdot \frac{k_{sc}}{s_{sc,eq}} \cdot \left[\frac{L}{\pi} \cdot \sin\left(\frac{\pi x}{L}\right)\right]_0^x$$

$$F_x(x) = \bar{s} \cdot \frac{k_{sc}}{s_{sc,eq}} \cdot \frac{L}{\pi} \cdot \sin\left(\frac{\pi x}{L}\right) - \bar{s} \cdot \frac{k_{sc}}{s_{sc,eq}} \cdot \frac{L}{\pi} \cdot \sin 0$$

$$F_x(x) = \bar{s} \cdot \frac{k_{sc}}{s_{sc,eq}} \cdot \frac{L}{\pi} \cdot \sin\left(\frac{\pi x}{L}\right) \tag{C.58}$$

Using equations (8.16) and (8.18), equation (8.7) becomes:

$$M_y(x) = \bar{s} \cdot \frac{\pi}{L} \cdot \sin\left(\frac{\pi x}{L}\right) \cdot \frac{E_a I_{y,eff}}{a} + \bar{s} \cdot \frac{k_{sc}}{s_{sc,eq}} \cdot \frac{L}{\pi} \cdot \sin\left(\frac{\pi x}{L}\right) \frac{I_{y,eff}}{a} \left(\frac{A_c + nA_a}{A_c A_a}\right)$$

$$M_y(x) = \bar{s} \cdot \sin\left(\frac{\pi x}{L}\right) \cdot \frac{I_{y,eff}}{a}\left(E_a \cdot \frac{\pi}{L} + \frac{k_{sc}}{s_{sc,eq}} \cdot \frac{L}{\pi}\left(\frac{A_c + nA_a}{A_c A_a}\right)\right) \tag{C.59}$$

Substituting equations (C.59) and (C.58) into equation (C.50) we obtain the effective second moment of area of composite beams with flexible shear connectors:

$$I_{y,eff} = \frac{I_{y,c}}{n} + I_{y,a} + \frac{\bar{s} \cdot \frac{k_{sc}}{s_{sc,eq}} \cdot \frac{L}{\pi} \cdot \sin\left(\frac{\pi x}{L}\right) \cdot a \cdot I_{y,eff}}{\bar{s} \cdot \sin\left(\frac{\pi x}{L}\right) \cdot \frac{I_{y,eff}}{a}\left(E_a \cdot \frac{\pi}{L} + \frac{k_{sc}}{s_{sc,eq}} \cdot \frac{L}{\pi}\left(\frac{A_c + nA_a}{A_c A_a}\right)\right)}$$

$$I_{y,eff} = \frac{I_{y,c}}{n} + I_{y,a} + \frac{\frac{k_{sc}}{s_{sc,eq}} \cdot \frac{L}{\pi} \cdot a^2}{E_a \cdot \frac{\pi}{L} + \frac{k_{sc}}{s_{sc,eq}} \cdot \frac{L}{\pi}\left(\frac{A_c + nA_a}{A_c A_a}\right)}$$

Dividing both the numerator and the denominator by $((k_{sc} \cdot L)/(s_{sc,eq} \cdot \pi))$

$$I_{y,eff} = \frac{I_{y,c}}{n} + I_{y,a} + \frac{a^2}{\frac{E_a}{\left(\frac{k_{sc}}{s_{sc,eq}}\right)}\left(\frac{\pi}{L}\right)^2 + \frac{A_c + nA_a}{A_c A_a}}$$

Multiplying both the numerator and the denominator by A_c/n

$$I_{y,eff} = \frac{I_{y,c}}{n} + I_{y,a} + \frac{\left(\frac{A_c}{n}\right) a^2}{\frac{E_a}{\left(\frac{k_{sc}}{s_{sc,eq}}\right)}\left(\frac{\pi}{L}\right)^2 \left(\frac{A_c}{n}\right) + \left(\frac{n}{A_c} + \frac{1}{A_a}\right)\left(\frac{A_c}{n}\right)}$$

$$I_{y,eff} = \frac{I_{y,c}}{n} + I_{y,a} + \frac{\left(\frac{A_c}{n}\right) a^2}{\frac{E_a}{\left(\frac{k_{sc}}{s_{sc,eq}}\right)}\left(\frac{\pi}{L}\right)^2 \left(\frac{A_c}{n}\right) + 1 + \frac{A_c}{nA_a}}$$

$$I_{y,eff} = I_{y,a} + \frac{I_{y,c}}{n} + \frac{A_c/n}{1 + \frac{A_c}{nA_s} + \left(\frac{E_a}{k_{sc}/s_{sc,eq}}\right)\left(\frac{\pi}{L}\right)^2 \left(\frac{A_c}{n}\right)} \cdot a^2 \tag{C.60}$$

C.5.3 Relationship between the end slip and the moment at mid-span

In order to determine the relationship between the end slip and the moment at mid-span, we need to rearrange equation (C.59) for the end slip:

$$M_y(x) = \bar{s} \cdot \sin\left(\frac{\pi x}{L}\right) \cdot \frac{I_{y,eff}}{a}\left(E_a \cdot \frac{\pi}{L} + \frac{k_{sc}}{s_{sc,eq}} \cdot \frac{L}{\pi}\left(\frac{A_c + nA_a}{A_c A_a}\right)\right) \tag{C.61}$$

With:

$$x = L/2$$

$$M_y(L/2) = \bar{s} \cdot \sin\left(\frac{\pi}{2}\right) \cdot \frac{I_{y,eff}}{a}\left(E_a \cdot \frac{\pi}{L} + \frac{k_{sc}}{s_{sc,eq}} \cdot \frac{L}{\pi}\left(\frac{A_c + nA_a}{A_c A_a}\right)\right)$$

With:

$$\bar{M} = M_y(L/2)$$

$$\bar{M} = \bar{s} \cdot 1 \cdot \frac{I_{y,eff}}{a}\left(E_a \cdot \frac{\pi}{L} + \frac{k_{sc}}{s_{sc,eq}} \cdot \frac{L}{\pi}\left(\frac{A_c + nA_a}{A_c A_a}\right)\right)$$

$$\bar{s} = \frac{\bar{M}}{\frac{I_{y,eff}}{a}\left(E_a \cdot \frac{\pi}{L} + \frac{k_{sc}}{s_{sc,eq}} \cdot \frac{L}{\pi}\left(\frac{A_c + nA_a}{A_c A_a}\right)\right)}$$

$$\bar{s} = \frac{\bar{M} \cdot a}{I_{y,eff}\left(E_a \cdot \frac{\pi}{L} + \frac{k_{sc}}{s_{sc,eq}} \cdot \frac{L}{\pi}\left(\frac{A_c + nA_a}{A_c A_a}\right)\right)}$$

$$\bar{s} = \frac{\bar{M} \cdot a \cdot \frac{\pi}{L}}{I_{y,eff}\left(\frac{E_a}{\left(\frac{L}{\pi}\right)^2} + \frac{k_{sc}}{s_{sc,eq}} \cdot \left(\frac{A_c + nA_a}{A_c A_a}\right)\right)}$$

$$\bar{s} = \frac{\bar{M} \cdot a \cdot \frac{s_{sc,eq}}{k_{sc}} \cdot \frac{\pi}{L}}{I_{y,eff}\left(\frac{E_a}{\left(\frac{k_{sc}}{s_{sc,eq}}\right)\left(\frac{L}{\pi}\right)^2} + \frac{A_c + nA_a}{A_c A_a}\right)}$$

With the introduction of the following parameter:

$$S_k = \frac{a}{\frac{E_a}{\left(\frac{k_{sc}}{s_{sc,eq}}\right)\left(\frac{L}{\pi}\right)^2} + \frac{A_c + nA_a}{A_c A_a}} \tag{C.62}$$

$$\bar{s} = \bar{M}\frac{S_k}{I_{y,eff}}\frac{s_{sc,eq}}{k_{sc}}\frac{\pi}{L} \tag{C.63}$$

Where $\bar{M}$ is the moment at mid-span.

Alternatively, the mid-span moment can be expressed based on the end slip:

$$\bar{M} = \bar{s}\frac{I_{y,eff}}{S_k}\frac{k_{sc}}{s_{sc,eq}}\frac{L}{\pi} \tag{C.64}$$

$$\bar{M} = \bar{s}\frac{I_{y,eff}}{S_k}\frac{k_{sc}}{s_{sc,eq}}\frac{L}{\pi} \tag{C.65}$$

C.5.4 Elastic deflection determination

The elastic deflection of a composite beam can be determined as the double integral of the curvature function.

$$\kappa(x) = \frac{M(x)}{E_a I_{y,eff}} \tag{C.66}$$

When the beam in consideration is prismatic, i.e. the cross-section is uniform along the length, the well-known formulations can be used for the calculation of the elastic deflections. These formulations are summarised here for the basic load cases.

For a point load *P* at mid-span:

$$\bar{w} = \frac{PL^3}{48 \cdot E_a I_{y,eff}} \tag{C.67}$$

For symmetric 2-point loads acting at a distance *e* measured from the supports:

$$\bar{w} = \frac{Pe}{24 \cdot E_a I_{y,eff}} \cdot (3L^2 - 4e^2) \tag{C.68}$$

For uniformly distributed load:

$$\bar{w} = \frac{5}{384} \cdot \frac{qL^4}{E_a I_{y,eff}} \tag{C.69}$$

C.5.5 Location of the elastic neutral axes

The slab and the steel beam have their own elastic neutral axis (see Figure C.2):

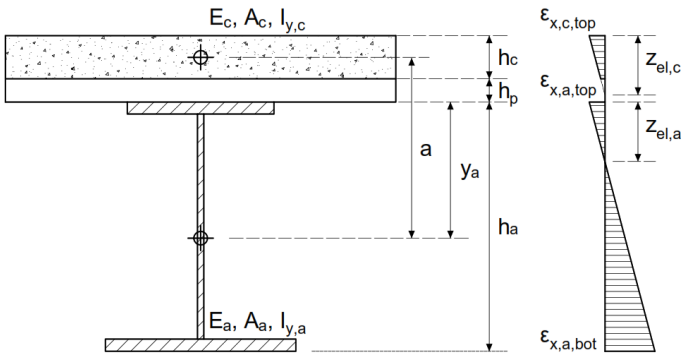

Figure C.2 Strain diagram of a composite beam with flexible shear connection

If there is no shear connection, each element has its neutral axis in its centroidal axis. Using the notations of the figure above, this means:

$$z_{el,c} = h_c/2 \tag{C.70}$$

$$z_{el,a} = y_a \tag{C.71}$$

where $z_{el,c}$ is the distance between the neutral axis of the concrete and its extreme fibre in compression, and $z_{el,a}$ is the distance between the neutral axis of the steel beam and its extreme fibre in compression.

If the connection between the slab and the steel beam is rigid, their neutral axes coincide:

$$z_{el,c} = h_c + h_p + z_{el,a} \tag{C.72}$$

In the case of a flexible shear connection, the location of the elastic neutral axes depends on the stiffness and spacing of the shear connectors.

Elastic neutral axis in the concrete

At any section, the concrete is subjected to a bending moment $M_{y,c}(x)$ and a compression force $F_x(x)$. The corresponding strains are presented in Figure C.3.

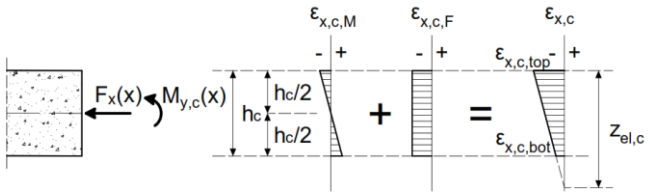

Figure C.3 Strains in the concrete slab

The strains on the top and on the bottom fibre are:

$$\varepsilon_{x,c}(x,z) = \frac{M_{y,c}(x)}{E_c I_{y,c}} \cdot z - \frac{F_x(x)}{E_c A_c} \tag{C.73}$$

$$\varepsilon_{x,c,top}(x) = \varepsilon_{x,c}\left(x, -\frac{h}{2}\right)$$

$$\varepsilon_{x,c,bot}(x) = \varepsilon_{x,c}\left(x, +\frac{h}{2}\right)$$

$$\varepsilon_{x,c,top}(x) = \frac{M_{y,c}(x)}{E_c I_{y,c}} \cdot \left(-\frac{h_c}{2}\right) - \frac{F_x(x)}{E_c A_c}$$

With:

$$M_{y,c}(x) = \frac{M_y(x)}{n \cdot I_{y,eff}} I_{y,c}$$

$$\varepsilon_{x,c,top}(x) = \frac{\frac{M_y(x)}{n \cdot I_{y,eff}} I_{y,c}}{E_c I_{y,c}} \cdot \left(-\frac{h_c}{2}\right) - \frac{F_x(x)}{E_c A_c}$$

$$\varepsilon_{x,c,top}(x) = \frac{1}{E_c}\left(-\frac{M_y(x)}{n \cdot I_{y,eff}}\left(\frac{h_c}{2}\right) - \frac{F_x(x)}{A_c}\right)$$

With:

$$\sigma_{x,c,M}(x) = \frac{M_y(x)}{n \cdot I_{y,eff}} \left(\frac{h_c}{2}\right)$$

and

$$\sigma_{x,c,F}(x) = \frac{F_x(x)}{A_c}$$

$$\varepsilon_{x,c,top}(x) = \frac{1}{E_c}\Big(-\sigma_{x,c,M}(x) - \sigma_{x,c,F}(x)\Big) \tag{C.74}$$

$$\varepsilon_{x,c,bot}(x) = \frac{1}{E_c}\Big(+\sigma_{x,c,M}(x) - \sigma_{x,c,F}(x)\Big) \tag{C.75}$$

At the neutral axis, the strains are zero. From similar triangles (see Figure C.3):

$$\frac{h_c}{\varepsilon_{x,c,top}(x) - \varepsilon_{x,c,bot}(x)} = \frac{z_{el,c}}{\varepsilon_{x,c,top}(x) - 0} \tag{C.76}$$

Rearranging the previous equation for $z_{el,c}$, and substituting equations (C.74) and (C.75):

$$z_{el,c} = \frac{h_c \cdot \varepsilon_{x,c,top}(x)}{\varepsilon_{x,c,top}(x) - \varepsilon_{x,c,bot}(x)}$$

$$z_{el,c} = \frac{h_c \cdot \frac{1}{E_c}\Big(-\sigma_{x,c,M}(x) - \sigma_{x,c,F}(x)\Big)}{\frac{1}{E_c}\Big(-\sigma_{x,c,M}(x) - \sigma_{x,c,F}(x)\Big) - \frac{1}{E_c}\Big(+\sigma_{x,c,M}(x) - \sigma_{x,c,F}(x)\Big)}$$

$$z_{el,c} = \frac{h_c\Big(-\sigma_{x,c,M}(x) - \sigma_{x,c,F}(x)\Big)}{-\sigma_{x,c,M}(x) - \sigma_{x,c,F}(x) - \sigma_{x,c,M}(x) + \sigma_{x,c,F}(x)}$$

$$z_{el,c} = \frac{-h_c\Big(\sigma_{x,c,M}(x) + \sigma_{x,c,F}(x)\Big)}{-2\,\sigma_{x,c,M}(x)}$$

$$z_{el,c} = \frac{h_c\Big(\sigma_{x,c,M}(x) + \sigma_{x,c,F}(x)\Big)}{2\,\sigma_{x,c,M}(x)} \tag{C.77}$$

Using the relationships between the compression force in the concrete $F_x(x)$ and the end slip $\bar{s}$ (Eq. (C.58)) and the between the end slip and the moment at mid span (Eq. (C.63)) the compression force can be expressed in the function of the mid-span moment $\bar{M}$:

$$F_x(x) = \bar{s} \cdot \frac{k_{sc}}{s_{sc,eq}} \cdot \frac{L}{\pi} \cdot \sin\left(\frac{\pi x}{L}\right)$$

With:

$$\bar{s} = \bar{M} \frac{S_k}{I_{y,eff}} \frac{s_{sc,eq}}{k_{sc}} \frac{\pi}{L}$$

$$F_x(x) = \bar{M} \frac{S_k}{I_{y,eff}} \frac{s_{sc,eq}}{k_{sc}} \frac{\pi}{L} \cdot \frac{k_{sc}}{s_{sc,eq}} \cdot \frac{L}{\pi} \cdot \sin\left(\frac{\pi x}{L}\right) \tag{C.78}$$

From equation (C.61), the moment $M_y(x)$ in the function of the mid-span moment is:

$$M_y(x) = \bar{M} \cdot \sin\left(\frac{\pi x}{L}\right) \tag{C.79}$$

Substituting the equations above into equation (C.77), the location of the elastic neutral axis can be expressed by equation (C.80)(8.32):

$$z_{el,c} = \frac{h_c \left(\sigma_{x,c,M}(x) + \sigma_{x,c,F}(x) \right)}{2\, \sigma_{x,c,M}(x)}$$

with:

$$\sigma_{x,c,M}(x) = \frac{M_y(x)}{n \cdot I_{y,eff}} \left(\frac{h_c}{2}\right)$$

and

$$\sigma_{x,c,F}(x) = \frac{F_x(x)}{A_c}$$

$$z_{el,c} = \frac{h_c \left(\frac{M_y(x)}{n \cdot I_{y,eff}} \left(\frac{h_c}{2}\right) + \frac{F_x(x)}{A_c} \right)}{2\, \frac{M_y(x)}{n \cdot I_{y,eff}} \left(\frac{h_c}{2}\right)}$$

$$z_{el,c} = \frac{h_c \left(\frac{\bar{M} \cdot \sin\left(\frac{\pi x}{L}\right)}{n \cdot I_{y,eff}} \left(\frac{h_c}{2}\right) + \frac{\bar{M} \frac{S_k}{I_{y,eff}} \frac{s_{sc,eq}}{k_{sc}} \frac{\pi}{L} \cdot \frac{k_{sc}}{s_{sc,eq}} \cdot \frac{L}{\pi} \cdot \sin\left(\frac{\pi x}{L}\right)}{A_c} \right)}{2\, \frac{\bar{M} \cdot \sin\left(\frac{\pi x}{L}\right)}{n \cdot I_{y,eff}} \left(\frac{h_c}{2}\right)}$$

$$z_{el,c} = \frac{h_c}{2} + \frac{n \cdot S_k}{A_c} \tag{C.80}$$

Elastic neutral axis in the steel

At any section, the steel beam is subjected to a bending moment $M_{y,a}(x)$ and a tension force $F_x(x)$. The corresponding strains are presented in Figure C.4.

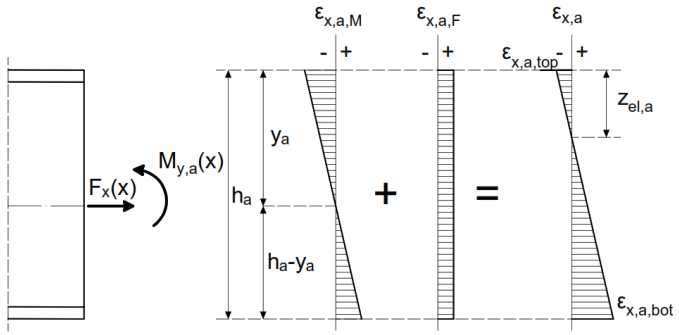

Figure C.4 Strains in the steel beam

The strains on the top and on the bottom fibre are:

$$\varepsilon_{x,a}(x,z) = \frac{M_{y,a}(x)}{E_a I_{y,a}} \cdot z - \frac{F_x(x)}{E_a A_a} \tag{C.81}$$

$$\varepsilon_{x,a,top}(x) = \varepsilon_{x,a}(x,-y_s)$$

$$\varepsilon_{x,a,bot}(x) = \varepsilon_{x,c}(x,h_a - y_s)$$

$$\varepsilon_{x,a,top}(x) = \frac{M_{y,a}(x)}{E_a I_{y,a}} \cdot (-y_s) + \frac{F_x(x)}{E_a A_a}$$

with:

$$M_{y,a}(x) = \frac{M_y(x)}{I_{y,eff}} I_{y,a}$$

$$\varepsilon_{x,a,top}(x) = \frac{\frac{M_y(x)}{I_{y,eff}} I_{y,a}}{E_a I_{y,a}} \cdot (-y_s) + \frac{F_x(x)}{E_a A_a}$$

$$\varepsilon_{x,a,top}(x) = \frac{1}{E_a}\left(-\frac{M_y(x)}{I_{y,eff}} \cdot y_s + \frac{F_x(x)}{A_a}\right)$$

and

$$\varepsilon_{x,a,bot}(x) = \frac{1}{E_a}\left(\frac{M_y(x)}{I_{y,eff}} \cdot (h_a - y_s) + \frac{F_x(x)}{A_a}\right)$$

With:

$$\sigma_{x,a,M,top}(x) = \frac{M_y(x)}{I_{y,eff}} \cdot y_s$$

$$\sigma_{x,a,M,bot}(x) = \frac{M_y(x)}{I_{y,eff}} \cdot (h_a - y_s)$$

and

$$\sigma_{x,a,F}(x) = \frac{F_x(x)}{A_a}$$

$$\varepsilon_{x,a,top}(x) = \frac{1}{E_a}\Big(-\sigma_{x,a,M,top}(x) + \sigma_{x,a,F}(x)\Big) \tag{C.82}$$

$$\varepsilon_{x,a,bot}(x) = \frac{1}{E_a}\Big(+\sigma_{x,a,M,bot}(x) + \sigma_{x,a,F}(x)\Big) \tag{C.83}$$

At the neutral axis, the strains are zero. From similar triangles (see Figure C.4):

$$\frac{h_a}{\varepsilon_{x,a,top}(x) - \varepsilon_{x,a,bot}(x)} = \frac{z_{el,a}}{\varepsilon_{x,a,top}(x) - 0} \tag{C.84}$$

Rearranging the previous equation for $z_{el,a}$, and substituting equations (C.82) and (C.83):

$$z_{el,a} = \frac{h_a \cdot \varepsilon_{x,a,top}(x)}{\varepsilon_{x,a,top}(x) - \varepsilon_{x,a,bot}(x)}$$

$$z_{el,a} = \frac{h_a \cdot \frac{1}{E_a}\Big(-\sigma_{x,a,M,top}(x) + \sigma_{x,c,F}(x)\Big)}{\frac{1}{E_a}\Big(-\sigma_{x,a,M,top}(x) + \sigma_{x,a,F}(x)\Big) - \frac{1}{E_a}\Big(+\sigma_{x,a,M,bot}(x) + \sigma_{x,a,F}(x)\Big)}$$

$$z_{el,a} = \frac{h_a \cdot \Big(-\sigma_{x,a,M,top}(x) + \sigma_{x,c,F}(x)\Big)}{-\sigma_{x,a,M,top}(x) + \sigma_{x,a,F}(x) - \sigma_{x,a,M,bot}(x) - \sigma_{x,a,F}(x)}$$

$$z_{el,a} = \frac{h_a \cdot \Big(\sigma_{x,a,M,top}(x) - \sigma_{x,c,F}(x)\Big)}{\sigma_{x,a,M,top}(x) + \sigma_{x,a,M,bot}(x)}$$

With:

$$\sigma_{x,a,M,top}(x) = \frac{M_y(x)}{I_{y,eff}} \cdot y_s$$

$$\sigma_{x,a,M,bot}(x) = \frac{M_y(x)}{I_{y,eff}} \cdot (h_a - y_s)$$

and

$$\sigma_{x,a,F}(x) = \frac{F_x(x)}{A_a}$$

$$z_{el,a} = \frac{h_a \cdot \left(\frac{M_y(x)}{I_{y,eff}} \cdot y_s - \frac{F_x(x)}{A_a} \right)}{\frac{M_y(x)}{I_{y,eff}} \cdot y_s + \frac{M_y(x)}{I_{y,eff}} \cdot (h_a - y_s)}$$

$$z_{el,a} = \frac{h_a \cdot \left(\frac{M_y(x)}{I_{y,eff}} \cdot y_s - \frac{F_x(x)}{A_a} \right)}{\frac{M_y(x)}{I_{y,eff}} \cdot y_s + \frac{M_y(x)}{I_{y,eff}} \cdot h_a - \frac{M_y(x)}{I_{y,eff}} \cdot y_s}$$

$$z_{el,a} = \frac{\frac{M_y(x)}{I_{y,eff}} \cdot y_s - \frac{F_x(x)}{A_a}}{\frac{M_y(x)}{I_{y,eff}}} \tag{C.85}$$

The magnitude of the tension force in the steel is equal to the compression force in the concrete. Substituting equations (C.78) and (C.79) in the equation above, we obtain the location of the neutral axis in the steel beam:

$$z_{el,a} = \frac{\frac{\bar{M} \cdot \sin\left(\frac{\pi x}{L}\right)}{I_{y,eff}} \cdot y_s - \frac{\bar{M} \frac{S_k}{I_{y,eff}} \frac{s_{sc,eq}}{k_{sc}} \frac{\pi}{L} \cdot \frac{k_{sc}}{s_{sc,eq}} \cdot \frac{L}{\pi} \cdot \sin\left(\frac{\pi x}{L}\right)}{A_a}}{\frac{\bar{M} \cdot \sin\left(\frac{\pi x}{L}\right)}{I_{y,eff}}}$$

$$z_{el,a} = y_s - \frac{S_k}{A_a} \tag{C.86}$$

C.6 Composite beams with nonlinear shear connection

C.6.1 Second moment of area for nonlinear connection

The derivation of the equations in the case of nonlinear connection is done similarly to the case where flexible shear connection is applied. The main difference is that instead of considering one single shear connector stiffness k_{sc}, which describes all shear connectors at all load levels, different shear connector stiffness values are considered for each shear connector based on the actual load that they observe. In other words, at every load level every shear connector has its own individual stiffness $k_{sc,i}$ (see Chapter 8.5.1.). The assumption of a cosine slip function is maintained:

$$s(x) = \bar{s} \cdot \cos\left(\frac{\pi x}{L}\right) \tag{C.87}$$

Therefore:

$$\frac{ds(x)}{dx} = -\bar{s} \cdot \frac{\pi}{L} \cdot \sin\left(\frac{\pi x}{L}\right) \tag{C.88}$$

The shear connector forces $P_{sc,i}(x)$ based on the slip function and their secant stiffness values can be described with the following expression:

$$P_{sc,i}(x) = s(x) \cdot \frac{k_{sc,i}}{s_{sc,eq}} = \bar{s} \cdot cos\left(\frac{\pi x}{L}\right) \cdot \frac{k_{sc,i}}{s_{sc,eq}} \tag{C.89}$$

Because this function is non-continuous along the length, the compression force $F_x(x)$ in the slab will be the sum of the integrals of the parts where the function is continuous:

$$F_x(x_m) = \sum_{i=1}^{m} \int_{\frac{(i-1)L}{2n_p}}^{\frac{i \cdot L}{2n_p}} P_{sc,i}(x)\, dx = \sum_{i=1}^{m} \int_{\frac{(i-1)L}{2n_p}}^{\frac{i \cdot L}{2n_p}} \bar{s} \cdot \cos\left(\frac{\pi x}{L}\right) \cdot \frac{k_{sc,i}}{s_{sc,eq}}\, dx$$

$$F_x(x_m) = \sum_{i=1}^{m} \bar{s} \cdot \left[\frac{k_{sc,i}}{s_{sc,eq}} \frac{L}{\pi} \cdot \sin\left(\frac{\pi x}{L}\right)\right]_{\frac{(i-1)L}{2n_p}}^{\frac{i \cdot L}{2n_p}}$$

$$F_x(x_m) = \bar{s} \sum_{i=1}^{m} \frac{k_{sc,i}}{s_{sc,eq}} \frac{L}{\pi} \cdot \left[\sin\left(\frac{i\pi}{2n_p}\right) - \sin\left(\frac{(i-1)\pi}{2n_p}\right)\right] \tag{C.90}$$

where m is the number of shear connectors (or pairs of shear connectors) and x_m is the distance from the support until the section in consideration. Using the equations (C.88) and (C.90) in the moment equation (C.46):

$$M_y(x) = -\frac{ds(x)}{dx} \cdot \frac{E_a I_{y,eff}}{a} + \frac{F_x(x) I_{y,eff}}{a} \left(\frac{A_c + nA_a}{A_c A_a}\right)$$

$$M_y(x_m) = \bar{s} \cdot \frac{\pi}{L} \cdot \frac{E_a I_{y,eff,m}}{a} \sin\left(\frac{m\pi}{2n_p}\right) + \\ + \bar{s} \sum_{i=1}^{m} \frac{k_{sc,i}}{s_{sc,eq}} \frac{L}{\pi} \cdot \left[\sin\left(\frac{i\pi}{2n_p}\right) - \sin\left(\frac{(i-1)\pi}{2n_p}\right)\right] \frac{I_{y,eff,m}}{a} \left(\frac{A_c + nA_a}{A_c A_a}\right) \tag{C.91}$$

If we substitute equations (C.90) and (C.91) into equation (C.50), we obtain the effective second moment of area at shear connection *m*:

$$I_{y,eff} = \frac{I_{y,c}}{n} + I_{y,a} + \frac{F(x) \cdot a \cdot I_{y,eff}}{M_y(x)} \tag{B.32}$$

$$I_{y,eff,m} = \frac{I_{y,c}}{n} + I_{y,a} + \frac{a^2}{\frac{\pi}{L} \cdot \frac{E_a \cdot \sin\left(\frac{m\pi}{2n_p}\right)}{\sum_{i=1}^{m} \frac{k_{sc,i}}{s_{sc,eq}} \frac{L}{\pi} \cdot \left[\sin\left(\frac{i\pi}{2n_p}\right) - \sin\left(\frac{(i-1)\pi}{2n_p}\right)\right]} + \left(\frac{A_c + nA_a}{A_c A_a}\right)} \tag{C.92}$$

As one can see, the second moment of area is not constant, nor continuous over the length, but it has a certain value at every shear connector. Its value at mid-span is:

$$I_{y,eff,n_p} = \frac{I_{y,c}}{n} + I_{y,a} + \frac{a^2}{\frac{\pi}{L} \cdot \frac{E_a}{\sum_{i=1}^{n_p} \frac{k_{sc,i}}{s_{sc,eq}} \frac{L}{\pi} \cdot \left[\sin\left(\frac{i\pi}{2n_p}\right) - \sin\left(\frac{(i-1)\pi}{2n_p}\right)\right]} + \left(\frac{A_c + nA_a}{A_c A_a}\right)} \tag{C.93}$$

C.6.2 Relationship between the end slip and the moment at mid-span

In order to determine the relationship between the end slip and the moment at mid-span, we need to rearrange equation (C.91) for the end slip.

With:

$$x = L/2$$

$$M_y(L/2) = \bar{s} \cdot \frac{\pi}{L} \cdot \frac{E_a I_{y,eff,n_p}}{a} + \bar{s} \sum_{i=1}^{n_p} \frac{k_{sc,i}}{s_{sc,eq}} \frac{L}{\pi} \cdot \left[\sin\left(\frac{i\pi}{2n_p}\right) - \sin\left(\frac{(i-1)\pi}{2n_p}\right) \right] \frac{I_{y,eff,n_p}}{a} \left(\frac{A_c + nA_a}{A_c A_a}\right)$$

$$M_y(L/2) = \bar{s} \cdot \frac{I_{y,eff,np}}{a} \left(\frac{\pi}{L} \cdot E_a + \sum_{i=1}^{n_p} \frac{k_{sc,i}}{s_{sc,eq}} \frac{L}{\pi} \cdot \left[\sin\left(\frac{i\pi}{2n_p}\right) - \sin\left(\frac{(i-1)\pi}{2n_p}\right) \right] \left(\frac{A_c + nA_a}{A_c A_a}\right) \right)$$

$$\bar{s} = \frac{M_y(L/2) \cdot a}{\left(\frac{\pi}{L} \cdot E_a I_{y,eff} + \sum_{i=1}^{n_p} \frac{k_{sc,i}}{s_{sc,eq}} \frac{L}{\pi} \cdot \left[\sin\left(\frac{i\pi}{2n_p}\right) - \sin\left(\frac{(i-1)\pi}{2n_p}\right) \right] I_{y,eff} \left(\frac{A_c + nA_a}{A_c A_a}\right) \right)}$$

With:

$$\bar{M} = M_y(L/2)$$

$$\bar{s} = \frac{\bar{M} \cdot a}{I_{y,eff,n_p} \left(\frac{\pi}{L} \cdot E_a + \sum_{i=1}^{n_p} \frac{k_{sc,i}}{s_{sc,eq}} \frac{L}{\pi} \cdot \left[\sin\left(\frac{i\pi}{2n_p}\right) - \sin\left(\frac{(i-1)\pi}{2n_p}\right) \right] \left(\frac{A_c + nA_a}{A_c A_a}\right) \right)} \quad \text{(C.94)}$$

Annex D Results of the plastic calculation method (Method PL1)

Table D.1 - Table D.3 show the comparison of the results of the numerical simulations (parametric study PS-2) and the developed calculation method for the calculation of the plastic moment resistance (described in Chapter 9.4.2). Those beams where non-demountable welded stud connectors (P0) were used and a not satisfy the minimum degree of shear connection requirement of Eurocode 4 [18] (see equation (2.44) and (2.45)) could not develop the assumed plastic stress distribution before shear connection failure took place at the slip of 6 mm. This observation illustrates well why the code does not allow to apply these beams. Therefore, these beams were excluded from the presented comparison.

On the other hand, demountable composite beams (with shear connection P3.3 or P15.1) that have a degree of shear connection lower than the minimum required by the code are still included in the comparison because their fundamental behaviour is significantly different from the one of welded studs (see Figure 7.3). They have a higher deformation capacity and a monotone increasing load-slip behaviour.

This shows that the minimum degree of shear connection rules may need to be redefined for demountable shear connections.

Table D.1 Comparison of the numerically and analytically obtained results (part 1)

#	Name	$M_{u,FEM}$ [kNm]	$P_{R.eff}$ [kN]	M_{pl} [kNm]	η [-]	η_{min} [-]	ψ [-]	$M_{pl.\eta}$ [kNm]	θ_i [-]
35	6E27-S3C45M-DP1-P0	389	109.0	490	0.61	0.40	0.52	407	0.96
36	6E27-S3C45M-DP1-P3.3	406	107.2	490	0.60	0.40	0.20	404	1.00
37	6E27-S3C45M-DP1-P15.1	411	115.6	490	0.64	0.40	0.26	416	0.99
38	6E27-S3C45M-DP2-P0	526	103.1	490	1.00	0.40	0.68	490	1.07
39	6E27-S3C45M-DP2-P3.3	503	88.4	490	0.98	0.40	0.33	496	1.01
40	6E27-S3C45M-DP2-P15.1	513	106.8	490	1.00	0.40	0.42	490	1.05
41	6E27-S3C20M-DP1-P0	383	108.9	469	0.61	0.40	0.53	398	0.96
42	6E27-S3C20M-DP1-P3.3	403	107.2	469	0.60	0.40	0.21	396	1.02
43	6E27-S3C20M-DP1-P15.1	407	115.6	469	0.64	0.40	0.27	407	1.00
44	6E27-S3C20M-DP2-P0	481	102.8	469	1.00	0.40	0.69	469	1.02
45	6E27-S3C20M-DP2-P3.3	466	87.3	469	0.97	0.40	0.34	473	0.98
46	6E27-S3C20M-DP2-P15.1	475	105.8	469	1.00	0.40	0.43	469	1.01
~~47~~	~~6E36-S3C45M-DP1-P0~~	~~625~~	~~109.0~~	~~883~~	~~0.38~~	~~0.40~~	~~0.43~~	~~673~~	~~0.93~~
48	6E36-S3C45M-DP1-P3.3	659	101.7	883	0.36	0.40	0.15	662	1.00
49	6E36-S3C45M-DP1-P15.1	663	115.6	883	0.41	0.40	0.20	682	0.97
50	6E36-S3C45M-DP2-P0	780	104.1	883	0.73	0.40	0.60	807	0.97
51	6E36-S3C45M-DP2-P3.3	820	85.9	883	0.60	0.40	0.26	760	1.08

Table D.2 Comparison of the numerically and analytically obtained results (part 2)

#	Name	$M_{u,FEM}$ [kNm]	$P_{R.eff}$ [kN]	M_{pl} [kNm]	η [-]	η_{min} [-]	ψ [-]	$M_{pl.\eta}$ [kNm]	θ_i [-]
52	6E36-S3C45M-DP2-P15.1	827	106.7	883	0.75	0.40	0.33	814	1.02
53	6E36-S3C20M-DP1-P0	621	109.0	827	0.41	0.40	0.44	664	0.94
54	6E36-S3C20M-DP1-P3.3	654	100.9	827	0.38	0.40	0.15	653	1.00
55	6E36-S3C20M-DP1-P15.1	658	115.6	827	0.44	0.40	0.21	673	0.98
56	6E36-S3C20M-DP2-P0	758	103.7	827	0.79	0.40	0.71	778	0.97
57	6E36-S3C20M-DP2-P3.3	747	84.8	827	0.64	0.40	0.30	738	1.01
58	6E36-S3C20M-DP2-P15.1	755	105.5	827	0.80	0.40	0.35	781	0.97
~~59~~	~~8E45-S3C45M-DP1-P0~~	~~1026~~	~~108.7~~	~~1369~~	~~0.34~~	~~0.44~~	~~0.47~~	~~1054~~	~~0.97~~
60	8E45-S3C45M-DP1-P3.3	1092	105.8	1369	0.33	0.44	0.17	1047	1.04
61	8E45-S3C45M-DP1-P15.1	1087	114.0	1369	0.35	0.44	0.23	1065	1.02
~~62~~	~~16E60-S3C45M-DP1-P0~~	~~2014~~	~~106.1~~	~~2644~~	~~0.45~~	~~0.71~~	~~0.69~~	~~2222~~	~~0.91~~
63	16E60-S3C45M-DP1-P3.3	2253	100.9	2644	0.43	0.71	0.34	2201	1.02
64	16E60-S3C45M-DP1-P15.1	2234	109.6	2644	0.47	0.71	0.42	2236	1.00
65	16E60-S3C45M-DP2-P0	2504	101.6	2644	0.90	0.71	0.82	2597	0.96
66	16E60-S3C45M-DP2-P3.3	2578	98.7	2644	0.87	0.71	0.50	2578	1.00
67	16E60-S3C45M-DP2-P15.1	2655	107.3	2644	0.95	0.71	0.60	2635	1.01
~~68~~	~~16E60-S3C20M-DP1-P0~~	~~1980~~	~~106.1~~	~~2552~~	~~0.45~~	~~0.71~~	~~0.70~~	~~2202~~	~~0.90~~
69	16E60-S3C20M-DP1-P3.3	2216	100.9	2552	0.43	0.71	0.34	2183	1.02
70	16E60-S3C20M-DP1-P15.1	2197	109.6	2552	0.47	0.71	0.43	2214	0.99
71	16E60-S3C20M-DP2-P0	2511	101.3	2552	0.90	0.71	0.82	2518	1.00
72	16E60-S3C20M-DP2-P3.3	2454	98.7	2552	0.87	0.71	0.51	2504	0.98
73	16E60-S3C20M-DP2-P15.1	2526	107.3	2552	0.95	0.71	0.60	2548	0.99
74	6E27-S3C45D-DP1-P0	325	78.2	432	0.48	0.43	0.52	336	0.96
75	6E27-S3C45D-DP1-P3.3	320	60.1	432	0.37	0.43	0.20	311	1.03
76	6E27-S3C45D-DP1-P15.1	337	81.5	432	0.50	0.43	0.27	341	0.99
77	6E27-S3C45D-DP2-P0	426	73.5	432	0.90	0.43	0.69	423	1.01
78	6E27-S3C45D-DP2-P3.3	394	47.7	432	0.59	0.43	0.34	360	1.09
79	6E27-S3C45D-DP2-P15.1	429	66.7	432	0.82	0.43	0.42	407	1.05
80	6E27-S3C20D-DP1-P0	322	78.2	372	0.62	0.43	0.53	326	0.99
81	6E27-S3C20D-DP1-P3.3	328	59.7	372	0.48	0.43	0.21	304	1.08
82	6E27-S3C20D-DP1-P15.1	352	81.1	372	0.65	0.43	0.27	329	1.07
83	6E27-S3C20D-DP2-P0	405	73.3	372	1.00	0.43	0.69	372	1.09
84	6E27-S3C20D-DP2-P3.3	364	47.2	372	0.75	0.43	0.34	343	1.06
85	6E27-S3C20D-DP2-P15.1	398	66.0	372	1.00	0.43	0.43	372	1.07
~~86~~	~~6E36-S3C45D-DP1-P0~~	~~536~~	~~78.3~~	~~769~~	~~0.30~~	~~0.43~~	~~0.43~~	~~574~~	~~0.93~~
87	6E36-S3C45D-DP1-P3.3	564	55.6	769	0.22	0.43	0.15	530	1.06
88	6E36-S3C45D-DP1-P15.1	583	79.3	769	0.31	0.43	0.20	576	1.01

Table D.3 Comparison of the numerically and analytically obtained results (part 3)

#	Name	$M_{u,FEM}$ [kNm]	$P_{R.eff}$ [kN]	M_{pl} [kNm]	η [-]	η_{min} [-]	ψ [-]	$M_{pl.\eta}$ [kNm]	θ_i [-]
89	6E36-S3C45D-DP2-P0	657	74.1	769	0.57	0.43	0.60	669	0.98
90	6E36-S3C45D-DP2-P3.3	589	46.3	769	0.36	0.43	0.26	597	0.99
91	6E36-S3C45D-DP2-P15.1	681	66.6	769	0.52	0.43	0.34	650	1.05
92	6E36-S3C20D-DP1-P0	536	78.3	614	0.62	0.43	0.45	563	0.95
93	6E36-S3C20D-DP1-P3.3	538	55.2	614	0.44	0.43	0.16	524	1.03
94	6E36-S3C20D-DP1-P15.1	569	78.9	614	0.63	0.43	0.21	564	1.01
95	6E36-S3C20D-DP2-P0	644	73.9	614	1.00	0.43	0.62	614	1.05
96	6E36-S3C20D-DP2-P3.3	579	45.7	614	0.73	0.43	0.27	581	1.00
97	6E36-S3C20D-DP2-P15.1	610	65.8	614	1.00	0.43	0.35	614	0.99
~~98~~	~~8E45-S3C45D-DP1-P0~~	~~871~~	~~78.3~~	~~1196~~	~~0.27~~	~~0.49~~	~~0.48~~	~~903~~	~~0.96~~
99	8E45-S3C45D-DP1-P3.3	898	65.7	1196	0.22	0.49	0.17	869	1.03
100	8E45-S3C45D-DP1-P15.1	924	83.9	1196	0.29	0.49	0.23	917	1.01
~~101~~	~~16E60-S3C45D-DP1-P0~~	~~1568~~	~~76.4~~	~~2343~~	~~0.36~~	~~0.74~~	~~0.69~~	~~1919~~	~~0.82~~
102	16E60-S3C45D-DP1-P3.3	1821	67.1	2343	0.32	0.74	0.34	1868	0.98
103	16E60-S3C45D-DP1-P15.1	1870	80.3	2343	0.38	0.74	0.43	1938	0.96
~~104~~	~~16E60-S3C45D-DP2-P0~~	~~2208~~	~~72.2~~	~~2343~~	~~0.70~~	~~0.74~~	~~0.82~~	~~2189~~	~~1.01~~
105	16E60-S3C45D-DP2-P3.3	2120	65.5	2343	0.64	0.74	0.51	2144	0.99
106	16E60-S3C45D-DP2-P15.1	2178	77.8	2343	0.76	0.74	0.60	2225	0.98
~~107~~	~~16E60-S3C20D-DP1-P0~~	~~1560~~	~~76.4~~	~~2158~~	~~0.36~~	~~0.74~~	~~0.70~~	~~1893~~	~~0.82~~
108	16E60-S3C20D-DP1-P3.3	1815	67.1	2158	0.32	0.74	0.35	1847	0.98
109	16E60-S3C20D-DP1-P15.1	1862	80.3	2158	0.38	0.74	0.43	1910	0.97
~~110~~	~~16E60-S3C20D-DP2-P0~~	~~2109~~	~~72.0~~	~~2158~~	~~0.70~~	~~0.74~~	~~0.82~~	~~2092~~	~~1.01~~
111	16E60-S3C20D-DP2-P3.3	2033	64.8	2158	0.63	0.74	0.51	2061	0.99
112	16E60-S3C20D-DP2-P15.1	2083	77.2	2158	0.75	0.74	0.60	2111	0.99

Annex E Results of the simplified calculation method (Method PL2)

The same comparison as presented in Annex D was performed for the simplified plastic calculation method (Chapter 9.4.3). Again, non-demountable beams with welded shear connection (P0) that have a lower degree of shear connection than the minimum required by Eurocode 4 [18] were excluded from the comparison.

Table E.1 Comparison of the numerically and analytically obtained results (part 1)

#	Name	$M_{u,FEM}$ [kNm]	$P_{eff,sim}$ [-]	M_{pl} [kNm]	η [-]	η_{min} [-]	$M_{pl.\eta,sim}$ [kNm]	θ_i [-]
35	6E27-S3C45M-DP1-P0	389	108.7	490	0.60	0.40	406	0.96
36	6E27-S3C45M-DP1-P3.3	406	69.1	490	0.38	0.40	349	1.16
37	6E27-S3C45M-DP1-P15.1	411	98.4	490	0.55	0.40	392	1.05
38	6E27-S3C45M-DP2-P0	526	108.7	490	1.00	0.40	490	1.07
39	6E27-S3C45M-DP2-P3.3	503	69.1	490	0.77	0.40	447	1.13
40	6E27-S3C45M-DP2-P15.1	513	98.4	490	1.00	0.40	490	1.05
41	6E27-S3C20M-DP1-P0	383	108.7	469	0.60	0.40	398	0.96
42	6E27-S3C20M-DP1-P3.3	403	69.1	469	0.38	0.40	345	1.17
43	6E27-S3C20M-DP1-P15.1	407	98.4	469	0.55	0.40	385	1.06
44	6E27-S3C20M-DP2-P0	481	108.7	469	1.00	0.40	469	1.02
45	6E27-S3C20M-DP2-P3.3	466	69.1	469	0.77	0.40	434	1.07
46	6E27-S3C20M-DP2-P15.1	475	98.4	469	1.00	0.40	469	1.01
~~47~~	~~6E36-S3C45M-DP1-P0~~	~~625~~	~~108.7~~	~~883~~	~~0.38~~	~~0.40~~	~~672~~	~~0.93~~
48	6E36-S3C45M-DP1-P3.3	659	69.1	883	0.24	0.40	603	1.09
49	6E36-S3C45M-DP1-P15.1	663	98.4	883	0.35	0.40	657	1.01
50	6E36-S3C45M-DP2-P0	780	108.7	883	0.76	0.40	819	0.95
51	6E36-S3C45M-DP2-P3.3	820	69.1	883	0.49	0.40	760	1.08
52	6E36-S3C45M-DP2-P15.1	827	98.4	883	0.69	0.40	793	1.04
53	6E36-S3C20M-DP1-P0	621	108.7	827	0.41	0.40	664	0.94
54	6E36-S3C20M-DP1-P3.3	654	69.1	827	0.26	0.40	599	1.09
55	6E36-S3C20M-DP1-P15.1	658	98.4	827	0.37	0.40	650	1.01
56	6E36-S3C20M-DP2-P0	758	108.7	827	0.83	0.40	787	0.96
57	6E36-S3C20M-DP2-P3.3	747	69.1	827	0.53	0.40	701	1.07
58	6E36-S3C20M-DP2-P15.1	755	98.4	827	0.75	0.40	767	0.98
~~59~~	~~8E45-S3C45M-DP1-P0~~	~~1026~~	~~108.7~~	~~1369~~	~~0.34~~	~~0.44~~	~~1054~~	~~0.97~~
60	8E45-S3C45M-DP1-P3.3	1092	69.1	1369	0.21	0.44	950	1.15
61	8E45-S3C45M-DP1-P15.1	1087	98.4	1369	0.31	0.44	1030	1.05
~~62~~	~~16E60-S3C45M-DP1-P0~~	~~2014~~	~~108.7~~	~~2644~~	~~0.46~~	~~0.71~~	~~2232~~	~~0.90~~
63	16E60-S3C45M-DP1-P3.3	2253	69.1	2644	0.29	0.71	2034	1.11

Table E.2 Comparison of the numerically and analytically obtained results (part 2)

#	Name	$M_{u,FEM}$ [kNm]	$P_{eff,sim}$ [-]	M_{pl} [kNm]	η [-]	η_{min} [-]	$M_{pl.\eta,sim}$ [kNm]	θ_i [-]
64	16E60-S3C45M-DP1-P15.1	2234	98.4	2644	0.42	0.71	2191	1.02
65	16E60-S3C45M-DP2-P0	2504	108.7	2644	0.96	0.71	2643	0.95
66	16E60-S3C45M-DP2-P3.3	2578	69.1	2644	0.61	0.71	2366	1.09
67	16E60-S3C45M-DP2-P15.1	2655	98.4	2644	0.87	0.71	2576	1.03
~~68~~	~~16E60-S3C20M-DP1-P0~~	~~1980~~	~~108.7~~	~~2552~~	~~0.46~~	~~0.71~~	~~2211~~	~~0.90~~
69	16E60-S3C20M-DP1-P3.3	2216	69.1	2552	0.29	0.71	2025	1.09
70	16E60-S3C20M-DP1-P15.1	2197	98.4	2552	0.42	0.71	2173	1.01
71	16E60-S3C20M-DP2-P0	2511	108.7	2552	0.96	0.71	2554	0.98
72	16E60-S3C20M-DP2-P3.3	2454	69.1	2552	0.61	0.71	2329	1.05
73	16E60-S3C20M-DP2-P15.1	2526	98.4	2552	0.87	0.71	2503	1.01
74	6E27-S3C45D-DP1-P0	325	78.3	432	0.48	0.43	336	0.96
75	6E27-S3C45D-DP1-P3.3	320	40.2	432	0.25	0.43	278	1.15
76	6E27-S3C45D-DP1-P15.1	337	64.2	432	0.39	0.43	317	1.06
77	6E27-S3C45D-DP2-P0	426	78.3	432	0.96	0.43	434	0.98
78	6E27-S3C45D-DP2-P3.3	394	40.2	432	0.49	0.43	339	1.16
79	6E27-S3C45D-DP2-P15.1	429	64.2	432	0.79	0.43	401	1.07
80	6E27-S3C20D-DP1-P0	322	78.3	372	0.62	0.43	326	0.99
81	6E27-S3C20D-DP1-P3.3	328	40.2	372	0.32	0.43	275	1.19
82	6E27-S3C20D-DP1-P15.1	352	64.2	372	0.51	0.43	310	1.14
83	6E27-S3C20D-DP2-P0	405	78.3	372	1.00	0.43	372	1.09
84	6E27-S3C20D-DP2-P3.3	364	40.2	372	0.64	0.43	328	1.11
85	6E27-S3C20D-DP2-P15.1	398	64.2	372	1.00	0.43	372	1.07
~~86~~	~~6E36-S3C45D-DP1-P0~~	~~536~~	~~78.3~~	~~769~~	~~0.30~~	~~0.43~~	~~574~~	~~0.93~~
87	6E36-S3C45D-DP1-P3.3	564	40.2	769	0.16	0.43	494	1.14
88	6E36-S3C45D-DP1-P15.1	583	64.2	769	0.25	0.43	548	1.06
89	6E36-S3C45D-DP2-P0	657	78.3	769	0.61	0.43	679	0.97
90	6E36-S3C45D-DP2-P3.3	589	40.2	769	0.31	0.43	578	1.02
91	6E36-S3C45D-DP2-P15.1	681	64.2	769	0.50	0.43	644	1.06
92	6E36-S3C20D-DP1-P0	536	78.3	614	0.62	0.43	563	0.95
93	6E36-S3C20D-DP1-P3.3	538	40.2	614	0.32	0.43	491	1.09
94	6E36-S3C20D-DP1-P15.1	569	64.2	614	0.51	0.43	541	1.05
95	6E36-S3C20D-DP2-P0	644	78.3	614	1.00	0.43	614	1.05
96	6E36-S3C20D-DP2-P3.3	579	40.2	614	0.64	0.43	566	1.02
97	6E36-S3C20D-DP2-P15.1	610	64.2	614	1.00	0.43	614	0.99
~~98~~	~~8E45-S3C45D-DP1-P0~~	~~871~~	~~78.3~~	~~1196~~	~~0.27~~	~~0.49~~	~~903~~	~~0.96~~
99	8E45-S3C45D-DP1-P3.3	898	40.2	1196	0.14	0.49	787	1.14

Table E.3 Comparison of the numerically and analytically obtained results (part 3)

#	Name	$M_{u,FEM}$ [kNm]	$P_{eff,sim}$ [-]	M_{pl} [kNm]	η [-]	η_{min} [-]	$M_{pl.\eta,sim}$ [kNm]	θ_i [-]
100	8E45-S3C45D-DP1-P15.1	924	64.2	1196	0.22	0.49	865	1.07
~~101~~	~~16E60-S3C45D-DP1-P0~~	~~1568~~	~~78.3~~	~~2343~~	~~0.37~~	~~0.74~~	~~1929~~	~~0.81~~
102	16E60-S3C45D-DP1-P3.3	1821	40.2	2343	0.19	0.74	1677	1.09
103	16E60-S3C45D-DP1-P15.1	1870	64.2	2343	0.30	0.74	1850	1.01
104	16E60-S3C45D-DP2-P0	2208	78.3	2343	0.76	0.74	2228	0.99
105	16E60-S3C45D-DP2-P3.3	2120	40.2	2343	0.39	0.74	1953	1.09
106	16E60-S3C45D-DP2-P15.1	2178	64.2	2343	0.63	0.74	2135	1.02
~~107~~	~~16E60-S3C20D-DP1-P0~~	~~1560~~	~~78.3~~	~~2158~~	~~0.37~~	~~0.74~~	~~1901~~	~~0.82~~
108	16E60-S3C20D-DP1-P3.3	1815	40.2	2158	0.19	0.74	1669	1.09
109	16E60-S3C20D-DP1-P15.1	1862	64.2	2158	0.30	0.74	1832	1.02
110	16E60-S3C20D-DP2-P0	2109	78.3	2158	0.76	0.74	2115	1.00
111	16E60-S3C20D-DP2-P3.3	2033	40.2	2158	0.39	0.74	1922	1.06
112	16E60-S3C20D-DP2-P15.1	2083	64.2	2158	0.63	0.74	2058	1.01

Annex F Example calculations

F.1 Task description

The following example shows the practical application of the developed calculation methods. In this example, the expected values of the material properties are used. The results of the calculations are compared to results coming from numerical simulations that use the same geometrical and material properties. The beam in consideration is denoted as 16E60-S3C45M-DP1-P3.3 in the parametric study PS-2 (in Annex B.2).

The presented example covers the following topics:

1) Section F.2 presents the geometric and material properties of the beam in consideration.
2) Section F.3 presents the elastic calculations assuming flexible shear connection on the basis of Chapter 8.4.
3) Section F.4 presents the calculation of elastic deflections assuming nonlinear shear connection on the basis of Chapter 8.5.
4) Section F.5 presents the calculation of the plastic moment resistance on the basis of Chapter 9.4.2.
5) Section F.6 presents the simplified calculation of the plastic moment resistance on the basis of Chapter 9.4.3.
6) Finally, section F.7 presents the summary of the obtained results.

F.2 Initial data

F.2.1 Geometry and loading

The beam in consideration is a simply supported beam subjected to a constant uniformly distributed load. Propped construction is assumed.

Length:	$L = 16200\ mm$
Steel beam	
Profile:	IPE 600
Profile height:	$h_a = 600\ mm$
Flange width:	$b = 220\ mm$
Flange thickness:	$t_f = 19\ mm$
Web thickness:	$t_w = 12\ mm$
Web height:	$h_w = h_a - 2\ t_f = 562\ mm$
Rounding radius:	$r = 24\ mm$

Cross-sectional area:	$A_a = 15598\, mm^2$
Second moment of area:	$I_{y,a} = 9.208 \cdot 10^8\, mm^4$
Centroid measured from the top:	$y_a = h_a/2 \ = 300\, mm$
Plastic section modulus (rounding neglected):	$W_{pl,y} = 3.376 \cdot 10^6\, mm^3$
Concrete slab	
Total depth:	$h_{tot} = 150\, mm$
Profiled sheeting:	$h_p = 0\, mm$ (solid slab)
Depth:	$h_c = h_{tot} - h_p = 150\, mm$
Width:	$B_{eff} = 2 \cdot L/8 = 4050\, mm$
Cross-sectional area:	$A_c = 607500\, mm^2$
Second moment of area:	$I_{c,y} = 1.139 \cdot 10^9\, mm^4$
Centroid measured from the top:	$y_c = h_c/2 \ = 75\, mm$

F.2.2 Material properties

Steel:	S355
Yield strength:	$f_y = 391$ MPa
Young's modulus:	$E_a = 200\, GPa$
Concrete :	C45/55
Cube strength:	$f_c = 54$ MPa
Young's modulus:	$E_c = 40.1\, GPa$
Modular ratio:	$n = E_a/E_c = 4.99$

F.2.3 Shear connection

Shear connection type:	P3.3
Nr. of shear connectors in a row:	$n_r = 2$
Transversal spacing:	$b_0 = 100\, mm$
Longitudinal spacing	$s_l = 600\, mm$
Equivalent longitudinal spacing:	$s_{sc,eq} = s_l/n_r = 300\, mm$

Nr. of shear connector rows on the critical length (*L/2*): $n_p = \frac{L/2}{s_l} = 13.5$, so $n_p = 13$

Nr. of shear connectors on the critical length (*L/2*): $n_{sc} = n_p \cdot n_r = 26$

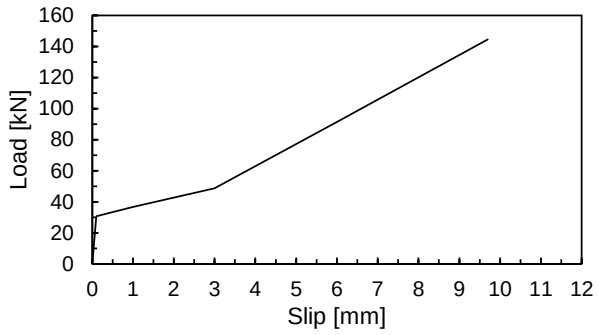

Figure F.1 Average load-slip curve of shear connection P3.3

F.3 Elastic calculation assuming flexible shear connection (Method EL1)

The shear connection behaviour is approximated by one single stiffness value.

Shear connection stiffness: $k_{sc} = 0.7 \cdot 0.9 \cdot P_{R,6}/s$

Shear resistance at 6 mm: $P_{R,6} = 91.4\ kN$

Slip at $0.7 \cdot 0.9 \cdot P_{R,6}$: $s = 3.62\ mm$

So the shear connection stiffness is:

$$k_{sc} = \frac{0.7 \cdot 0.9 \cdot P_{R,6}}{s} = 15.9\ kN/mm \tag{F.1}$$

Distance between the centroid of the steel and the concrete:

$$a = h_c - y_c + h_p + y_a = 150\ mm - 75\ mm + 0\ mm + 300\ mm = 375\ mm \tag{F.2}$$

Second moment of area:

$$I_{y,eff} = I_{y,a} + \frac{I_{y,c}}{n} + \frac{A_c/n}{1 + \frac{A_c}{nA_a} + \left(\frac{E_a}{k_{sc}/s_{sc,eq}}\right)\left(\frac{\pi}{L}\right)^2\left(\frac{A_c}{n}\right)} \cdot a^2 = 1.805 \cdot 10^9\ mm^4 \tag{F.3}$$

Auxiliary parameter S_k:

$$S_k = \frac{a}{\frac{E_a}{\left(\frac{k_{sc}}{s_{sc,eq}}\right)\left(\frac{L}{\pi}\right)^2} + \frac{A_c + nA_a}{A_c A_a}} = 1.749 \cdot 10^6\ mm^3 \tag{F.4}$$

Neutral axis of the concrete (measured from the top fibre of the concrete):

$$z_{el,c} = \frac{h_c}{2} + \frac{n \cdot S_k}{A_c} = 89.4\ mm \tag{F.5}$$

Neutral axis of the steel (measured from the top fibre of the steel):

$$z_{el,a} = y_s - \frac{S_k}{A_a} = 187.9\ mm \tag{F.6}$$

Elastic moment resistance (concrete cracking neglected):

Concrete compression:

$$M_{el,cc} = \frac{f_c \cdot n \cdot I_{y,eff}}{z_{el,c}} = 5444\ kNm \tag{F.7}$$

Steel compression (top flange):

$$M_{el,ac} = \frac{f_y \cdot I_{y,eff}}{z_{el,a}} = 3756\ kNm \tag{F.8}$$

Steel tension (bottom flange):

$$M_{el,at} = \frac{f_y \cdot I_{y,eff}}{h_a - z_{el,a}} = 1712\ kNm \tag{F.9}$$

The steel bottom flange is decisive. The corresponding elastic moment resistance is:

$$M_{el} = \min(M_{el,cc}; M_{el,ac}; M_{el,at}) = 1712\ kNm \tag{F.10}$$

The corresponding uniformly distributed load is:

$$q_{el} = \frac{M_{el} \cdot L^2}{8} = 52.2\ kN/m \tag{F.11}$$

Deflection at M_{el}:

$$\overline{w} = \frac{5}{384} \cdot \frac{qL^4}{E_a I_{y,eff}} = 129.7\ mm \tag{F.12}$$

The comparison of the numerically and analytically obtained results are presented in Figure F.2.

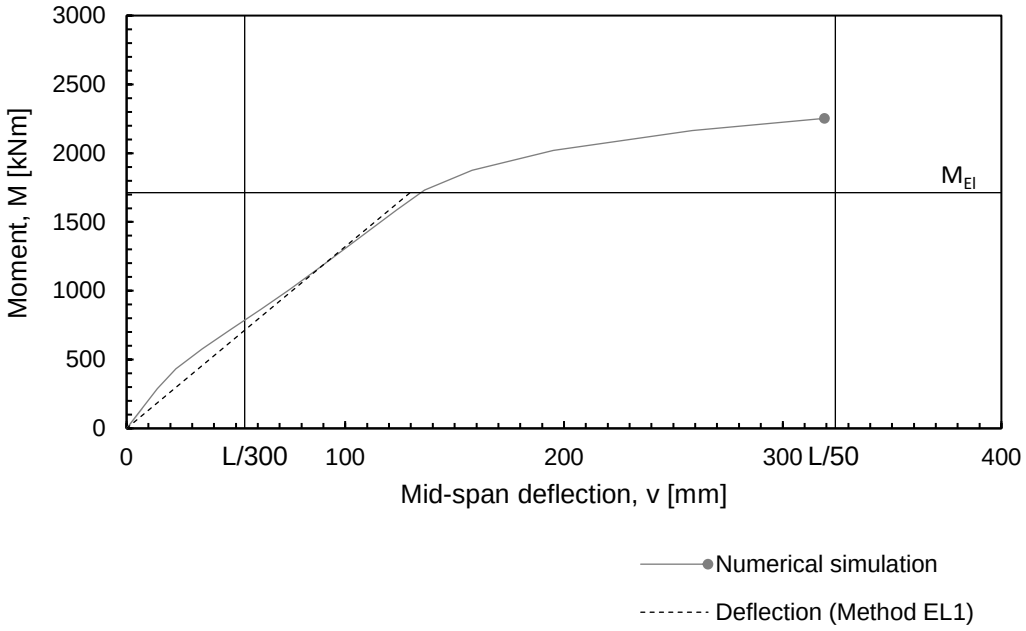

Figure F.2 Numerically and analytically obtained deflections (Method EL1)

F.4 Elastic calculation with nonlinear connection (Method EL2)

F.4.1 General

The presented example shows the elastic deflection calculation at an arbitrary selected load level ($M < M_{el}$). To obtain the complete moment-deflection curve, the calculation needs to be repeated at different load levels. This was performed at 30 load levels and the results are summarised in section F.4.3.

F.4.2 Deflection calculation at 800 kNm mid-span moment

This section shows the deflection calculation that corresponds to $\overline{M}$ = 800 kNm mid-span moment. The elastic calculation with nonlinear connection is an iterative procedure according to Figure F.3.

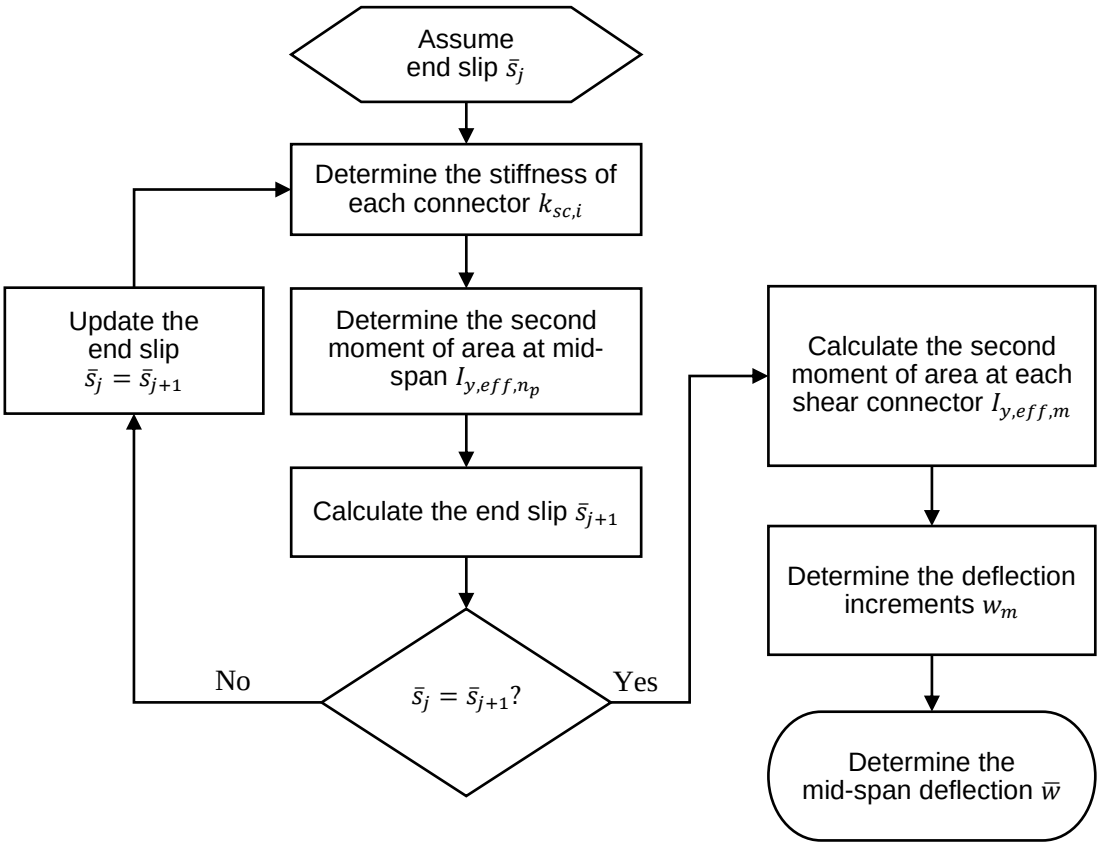

Figure F.3 Flowchart of the iterative procedure

Step 1: Assume an arbitrary end slip

In this example it is assumed to be 3 mm:

$$\bar{s}_j = 3\ mm \tag{F.13}$$

Step 2: Determine the secant stiffness of each shear connector

In order to be able to determine the secant stiffness values, the occurring slip and the corresponding load should be determined at each connector.

The slip function is described by a cosine function:

$$s(x) = \bar{s}_j \cdot \cos\left(\frac{\pi \cdot x}{L}\right) \tag{F.14}$$

where *x* is the position along the length. For equidistant spacing the equation above can be written as:

$$s_i = \bar{s}_j \cdot \cos\left(\frac{(i-1)}{n_p} \cdot \frac{\pi}{2}\right) \tag{F.15}$$

where *i* is the number of the shear connector counted from the support.

The corresponding shear force can be determined with the help of the load slip curve:

$$s_i \rightarrow P_i \tag{F.16}$$

The secant stiffness of the connectors can be determined as:

$$k_{sc,i} = \frac{P_{sc,i}}{s_i} \tag{F.17}$$

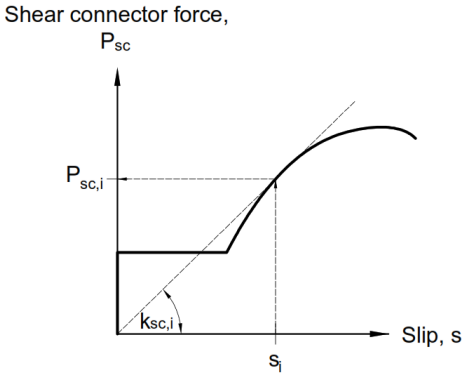

Figure F.4 Determining the secant stiffness of the connectors

The following table summarises the obtained slip, force and stiffness values:

Table F.1 Obtained slip, force and secant stiffness values

Nr. of the shear connector, i **[-]**	$\frac{(i-1)}{n_p}\cdot\frac{\pi}{2}$ **[deg]**	$\cos\left(\frac{(i-1)}{n_p}\cdot\frac{\pi}{2}\right)$ **[-]**	**Slip, s_i [mm]**	**Force, $P_{sc,i}$ [kN]**	**Secant stiffness, $k_{sc,i}$ [N/mm]**
1	0.000	1.000	3.00	48.67	16222
2	6.923	0.993	2.98	48.54	16297
3	13.846	0.971	2.91	48.15	16529
4	20.769	0.935	2.81	47.50	16934
5	27.692	0.885	2.66	46.61	17547
6	34.615	0.823	2.47	45.49	18425
7	41.538	0.749	2.25	44.15	19662
8	48.462	0.663	1.99	42.62	21424
9	55.385	0.568	1.70	40.91	24007
10	62.308	0.465	1.39	39.06	28016
11	69.231	0.355	1.06	37.08	34857
12	76.154	0.239	0.72	34.82	48499
13	83.077	0.121	0.36	32.44	89721

Step 3: Determine the second moment of area at mid-span

The second moment of area at mid-span can be determined using the following expression:

$$I_{y,eff,n_p} = I_{y,a} + \frac{I_{y,c}}{n} + \frac{a^2}{\frac{\pi}{L}\cdot\frac{E_a}{\sum_{i=1}^{n_p}\frac{k_{sc,i}}{s_{sc,eq}}\frac{L}{\pi}\cdot\left[\sin\left(\frac{i\pi}{2n_p}\right)-\sin\left(\frac{(i-1)\pi}{2n_p}\right)\right]}+\left(\frac{A_c+nA_a}{A_cA_a}\right)} \qquad \text{(F.18)}$$

In this formulation there is a part in the denominator which needs to be determined at every shear connector:

$$K_i = \frac{k_{sc,i}}{s_{sc,eq}}\frac{L}{\pi}\cdot\left[\sin\left(\frac{i\pi}{2n_p}\right)-\sin\left(\frac{(i-1)\pi}{2n_p}\right)\right] \qquad \text{(F.19)}$$

The following table summarises the calculated values of K_i:

Table F.2 Auxiliary values for the calculation

Nr. of the shear connector, *i* **[-]**	K_i **[N/mm]**
1	33610
2	33274
3	32754
4	32052
5	31168
6	30104
7	28859
8	27425
9	25780
10	23866
11	21525
12	18146
13	11244
SUM:	349807

$$\sum_{i=1}^{n_p} \frac{k_{sc,i}}{s_{sc,eq}} \frac{L}{\pi} \cdot \left[\sin\left(\frac{i\pi}{2n_p}\right) - \sin\left(\frac{(i-1)\pi}{2n_p}\right) \right] = \sum_{i=1}^{n_p} K_i = 349807\ N/mm \tag{F.20}$$

The second moment of area at mid-span is then:

$$I_{y,eff,n_p} = 1.917 \cdot 10^9 \cdot mm^4 \tag{F.21}$$

Step 4: Calculation of the end slip

The end slip can be determined with the following expression.

$$\bar{s}_{j+1} = \frac{\bar{M} \cdot a}{I_{y,eff,n_p} \left(\frac{\pi}{L} \cdot E_a + \sum_{i=1}^{n_p} \frac{k_{sc,i}}{s_{sc,eq}} \frac{L}{\pi} \cdot \left[\sin\left(\frac{i\pi}{2n_p}\right) - \sin\left(\frac{(i-1)\pi}{2n_p}\right) \right] \left(\frac{A_c + nA_a}{A_c A_a} \right) \right)} \tag{F.22}$$

In this equation the summation in the denominator is the same as equation (F.20).

The calculated end slip is:

$$\bar{s}_{j+1} = 2.44\ mm \tag{F.23}$$

Step 5: Verifying the initial assumption

The discrepancy in our initially assumed and then later calculated end slip can be determined as:

$$\Delta = 1 - \frac{\bar{s}_{j+1}}{\bar{s}_j} = 1 - \frac{2.44\ mm}{3\ mm} = 0.1858 = 18.58\% \tag{F.24}$$

Step 6: Updating the end slip

If $\Delta > 0.01$, update the end slip:

$$\bar{s}_j \equiv \bar{s}_{j+1} \tag{F.25}$$

Iteration

Repeat the calculations from Step 2 to Step 6 (equations (F.15)- (F.25)) until the error becomes less than 1 % (until $\Delta < 0.01$).

In this example, after 5 iterations the discrepancy decreased below 1%:

Table F.3 Iterations and discrepancy in the end slip

Iteration	$\bar{s}_j$	$\bar{s}_{j+1}$	Δ
0	3.00	2.44	0.1858
1	2.44	2.22	0.0929
2	2.22	2.11	0.0487
3	2.11	2.05	0.0261
4	2.05	2.02	0.0142
5	2.02	2.01	0.0077

Step 7: Calculate the second moment of area at each shear connector

The second moment of area at shear connector *m* can be calculated using the following expression:

$$I_{y,eff,m} = \frac{I_{y,c}}{n} + I_{y,a} + \frac{a^2}{\frac{\pi}{L} \cdot \frac{E_a \cdot \sin\left(\frac{m\pi}{2n_p}\right)}{\sum_{i=1}^{m} \frac{k_{sc,i}}{s_{sc,eq}} \frac{L}{\pi} \cdot \left[\sin\left(\frac{i\pi}{2n_p}\right) - \sin\left(\frac{(i-1)\pi}{2n_p}\right)\right]} + \left(\frac{A_c + nA_a}{A_c A_a}\right)} \tag{F.26}$$

Where *m* is the number of shear connectors (or pairs of shear connectors) until the section in consideration.

The previous equation takes a simpler form if we use equation (F.19):

$$I_{y,eff,m} = \frac{I_{y,c}}{n} + I_{y,a} + \frac{a^2}{\frac{\pi}{L} \cdot \frac{E_a \cdot \sin\left(\frac{m\pi}{2n_p}\right)}{\sum_{i=1}^{m} K_i} + \left(\frac{A_c + nA_a}{A_c A_a}\right)} \quad \text{(F.27)}$$

The following table summarises the determined second moment of area values:

Table F.4 Second moment of area at each shear connector

Nr. of the shear connector, *i* **[-]**	K_i **[N/mm]**	$\sum_{i=1}^{m} K_i$ **[N/mm]**	$I_{y,eff,m}$ **[mm2]**
1	43845	43845	1.935E+09
2	43433	87278	1.936E+09
3	42836	130115	1.939E+09
4	42052	172167	1.943E+09
5	41078	213245	1.950E+09
6	39912	253157	1.958E+09
7	38545	291702	1.967E+09
8	36960	328662	1.979E+09
9	35117	363779	1.992E+09
10	32884	396663	2.008E+09
11	29961	426625	2.025E+09
12	25697	452322	2.042E+09
13	16266	468588	2.056E+09

Step 8: Calculating the deflection increments between the sections

The deflection increments for uniformly distributed load is given by the following equation:

$$w_m = \frac{q}{24E_a I_{y,eff,m}} \cdot [L^3(A-B) + 2L(B^3 - A^3) + A^4 - B^4] \quad \text{(F.28)}$$

Where:

$$A = \frac{m \cdot L}{2n_p}$$

$$B = \frac{(m-1)L}{2n_p}$$

The uniformly distributed load that corresponds to 800 kNm bending moment is:

$$q = \frac{\overline{M} \cdot L^2}{8} = 24.4\ kN/m \quad \text{(F.29)}$$

The calculated deflection increments are summarised in the following table:

Table F.5 Deflection increments

Nr. of the section in consideration, m **[-]**	**w_m** **[mm]**
1	6.94
2	6.81
3	6.58
4	6.24
5	5.80
6	5.29
7	4.70
8	4.06
9	3.37
10	2.64
11	1.89
12	1.14
13	0.38

Step 9: Calculating the total deflection

Finally, the total mid-span deflection can be calculated as the sum of the deflection increments:

$$\bar{w} = \sum_{m=1}^{n_p} w_m = 55.82\ mm \tag{F.30}$$

F.4.3 Summary of the results

The calculation presented in the previous section was repeated for 30 equally spaced load increments between 0 and M_{el} given by equation (F.10) . The following table summarises the obtained results:

Table F.6 Mid-span deflection at different load steps

Step	Moment [kNm]	Deflection [mm]
0	0	0
1	57.1	2.68
2	114.2	5.35
3	171.2	8.03
4	228.3	10.71
5	285.4	13.39
6	342.5	16.10
7	399.5	19.14
8	456.6	22.90
9	513.7	27.69
10	570.8	33.09
11	627.9	38.60
12	684.9	44.25
13	742.0	49.85
14	799.1	55.37
15	856.2	60.95
16	913.2	66.39
17	970.3	71.90
18	1027.4	76.92
19	1084.5	81.57
20	1141.6	86.12
21	1198.6	90.64
22	1255.7	95.10
23	1312.8	99.58
24	1369.9	104.06
25	1426.9	108.52
26	1484.0	112.99
27	1541.1	117.45
28	1598.2	121.90
29	1655.3	126.35
30	1712.3	130.80

The comparison of the analytically and numerically obtained deflections is presented in the following figure:

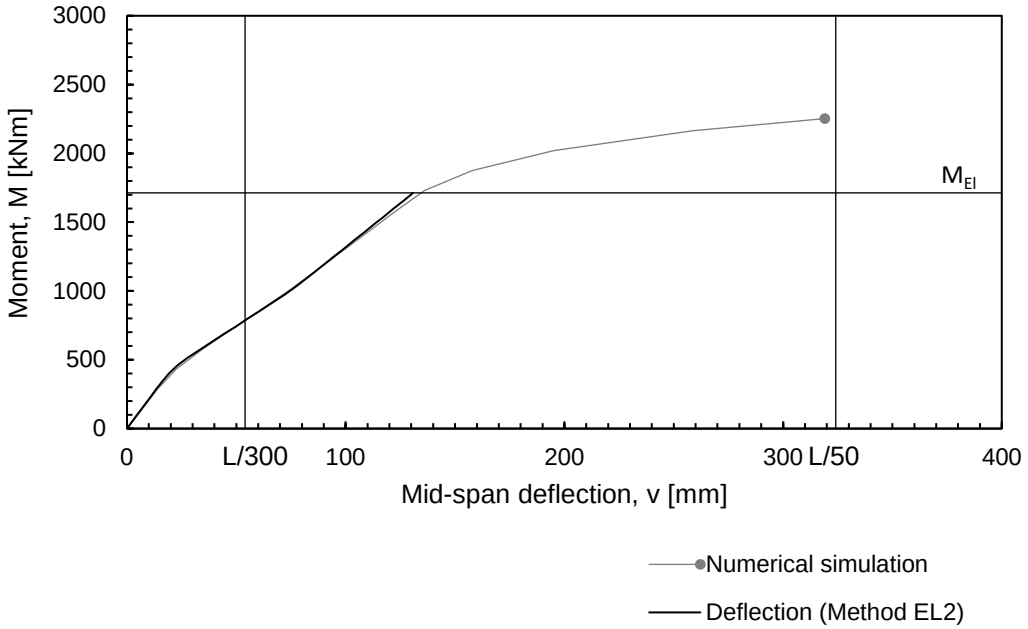

Figure F.5 Comparison of the analytically and the numerically obtained results (Method EL2)

F.5 Plastic moment resistance calculation (Method PL1)

For the determination of the plastic moment resistance, it is necessary to assume an end slip and a slip distribution function.

The assumed slip distribution function is a cosine function:

$$s(x) = \bar{s} \cdot \cos\left(\frac{\pi \cdot x}{L}\right) \tag{F.31}$$

The end slip that can be taken into account can be approximated with the following formulation:

$$\bar{s} = \min\left\{\begin{matrix}\delta_u \\ s_{ult,0} \cdot (1-\psi)\end{matrix}\right\} \tag{F.32}$$

Where:

$\delta_u = 9.7\ mm$ is the slip capacity of the shear connection.

In the equation below σ = 0 because of propped construction and α = 2/3 for a uniformly distributed load.

$$s_{ult,0} = \alpha \cdot \frac{L}{2} \cdot \frac{1.5 \cdot f_y - \sigma}{E_a}\left(1 + \frac{h_c + h_p}{0.5 \cdot h_a}\right) = 23.8\ mm \tag{F.33}$$

The degree of interaction can be calculated as:

$$\psi = \frac{I_{y,eff} - \left(I_{y,a} + \frac{I_{y,c}}{n}\right)}{I_{y,rigid} - \left(I_{y,a} + \frac{I_{y,c}}{n}\right)} \tag{F.34}$$

The effective second moment of area has been determined by equation (F.3):

$$I_{y,eff} = 1.809 \cdot 10^9\ mm^4 \tag{F.35}$$

The second moment of area for rigid connection is:

$$I_{y,rigid} = I_{y,a} + \frac{I_{y,c}}{n} + \frac{A_c A_a}{A_c + nA_a} \cdot a^2 = 3.093 \cdot 10^9\ mm^4 \tag{F.36}$$

The degree of interaction is then:

$$\psi = \frac{1.809 - \left(0.921 + \frac{1.139}{4.99}\right)}{3.093 - \left(0.921 + \frac{1.139}{4.99}\right)} = 0.34 \tag{F.37}$$

The end slip to be taken into account:

$$\bar{s} = \min\begin{Bmatrix} \delta_u \\ s_{ult,0} \cdot (1-\psi) \end{Bmatrix} = \min\begin{Bmatrix} 9.7 \\ 23.8 \cdot (1-0.34) \end{Bmatrix} = 9.7\ mm \qquad \text{(F.38)}$$

It is now possible to determine the occurring slip at each shear connector, and to calculate the corresponding shear forces:

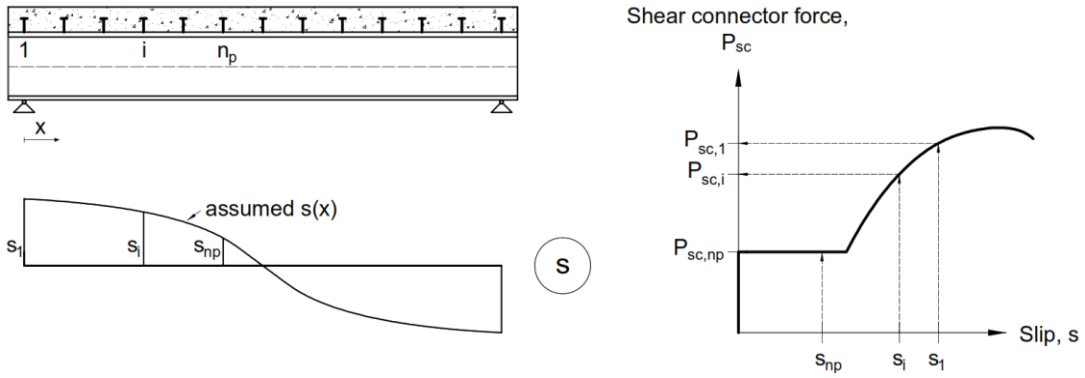

Figure F.6 Determination of the shear connector forces using the load-slip curve

Table F.1 Obtained slip and force values

Nr. of the shear connector, i **[-]**	$\frac{(i-1)}{n_p} \cdot \frac{\pi}{2}$ **[deg]**	$\cos\left(\frac{(i-1)}{n_p} \cdot \frac{\pi}{2}\right)$ **[-]**	**Slip, s_i [mm]**	**Force, $P_{sc,i}$ [kN]**
1	0.000	1.000	9.73	144.40
2	6.923	0.993	9.66	143.39
3	13.846	0.971	9.45	140.38
4	20.769	0.935	9.10	135.41
5	27.692	0.885	8.62	128.56
6	34.615	0.823	8.01	119.92
7	41.538	0.749	7.29	109.63
8	48.462	0.663	6.45	97.82
9	55.385	0.568	5.53	84.67
10	62.308	0.465	4.52	70.35
11	69.231	0.355	3.45	55.09
12	76.154	0.239	2.33	44.65
13	83.077	0.121	1.17	37.74

The effective shear connection force is defined as the average shear force:

$$P_{R,eff} = \frac{1}{n_p}\sum_{i=1}^{n_p} P_{sc,i} = 100.9\ kN \tag{F.39}$$

The maximum normal force that can be taken by the steel beam:

$$N_{pl,a} = A_a \cdot f_y = 6099\ kN \tag{F.40}$$

The maximum normal force that can be taken by the flanges:

$$N_{pl,f} = 2 \cdot b \cdot t_f \cdot f_y = 4369\ kN \tag{F.41}$$

The maximum normal force that can be taken by the web:

$$N_{pl,w} = \left(h_a - 2 \cdot t_f\right) \cdot t_w \cdot f_y = 2637\ kN \tag{F.42}$$

The maximum normal force that can be taken by the concrete:

$$N_{c,max} = A_c \cdot 0.85 \cdot f_c = 27884\ kN \tag{F.43}$$

The normal force in case of full connection:

$$N_{c,f} = \min(N_{pl,a}; N_{c,max}) = 6099\ kN \tag{F.44}$$

The normal force that develops in the concrete:

$$N_c = \min(N_{c,f}; n_{sc} \cdot P_{R,eff}) = \min(6099\ kN; 26 \cdot 100.9\ kN) = 2624\ kN \tag{F.45}$$

The degree of shear connection:

$$\eta = \frac{N_c}{N_{c,f}} = 0.43 \tag{F.46}$$

The minimum degree of shear connection:

$$\eta_{min} = 1 - \left(\frac{355}{f_y}\right)(0.75 \cdot 0.03 L_e) = 0.44 \tag{F.47}$$

Note: In this example, the requirement for the minimum degree of shear connection (equation (F.47)) is not taken into account.

Plastic neutral axis of the concrete (measured from the top fibre of the concrete):

$$z_{pl,c} = \frac{N_c}{B_{eff} \cdot 0.85 \cdot f_c} = 14.1\ mm \tag{F.48}$$

Location of the plastic neutral axis of the steel:

If $N_{pl,a} > N_c > N_{pl,w,}$, the plastic neutral axis is in the flange. (F.49)

If $N_{pl,w} > N_c$, the plastic neutral axis is in the web. (F.50)

$N_{pl,w}$ = 2637 kN > N_c =2624 kN, so the plastic neutral axis is in the web.

The corresponding stress distribution:

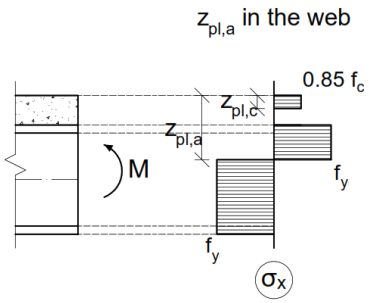

Figure F.7 Stress distribution according to the partial shear theory

Location of the plastic neutral axis of the steel from the equilibrium equation (measured from the top fibre of the concrete):

$$z_{pl,a} = \frac{N_{pl,w} - N_c}{2 \cdot N_{pl,w}} \cdot \left(h_a - 2 \cdot t_f\right) + h_{tot} + t_f = 170.4\ mm \tag{F.51}$$

The plastic moment resistance from the moment equation

$$\begin{aligned} M_{pl,\eta} = {} & N_{pl,a}\left(h_{tot} + y_a - \frac{z_{pl,c}}{2}\right) - N_{pl,f}\left(h_{tot} - \frac{z_{pl,c}}{2} + \frac{t_f}{2}\right) \\ & - 2\left(z_{pl,a} - h_{tot} - t_f\right) t_w f_y \left(\frac{z_{pl,a} - h_{tot} - t_f}{2} + h_{tot} + t_f - \frac{z_{pl,c}}{2}\right) \end{aligned} \tag{F.52}$$

$M_{pl,\eta} = 2201\ kNm$

Figure F.8 shows the calculated moment capacity on the moment-deflection curve obtained by numerical simulation.

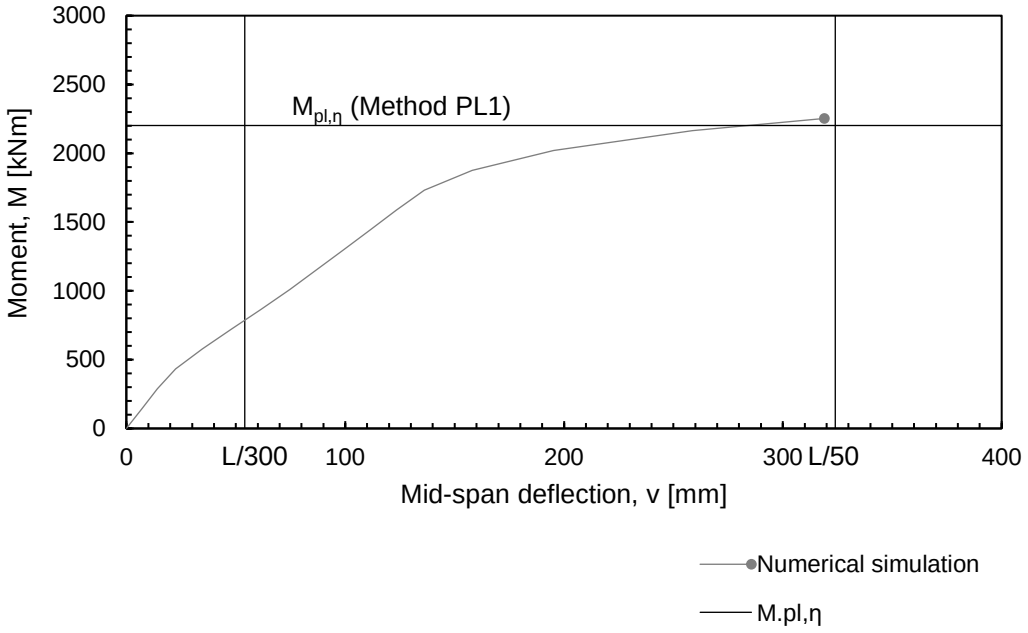

Figure F.8 Comparison of the numerically and analytically obtained plastic moment resistance (Method PL1)

F.6 Simplified calculation of the plastic moment resistance (Method PL2).

The simplified calculation method uses a shear connector specific k_{flex} reduction factor that was determined based on the assumptions presented in chapter 9.4.3.

The reduction factor that belongs to shear connection type P3.3 is k_{flex} = 0.756. The effective shear connector resistance is:

$$P_{R,eff} = k_{flex} \cdot P_{R,6} = 0.756 \cdot 91.4\ kN = 69.1\ kN \quad \text{(F.53)}$$

The normal force that develops in the concrete:

$$N_c = \min(N_{c,f}; n_{sc} \cdot P_{R,eff}) = \min(6099\ kN; 26 \cdot 69.1\ kN) = 830\ kN \quad \text{(F.54)}$$

The degree of shear connection:

$$\eta = \frac{N_c}{N_{c,f}} = 0.14 \quad \text{(F.55)}$$

Note: In this example, the requirement for the minimum degree of shear connection (equation (F.47)) is not taken into account.

Plastic neutral axis of the concrete (measured from the top fibre of the concrete):

$$z_{pl,c} = \frac{N_c}{B_{eff} \cdot 0.85 \cdot f_c} = 4.5\ mm \quad \text{(F.56)}$$

Location of the plastic neutral axis of the steel:

If $N_{pl,a} > N_c > N_{pl,w,}$, the plastic neutral axis is in the flange. (F.57)

If $N_{pl,w} > N_c$, the plastic neutral axis is in the web. (F.58)

$N_{pl,w}$ = 2637 kN > N_c =830 kN, so the plastic neutral axis is in the web.

The corresponding stress distribution:

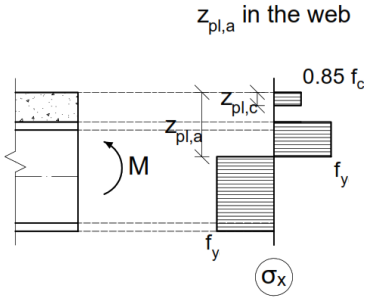

Figure F.9 Stress distribution according to the partial shear theory

Location of the plastic neutral axis of the steel from the equilibrium equation (measured from the top fibre of the concrete):

$$z_{pl,a} = \frac{N_{pl,w} - N_c}{2 \cdot N_{pl,w}} \cdot \left(h_a - 2 \cdot t_f\right) + h_{tot} + t_f = 3601.6\ mm \tag{F.59}$$

The plastic moment resistance from the moment equation

$$M_{pl,\eta} = \left(N_{pl,a}\left(h_{tot} + y_a - \frac{z_{pl,c}}{2}\right) - N_{pl,f}\left(h_{tot} - \frac{z_{pl,c}}{2} + \frac{t_f}{2}\right) - 2\left(z_{pl,a} - h_{tot} - t_f\right) t_w f_y \left(\frac{z_{pl,a} - h_{tot} - t_f}{2} + h_{tot} + t_f - \frac{z_{pl,c}}{2}\right)\right) \tag{F.60}$$

$M_{pl,\eta} = 1741\ kNm$

The following figure shows the calculated moment capacity on the moment-deflection curve obtained by numerical simulation:

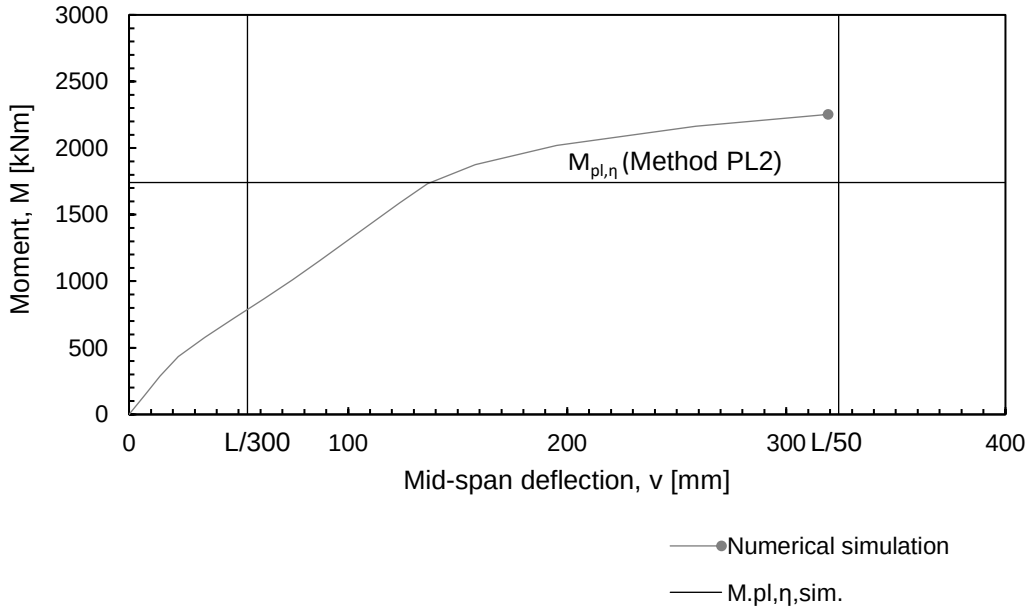

Figure F.10 Comparison of the numerically and analytically obtained plastic moment resistance (Method PL2)

F.7 Summary of the results

The following figure summarises the results of the presented calculation example:

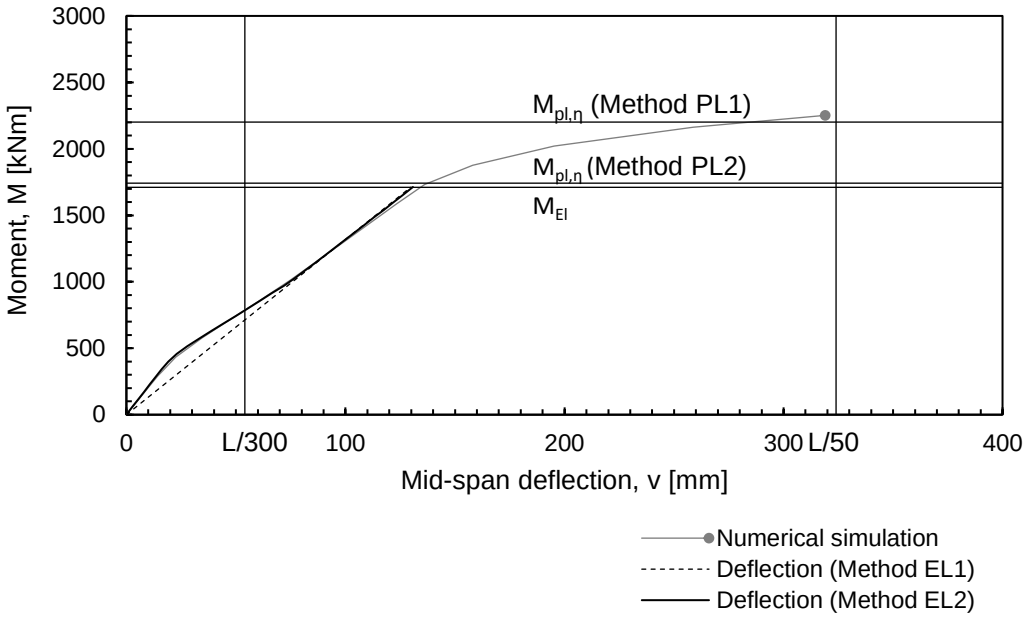

Figure F.11 Comparison of the numerically and analytically obtained results

Annex G Analytical calculations vs. experimental measurements

The calculations presented in Annex F were performed for the tested beams (Chapter 5) and the results of the calculations were compared to the experimental measurements. The following figure shows the obtained moment-deflection curves.

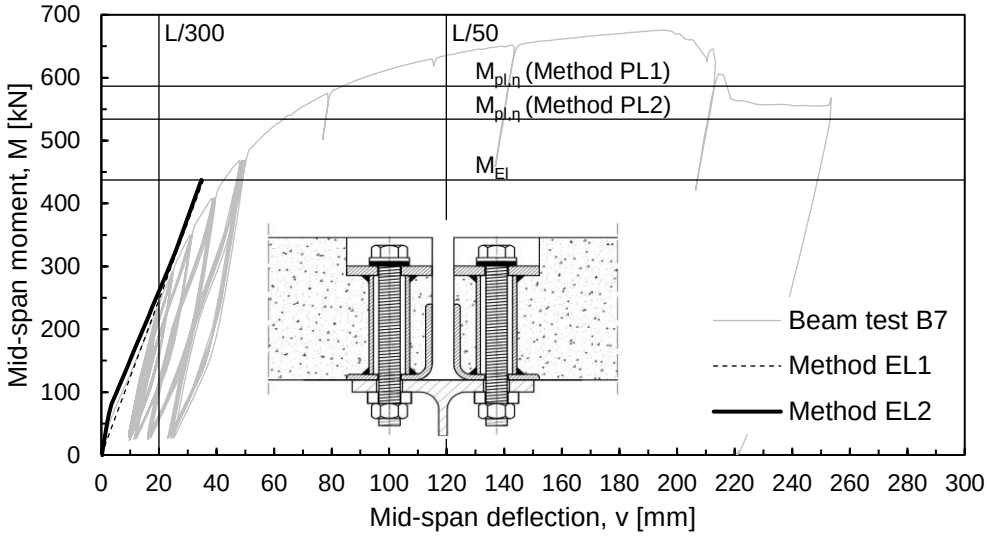

Figure G.1 Comparison of the experimentally and analytically obtained results (Beam B7)

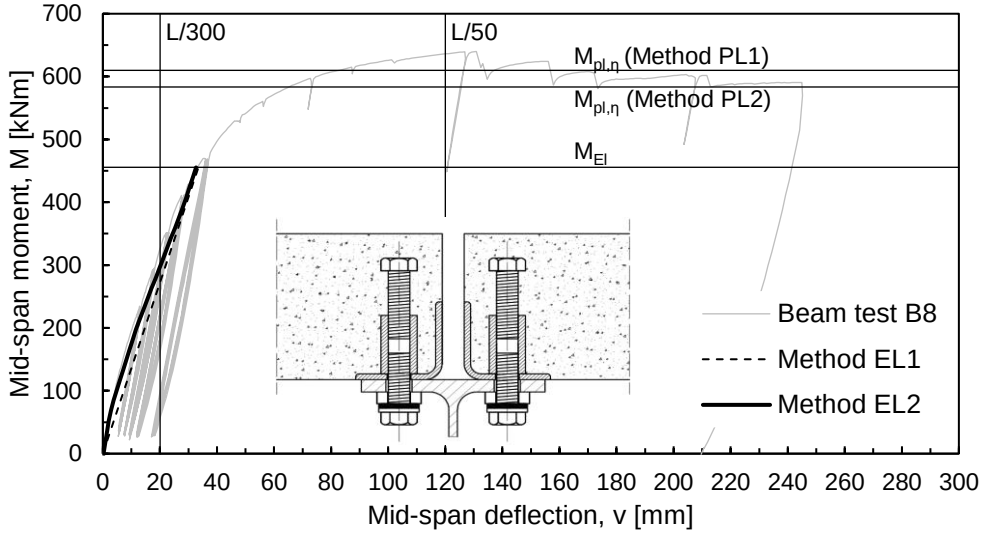

Figure G.2 Comparison of the experimentally and analytically obtained results (Beam B8)